Revisiting key observational evidence for dark matter and dark energy

A dissertation submitted by

Clémentine Hauret

in partial fulfillment of the requirements
for the degree of Doctor of Philosophy in Science

Université de Liège

Faculté des Sciences
Département AGO - Unité de recherche STAR

Members of the Jury:

Pr. Pierre Magain	Supervisor
Pr. Marc-Antoine Dupret	President
Dr. Dominique Sluse	Secretary
Dr. Christian Barbier	
Pr. Frédéric Courbin	
Dr. Damien Hutsemekers	

If people sat outside and looked at the stars each night,
I'll bet they'd live a lot differently.

Bill Watterson
Calvin and Hobbes, 30 June 1992

Abstract

Nowadays, one of the most decisive challenge Science has to face arises from cosmology and its representation of the universe as vastly dominated by its elusive dark content. In this thesis, we focus on two key observations that first imposed dark matter and dark energy into the models of the universe: the rotation curves of spiral galaxies and the distance-redshift relation of type Ia supernovae. For both these observations, we analyze the methodologies currently implemented to process the data and hence, constrain the dark content of the universe. Pointing out some common approximations and simplifications, we develop more realistic alternatives in order to quantify their impacts.

Concerning the spiral galaxies, we perform a multiwavelength modeling of all their luminous components (stars, atomic and molecular gases, dust). Comparing the rotation curve predicted by this modeling and the observed one for a sample of six galaxies, we characterize their dark matter content. In this analysis, we bring to light the significant impact of the simplifications usually implemented when modeling the stellar populations.

When studying type Ia supernovae, we warn about the potential bias caused by the use of a cosmological model when standardizing these data. We thus develop a cosmology-independent calibration, with the same degree of complexity as the usual one. When tested on a compilation of several hundreds of these objects, we find no problem of bias in data but we nevertheless advise to use our model-independent methodology if other objects in smaller samples are considered.

Résumé

L'un des défis les plus importants auquel la Science doit faire face aujourd'hui est issu du domaine de la cosmologie et de sa représentation de l'Univers comme d'un object dominé par un déconcertant contenu en matière et énergie sombres. Dans cette thèse, nous nous concentrons sur deux observations clés, les premières à imposer ces deux composants dans les modèles représentants l'Univers: les courbes de rotation de galaxies spirales et la relation distance-redshift des supernovae de type Ia. Pour chacune de ces observations, nous analysons les méthodologies actuellement mises en place pour traiter ces données et contraindre le contenu sombre de notre Univers. Ainsi, nous nous concentrons sur différentes approximations ou simplifications couramment réalisées et en évaluons les impacts en développant des alternatives plus réalistes.

Concernant les galaxies spirales, nous en modélisons tous les composants (étoiles, gaz atomique et moléculaire, poussière) à partir d'images obtenues dans différents domaines de longueur d'onde. De la comparaison entre les courbes de rotation observées et celles prédites par nos modélisations, nous caractérisons le contenu en matière sombre d'un échantillon de six galaxies. Lors de notre analyse, nous mettons en évidence l'impact significatif des simplifications habituellement utilisées lors de la modélisation des populations stellaires de ces galaxies.

Pour les supernovae de type Ia, nous mettons en garde contre un biais potentiel causé par l'utilisation d'un modèle cosmologique lors de la standardisation de ces objects. Nous développons donc une calibration indépendente de toute cosmologie et de même degré de complexité que celle couramment utilisée. En l'appliquant sur un ensemble de plusieurs centaines de supernovae, nous ne trouvons aucune trace de biais en faveur du modèle cosmologique employé. Nous conseillons néanmoins d'utiliser notre calibration lorsque le nombre d'objects à standardiser est restreint.

Remerciements

It is good to have an end to journey toward;
but it is the journey that matters, in the end.

Ursula K. Le Guin
The Left Hand of Darkness, 1969

... As well as the company with whom you travel.

Clémentine Hauret
This thesis, 2022

Parce que cette thèse n'aurait jamais pu être menée à son terme sans les nombreuses personnes que j'ai rencontrées, avec qui j'ai travaillé et vécu durant toutes ces années, voici aujourd'hui ma chance de pouvoir tous vous remercier.

Merci tout d'abord aux membres du jury d'avoir pris sur leur temps pour lire et juger ce travail.

Pierre, sans toi, je n'aurais jamais pu vivre cette aventure qu'est le doctorat. Merci d'avoir cru en moi et de m'avoir donné la possibilité de réaliser cette thèse. J'ai tellement appris sur moi et sur ce à quoi je voulais que ma vie ressemble grâce à ça. Merci pour nos discussions d'où je ressortais toujours pleine d'enthousiasme et de motivation, toi qui ne manque jamais d'idées folles et inspirantes.

Merci à tous mes collègues, anciens et actuels, d'avoir fait de ce petit coin du Sart-Tilman un endroit aussi agréable. Merci à Pierre, Dominique, Manu, Michaël et Michaël, Marc-Antoine, Valérie et Damien de m'avoir accueillie si naturellement et de façon si bienveillante à l'étage. Merci à Sandrine et à Angela de toujours réagir au quart de tour quelque soit le problème que je peux rencontrer et de prendre tant soin de l'étage et du département. Merci également à tous mes collègues physiciens qui ont aussi

grandement contribué à rendre mon travail agréable et amusant. Merci à Christelle, à Jack (notre maman des TPs), à Jean-Marc, à tous les assistants et assistantes, aux motivés de chez Young Minds et aux superbes projets que nous avons développé ensemble.

Merci à tous les doctorants et post-docs qui sont passés au cours de ces dernières années. Merci à ceux qui m'ont accueillie et appris les ficelles du métier, Maïté, Laeti, Cyrielle, Audrey, Sébastien, Gaël. Merci à ceux qui m'ont accompagné pendant quelques années, Sylvain, Artem, Sampath, Aurore, Catarina, Sophie, Matt. Et merci aux (plus ou moins) petits nouveaux, Lorenzo, Guillaume, Mathieu, Mathilde, Loïc, Antoine (grâce à qui la cuisine se transforme petit à petit en forêt amazonienne, merci d'avoir apporté l'émerveillement du jardinage dans ma fin de thèse), Irene (merci pour ton aide pour les PhD Days et pour ton implication pour les doctorants du département). Merci à Fran et à Manu pour les pauses thés/papote, les concours puzzle, les soupers de Noël pour lesquels il va nous falloir privatiser *Les folies gourmandes*. Enfin, un énorme merci à cette incroyable bande qu'ont été Charly, Elsa, Martin et Lionel. Impossible de décrire l'ambiance géniale des années où nous étions tous là. Merci pour les temps de midi esquisse, les matchs de minifoot, les pauses cafés, les soirées crêpes ou boudin, les barbecues dans le jardin de l'AGO et toutes ces petites choses que j'oublie mais qui font que, plus que des collègues, ce sont de vrais amis que je me suis fait en chemin.

Comment parler de personnes incroyables sans évoquer mes merveilleuses collègues de bureau? Vous avez mis la barre tellement haut pour les prochains, je ne sais vraiment pas si vous pourrez être égalées. Merci à toutes les deux pour les nombreuses discussions, questionnements, projets scientifiques ou non et surtout pour l'aide que vous n'avez jamais hésité à m'apporter. Jude, qui de mieux que toi pour découvrir avec moi l'aventure du doctorat! Merci d'avoir redécoré le bureau de jouets et d'affiches de Star Wars. J'ai par contre le regret de te dire que nous n'avons plus eu d'attaques de velociraptors depuis ton départ. Fais bien attention, c'est sûrement toi qui les attirais. Lyne, merci pour ton enthousiasme à toute épreuve, pour la fraicheur que tu apportes au bureau, pour la cagnotte à glace et les Happy Hours. Avec toi comme nouveau parrain de l'étage, je ne me fais pas de doute quant à l'ambiance qui y règnera cette prochaine année.

Il m'est impossible de lister les gens qui ont permis à cette thèse de voir le jour sans parler de Jerem, d'Élo, de Lulu, d'Antoine, de Maju et de Jipé,

mes compagnons d'aventure, mes acolytes toujours là pour me soutenir et me donner des idées de projets fous. Merci les gars, il n'y a pas de mots pour décrire la chance que j'ai d'avoir des amis comme vous.

Je ne serais pas non plus arrivée là où j'en suis sans ma famille qui m'a toujours poussée à poursuivre mes rêves. Maman, Papa, je vous dois tout, vous qui m'avez donné les moyens d'y arriver. Vous ne pouvez pas savoir à quel point je vous en serai à jamais reconnaissante. Merci Math, toi qui as toujours cru en moi, j'espère être à la hauteur de tes attentes. Merci à Bon-Pa, Bonne-Ma, parrain, marraine de m'avoir toujours aidée et soutenue. Merci aussi à Jimmy, Évelyne, Hugues et Yves de m'avoir accueillie, vous êtes maintenant ma famille liégeoise.

Enfin, je n'aurai jamais les mots pour remercier Sylvain à la hauteur de tout ce qu'il a fait pour moi pendant toutes ces années. Jamais cette thèse n'aurait pu voir le jour sans toi, sans ton infaillible soutien, tes folles idées et ta façon si singulière de voir le monde. Tout le temps que tu as passé sur le manuscrit n'est que la pointe émergée d'un immense iceberg. Merci pour tout!

Contents

Introduction

There is a theory which states that if ever anyone discovers
exactly what the Universe is for and why it is here,
it will instantly disappear and be replaced by
something even more bizarre and inexplicable.
There is another theory which states that this has already happened.

Douglas Adams
The Restaurant at the End of the Universe, 1980

The 20th century witnessed the explosion of a great number of scientific fields, completely reshaping our views of the universe on all scales, infinitely large as well as infinitely small. In less than a hundred years, cosmology sprung up and metamorphosed from a highly speculative discipline to a mature and predictive science, with complementary theoretical and observational faces that brought to the surface some of the most mysterious and challenging questions Science has nowadays to answer. If the world in the 1900s was limited to our own galaxy, the universe is now seen as an infinitely vast object of puzzling composition.

Our best model of the universe portrays it as spatially flat, in an accelerated expansion and composed of only 5% of ordinary matter, that is to say, of matter effectively described by the current Standard Model of particle physics. The rest of its content is still not formally understood and constitutes nowadays the biggest challenge new-born cosmology has to face. Over the unknown remaining 95%, around a quarter is expected to be made of dark matter, a massive non-luminous component, only indirectly observable through its gravitational interaction with ordinary matter. Despite decades of intensive experimental, observational and theoretical efforts, no

proposed explanation on its nature has been confirmed to date. Even more elusive, the last constituent of the universe is called dark energy and manifests itself only at incredibly large scales, when the universe as a whole is modeled.

Nevertheless, despite these blanks in our theories, the mathematical description of the universe and of its constituting objects has succeeded for two decades in explaining an increasingly varied and precise number of observations. Among these, two observations have been the pillars on which this standard model of cosmology is built: the rotation curves of spiral galaxies and the distance-redshift relation of type Ia supernovae. Those two key observations each lifted the veil, in the early 1980s and in the late 1990s, on respectively dark matter and dark energy and imposed these components on the cosmological chessboard.

The mass distribution of a spiral galaxy can be deduced from two different observations, either directly from its luminous matter or indirectly from the velocity at which the galaxy rotates on itself. These two modelings not being in agreement with each other, the study of such objects suggests that a dominant portion of the galaxies is composed of non-luminous, or dark matter. Similarly, modeling the relation between the distance and the redshift of the constitutive objects of the universe is the most direct method to probe its dynamical evolution, the more distant the object, the more constrained the results. When computed for type Ia supernovae, this relation reveals an unexpected feature of the evolution of the universe, the acceleration of its expansion, sign that its mass/energy budget is dominated by an exotic, repulsive component called dark energy.

In this thesis, we focus on these two key observations and study the methodologies usually followed to analyze them and hence characterize the dark content of the universe. We question the approximations and assumptions, inherent to these methodologies, and implement more realistic, coherent and sound alternatives. This manuscript is thus divided into three parts. The first one is dedicated to the study of spiral galaxies and of their rotation curves. In this, we develop a complete modeling of all the luminous and dark components of these objects. The second part of this work is centered on the observations and on the use of type Ia supernovae data. The conclusions and perspectives of these two different works are then gathered in the last part of this thesis.

I

Part I

Dark matter & Galactic rotation curves

Chapter 1

Galactic rotation curves
Principles and theoretical bases

In mechanics, gravitation connects the two concepts of velocity and mass, velocity being a primary tool to indirectly probe the mass of objects. This powerful relation has lead to incredible revolutions in astrophysics and cosmology. Notable examples are the characterization of the Sun and of the Solar System, the discoveries of the very first exoplanets or the observations of mass discrepancies in galactic and in extragalactic environments, leading to postulate the existence of an entirely new kind of matter, the dark matter (DM). All of these opened entirely new fields of study and triggered complete reshapings of our vision of the world. In this work, we will focus on the application of this velocity-mass relation on galactic scales, particularly when it is used to study and analyze the composition of spiral galaxies.

Constituted of stars and of interstellar medium (ISM) gas and dust clouds distributed in a thin disk, these galaxies display a global rotation. Their rotation curves (RC), that is to say, the evolution of their rotation velocity with respect to the distance to their centers, are then one of the primary tool to understand and probe their mass distributions. As will be explained in Section 1.1, these RCs are constructed from measurements of the Doppler shifts observed on particular lines emitted or absorbed by the rotating matter within galaxies.

To be a good tracer of the galactic rotation, the emitting/absorbing objects have to be dynamically cold, that is to say, their velocity dispersion

has to be low compared to their rotation velocity. For such objects, it is then reasonable to approximate their motions by circular orbits around the galaxy center and to compute their rotation velocities from the observed shift of their spectral lines. In spiral galaxies, the disk is principally composed of gas clouds and of population I stars, two components well suited to play the role of a rotation tracer.

On the contrary, population II stars (mostly found in the galactic bulges and halos) are not used in RC context as they have less-organized motions with higher velocity dispersions. Similarly, the other main type of galaxies, the elliptical ones, cannot be the objects of RC studies either as they are pressure-supported systems. Their constitutive stars present random, non-organized motions. If the total mass of such elliptical galaxies is easily computable from the determination of their mean stellar velocities via the Virial theorem, the derivation of their mass distributions necessitates advanced observations and more complicated methods (such as spatially resolved stellar kinematics, X-ray observations or gravitational lensing).

Logically, the first studies computing the mass distributions of galaxies from velocity measurements came from the simpler systems that are the rotation-supported spiral galaxies. To do so, assumptions have to be made on the three-dimensional (3D) structure of the galaxies. The most simplifying hypothesis describes the mass distributions of spiral galaxies as spheres instead of thin disks. If this assumption is largely incorrect, it is nevertheless useful here to describe the general idea behind the analyses of spiral galaxies RCs. In the case of spherical symmetry, it is well known that the motion of a test particle of negligible mass located at a distance r from the center of the galaxy is only impacted by the total mass $M(r)$ of the sphere embedded inside the circular orbit of that particle, independently of both the mass outside or the mass distribution inside the orbit. The particle will then move as if all the mass $M(r)$ was located at the center of the galaxy.

Mathematically, the gravitational and the centripetal accelerations on this particle being equal, its circular velocity[1] is given by the very simple

[1]Strictly speaking, a distinction should be made between the circular velocity v_c (i.e. the theoretical velocity of test particles on circular orbits) and the rotation one $v_{\rm rot}$ (i.e. the measured velocity of the objects within the galaxy). However, when the movement of these objects is dominated by a global rotation and not by random motions, that is to say, when these objects are dynamically cold, these two velocities are equivalent. As RCs of spiral galaxies are derived from observations of such objects, we will use these terms interchangeably in this work, unless explicitly noted.

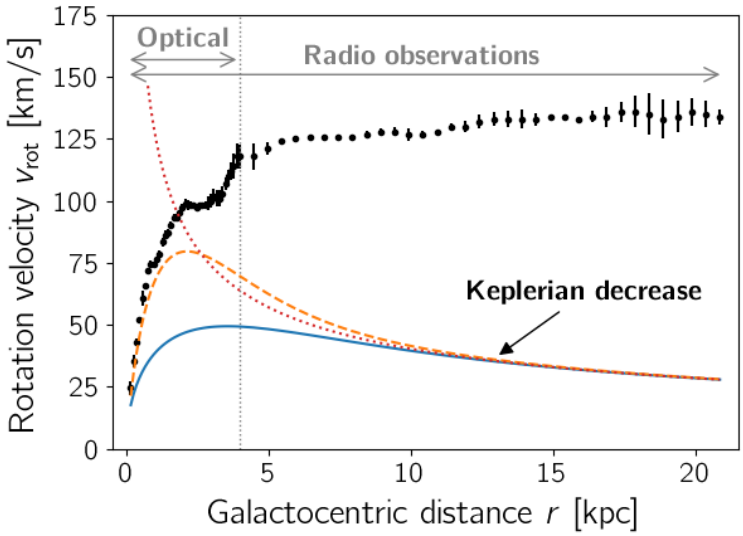

Figure 1.1: RC of a typical spiral galaxy (NGC2403): discrepancy between the observed RC (black dots) and the ones expected from modeling the galactic luminous matter (curves). The observed RC is derived from optical and radio images combined by Lelli et al. (2016a) from observations by Daigle et al. (2006) (Hα line) and Fraternali et al. (2002) (HI 21 cm line). The optical observations are restricted to the visible disk whose limit is symbolized by the vertical grey line. The predicted RCs assume various galactic mass distributions: (i) all the mass is located at the center (pure keplerian decrease; dotted red line), (ii) spherically symmetric distribution (from Equation 1.1; solid blue line) and, (iii) a more physically accurate distribution as a thin disk (from the analytical formula by Freeman 1970; dashed orange line). In all cases, the observed RC and its flat plateau cannot be explained by the luminous matter only.

expression

$$v_c(r) = \sqrt{\frac{GM(r)}{r}} \tag{1.1}$$

where G is the gravitational constant. This behavior is illustrated by the solid blue line in Figure 1.1. Far from the galactic center, when the ob-

served luminous matter fades away (at the right of the vertical grey line), we can reasonably assume that the mass embedded in test particles' orbits tends towards a constant, the total mass of the galaxy. At these distances, the associated circular velocity varies as $v_c(r) \sim r^{-1/2}$, often referred as a keplerian decrease. Nevertheless, since the first observations and computations of RCs, this decrease has virtually never been recorded. Real spiral galaxies rather show a flat RC, i.e. a RC whose velocity at medium and high galactocentric distances reaches and stays on a plateau of constant value, shown by the data points in the figure.

This discrepancy between the observed flat RC (whose shape will be further described in Section 1.2) and the keplerian decrease, that is expected from the galactic distribution of luminous matter (developed in Section 1.3.1), has lead to the idea that spiral galaxies contain more mass than originally thought and more importantly, that this mass in excess should be emitting little to no light at all (as explained in details in Section 1.3.2). The idea of DM was born and slowly pervaded cosmology to become nowadays an unmissable component in the models of our universe and of its constituents (galaxies but also clusters and superclusters).

1.1 Computing rotation curves, a historical perspective

Historically, RCs were first obtained from measurements in the visible domain with long-slit spectroscopy. Aligning the slit with the galaxy major axis, as shown in panel (a) of Figure 1.2, several spectra are taken at various galactocentric distances, revealing the absorption lines of stars and the emission lines of ionized gas (panel (b)). A line particularly useful in this domain is the brightest line of the Balmer series, the Hα line at 656nm, that traces the ionized hydrogen gas. The Doppler shifts as well as the intensities and profiles of the observed lines are then converted into a position-velocity (PV) diagram (panel (c)), showing the receding (left) and the approaching (right) portions of the galaxy. This methodology can only be used on galaxies that are inclined with respect to the plane of the sky as the Doppler shifts only measure the velocities components that are directly aligned with the line-of-sight of the observer. Hence, the more face-on the galaxy, the smaller the shifts and the more uncertain the final RC (with the extreme case that RCs of face-on galaxies are impossible to construct from these observations). Finally, the RC (panel (d)) is obtained through a

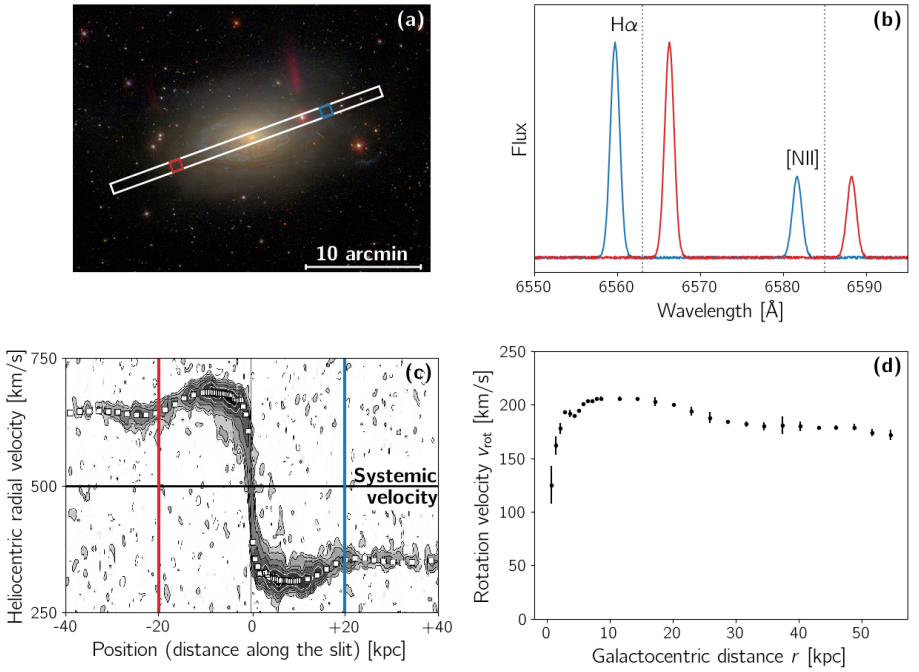

Figure 1.2: Illustration of the principle and final products of long-slit spectroscopy. *Panel (a):* SDSS optical image of NGC5055 (© 2006 M.R. Blandon and D.W. Hogg) and representation of a slit aligned with its major axis. *Panel (b):* Schematic of the spectra taken in the red (resp. blue) portion of the slit and associated to a receding (resp. approaching) zone of the galaxy. The vertical lines correspond to the rest wavelength of the emission lines Hα and [NII]. *Panel (c):* Position-velocity diagram (Battaglia et al. 2006) built from the Doppler shift converted in radial velocity and from the profile of one of the emission lines. The red and blue marks indicate the position of the red and blue squares of panel (a). *Panel (d):* Associated RC, computed from the deprojection of the PV diagram (data combined by Lelli et al. (2016a) from observations by Battaglia et al. 2006 and Blais-Ouellette et al. 2004).

deprojection of the PV diagram, transforming the observed radial velocity into a rotation velocity and taking into account the systemic velocity of the galaxy (i.e. its velocity with respect to the observer due to the Hubble flow and to its peculiar motion). Using this method, the RC of our closest galactic neighbor, Andromeda, was computed in 1939 by Babcock during its PhD thesis (Babcock 1939) and thereby became the first of a long list of flat RCs destined to shake up the astrophysical and cosmological communities.

These first RCs were nevertheless limited, both spatially, by the extension of the visible disk they were observing, and photometrically by the amount of light received. Indeed, dust within the observed galaxy attenuates and even hides some portions of it. But this situation was about to completely change as a whole new range of wavelengths opened to the astronomers in the 1930s: the radio domain and, with it, the most famous emission line in astrophysics, the 21 cm line of neutral hydrogen (HI). This line, theoretically predicted in 1944 (van de Hulst 1945) and effectively observed seven years later (Ewen & Purcell 1951; Muller & Oort 1951), is the result of the spin transition of the electron in the ground state of a hydrogen atom, the electron passing from a situation where its spin is parallel to the one of the proton to a situation where they are anti-parallel. Despite being a forbidden transition with a very low probability of spontaneous emission (the mean lifetime of an electron in the associated high-energy level reaches 11 Myr; Wiese & Fuhr 2009), this line is nevertheless observable in a variety of astrophysical environments due to the immense number of hydrogen atoms in the universe.

The ISM of spiral galaxies being principally composed of clouds of neutral gas, dynamically cold and distributed more or less uniformly across the whole galaxy, the 21 cm line quickly became the primary tool to study galactic kinematics. The first maps of neutral hydrogen in the Milky Way (MW) and their associated RCs were computed only one year after the first detection of the 21 cm line (Longair 2006) and the first RC of another galaxy than ours (once again our neighbor Andromeda) was published quickly after (van de Hulst et al. 1957). With the latter came the discovery of another important but unexpected advantage of using neutral hydrogen for the study of galactic kinematics: the neutral gas' spatial extension allows to construct RCs up to the far outskirts of the galaxies, way beyond the visible disk probed by the previous studies. Probing the outskirts, however, still showed no sign of velocity decrease.

Due to the longer wavelengths used in radio astronomy, an intrinsic limitation comes from the difficulty to acquire spatially resolved images and compute the associated RCs. Historically, the single-dish telescopes used during measurements only allowed resolved observations of galaxies up to distances of 2–3 Mpc (Sanders 2010). Despite this limitation, the single-dish radio astronomy still brought important results to the domain, such as the Tully-Fisher relation[2] (Tully & Fisher 1977).

To reach spatial resolutions sufficient to compute RCs of distant galaxies with observations of the 21 cm line, it is necessary to increase the size of the telescopes by splitting the main dish into several antennas, using interferometry to combine the signals. This technique, first developed with optical telescopes in the 1920s (Michelson & Pease 1921), has quickly been adopted in radio astronomy for obvious resolution reasons (Pawsey et al. 1946; Ryle & Vonberg 1946). It then became an essential tool for all applications, specially for studying the galactic kinematics. The first RC produced by interferometric observations dates back to 1972 (Rogstad & Shostak 1972).

In addition to its enormous gain in resolution, interferometry has the other advantage to produce, in only one observation, two-dimensional (2D) maps of the observed radial velocity of the neutral hydrogen in the galaxy. It is possible to obtain such velocity-field maps with a single-dish radiotelescope or with optical spectroscopy but they require multiples observations aimed at different portions of the galaxy, which greatly complicates the process. With interferometry, it is possible to directly map the galaxy in different channels associated to different wavelength ranges around the particular wavelength of the studied line, each channel being thus associated with a velocity range, as can be seen in panel (a) of Figure 1.3. All the channels can then be combined together to give the global map of the galaxy with its isovelocity curves, also called a spider diagram. A typical example of the latter is given in panel (b) of the same figure. From this 2D map, the PV diagram and the RC can be retrieved in decomposing the galaxy and its velocity-field in concentric rings, a technique called the tilted-ring model. Such decomposition also provides important information on the geometry of the galaxy, such as indications on the wraping of the galactic disk or on the existence of non-circular motions within the galactic disk due to the

[2]Nowadays considered as the most robust empirical relation in astrophysics (Combes 2009), particularly in its baryonic version (McGaugh et al. 2000), this relation provides strict constraint for scenarios of galaxy formation and evolution.

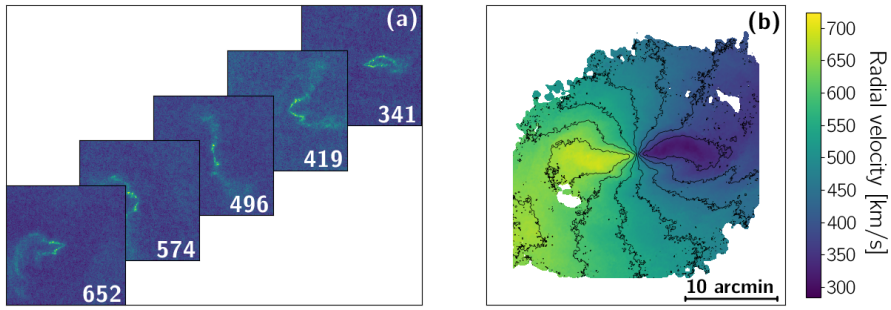

Figure 1.3: Radio interferometry final products. *Panel (a):* Examples of 5 slices of the interferometry data cube. Each image corresponds to a channel of observation and shows the zones of the galaxy moving at a given radial velocity (written in the lower right corners in km/s). *Panel (b):* 2D radial velocity-field map (or spider diagram) obtained by combining all the channels of the data cube. Data: HI 21 cm line observations of NGC5055 realized by THINGS (The HI Nearby Galaxies Survey; Walter et al. 2008).

presence of a bar or of the spiral arms.

Nowadays, these 2D maps can be produced in other wavelength domains than in radio, particularly in near-infrared (NIR) and in visible thanks to integral-field spectroscopy, a technique introduced in the 1980s (Courtes 1982). Hence, high-resolution RCs of the different components of the galaxies can be constructed from observations in all wavelength domains. Apart from the widely used radio (21 cm) and visible (Hα) lines that probe the gas (neutral or ionized) and younger stars in galaxies, RCs can also be computed from observations in the microwave or in the IR domains. Their low sensitivity to dust extinction make these two domains particularly suited to probe regions highly impacted by this phenomenon, that is to say, central regions of the galactic disks[3] as well as edge-on or nearly edge-on galaxies.

[3]Often, the 21 cm line cannot either be used to probe the inner disks. A lot of galaxies show a lack of neutral hydrogen in their central regions as it is preferentially in its molecular form, a form of which the CO, emitting in the microwave domain, is a particularly good tracer (as will be seen later in Section 1.3.1.1).

1.2 Typical shapes of rotation curves

Over the years, the RCs of thousands of spiral galaxies, in our neighborhood as well as at high redshift, have been computed in various wavelength domains. If they present a certain diversity of shape and of amplitude, this can be globally explained by taking into account the luminosity and the size of the galaxy, leading to the idea of a universal rotation curve (Persic & Salucci 1991; Persic et al. 1996; Salucci et al. 2007).

The most commonly observed RCs are the well-known flat ones, depicted on panel (d) of Figure 1.4. This kind of RC is typical of the intermediate-luminosity and intermediate-mass spirals (principally of the Sb and Sc types). In their centers, they exhibit a nearly rigid-body rotation, their rotation velocity increasing linearly with the distance to their center (dashed red line on the RC). Nevertheless, at some point, the rotation becomes differential, the curve flattens and the velocity keeps its constant value (in orange) as far as can be probed. These different regimes of rotation can also be observed and deduced from the spider diagram displayed in panel (c) of the figure. Indeed, for a rigid-body rotation, the isovelocity contours (black lines) are perpendicular to the major axis of the galaxy (as can be seen in the very center of the galaxy on panel (c)). On the contrary, a rotation at a constant velocity, as displayed in the galactic outskirts, will produce hyperbolic contours, symmetrical with respect to the major axis of the galaxy. In the rest of this work, we will qualify this type of RC as a RC of category II.

Analyzing the rotation of more luminous and massive galaxies (mainly of the Sa and Sb types), we find that the portion of their RC showing a rigid-body rotation is so localized in the inner cores that spatially resolving them constitutes a real observational challenge. Their RCs thus begin with a very steep increase of the rotation velocity, followed by a broad maximum and a slight decrease towards a flat plateau (as shown in panel (b) of Figure 1.4). These will be referred as RCs of category I. On the contrary, the low-mass dwarf Sc, the irregulars but also the low-surface brightness (LSB) spiral galaxies have RCs with a very different shape: their rotation velocity evolves more slowly and rises monotonically across the whole galaxy (see panel (f) of Figure 1.4; called RC of category III). Their spider diagram (panel (e)) clearly shows this rigid-body rotation across the whole galaxy, with all isovelocity contours nearly parallel to each other.

Furthermore, as visible when comparing the right panels of the figure,

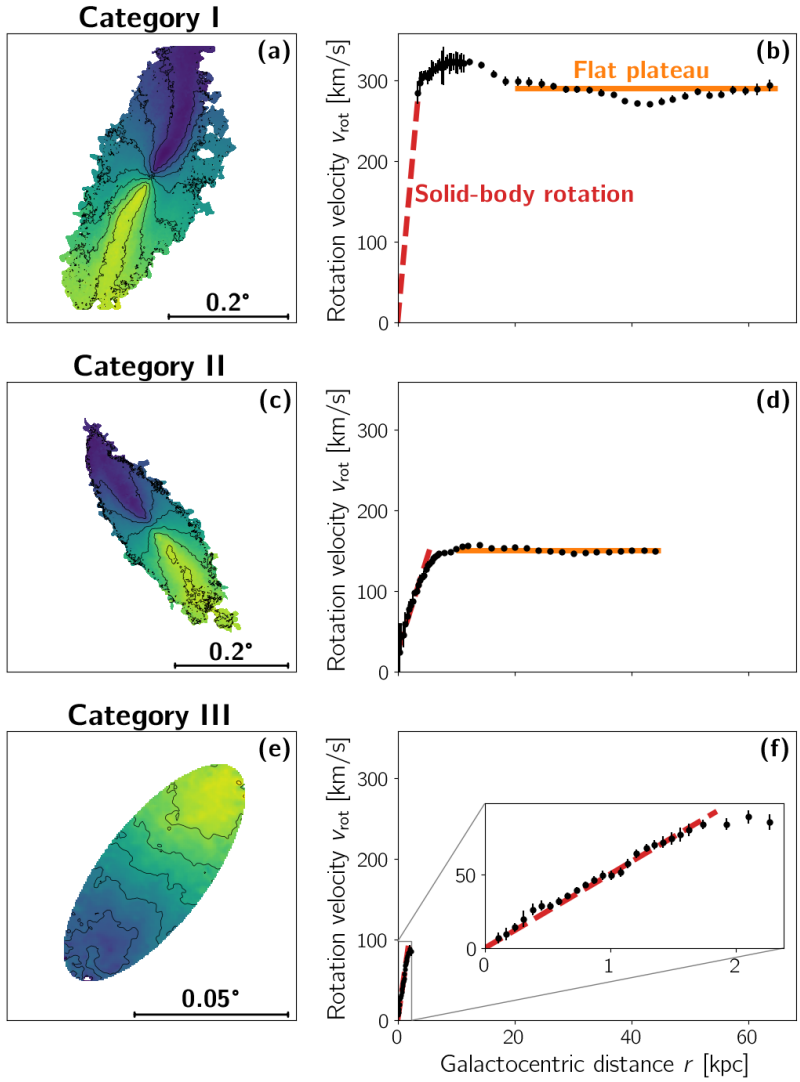

Figure 1.4: Diversity of RC shapes within the spiral galaxies. Spider diagrams (based on HI observations by Walter et al. 2008; *left panels*) and associated RCs (from Lelli et al. (2016a); *right panels*) representatives of different categories of spiral galaxies: (i) *upper panels*, the most massive and luminous (category I RCs; NGC2841), (ii) *middle panels*, the intermediate (cat. II; NGC3198) and, (iii) *lower panels*, the dwarf late-type and LSB (cat. III; NGC2976) galaxies.

the maximum velocity of a galaxy greatly depends on its category, the earlier types rotating the fastest.

Some differences between RCs can be explained by looking at the quantity of (luminous) matter and at its distribution within the galaxy. Physically, the more massive the galaxy, the greater its rotation velocity, explaining the differences of RC amplitude between the various types of spiral galaxies. This explanation also applies for the components of the galaxies. The earlier the spiral type, the more prominent and massive its bulge, corresponding to a steeper increase in the inner parts of its RC. On the other side, the late-type spirals have no or very small bulges, their RCs rising thus slowly.

The RCs also display fluctuations that are associated to the inhomogeneities of the galaxies, such as the spiral arms which create features of the order of 10–20 km/s (Sofue & Rubin 2001). Additionally, in barred galaxies, motions along the central bar can imprint the RCs with fluctuations of greater amplitude (from 30 to more than 100 km/s; Sofue & Rubin 2001). These non-circular motions make the RCs of such galaxies more difficult to retrieve, requiring advanced methods with the creation of 2D velocity maps, and less straightforward to analyze. Hence, even if they constitute more than half the total number of spiral galaxies in the universe, RCs of barred spirals are still less studied than for the 'normal' ones.

Even if the observed distribution of matter explains well the inner parts as well as some features of spiral galaxies' RCs[4], this explanation does not hold for the outskirts of the galaxies where the decrease in observed matter should result in an equivalent (keplerian) decrease in rotation velocity. This is at odds with the actual behavior of spiral galaxies in our universe (with rotation velocities that stay constant or even increase with the distance to the galactic center).

1.3 Modeling the mass distributions of spiral galaxies

The discrepancy between the observed RCs of galaxies and the ones expected from the distribution of their luminous components, particularly

[4]This can be summed up by Renzo's rule, stating that *for any feature in the luminosity profile there is a corresponding feature in the rotation curve, and vice versa* (Sancisi 2004), which is somewhat unnatural in the paradigm of galaxies heavily dominated by their DM halos.

in their outskirts, is explained by the presence of non-luminous but massive matter within the galaxies. To quantify and study this DM, it is thus of utmost importance to determine precisely the mass distributions of the observable components, that is to say, of the matter that emit some electromagnetic radiation and hence can be studied independently of its gravitational influence.

1.3.1 Luminous components

Spiral galaxies are mainly constituted of stars distributed either in a central bulge, in a rotating extended thin disk displaying spiral arms or in a spherical halo. Principally composed of individual population II stars, globular clusters and streams of stars created by tidal interactions and merging events between the galaxy and its neighbors, this halo is very faint and its total mass is small ($\sim$1%) compared to the other two reservoirs of stars that are the bulge and the disk. Hence, as it is done in the vast majority of galactic studies, we will neglect it in the rest of this work, when modeling both its luminous emission and its mass distribution.

Within the disks and the bulges, the space between the stars is filled with ISM, i.e. gas clouds in various forms (neutral, molecular, or ionized either by shock waves or by the radiation emitted by the neighboring hottest and youngest stars) mixed with dust grains. The latter, even though they make up a nearly insignificant portion of the total mass of galaxies, are essential components to understand their aspect and evolution.

1.3.1.1 Spectral energy distribution

All these components emit and/or absorb light in different wavelength domains, resulting in a global emission often represented, under the form of a spectral energy distribution (SED). The SED of a normal[5] spiral galaxy is illustrated by the black line in Figure 1.5. This emission, with its characteristic double-peak shape, can be divided in three portions associated to the three sources at their origin: the stellar (in blue), the gaseous (in green) and the dusty (in red) components.

[5] A normal spiral galaxy is a galaxy without an active galactic nucleus (AGN). When an AGN is present at the very center of a galaxy, its radiation may outshine the emission from the galaxy itself, modifying completely the amplitude, the shape and even the wavelength extension (with, for example, potential strong emissions in X- and γ-rays) of the associated SED.

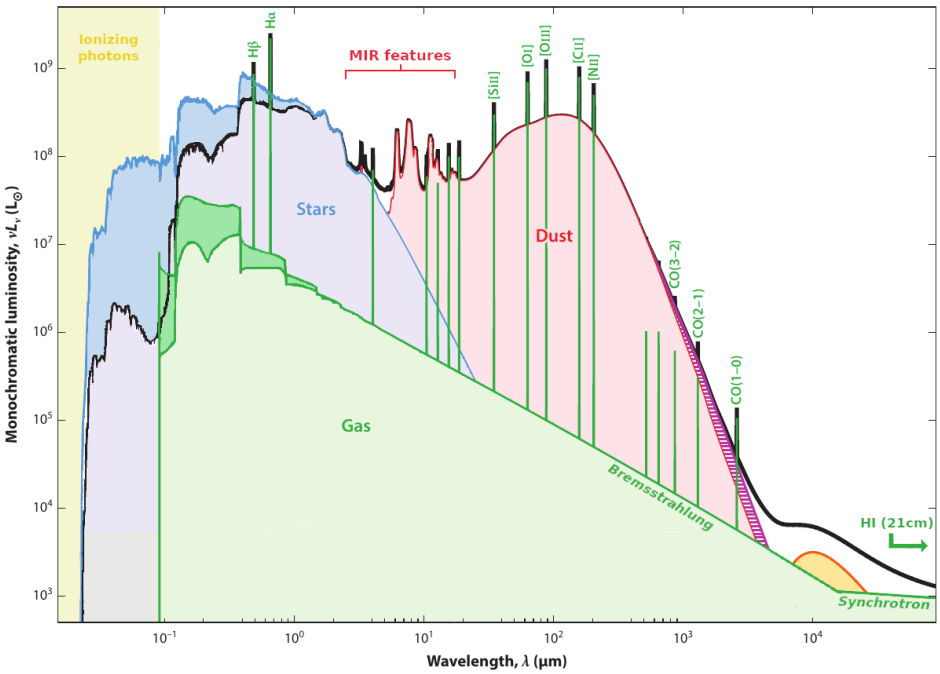

Figure 1.5: Spectral energy distribution of a normal spiral galaxy. The emitted stellar light (blue line) is partially processed by the ISM gas and dust via scattering and/or absorption (dark blue regions). The absorbed energy is then emitted broadly in IR by the dust (red line) and at specific wavelengths across the whole spectrum by the gas (green line). In the MIR domain, the existence and the amplitude of the various features both depend on the composition of the dust grains (silicate, PAH, ...). The gas also emits light via non-thermal processes (bremsstrahlung and synchroton radiations) whose short-wavelength portion is partly processed by dust (dark green region). The observed SED (in black) is thus a very complex entanglement of the three galactic components emissions. Figure modified from Galliano et al. (2018).

At short wavelengths, the galactic SED is dominated by the emission originating from the many photospheres of the constituting stars. Due to their diversity of ages, masses and metallicities, the global emission spans continuously from ultraviolet (UV) to NIR (blue profile in the figure), resulting in a peak around 0.5–1 μm. The galactic bulge and disk are not composed of the same stellar populations. The youngest stars are principally localized within the disk, in the spiral arms where the regions of star formation, the HII regions, are found. On the contrary, the bulge contains older, population II stars. Due to these differences, the observed SED will vary depending on the imaged region, the central regions emitting less UV and visible light than the spiral arms, for example.

A part of this light is then processed, principally by the ISM dust grains whose small size (typically between 0.3 mm and 0.3 μm; Galliano et al. 2018) allows them to scatter and, more importantly for what interests us here, to absorb the UV and visible radiations (the darker blue regions on the figure). The absorbed energy heats up the dust grains, making them radiate in the mid-infrared (MIR), far-infrared (FIR) and sub-millimeter (sub-mm) domains (in red in the figure). At these long wavelengths, this dust emission is the main contributor to the galactic SED. As will be explained in more details in Chapter 3, the heating of the grains is dependent on their size, smaller grains reaching higher temperatures and having more complex emission patterns than the larger, colder ones. Variations in the compositions of grains also modify the emission, specially in MIR with numerous features typical of the silicates or of the polycyclic aromatic hydrocarbons (PAH). This is illustrated in the figure, along with the more regular FIR/sub-mm emission, well fitted by one or two simple grey-body spectra, peaking around 100–200 μm.

On top of that, the gaseous component, distributed in clouds of various chemical state, temperature and density, produces very strong emission lines (depicted in green in the figure). Under its molecular form, hydrogen is very difficult to detect, particularly at the conditions of low temperature and high density ($T < 40$ K and $N_H > 10^{21}$ cm^{-2}; Cimatti et al. 2020) that allow the molecules to exist and survive. Indeed, as this molecule is made of two identical atoms, its electronic, vibrational and rotational lines are associated to either too long lifetime or too hot temperatures, resulting in very faint, nearly undetectable, signatures in galactic SEDs. Fortunately, the molecular gas clouds can nevertheless be traced via the emission lines of other molecules, mainly the rotational lines of the second most abundant

molecule in these clouds, carbon monoxide (CO).

In the HII regions and in the planetary nebulae, young massive stars and white dwarfs produce high-energy photons that ionize the surrounding gas (for energies higher than the ionizing potential of hydrogen, 13.6 eV, equivalent to wavelengths smaller than 91 nm). This photoionized gas then emits strong lines in UV and visible when the free electrons are recaptured by ions (recombination lines as Hα) or when the ions, excited by collisions with the free electrons, spontaneously decay (forbidden lines). These ionized gas regions also produce an emission continuum through the bremsstrahlung radiation when electrons are deviated by ions and decelerate. Nevertheless, as can be seen in Figure 1.5, this continuum is considerably weaker than the star and dust radiations from UV to sub-mm. It is only a major contributor to the galactic SED in the radio domain.

Hence, the global SED of each galaxy is the unique result of all its current content in stars, gas and dust grains. By itself, it contains multiple and diverse information on the quantity of the galactic components but also on the 3D geometry of the galaxy, on the way the components are distributed and mixed together, on the initial mass function (IMF) when populations of stars are formed, on the history of the stellar formation along the life of the galaxy, on the evolution of its metallicity and of its abundance pattern, or on the physical and chemical states of dust grains and gas clouds.

For all the reasons described above, the galactic SEDs are keys tools to probe and understand the formation and evolution of the galaxies as well as the physical processes occurring within them. Nevertheless, the emissions from the different components are extremely difficult to disentangle in order to retrieve valuable information. Indeed, as can be guessed from the multitude of processes and factors impacting the shape and appearance of galactic SEDs, several degeneracies between those exist, the most famous example (to which we will come back in Chapters 3 and 4) being that the red color of a galaxy can be explained by either old stars, high-metallicity stars or high quantities of dust.

1.3.1.2 In rotation curves studies

Within the scope of RC studies, galactic mass distributions have to be estimated and converted in rotation velocities in order to check if the luminous matter can explain the observed RC. Due to the inherent complexity of

galactic SEDs, it is often preferred to work on photometric bands where components are the least entangled or, in other words, where one component outshines the others.

Gas and dust components

In spiral galaxies, the stars dominate the mass budget, followed by the gas (neutral, molecular and ionized, in this order) and far behind, by the dust (whose mass constitutes about 1% of the total mass of gas). Hence, the latter is simply neglected when estimating the total mass distribution. For the other two components, the gaseous one is the easiest to process due to its strong emission lines, each of them associated to a specific gas state. Thus, the same observations that are used to compute the galactic 2D velocity maps (and the associated RCs) also produce direct images from which we can derive the gaseous mass distributions. In the ISM of spiral galaxies, the gas is predominantly neutral and can be easily traced by the 21 cm line of the hydrogen atom.

For the molecular and the ionized gas, the situation is different. Indeed, as these gases are found in small and compact clouds in the central regions of galaxies, their study requires observations of higher resolution, hence more difficult to perform, than for the neutral gas. As a consequence, less galaxies have been observed in the wavelength bands useful to probe these contents (i.e. mainly the CO rotational lines for the molecular gas and the Hα line for the ionized one). Thus, RC studies, particularly of large samples of galaxies, do not model directly these components. The ionized gas is simply ignored as its total mass is nearly insignificant compared to the mass of the other two forms of gas. The molecular gas clouds are either ignored or assumed to follow the same distribution than stars and are then incorporated into the stellar modeling (de Blok et al. 2008; Lelli et al. 2016a).

Nevertheless, this last simplifying assumption is not valid for galaxies with relatively high content in molecular gas. It has been shown that correctly modeling this gas can have significant impacts on the total mass distribution in the inner regions of the galaxies, and thus on the quantity of non-luminous matter to add to explain the observed RCs (Frank et al. 2016). With time and technical improvements, the resolution of images of the CO emission lines increased and larger surveys of nearby galaxies

emerged (Helfer et al. 2003; Leroy et al. 2009; Young et al. 2011; Bolatto et al. 2017), allowing the molecular gas of some spiral galaxies to be independently modeled in a few recent RC studies (12 galaxies for Frank et al. 2016, 20 for Richards et al. 2018, 11 for Relatores et al. 2019).

Finally, to compute the RCs associated to the neutral and, when independently modeled, molecular gases, their 3D distributions have to be assumed. As the thickness of gaseous disks is lower than the stellar ones, the gas components have so far been taken as simple, infinitely thin disks. Nevertheless, observations of edge-on galaxies have shown for a long time that the gaseous disk rather show some flaring, that is to say, some systematic increase of their thickness with the galactocentric distance (Sancisi & Allen 1979; van der Kruit 1981). However, such more realistic distributions have not been used so far in RC studies.

Stellar component: mass-to-light ratios

The stellar component is the one for which the transformation from an observed luminosity into a mass distribution is the most complex and challenging. This is due to the diversity of the stars' ages, masses and metallicities as well as to the processing of the stellar radiation by the neighboring gas and dust. Using only observations of the galaxy in one wavelength band Λ, the most widespread and easiest way to convert the luminosity L_Λ in that band into a stellar mass M_* is simply to multiply it by the stellar mass-to-light ratio Υ_*^Λ of the band. This ratio is expressed in solar units as

$$\Upsilon_*^\Lambda = \frac{M_*/L_\Lambda}{M_\odot/L_{\Lambda,\odot}}$$

where $L_{\Lambda,\odot}$ is the solar luminosity in band Λ and $M_\odot$ the mass of the Sun.

Depending on the chosen band Λ, the ratio can vary strongly from one galaxy to another. Indeed, these ratios reflect the stellar content of the galaxy at the moment of the observations and this content is itself the result of the whole history of the galaxy. It thus depends notably on the evolution of the star formation along the life of the galaxy, on the stellar IMF, on the evolution of the galactic metallicity as well as on the current quantity of stars in particular (late) stages of evolution. In these stages, the stars can be extremely luminous while representing a very small fraction of the total stellar mass, which highly impact the ratio values. In fact,

the complexity inherent to the whole galactic SED partly translates into the determination of the stellar mass-to-light ratios. These factors are thus the ones that bring the largest uncertainties in the whole modeling of the galactic mass distributions.

Consequently, extensive efforts have been and are still carried out to further understand and constrain the estimates of these ratios in various observing bands. In general, those are based on theoretical models of synthetic stellar populations combined with observations of real galaxies to either determine a unique value of some specific mass-to-light ratios for all galaxies (e.g. Meidt et al. 2014; McGaugh & Schombert 2014) or to find correlations with some properties of the galaxies, principally their optical or NIR colors (e.g. Bell & de Jong 2001; Meidt et al. 2014; McGaugh & Schombert 2014; Norris et al. 2014, 2016; Schombert et al. 2019). Estimates of these ratios can also be derived for specific galaxies from the direct observations of resolved stars (Eskew et al. 2012; Just et al. 2015) or from the analyses of their local (Bottema 1993; Herrmann & Ciardullo 2009; Martinsson et al. 2013; Angus et al. 2016) or global kinematics (McGaugh & Schombert 2015; den Heijer et al. 2015; Lelli et al. 2016b).

As all methods to evaluate these mass-to-light ratios imply assumptions, a wise choice of the wavelength domain is crucial to minimize the associated uncertainties. Hence, over the time, the use of mass-to-light ratios converged towards the NIR domain, shown to be more robust than the optical one for the modeling of the stellar content of the galaxies (e.g. Norris et al. 2014; McGaugh & Schombert 2014, 2015). Indeed, the optical domain principally traces the short-lived, very luminous, main-sequence stars that, despite being individually very massive, are not numerous and thus do not represent an important proportion of the total stellar mass of the galaxy. On the contrary, the NIR light is emitted by the numerous, less massive, stars that constitute the majority of the galactic total stellar mass and is not polluted by recent bursts of stellar formation.

Moreover, numerous works modeling synthetic stellar populations showed that the mass-to-light ratios varied significantly less with the population's age and metallicity in the NIR domain than in the optical one (e.g. Bell & de Jong 2001; Meidt et al. 2014; McGaugh & Schombert 2014; Norris et al. 2014, 2016; Schombert et al. 2019; Korsaga et al. 2019). Similarly, the correlations between the ratios and the colors of the galaxies are the strongest in NIR . More specifically, the use of the 3.6 μm band of the *Spitzer* Space Telescope recently exploded for the modeling of the stellar

component of galaxies in the context of RC studies. Indeed, various estimates of the mass-to-light ratio in this band converged towards a unique value of $\Upsilon_*^{3.6\mu m} \simeq 0.5 \pm 0.1$, whatever the galaxy history and composition. These works include the theoretical use of synthetic stellar populations (Meidt et al. 2014; McGaugh & Schombert 2014), the study of the baryonic Tully-Fisher relation (den Heijer et al. 2015; McGaugh & Schombert 2015), the precise modeling of the Large Magellanic Cloud (Eskew et al. 2012), the observations of the stars in the Sun's neighborhood (Just et al. 2015) and even the measurements of stellar velocity dispersions (Swaters et al. 2014; Angus et al. 2016) if corrected with Aniyan et al. 2016 results, as proposed by Lelli et al. 2016a. Moreover, the decomposition of the RCs of spiral galaxies is also compatible with this given value of mass-to-light ratio in the 3.6 μm band (Lelli et al. 2016a). The uncertainties on this ratio value allow to incorporate a certain quantity of non-modeled matter in the galactic disk. This explains why the distribution of molecular gas is often considered similar to the one of the stars and hence, why this component is not independently modeled in the vast majority of RC studies.

Last but not least, this wavelength range displays the smallest entanglement between the stellar and the dusty components as the extinction by dust decreases with the wavelength and is thus negligible in NIR.

One may nevertheless notice that this wavelength domain is not exempt of flaws as NIR emission can be slightly polluted by emission from hot dust and PAH (which have an emission feature at 3.3 μm; Flagey et al. 2006) as well as from intermediate-mass evolved stars, like the red supergiant stars and the asymptotic giant branch (AGB) stars, amongst which the thermally pulsating (TP-AGB) ones are particularly critical but complex to include in models of stellar populations (e.g. Maraston 1998; Meidt et al. 2012; Eskew et al. 2012; Melbourne & Boyer 2013; Gerke & Kochanek 2013). Fortunately, the process usually developed to decompose RCs has the advantageous side effect to minimize the contamination by hot dust. Indeed, the RC studies deal with one-dimensional (1D) RCs and thus have to compute 1D mass profiles from 2D images. This is done by decomposing the galaxies in various elliptical rings and by azimuthally averaging the pixels values of these rings (as will be done in this work and explained later in Chapter 3). Hence, as the regions polluted the most by hot dust (the star-forming regions) are very localized, their impact on NIR observations are reduced when averaging to derive the 1D profiles (de Blok et al. 2008).

In consequence, nowadays, the modeling of stellar mass distributions in

the vast majority of RC studies is based on the use of mass-to-light ratios in the NIR domain, particularly with the launch in the last two decades of IR telescopes such as *Spitzer* and WISE (Wide-field Infrared Survey Explorer), that greatly facilitated the access to observations of extragalactic objects at these long wavelengths. The *Spitzer* 3.6μm and, to a lesser extend, the WISE 3.4μm bands allowed the analysis of large samples of galaxies (see de Blok et al. 2008; Lelli et al. 2016a; Richards et al. 2018; Korsaga et al. 2018, and the multiple papers based on these works).

Stellar component: inherent RC degeneracies

In RC studies, one can use the mass-to-light ratios estimated through independent methods but it is also possible to constraint these ratios. In fact, for each galaxy, the upper limit on its ratio can be directly derived from the decomposition of its RC. Indeed, as the observed RC cannot be fully explained by the luminous matter of the galaxy, there exist an degeneracy between the stellar component (i.e. the luminous component known with the largest uncertainties) and the additional non-luminous one. If the quantity and distribution of the latter can be constrained from simulations or theoretical considerations (as we will discuss in Section 1.3.2), these constraints are not as strong as would be observational ones. In consequence, when decomposing a RC, the non-luminous mass distribution ends up being directly correlated with the chosen stellar one. Thus, if the mass-to-light ratio is not fixed independently, any observed RC can be well fitted by a variety of stellar mass distributions coupled with non-luminous halo models (see Bershady et al. 2010, for an example of this degeneracy in NGC3198 where the observed RC can be equivalently well fitted with values of Υ_*^K varying by a factor of 20). The best RCs decompositions are incidentally often found for clearly incorrect null values of Υ_* (e.g. Simon et al. 2003).

Exact values of stellar mass-to-light ratios are thus impossible to derive from RC observations only but the upper bounds can be found relatively easily through the maximum-disk hypothesis, illustrated in Figure 1.6. This hypothesis consists in choosing the value of Υ_* (taken as constant across the whole galaxy) such that it maximizes the stellar contribution (dashed blue line) to the RC or, in other words, such that the RC associated to the luminous component of the galaxy (solid blue line) does not exceed the observed one. As can be seen in the figure, the inner parts of the

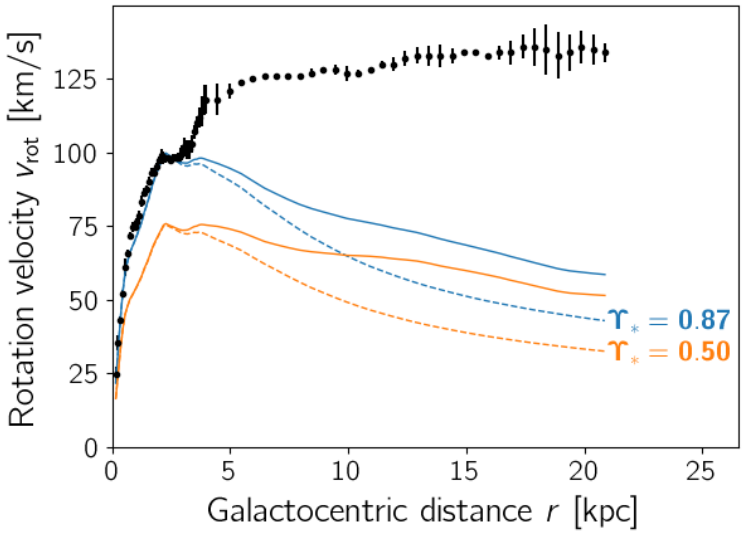

Figure 1.6: Effect of the choice of the stellar mass-to-light ratio Υ_* on the RCs from stars (dashed lines) and from the total luminous matter (stars + neutral gas; solid lines). The observed and modeled RCs are given by Lelli et al. (2016a) for the galaxy NGC2403. The stellar distribution has been estimated from 3.6 μm images. In that case, 0.5 is the value of $\Upsilon_*^{3.6\mu m}$ recommended by various independent estimates (orange lower lines). However, the RC allow for a higher stellar contribution through the maximum-disk hypothesis ($\Upsilon_*^{3.6\mu m} \approx 0.87$; blue higher lines), the restriction coming from the inner regions of the galaxy.

galaxy are the ones that restrict the most the ratio value. For the galaxy presented here, the value of the stellar mass-to-light ratio recommended by independent means (orange curves) gives a sub-maximal disk but this is not always the case, the level of 'sub-maximality' varying from one galaxy to each other (e.g. Lelli et al. 2016a).

One may note that this maximum-disk hypothesis is not aptly named as the galactic stellar component is not only distributed as a disk but also as a bulge, whose contribution can be important in the central regions of the galaxies, particularly for the earliest types of spirals. As the bulges are composed of older stars, two different mass-to-light ratios are usually

assumed for the bulge and for the disk. They can then be fitted separately for the bulge and the disk (e.g. de Blok et al. 2008; Richards et al. 2018) or their correlation can be fixed $\Upsilon_{*,\mathrm{bulge}} = \alpha\Upsilon_{*,\mathrm{disk}}$ (with α generally equal to $\sim$1.4; e.g. Lelli et al. 2016a; Cimatti et al. 2020). Hence, it is the total stellar mass that is maximized, not only the disk mass, so that 'maximum-stellar mass' could be a more appropriate name for this hypothesis.

Stellar component: final assumptions

In most RC studies, multiple decompositions of the observed RCs are performed with different hypotheses on the stellar mass-to-light ratio value (maximum-disk, Υ_* fixed for all galaxies, Υ_* derived from optical or NIR colors, ...) to investigate the effect on the non-luminous matter quantity and distribution (Verheijen 1997; de Blok et al. 2008; Lelli et al. 2016a; Korsaga et al. 2018; Richards et al. 2018, for a few examples). In any case, the stellar mass-to-light ratio is taken as constant over the whole galaxy[6], the stellar mass thus following directly the luminosity. *A priori*, this hypothesis does not reflect the reality of spiral galaxies as the stellar populations as well as the quantity of dust vary within the galaxy, either locally (with the existence of star-forming regions within the spiral arms, for example) or globally (as suggested by observed colors and metallicity gradients as well as by models of galaxy formation; see Portinari & Salucci 2010 and references within or Zibetti et al. 2009, for examples). As already said, the NIR domain is chosen in order to reduce these variations of Υ_* within the galaxy. Hence, only a handful of RC studies allowing varying stellar mass-to-light ratios have been performed (Kranz et al. 2003; Kassin et al. 2006; de Blok et al. 2008; Portinari & Salucci 2010; de Denus-Baillargeon et al. 2013; López Fune et al. 2017). If the global RC decomposition is not strongly affected by the relaxing of the hypothesis of constant mass-to-light ratio, these studies nevertheless showed that it had a significant impact on the details of the RC decomposition and highlighted the fact that variations of Υ_* should not be neglected in future works (Portinari & Salucci 2010).

Finally, as for the gaseous component, a 3D distribution has to be assumed for the stars within the galaxy. In RC studies, very classical ap-

[6]The galactic bulge and the disk can be separated, as already mentioned, specially for the earlier types of spirals but even in this case, the two Υ_* are considered to be constant with the distance to the center of the bulge/disk.

proximations are made. The bulge is modeled only when it really improves the RC decomposition (e.g. de Blok et al. 2008; de Denus-Baillargeon et al. 2013; Lelli et al. 2016a; Richards et al. 2018) and it is usually taken as spherically symmetric. For the disk, its vertical distribution is approximated by simple mathematical functions (exponential, squared hyperbolic secant, ...) with a direct correlation between the disk thickness and its radial extension.

1.3.2 The dark matter explanation

Once the luminous components of a galaxy are modeled, the discrepancy between their associated RC and the one effectively observed is obvious. Present since the very first computation of a galactic RC by Babcock (1939), the revolutionary nature of this puzzling result was not immediately appreciated.

1.3.2.1 A change of paradigm

Until the 1980s, this discrepancy did not really worry the scientific community. The RCs built on optical observations could globally be explained by the presence of undetected matter with high mass-to-light ratios (i.e. planets, low-mass stars, stellar remnants and molecular gas clouds) distributed as the visible matter (e.g. Schwarzschild 1954; Kalnajs 1983; Kent 1986). Even the first radio RCs, that extended in the galactic outskirts where stars were not detected anymore and nevertheless displayed an inexplicable flat behavior, were received with skepticism. The community thought that this newly-born radio astronomy discipline was still subject to systematic errors that were not correctly taken into account (Sanders 2010). Then, it was just a question of time for new and more precise observations to naturally take the discrepancy out of the equation.

The revolutionary nature of these observations was thus not yet understood, except by a few precursors, such as Finzi that has been one of the first to get the measure of the situation and to link this discrepancy with what was observed in another astrophysical environment, the clusters of galaxies (Finzi 1963). Indeed, the application of the Virial theorem to clusters (such as the Coma cluster and later the Virgo cluster; Zwicky 1933; Smith 1936; Zwicky 1937) had also revealed huge discrepancies between the luminous and the dynamical masses of these objects (with ratios of around

1 to 100; Longair 2006). But as for the first RC studies, these results have not been seriously considered by the community until decades later.

In the 1980s, with the accumulation of flat RCs in visible (Rubin et al. 1978, 1980) as well as in radio (Bosma 1978), probing farther and farther away in the outskirts of the galaxies, the consensus evolved: the reality of the discrepancy and of the underlying missing mass problem widespread amongst the community. This change of paradigm in our vision of spiral galaxies was also pushed by numerical simulations of these objects performed in the 1970s. They showed that a disk dominated by a global rotation is unstable on its own but could be stabilized if surrounded by a pressure-supported spherical massive halo (Ostriker & Peebles 1973), a halo that revealed itself to be also capable of explaining the observed flat RCs (Ostriker et al. 1974).

These theoretical and observational considerations thus lead to the current model of the composition of spiral galaxies where the visible disk is embedded in an immense halo composed of non-luminous, or dark, matter whose mass largely dominates the luminous matter (with a ratio of about 10 to 1 for the large spirals and even bigger for dwarfs or LSB galaxies; Longair 2006). This halo can only be probed through its gravitational interaction on its luminous neighborhood and is also present around the other types of galaxies (elliptical and lenticulars).

Moreover, the existence of this new dominant type of matter explains not only the galactic observations but also a multitude of very different extragalactic and cosmological ones, the most famous examples being the study of the anisotropies of the cosmic microwave background, the formation of the large structures of the universe, the gravitational lensing observations, the distance-redshift relation of various astrophysical objects, or the (already mentioned) kinematics within the clusters of galaxies.

Over the years, different models to understand what was constituting the DM were considered, beginning by the most straightforward one: a baryonic DM made of objects emitting very few to no light at all (black holes, white dwarfs, low-mass stars, ...). Hence, in the 1990s and early 2000s, ambitious large-scale projects looking for massive compact halo objects around our galactic disk showed that such objects did not exist in sufficient proportions to explain the expected mass of the MW halo (Alcock et al. 2000; Afonso et al. 2003). Equivalently, in the intergalactic medium within clusters, hot gas filaments have been found in quantities much larger than the visible matter but still not enough to account for all

the missing mass of these objects (see Bregman 2007 and references within, as well as de Graaff et al. 2019; Tanimura et al. 2019 for the recent solving of the missing baryons problem).

Studies on the timescale of the formation of the large scale structures in the universe coupled with observations of the cosmic microwave background revealed the necessity to have an exotic component that decoupled from the primordial soup earlier than the baryons (e.g. Gunn et al. 1978; Peebles 1982; Bond & Szalay 1983; Vittorio & Silk 1984). This component could then began to concentrate and create potential wells into which the baryons would quickly fall after their own decoupling, allowing the quick formation of the large-scale structures of the universe. This non-baryonic component would thus be enter into the composition of these structures, solving their missing mass problems.

Depending on the mass of the particle constituting this non-baryonic DM, different structures should form first. The relativistic particles (such as the neutrinos that were once valid candidates of non-baryonic DM) create large-scale structures first (i.e. the superclusters and clusters) that then fragment into galaxies in a top-down scenario. However, observations of galaxies at high redshift suggest the opposite with galaxies formed first. In that case, the DM is characterized as cold and is constituted of more massive particles. Many hypothetical candidates (weakly-interacting massive particles deriving from extensions of the Standard Model of particles, axions, sterile neutrinos, primordial black holes, ...) have been proposed but none of them has already been directly observed and confirmed yet.

In consequence, within a few decades, our view of the galaxies and of the universe as a whole have been profoundly transformed by the revelation that the immense majority of the matter in our universe (around 80%; Planck Collaboration 2020) is expected to be this mysterious cold DM (CDM) component, made of still unknown non-baryonic massive particles, only detectable through their gravitational effects on their neighborhood.

1.3.2.2 In rotation curve studies

On top of being the observations that installed DM in our cosmological models, RC studies are particularly important to understand the distribution of this component around the building blocks of our universe that are the galaxies. By studying the shape of the DM halos, it is possible to test

the theoretical models that try to describe the behavior of this unknown constituent.

When decomposing RCs, the luminous components are observed and directly converted into mass profiles (as described in Section 1.3.1.2). On the contrary, the DM component is modeled through theoretical analytical distributions. The halo parameters (and the stellar mass-to-luminosity ratio, when left free) are then adjusted in a global fit to retrieve the observed RC. Two significantly different types of halo models are used to represent the DM distribution around the visible disks of galaxies. The main difference between the two lies in the center of the halo, where the DM density either stays constant (core models) or continuously increases towards the galactic center (cusp models).

At first glance (using Equation 1.1), to explain the observed flat plateau in their outskirts, the spiral galaxies need DM halos whose embedded mass increases linearly with the galactocentric distance r, hence whose density decreases in r^{-2}. Moreover, in numerous cases (i.e. for the most massive and luminous galaxies), the luminous matter within the galaxy explains relatively well the inner parts of the RCs, as explained in Section 1.2. The necessity of DM in these regions is thus greatly reduced compared to the outer parts and the halo density should not continue to vary at this r^{-2} rate, at the risk of a complete non-observed dominance of DM in the center. This constraint remains even for galaxies most heavily dominated by DM (low-mass, late-type and LSB spirals). As shown in panel (f) of Figure 1.4, these galaxies generally exhibit a rigid-body rotation in their central regions (i.e. a linear increase of their velocity with the distance), implying the necessity for the dominant DM embedded mass to vary as r^3 in these regions and for the DM density to stagnate.

An analytical model that reproduces well these constraints is the pseudo-isothermal sphere (PIS), an isothermal sphere of DM with a central core of constant density. It has been extensively used in RC studies since the proposal of spherical halos to stabilize the disk as well as the acceptance of the reality of flat RCs in the late 1970s (Bahcall & Soneira 1980; Caldwell & Ostriker 1981; van Albada et al. 1985; Kent 1986; Begeman 1987, for some of the first examples). Mathematically, such a model is described by

$$\rho_{\mathrm{PIS}}(r) = \frac{\rho_0}{1 + (r/r_c)^2} \tag{1.2}$$

with ρ_0 the central DM density and r_c the radius of the core, into which

the density stabilizes. It is represented by the solid blue line in panel (a) of Figure 1.7. Converting this density into the effect it has on the circular velocity of test particles in the plane of the galaxy, we obtain

$$v_{c,\mathrm{PIS}}^2(r) = v_\infty^2 \left[1 - \frac{r_c}{r} \arctan\left(\frac{r}{r_c}\right)\right],$$

where v_∞, the asymptotic velocity, is roughly the velocity of the plateau ($v_\infty = \sqrt{4\pi G \rho_0 r_c^2}$). This velocity profile is represented in panel (b) of the same figure (solid blue line).

At the opposite of this model derived from RC observations, it is also possible to compute the shape of DM halos from theoretical considerations in the context of the ΛCDM cosmological model[7]. In the 1990s, the first N-body simulations of CDM fluids developed (Dubinski & Carlberg 1991; Navarro et al. 1996), resulting in a universal description of DM halos with a central cusp rather than a core, and this, whatever the nature or the mass of the objects (galaxies or clusters; Navarro et al. 1997). Over the years, the improvements of computers capabilities and the increases of simulations resolutions confirmed the cuspy nature of these simulated halos of DM particles.

One of the first (and nowadays the most famous) analytical function that universally fits such simulated halos is the so-called Navarro-Frenk-White (NFW) profile (Navarro et al. 1997):

$$\rho_{\mathrm{NFW}}(r) = \frac{4\rho_s}{(r/r_s)\,(1 + r/r_s)^2}, \tag{1.3}$$

where r_s is the characteristic radius of the halo, called the scale radius, and ρ_s is the density at this radius. As can be seen with the dashed orange line in panel (a) of Figure 1.7, the DM density changes from a variation in r^{-1} in the inner regions (hence, the central cusp) to a r^{-3} one in the outskirts, to compare respectively with the r^0 (the core of constant density) and the r^{-2} variations of the PIS model. In term of circular velocity of test particles, this NFW particularization translates into:

$$v_{c,\mathrm{NFW}}^2(r) = \frac{v_\Delta^2}{x} \frac{\ln(1 + c_\Delta x) - \frac{c_\Delta x}{1 + c_\Delta x}}{\ln(1 + c_\Delta) - \frac{c_\Delta}{1 + c_\Delta}}$$

[7]This model, considered as the standard model of cosmology, describes the universe as spatially flat and is composed of ordinary matter, of cold dark matter (CDM), and of dark energy, mathematically described by a cosmological constant Λ.

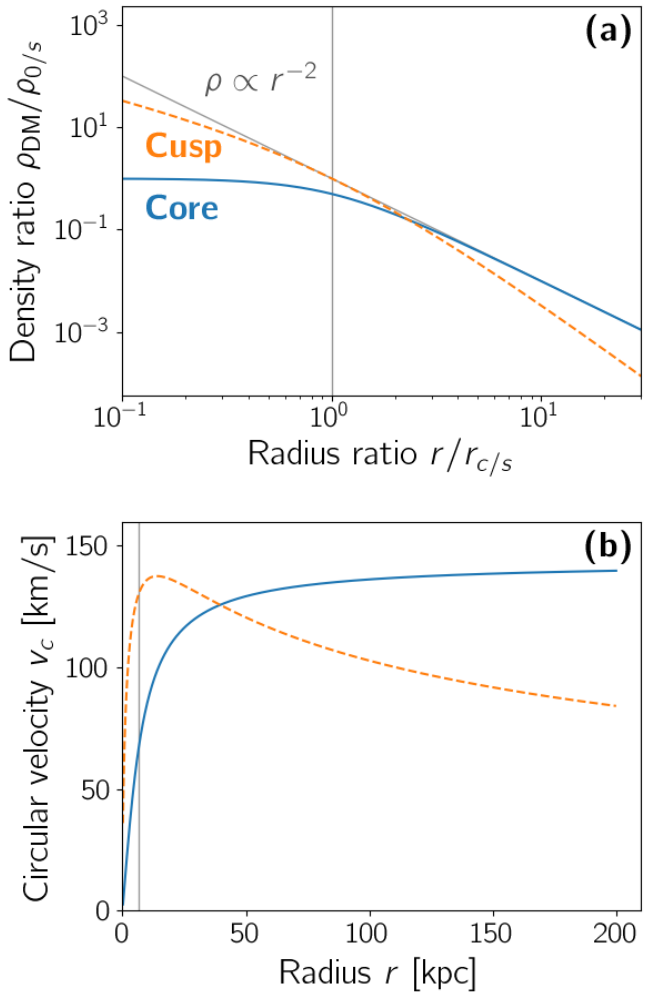

Figure 1.7: Typical DM halo models with a central core (PIS; solid blue lines) or cusp (NFW; dashed orange lines). *Panel (a):* Radial evolution of the DM density relative to the halo characteristic density and radius. The r^{-2} variation followed by the core model in the outskirts of the galaxy is extrapolated in the central regions for reference. *Panel (b):* Circular velocity of test particles located within the galactic disk resulting from these two density distributions. The characteristic radius is the same for both models (whose value is shown by the vertical lines).

where $x = r/r_\Delta$, r_Δ being the radius at which the average density of the halo is equal to Δ times the critical density of the universe. Most of the times, the halos are characterized with Δ values of 200, r_{200} being roughly equal to the Virial radius of a halo for a ΛCDM model. The NFW halo RC (shown by the dashed orange line in panel (b) of Figure 1.7) is thus also a function of two parameters, either the radii r_Δ and r_s or, equivalently, the velocity v_Δ (as $v_\Delta = 0.5\Delta H_0 r_\Delta$, H_0 being the Hubble constant) and the parameter c_Δ that characterizes the concentration of the halo (given by the fraction r_Δ/r_s).

Whatever the chosen ones, the two parameters describing the RC of a NFW halo should not be considered as independent from each other. They are in fact strongly correlated through the formation process of the halos and thus through the assumed cosmological model. In the ΛCDM paradigm, the less massive halos (associated with lower circular speed) collapsed earlier, when the density of the universe was higher, and are thus more compact (Navarro et al. 1997). This is known as the mass-concentration relation and it has to be taken into account when fitting NFW halos on RCs.

These theoretical cuspy halos do not fit the RC observations as well as the cored ones, especially for the low-mass, dwarf and LSB galaxies (e.g. Moore 1994; Flores & Primack 1994; McGaugh & de Blok 1998; Côté et al. 2000, for the very first examples). At first, it was thought to be due to observational (beam smearing effects of the low-resolution radio observations, problems in the pointing and positioning of the slit in optical spectroscopy) or physical (existence of non-circular motions, non-axisymmetry of the galaxy) systematic errors that gave to the cusp the appearance of a core (see de Blok 2010, and references within). Wevertheless, even with the advent of high-resolution 2D velocity maps in radio as well as in optical, this core/cusp problem still persists today:. Core models provide better fits to the observed RCs (e.g. Katz et al. 2017; Korsaga et al. 2018, 2019; Li et al. 2020, for some of the latest examples) even if a few dwarf galaxies sometimes show cuspier behavior (Relatores et al. 2019).

Various solutions to this problem are thus currently proposed. New models of DM are developed with more or less success, the most promising being the self-interacting DM (Spergel & Steinhardt 2000; Kaplinghat et al. 2000) whose implications are numerous, on individual galaxies as well as on clusters (e.g. Harvey et al. 2015; Robertson et al. 2018; Kaplinghat et al. 2020). Parallel to these theoretical considerations, numerical simulations

have also improved and now take into account the effects of baryons on the DM halos (e.g. Di Cintio et al. 2014; Read et al. 2016a,b). Indeed, in the first simulations, only DM was considered, as this component is supposed to completely dominate the matter budget of galaxies and as baryons were thus thought to have a negligible importance. However, the interplay between the baryons and the DM particles could play a role in the resolution of the core/cusp problem. Nevertheless, this very complex interplay is still not well understood and has contradictory effects (see de Blok 2010, and references within). On one hand, DM cores could be created from initial cusps after the expulsion of large quantities of gas by supernovae during violent and large-scale bursts of star formation. These bursts would be consistent with the expected lives of gas-rich dwarf galaxies but not with the lives of the massive or of the LSB spirals. Similarly, the dynamical friction between baryons and DM particles could slow down baryonic structures (such as bars) while heating up the DM halos, disrupting their central cusps and turning them into cores. On the other hand, the gravitational effect of baryons concentrated at the centers of DM halos result in a contraction of the latter and thus in even cuspier profiles. Similarly, the merging processes of halos naturally tend towards steeper and steeper density profiles.

This core/cusp problem is thus still an important open subject in the field and a special attention is drawn towards the observations and analyses of RCs of galaxies' central regions as well as towards a very careful modeling of the luminous components.

1.4 In this work

This work, partially based on the preliminary results obtained by Van de Vyvere (2018) during her master thesis, aims at developing a RC decomposition that goes one step further towards a realistic description of the luminous as well as non-luminous components of spiral galaxies. To do so, we relax several commonly used simplifying assumptions associated to the modeling of these components mass distributions. If the effect of two of these hypotheses (i.e. the independent modeling of the molecular gas and the possibility to have varying stellar mass-to-light ratios) have already been shown as significant by previous studies (respectively Frank et al. 2016 and Portinari & Salucci 2010), other hypotheses, and particularly the way the stellar component is obtained, have not been investigated yet in a

RC context.

Moreover, all these new modelings have never been combined together to understand their global influence on the composition of galaxies. The usual simplifications having already been described in great details in the previous two sections, this section focuses on the innovations we implemented to replace them and develop more realistic descriptions of galaxies. A summary of both the assumptions usually made as well as of the alternatives developed in this work can be found in Table 1.1.

The main innovation in this work relates to the modeling of the stellar component. Instead of using one single NIR image of the galaxy, allowing only to probe its low-mass stellar populations, we choose to model the whole stellar photometric SED from images taken in 9 bands from FUV to NIR. With this more complex method, we are able to understand the distributions of all stellar populations, leading to a more realistic view of galaxies (de Denus-Baillargeon et al. 2013). Moreover, the synthetic models of stellar populations used for this global modeling have the advantage of determining the populations' mass-to-light ratios. Their values is thus neither fixed or forced to be constant across the whole galaxy. Realistic radially varying ratios (as supported by de Blok et al. 2008, Portinari & Salucci 2010 or de Denus-Baillargeon et al. 2013 results) thus naturally derive from this multiwavelength modeling.

If this SED fitting methodology is widespread in general galactic studies to derive properties (star formation rate, ISM properties, stellar IMF, AGN contribution, ...) of galaxies, it is rarely used for the determination of mass distributions in a RC context. The complexity of fitting a whole SED is often not seen as being worth the effort (e.g. McGaugh & Schombert 2014). In this work, we question this idea and evaluate whether this more realistic multiwavelength stellar modeling has a significant impact on the resulting RC decomposition.

The collateral negative side effect is that the short-wavelength observations used in our methodology are highly impacted by the presence of dust. We thus have to model the dust content of the galaxies. To do so, we use 9 supplementary images (in MIR, FIR and sub-mm) of the dust thermal emission and estimate the dust mass distribution as well as its effects on the stellar light in UV and in optical. The dust mass being an accessory byproduct of our methodology, we also use it to analyze its impact on the modeled RC, even if this component accounts for a negligible fraction of the mass budget.

Table 1.1: Improvements implemented in this work compared to the simplifying hypotheses usually assumed when modeling radial (R) and vertical (V) mass distributions of galactic components in RC studies.

Component		Usually	This work
Dust		Neglected	Estimated from MIR, FIR and sub-mm emissions
Gas			
ionized		Neglected	*Same as usually*
molecular	R	Neglected or included in the stellar modeling	Estimated from CO emission (considering metallicity dependency)
neutral	R	Estimated from 21 cm emission	*Same as usually*
all	V	Infinitely thin disk	Disk thickness derived from hydrotatic equilibrium modeling of the galaxy
Stars	R	Estimated from single-image NIR emission with fixed or free $\Upsilon_*^{\mathrm{NIR}}$ value (constant across the galaxy)	Estimated from multiwavelength (FUV to NIR) emission (photometric SED fitting) with radially varying Υ_* derived from stellar population models
	V	Spherical bulge (if modeled) and thick disk	*Same as usually* (with a systematic modeling of the bulge)
DM		Analytical halo model	Direct characterization (spherical and thin disk distributions)

Concerning the remaining luminous components, the degree of innovation of our method varies with the type of gas modeled. As usually done, we neglect the ionized gas contribution and use radio observations at 21 cm to estimate the (radial) distribution of the neutral one. In 3D, the neutral gas is nonetheless derived from the modeling of the whole galaxy as an 3D object in hydrostatic equilibrium (as done by Bacchini et al. (2019) or Patra (2020) but not in a RC context). This way, we allow this gas to be distributed as a flaring disk, a more realistic description than the infinitely thin disk that is usually assumed. Moreover, as recommended by Frank et al. (2016), we independently estimate the molecular gas mass distribution through observations of the CO molecule rather than by incorporating it in the stellar modeling.

Finally, while DM is usually assumed to be distributed in a spherical halo, following particular analytic distributions, we decide to get rid of these hypotheses and to retrieve and characterize directly the missing mass distribution. We are thus not restricted to the DM models resulting from cosmological or theoretical considerations. We assume two extreme 3D distributions (i.e. a spherical and a thin disk geometries). Obviously, the usual halo parametrizations can still be fitted afterwards on our spherical distributions and compared to the results from the other RC studies. One may note that this characterization is only made possible by the fact that the degeneracy between the stellar and the DM components is broken with our methodology. Indeed, our stellar mass-to-light ratios are not left free but are determined by the synthetic stellar models we used when fitting our stellar photometric SED.

In summary, in this work, we develop a methodology to model the luminous components of spiral galaxies with more physically accurate assumptions than what is usually done in RC studies. The main idea is to analyze the effects of this improved method on the mass discrepancy between the observed and the expected RCs and hence, on the necessary non-luminous matter. In addition to this main result, several accessory byproducts can also be retrieved such as the galactic star formation history, the radial evolution of its metallicity or of its dust grain physical conditions. This thus makes of our alternative methodology a particularly versatile tool for studies of spiral galaxies in general, not only of their RCs.

Practically, our new RC decomposition is implemented into a semi-automatic Python pipeline. It is tested and shown to work on a sample of six nearby spiral galaxies, each of them being an archetype for their RC

category.

1.5 Outline

In Chapter 2, we present the sample of galaxies used to test our new methodology as well as all the images necessary to derive the mass distributions of their luminous components (i.e. broad band images from FUV to sub-mm for the stars and dust as well as images of HI and CO emission lines for the gas). We then explain, in Chapter 3, how we converted the images into luminosity profiles and how we disentangled the components emissions. Our subsequent mass modelings are described in Chapters 4 (for the radial distribution of the stellar component) and 5 (for the other innovations of our new methodology), a particular attention being paid to the testing of the more complex but more realistic stellar SED modeling. Finally, we analyze in Chapter 6 the global impact of all the implemented innovations on the RC decomposition and on the resulting DM content of the galaxies.

Chapter 2

Introducing the actors
Galaxy sample & data description

To probe the different luminous components of spiral galaxies with our multiwavelength methodology, we need high-resolution images in multiple bands going from FUV to sub-mm to build the stars and dust photometric SEDs. For the gaseous component, images at particular wavelengths corresponding to prominent emission lines are also required. Once modeled, the mass distributions of these luminous components will be converted in rotation velocity and compared to the galaxies' high-resolution RCs. These constraints limit the number of galaxies that will be analyzed and on which our new methodology will be tested. We end up with a sample of six nearby spiral galaxies, with a certain variety of morphology, of mass and, more importantly, of RC shape.

In this chapter, we describe the data at the base of this work with first, the RCs (Section 2.1), from which we derived our final sample of galaxies (Section 2.2). We then present all the images used in our multiwavelength galaxy modeling in Sections 2.3 (for the stellar and dust components) and 2.4 (for the gaseous one). The preprocessing steps performed in this work are also described in these last two sections.

2.1 Rotation curves

For this work, we used the SPARC (*Spitzer* Photometry and Accurate Rotation Curves) database compiling high-quality RCs of 175 spiral and

irregular galaxies from studies stretching over more than 30 years (Lelli et al. 2016a). These galaxies constitute a representative sample of the late-type galaxies in our neighborhood and cover a broad range of morphologies, radii, luminosities, surface brightnesses, rotation velocities and gas-to-stars proportions. The RCs are principally built on HI interferometric observations and about one third of the RCs have been upgraded in their central regions with high-resolution Hα data from long-slit spectroscopy, integral-field spectrography or Fabry-Perot interferometry.

As suggested by the name of the database, all the SPARC galaxies have been observed by the *Spitzer* Space Telescope (Werner et al. 2004), hence in its NIR 3.6 μm band. Therefore, the usual simplified estimation of the stellar content of a galaxy can be (and has been) implemented. Using the galaxies from this database ensured us the possibility to assess and compare our new methodology with the classical one when computing the stellar mass distributions.

Moreover, all these compiled RCs have been build and checked to reduce to a minimum the beam smearing effects associated to low-resolution radio observations. Indeed, if the size of the radio beam is not small enough, the emission of the galaxy will be smeared out, the disks appearing larger than they really are, the velocity gradients shallower and the resulting DM halo more cored. The SPARC database was also chosen because their RCs are processed with a particular attention to reduce these effects, particularly in the central regions of the galaxies. This is done (i) by replacing the inner portions of the HI RCs with high-resolution Hα RCs when such observations are available or (ii) by developing techniques to take the existing beam smearing effect into account (Lelli et al. 2016a). With such RCs at the base of our analysis, we have the guarantee to reliably characterize the DM halos shapes at the centers of the galaxies.

2.2 Galaxy sample

2.2.1 Choice of the studied galaxies

In the SPARC database, the RCs are classified in 3 categories according to the quality of the observations and to the existence of galactic features that are difficult to model and can thus bias the final RC. Following the team recommendations (Lelli et al. 2016a), we excluded from our sample the galaxies with low inclinations, strong non-circular motions, high asym-

metries between the approaching and receding parts of their RC and/or offsets between the stellar and the gas distributions. This corresponds to 22 objects on the 175 in the database.

On top of that, we further reduced our sample to galaxies whose distance is known precisely and independently from the Hubble flow. This was done to avoid any impact of the assumed cosmological model on our analysis. 50 objects fulfill this requirement, their distance being determined from primary distance indicators (i.e. tip of the red giant branch, Cepheid or type Ia supernovae methods). They were thus selected to implement and test our new methodology.

Another set of SPARC objects have their distance estimated independently from the cosmology, the 28 galaxies of the *Ursa Major* cluster whose average distance is determined precisely via the Tully-Fisher relation. Nevertheless, due to the estimated depth of the cluster, the individual distances of these objects are more uncertain. They were thus not included in our first sample of galaxies but are prime candidates to extend this work.

Finally, to model the stellar and dust emissions via a photometric SED, we needed images of the galaxies in various domains spanning from FUV to sub-mm. Moreover, images in one of the emission lines of CO were also necessary in order to trace the molecular gas within the galaxies. All the information on the specific bands used in this study will be given in Section 2.3. This multiwavelenth constraint reduced our sample to 8 objects, the most restrictive observations being the FIR and sub-mm ones, necessary to model the dust physical characteristics but only detectable by very few telescopes.

Among the last 8 objects, 2 were irregular galaxies not appropriate for our methodology modeling due to their morphological aspect (NGC4214) or their lack of emission at long wavelengths (DDO154). They were thus also excluded from the sample used in this work, leaving 6 objects whose principal characteristics are compiled in Tables 2.1 (for the galaxies in themselves) and 2.2 (for their RCs).

Extensively used in RC studies since the very beginning (e.g. Bosma 1981; Begeman et al. 1991), these 6 galaxies constitute an ideal sample for us to implement and test our methodology. Indeed, they cover all the categories of spiral galaxies' RCs described in Section 1.2, going from massive early- to dwarf late-type spirals.

Table 2.1: General properties of our sample of galaxies

Galaxy	Hubble type[†]	Hubble stage[†]	Distance[‡,*] [Mpc]	Inclination[*] [deg]	Size[**] [kpc]	Components masses[§] $[M_\odot]$ $\log(M_*)$	$\log(M_{\rm HI})$	$\log(M_{\rm H_2})$
NGC2403	SABc	6.0 ± 0.3	3.16 ± 0.16	63 ± 3	6.99 ± 0.46	9.7	9.5	7.3
NGC2841	Sb	2.9 ± 0.5	14.1 ± 1.4	76 ± 10	15.1 ± 4.6	10.8	10.1	8.5
NGC2976	Sc	5.2 ± 1.1	3.58 ± 0.18	61 ± 10	3.42 ± 0.47	9.1	8.3	7.8
NGC3198	SBc	5.2 ± 0.6	13.8 ± 1.4	73 ± 3	12.1 ± 1.4	10.1	10.1	8.8
NGC5055	Sbc	4.0 ± 0.2	9.9 ± 0.3	55 ± 6	18.9 ± 1.0	10.8	10.1	9.7
NGC7331	Sbc	3.9 ± 0.3	14.7 ± 1.5	75 ± 2	22.5 ± 4.8	10.9	10.1	9.7

[†] Compiled by the DustPedia project (Clark et al. 2018) from the HyperLEDA database (Makarov et al. 2014). The Hubble stage T quantifies by a numerical value the Hubble type of the galaxy ($T \leq -4$ for the elliptical galaxies, $-4 < T \leq 0$ for lenticulars, $0 < T \leq 8$ for spirals and $T > 8$ for irregulars).

[‡] Distance methods: Cepheid period-magnitude relation (NGC2841, NGC3198, NGC7331) or magnitude of the tip of the red giant branch (NGC2403, NGC2976, NGC5055)

[*] Given by the SPARC database (Lelli et al. 2016a)

[**] Characteristic size r_{25}, defined as the radius at which the galaxy apparent magnitude in the B band equals 25 mag arcsec^{-2}; computed by us (see Footnote 6 on page 80 for more details)

[§] Computed from 3.6 μm, 21 cm and CO images for respectively the stellar, the neutral gas and the molecular gas components (Leroy et al. 2008)

Table 2.2: Properties of the rotation curves of our sample of galaxies (compiled from literature by the SPARC database; Lelli et al. 2016a)

Galaxy	Quality	Category†	Ref. HI	Ref. Hα
NGC2403	High	II	(1)	(2)
NGC2841	High	I	(3)	(4)
NGC2976	Medium	III	-	(5)‡
NGC3198	High	II	(3,6)	(2)
NGC5055	High	I	(7)	(8)
NGC7331	High	I	(3,6)	-

† Described in Section 1.2. I: RC with a steep inner increase followed by a slight decrease towards a plateau; II: typically flat RC; III: monotonically rising RC
‡ RC derived from Hα and CO observations
References: (1) Fraternali et al. (2002); (2) Daigle et al. (2006); (3) Begeman et al. (1991); (4) Dicaire et al. (2008); (5) Simon et al. (2003); (6) Begeman (1987); (7) Battaglia et al. (2006); (8) Blais-Ouellette et al. (2004)

2.2.2 Individual descriptions

All but one of the RCs of the galaxies constituting our sample can be found in the various figures of the Chapter 1 but for clarity and readability reasons, we reproduce them in Figure 2.1.

Before describing each galaxy individually, an important common characteristics has to be pointed out in the context of this study. As mentioned in Chapter 1, when estimated from measurements of the gas velocity dispersion, the thickness of spiral galaxies gaseous disk seems to systematically increase with the distance to their center. This is also the case for the six galaxies in our sample. Indeed, the thickness of their gas disk is expected to be multiplied by $\sim$3 between their inner and their outer regions, with NGC5055 having an even more important flaring factor of $\sim$8 (Bacchini et al. 2019; Patra 2020). It is thus pertinent here to model the vertical extension of the gas disk and to analyze its effects on RC decompositions.

NGC2403

This late-type spiral is the archetype of category II RCs. It displays an almost rigid-body rotation in its center, followed by a typically flat plateau as can be seen in panel (a) of the Figure 2.1.

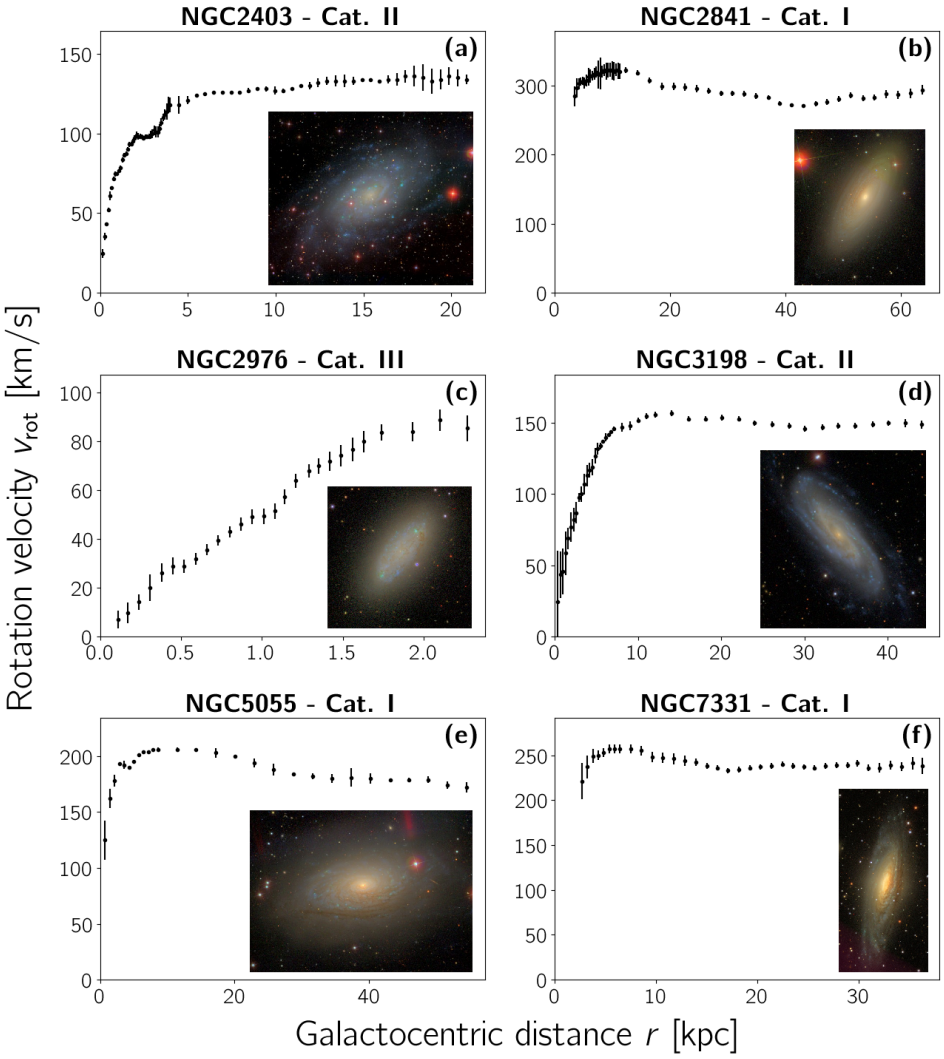

Figure 2.1: Rotation curves and multi-color optical images of the galaxies in our sample. For NGC2403, NGC2841, NGC3198 and NGC5055, the difference in spatial resolution corresponds to the transition from the inner Hα RC to the outer HI one. The RC of NGC2976 is based on Hα and CO observations while the one of NGC7331 is derived only from HI emissions. Data: RCs compiled by the SPARC database (Lelli et al. 2016a), images taken by the SDSS collaboration (NGC7331: retrieved via the *Aladin sky atlas*; other galaxies: © 2006 M.R. Blandon and D.W. Hogg)

Despite belonging to the M81 group, this galaxy has an undisturbed disk. Its HI and Hα velocity fields are very regular and symmetric (Blais-Ouellette et al. 2004; de Blok et al. 2008). Even if NGC2403 shows signs of a central bar, it is weak (hence the SAB classification) and has no notable effect on the galaxy kinematics (Hernandez et al. 2005). Similarly, the effects of its spiral arms are visible on the final RC due to streaming motions along them (Blais-Ouellette et al. 2004; de Blok et al. 2008) but globally, the non-circular motions in the disk have been found to be negligible (Schoenmakers et al. 1997; Fraternali et al. 2002). This galaxy RC is thus particularly reliable.

Concerning the stellar populations of NGC2403, de Blok et al. (2008) observed a clear trend of its NIR J–K color with galactocentric distance, indicating a change of populations across the galaxy and the necessity of varying mass-to-light ratios (even when considering only NIR images). Moreover, the galactic disk contains numerous active star-forming regions with hot and young (age $\sim$20 Myr) supergiant stars (Leitherer et al. 2002) that are not usually modeled in RC decompositions.

Lastly, if taking into account the molecular gas does not seem to impact considerably the galaxy modeling and its DM content (Frank et al. 2016), the neutral gas of this galaxy is distributed in a thin layer surrounded by a thicker clumpier one (corresponding to 10–20% of the total gas mass; Schaap et al. 2000; Fraternali et al. 2002; Marasco et al. 2019).

NGC2841

This early-type spiral is the archetype of a flocculent galaxy, that is to say, a galaxy without a global spiral pattern. Being also very massive, its RC thus displays features typical of the category I.

It is an active galaxy with a weak LINER (Low-Ionization Nuclear Emission-line Region) nucleus (Filippenko & Sargent 1985). The Hα lines emitted from this region (under $\lesssim$ 50 arcsec or 3.35 kpc; Dicaire et al. 2008) are thus not only broadened by the global rotation of the galaxy. The RC associated to the very center of the galaxy is not accessible. This can be seen in panel (b) of Figure 2.1, the innermost point of the RC corresponding to a distance of 3.44 kpc. However, in the rest of the galaxy, the HI and Hα velocity fields are regular, except at very large radii where signs of a warp of the gaseous disk are visible (Dicaire et al. 2008; de Blok et al. 2008; Zhang et al. 2018; Bacchini et al. 2019). This is taken into account when deriving

the RC but it inevitably brings more uncertainties in the final modeling than if the galaxy was not warped (Bottema & Pestaña 2015).

NGC2841 clearly lacks gas (be it atomic or molecular) in its central regions (Frank et al. 2016). Its gaseous disk seems nevertheless rather thick (Patra 2020) and it is composed of a prominent ring of molecular clouds between 2 and 7 kpc (Young & Scoville 1982). It is important to take this gas thickness and this molecular content into account in the RC decomposition (as shown by Frank et al. 2016 for the molecular gas). Additionally, this ring region is thought to be associated to enhanced star formation with young stars populations (Prieto et al. 1985). Variations in stellar populations are also observed in the whole stellar and HI disk via UV emissions and gradient of NIR colors (Thilker et al. 2007a; de Blok et al. 2008).

NGC2976

NGC2976 is the smallest and the least massive galaxy in our sample. Combined with its low luminosity, this late-type spiral is at the upper limit of the dwarf category (Bronkalla et al. 1992). Hence its nearly linear RC, only flattening at the very edge of the HI disk (Stil & Israel 2002b), is typical of the RC category III, of which it is the only representative in our sample. NGC2976 is of particular interest for us as galaxies of this kind provide the most restrictive constraints on the DM halo models in the context of the core/cusp problem. The RCs of category III in general and the one of NGC2976 in particular tip the scale in favor of cored models (Simon et al. 2003).

If circular motions are a good description of NGC2976 kinematics at first order, particularly at average and large radii, there is evidence of non-circular motions in its inner parts (Simon et al. 2003; de Blok et al. 2008; Spekkens & Sellwood 2007). They appear whatever the probed galactic component (molecular, neutral and ionized forms of gas as well as old stars and dust lanes; Spekkens & Sellwood 2007; Valenzuela et al. 2014). Thought to be due to the presence of gas-rich features (a central bar and two symmetric spiral arms), these motions degrade the quality of the retrieved RC. This galaxy is thus the only one of our sample with a RC quality categorized as “Medium” by the SPARC database (see Table 2.2). The origin of these unusual gaseous features is still a matter of debate but, according to Valenzuela et al. (2014), the two possible explanations are (a combination

of) the initial triaxiality of the DM halo surrounding the galaxy and the direct impact of its neighborhood (the M81 group and its complex landscape of HI giant clouds and bridges; Appleton et al. 1981; Chynoweth et al. 2008).

Even if NGC2976 is rich in CO for a dwarf galaxy with the existence of a molecular ring at $\sim$ 1.4 kpc (Kaneda et al. 2007), its molecular gas content is negligible compared to its other components (Simon et al. 2003). Hence, with no surprise, the modeling of this gas has been shown to have no significant impact on the dynamics of the galaxy (Simon et al. 2003; Frank et al. 2016). Yet, a unusual characteristics of this galaxy is that its CO emission is as extended as its HI one (Stil & Israel 2002a), making NGC2976 the only galaxy of our sample with a RC partially derived from CO observations.

Despite this low importance of molecular gas, NGC2976 is pertinent to study with our new methodology for its stellar content. Indeed, if the older stars populations of NGC2976 are uniformly distributed, the young ones greatly vary within the galaxy. Traces of recent star formation are visible in the molecular ring region (Kaneda et al. 2007) and, more globally, in the whole central half of the galaxy (under distances up to 3 kpc; Williams et al. 2010). This situation, potentially due to a recent ($\gtrsim$ 1 Gyr; Williams et al. 2010) interaction event with the core of the M81 group, is of particular interest in the context of our modeling of the whole stellar content of the galaxy.

NGC3198

Among RC studies, NGC3198 is a must-have galaxy in any sample. In addition to having a very reliable RC due to its regular HI kinematics (van Albada et al. 1985; de Blok et al. 2008), this galaxy is also rich in gas compared to the S(B)c galaxies (Bottema & Pestaña 2015) and its RC extends particularly far in its outskirts (Begeman 1987). This last peculiarity made it emblematic of the mass discrepancy problem in spiral galaxies since the very beginning of the field (van Albada et al. 1985). Hence, over the years, NGC3198 has been extensively observed and studied in a wide variety of wavelength domains, making it perfect for this study.

Recently, small streaming motions along its spiral arms as well as a slight warp of its disk at large radii have been detected (Bottema et al. 2002; de Blok et al. 2008). Fortunately, these imperfections do not have a

significant impact on the RC. The inner kinematics of NGC3198, however, is quite complex due to the presence of a bar creating important non-circular motions (Hernandez et al. 2005; de Blok et al. 2008; Bottema & Pestaña 2015). These are taken into account when deriving the Hα RC (Daigle et al. 2006) but they nevertheless increase the associated uncertainties.

In addition to having a gaseous component more radially extended than usual, this galaxy also shows signs of a vertical extension of its neutral gas content, its thick disk corresponding to about 10–15% of its total HI mass (Gentile et al. 2013; Marasco et al. 2019). This gas richness seems nevertheless limited to the neutral component. Indeed, NGC3198 molecular gas does not appear to play a significant role on the galaxy global kinematics (Frank et al. 2016).

NGC5055

NGC5055, also called M63, is a massive flocculent galaxy with multiple loose spiral arms (Bosma 1981; Thornley 1996) and a category I RC.

Its HI content can be probed relatively far in its outskirts and is distributed as a disk with an extended and symmetric warp that is thought to be a dynamically stable structure (Bosma 1981; Battaglia et al. 2006). Even if the warp is oriented in the direction of a nearby companion galaxy (UGC8313), tidal interactions do not seem to explain the disk deformation. A misalignment between the disk and its DM halo is rather preferred (Battaglia et al. 2006). In any case, as explained for the other galaxies with a warp, this features complicates the retrieval of the associated RC.

Despite the fact that the galaxy has no central bar visible, strong non-circular motions are detected in its inner regions and have to be taken into account when deriving the Hα RC (Blais-Ouellette et al. 2004). On top of that, the RC can not be reliably computed at the very center of the galaxy (for distances under $\sim$8arcsec or 0.35kpc; Blais-Ouellette et al. 2004). Indeed, the nucleus of NGC5055 (which is also a weak LINER; Ho et al. 1997) displays a complex and strange kinematics with the superposition of two velocity components, one that follows the global rotation of the galaxy and another one probably associated to a bipolar outflow (Blais-Ouellette et al. 2004). This central region is excluded from the SPARC database, the RC in panel (e) of Figure 2.1 starting at 0.72kpc.

The RC of NGC5055 displays the typical characteristics of a category I RC. The broad maximum of its rotation velocity is followed by a decrease

which, for this galaxy, is rather large and starts at the end of the stellar disk. According to Battaglia et al. (2006), these two features are reproducible at the same time only by the maximum-disk hypothesis. This is typical of this family of massive galaxies as they generally present two well-distinct rotation states: one that is almost exclusively dominated by the stellar content (in the visible disk) and one dominated by their DM halo (in the outskirts). The study of such galaxies, and in particular of NGC5055, is thus interesting as it provides a way of investigating if our alternative modeling of the galactic stellar component comes to the same conclusions.

Additionally, NGC5055 is pertinent for all the modelings implemented in our new methodology. Firstly, even if NGC5055 is considered as a superthin galaxy by Patra (2020) (despite its particularly important flaring mentioned earlier), it shows signs of gas clouds rotating at velocities smaller than the ones of the galactic mid-plane (Battaglia et al. 2006; de Blok et al. 2008). This situation is usually encountered if the galaxy has a thick gaseous disk, as observed for NGC2841 and NGC3198. Marasco et al. (2019) even evaluated its thick disk to represent around 5% of its HI mass in the inner half of the galaxy ($\lesssim$ 20 kpc). Our 3D modeling of this gas component may be able to discriminate between these two possibilities. Secondly, NGC5055 has already been analyzed by Frank et al. (2016), showing the significant impact of the modeling of the galaxy molecular gas content on the RC decomposition. Finally, NGC5055 stellar properties are also known to change across the galaxy with the existence of star formation zones even in the outer HI disk (Thilker et al. 2007a) and varying stellar mass-to-light ratios measured in optical as well as in NIR (de Blok et al. 2008; Takamiya & Sofue 2000).

NGC7331

NGC7331 is the largest, the most massive and the most distant galaxy of our sample. It has been extensively studied, particularly because of its similarities (in terms of morphology, of total mass, of gas, and of dust content) with the MW and Andromeda (e.g. Israel & Baas 1999; Thilker et al. 2007b).

Its HI velocity field is regular despite a few signs of streaming motions along its prominent spiral arms (de Blok et al. 2008). Its outer RC is thus quite precisely known while it is less the case for its inner Hα RC. Indeed, the receding part of the galaxy is hidden at this wavelength by the presence

of an important dust component (Daigle et al. 2006). This results in an inner RC computed only from the approaching portion and thus to larger uncertainties. Moreover, the RC of its very central parts is usually not provided as its gas kinematics displays very unusual behaviors (Bottema & Pestaña 2015) and as its nucleus is a weak LINER (Ho et al. 1997). Hence, as for NGC5055, the RC provided by the SPARC database for NGC7331 is only derived from HI observations.

The dust component that hides a portion of NGC7331 is in fact distributed as a ring between ∼1.5 and 6 kpc (Sutter & Fadda 2022) which is visible in various wavelength domains (Regan et al. 2004). Indeed, besides dust, this ring also contains a large proportion of the molecular gas of the galaxy, a component whose modeling has to be included in RC decompositions (Frank et al. 2016).

Concerning its stellar content, NGC7331 largely resembles NGC2841 with regions of intense star formation associated to the molecular ring[1] (Thilker et al. 2007b), strongly varying NIR colors across the galaxy (de Blok et al. 2008) and a prominent and extended bulge[2] (Arp & Kormendy 1972) whose stellar populations differ from the ones of the disk. de Blok et al. (2008) pointed out that the quantities of dust within the galaxy could significantly bias the stellar mass-to-light ratios derived from the NIR colors, resulting in an overestimation of the mass of the stellar components. From observations of stellar velocity dispersion, Bottema (1999) also comes to the conclusion that the NGC7331 disk is greatly sub-maximal, its rotation being dominated by its bulge and by its DM halo. An independent determination of stellar mass distribution like the one developed in this work will thus be particularly useful for this galaxy.

[1] Its molecular ring also contains dust. The extinction by the grains is thus a factor that has to be taken into account here (Thilker et al. 2007b) while it is less significant in NGC2841.

[2] Kinematically, this bulge could (Prada et al. 1996) or could not (Mediavilla et al. 1997; Bottema 1999) counter-rotate with no firm evidence at this stage for either of the two solutions.

2.3 Stellar and dust components

2.3.1 Images

To probe the stellar and the dust components of spiral galaxies, we used images from the DustPedia database[3] (Davies et al. 2017). This database provides partially preprocessed images of 875 nearby galaxies in various observing bands. We selected 18 bands spanning from the FUV to the sub-mm from 6 facilities: the GALaxy Evolution eXplorer (GALEX; Morrissey et al. 2007), the Sloan Digital Sky Survey (SDSS; York et al. 2000; Eisenstein et al. 2011), the *Spitzer* Space Telescope (Werner et al. 2004) and the *Herschel* Space Observatory (Pilbratt et al. 2010). More information about the bands used in this work can be found in Table 2.3 while their transmission curves, retrieved from the SVO Filter Profile Service[4], are shown in Figure 2.2.

For details about the preprocessing performed by the DustPedia team, the reader is invited to directly see the associated paper by Clark et al. (2018). To summarize, all images of each galaxy were retrieved and gathered from the official archives of each facility. They were then mosaicked together and rotated into a North up, East left orientation. Their pixels values were converted into the same unit, the Jansky (Jy), and the images were centered on the galaxy and resized to square images of 0.5° (or of 1° for the most spatially extended galaxies). For some observing bands, namely the MIR, FIR and sub-mm ones, error images were also provided.

2.3.2 Preprocessing finalization

As the preprocessing from the DustPedia team was only partial, we implemented the late steps by ourselves. For each galaxy, we thus homogenized all the images in term of pixel size. Once the images were consistent with one another, the light from the galaxy has been isolated, first by removing the foreground stars and the background galaxies, then by subtracting the sky background to each image.

[3] `http://dustpedia.astro.noa.gr/`
[4] `http://svo2.cab.inta-csic.es/theory/fps/`

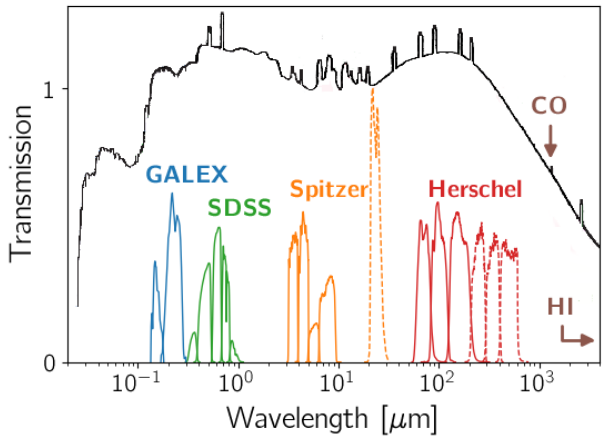

Figure 2.2: Transmission curves of observing bands (stellar and dust components) and gaseous emission lines used in this work. The background of the image (black line) represents the observed SED for a normal spiral galaxy (taken from Figure 1.5). For *Spitzer* and *Herschel*, the transmission curves of the different instruments are differentiated by the line style (IRAC/MIPS: solid/dashed orange lines, PACS/SPIRE: solid/dashed red lines).

2.3.2.1 Image homogenization

Once all the DustPedia images of a galaxy were retrieved, we rebinned them to the smallest pixel size of all the images (i.e. to the SDSS pixel size). Each small-pixel value has been computed via a bilinear interpolation of its four big-pixel neighbors and multiplied by a factor taking into account the pixel surface modification. The rebinned images were then aligned on the same pixel grid. In parallel, the same modifications have been realized on the associated error images.

2.3.2.2 Foreground cleaning

To clean images from their foreground stars, we looked for stars in the fields of view of our images and retrieved their positions from the second

Table 2.3: Observing bands used in this work (stellar and dust components)

Facility	Band name	Domain	Eff. wavelength† [μm]	Pixel size [arcsec]	Calib. uncertainty‡ [%]
GALEX	FUV	UV	0.155	3.2	4.5
	NUV	UV	0.230	3.2	2.7
SDSS	u	UV	0.361	0.45	1.3
	g	visible	0.467	0.45	0.8
	r	visible	0.614	0.45	0.8
	i	NIR	0.746	0.45	0.7
	z	NIR	0.892	0.45	0.8
Spitzer	IRAC-3.6	NIR	3.5	0.6* - 0.75	3
	IRAC-4.5	NIR	4.4	0.6* - 0.75	3
	IRAC-5.8	MIR	5.6	0.6	3
	IRAC-8.0	MIR	7.6	0.6	3
	MIPS-24	MIR	23.2	1.5 - 2.45**	5
Herschel	PACS-70	FIR	69	2	7
	PACS-100	FIR	98	3	7
	PACS-160	sub-mm	154	4	7
	SPIRE-250	sub-mm	243	6	5.5
	SPIRE-350	sub-mm	341	8	5.5
	SPIRE-500	sub-mm	483	12	5.5

† Computed by the SVO Filter Profile Service

‡ Calibrations uncertainties have been compiled from the different facilities and instruments handbooks by Clark et al. (2018) (see references within for more details)

* For NGC2403 and NGC7331

** For NGC2403

data release of the *Gaia* archive[5] (Gaia Collaboration 2016, 2018). We did not correct images where stars were not visible, that is to say MIR, FIR and sub-mm images as only dust emits at these long wavelengths. The positions of the background galaxies were retrieved from the SIMBAD astronomical database[6] (Wenger et al. 2000) via the use of the *Aladin sky atlas*[7] (Bonnarel et al. 2000; Boch & Fernique 2014).

For each star in each image, our automatic algorithm[8] detected the presence of the star around the position given by the *Gaia* database. We then manually checked and selected the circular zone impacted by the stellar light. To replace the pixels of this zone, a two-dimensional polynomial fit was performed on a surrounding annulus. The polynomial degree was left free from 0 to 2, to account for the local background of the star. Finally, the central pixels were replaced by the extrapolation of this fit and the errors on the fit were propagated to the associated error images.

For one of our galaxies (NGC5055), the images from the SDSS bands presented a saturated foreground star located on the apparent edge of the galaxy. As the impacted zone was quite large, we chose to simply not use the pixels of the saturated zones instead of replacing them by an extrapolation that would have been biased by the presence of the galaxy. For two of these bands (SDSS-u and SDSS-i), an additional artifact was present next to this star (due to the saturation of the CCD) and the corresponding pixels were also erased from the image.

Concerning the background galaxies within the field of view of our images, the correction depended on the apparent size of the objects. For the smallest galaxies, we performed extrapolations of fits as for the stars while we preferred to discard the pixels associated to the largest galaxies for the same reasons as for NGC5055.

2.3.2.3 Background subtraction

Once the images were cleaned from the stars and from other galaxies in the field of view, we modeled the sky background by fitting a two-dimensional polynomial on the zone of the image not impacted by the light from the

[5] `https://www.cosmos.esa.int/gaia`

[6] `http://simbad.u-strasbg.fr/simbad/`

[7] `https://aladin.u-strasbg.fr/`

[8] Based on the Python package Photutils (`https://photutils.readthedocs.io`) and its implementation of the DAOFIND algorithm (Stetson 1987).

galaxy. To correct for eventual instrumental gradient (as GALEX and *Spitzer* images are likely to display; Clark et al. 2018) while avoiding overfitting, we limited ourselves to two-dimensional polynomials of the first order. These modeled backgrounds were subtracted from their respective images and the errors associated to these fits were propagated to the global error image.

2.4 Gaseous components

2.4.1 Atomic gas

To probe the neutral hydrogen, we used the emission line at 21 cm. The observations at this wavelength came from the The HI Nearby Galaxy Survey[9] (THINGS; Walter et al. 2008) using the Very Large Array of the National Radio Astronomy Observatory as well as from the Westerbork Hydrogen Accretion in Local GAlaxieS survey[10] (HALOGAS; Heald et al. 2011) performed by the Westerbork Synthesis Radio Telescope. If the latter have a lower spatial resolution (pixel size of 4 arcsec for HALOGAS compared to 1.5 arcsec for THINGS), their field of view is wider, which allowed us to analyze as a whole the most extended galaxies of our sample (NGC2403, NGC3198 and NGC5055).

As explained in Section 1.1, the radio observations are originally under the form of datacubes that can be condensed to generate velocity-integrated maps of HI emission. To only keep the genuine emissions of the galaxy in the final image, the individual slices are blanketed and corrected from primary beam attenuation. They are then all summed up to create the integrated or "moment 1 map", a single map probing the whole neutral hydrogen emission. These maps, provided by the HALOGAS and THINGS teams, are the ones used in this work.

Additionally, we converted the maps of our different galaxies in units easier to handle (in Jy km s^{-1}). For that, we took into account the beam sizes (assumed to be a Gaussian with major and minor axes given in Table 2.4) and compared them with the spatial resolution of each integrated map.

[9] `https://www2.mpia-hd.mpg.de/THINGS/Data.html`
[10] `https://www.astron.nl/halogas/data.php`

Table 2.4: Specific information on the integrated maps of atomic hydrogen for our sample of galaxies and on the datacubes† from which they have been generated

Galaxy	Survey	θ_{maj}‡ [arcsec]	θ_{min}‡ [arcsec]	Number of channels	Channel noise level [mJy/beam]	Velocity resolution [km/s]	Ref.
NGC2403	HALOGAS	15.18	13.32	60	0.28	5.1	(1,3)
NGC2841	THINGS	11.06	9.37	132	0.35	5.2	(2)
NGC2976	THINGS	7.41	6.42	42	0.36	5.2	(2)
NGC3198	HALOGAS	19.89	13.56	99	0.20	4.12	(3)
NGC5055	HALOGAS	19.92	13.37	169	0.23	4.12	(3)
NGC7331	THINGS	6.13	5.61	116	0.44	5.2	(2)

† Calculated with natural weighting by the HALOGAS and THINGS teams
‡ Major and minor axes of the synthesized (Gaussian) beam associated to each integrated map
References: (1) Fraternali et al. (2002); (2) Walter et al. (2008); (3) Heald et al. (2011)

2.4.2 Molecular gas

As it is made from two identical atoms, the molecular hydrogen is extremely difficult to detect in astrophysical environments, as explained in Section 1.3.1. It is thus necessary to find another gas to trace H_2. For that purpose, CO, the second most abundant molecule in ISM, is the perfect candidate. Indeed, CO has several rotational transitions in the millimeter domain that are easily excited by the collisions with the neighboring H_2 molecules in the conditions of temperature and density of molecular clouds. The two main transitions of CO are the J=1→0 line (at 2.6 mm or 115 GHz) and the J=2→1 line (at 1.3 mm or 230 Hz).

In this study, we used observations from the Heterodyne Receiver Array CO Line Extragalactic Survey[11] (HERACLES; Leroy et al. 2009). These were taken with the IRAM 30-meter telescope and they map the CO emission from nearby galaxies (including the sample we study) in the J=2→1 line. As for atomic hydrogen, the end products given by the HERACLES team that are useful in this work are the integrated maps (and their associated error maps).

An additional correction, taking into account the pixel size of the images (4 arcsec) and the wavelength of the emission line (1.3 mm), has been applied to transform the units of the maps into the same units as the images of the atomic hydrogen component (Jy km s^{-1}).

2.5 Conclusion

At this point, we have selected the sample of galaxies on which we will implement and test our new methodology of RC decomposition. To model these galaxies luminous components, images, spanning from the FUV to the radio domain, have been gathered, preprocessed and homogenized. If the ones corresponding to the gaseous lines (21 cm for atomic hydrogen and CO J=2→1 for the molecular one) are usable directly, the images from FUV to sub-mm display emissions from both the stellar and the dust components. They have to be disentangled before performing any modeling.

[11] https://www.iram-institute.org/EN/content-page-242-7-158-240-242-0.html

Chapter 3

Setting up the stage
Disentangling the different components

The modeling of the mass distributions of the three luminous components of our galaxies is based on the distribution of their light emissions at different wavelengths. As the final goal of this work is to analyze the effects of our new mass modeling on the expected RCs of the galaxies and as RCs are, by definition, 1D velocity profiles, it is necessary for us to transform, at some point in our process, the 2D images into 1D profiles. Here, we decided to compute the profiles of our galaxies before any mass modeling. With this choice, the conversion from luminosity to mass will be performed on 1D profiles and not on 2D maps, greatly saving computation time without impacting the spatial resolution of the results. Even if it is a common practice in RC studies, the computation of 1D profiles before any mass conversion is of greater importance for us as our stellar component modeling is more complex and hence takes more time than the usual methodology using only a NIR profile.

In addition to the conversion of our images into luminosity profiles, it is also necessary to disentangle the intrinsic emission of the stellar component from the other ones. To do so, we have to correct our shortest wavelengths profiles from the effects of extinction by the dust present within the MW but also, and more importantly, within the galaxies themselves.

In this chapter, we thus describe the computations to derive 1D luminosity profiles from 2D images (Section 3.1) and to disentangle the stellar and dust components' emissions (Section 3.2) in order to develop the mass modeling of each component separately in the next chapters.

3.1 Luminous components profiles

The transformation from a 2D image of a galaxy to its corresponding 1D profile necessitates to compute azimuthal averages over all the regions located at the same distance from the galactic center. If these regions are straightforward to isolate on face-on galaxies, it is not the case for the kind of galaxies found in RC studies. Indeed, the galaxies we have to deal with are inclined with respect to the plane of the sky, they thus appear elliptical. Their shape parameters, that is to say, their position angle and their apparent ellipticity, have thus to be determined in order to derive their luminosity profiles.

3.1.1 Galaxy shape parameters

The position angle (PA) of a galaxy quantifies its orientation. If it has several definitions depending on the chosen reference, we define it in this work as the angle between the galaxy major axis and the North direction (here, the vertical) of the image. The angle is taken as positive in the counterclockwise direction and has values between -90 and +90 deg. The ellipticity ϵ of a galaxy is given by $\epsilon = 1 - \frac{b}{a}$ where a and b are respectively the values of its semi-major and of its semi-minor axes.

To compute the shape parameters of our sample of galaxies, we used the methodology developed by Biernaux et al. (2016). To do so, circular (respectively, elliptical annulus) masks with various PA (resp. ϵ) were divided in quadrants and superimposed on each image of each galaxy. By averaging and comparing the flux values in the different quadrants, this gave us the values of the PA (resp. ϵ) of each galaxy for our different observing bands.

As all the images do not probe the same components of the galaxy, it is possible that the resulting shape parameters vary from one image to another. Using different values of PA and ϵ for different images would thus results in probing different regions of the same galaxy, and would completely invalidate our future multi-wavelength mass modeling. Therefore,

we associated each galaxy with one set of shape parameters by averaging the individual PA and ϵ values over all the images of the given galaxy.

One may note that the Biernaux et al. (2016) methodology was developed for early-type galaxies. The hypotheses at the base of the ellipticity determination is then that the galactic isophotes really are ellipses. In the case of spiral galaxies, this does not hold because of features like the spiral arms, bars, bulges, and other irregularities that could bias the parameters computations. We limited this issue by creating large (resp. thick) masks which allowed us to average over broad enough quadrants to smooth the smallest of these inhomogeneities. Additionally, we computed the individual PA and ϵ only for the images displaying the most homogeneously distributed components, that is to say, for images of the HI gas and of the stars (from UV to NIR domains included). Indeed, the dust and the molecular gas components usually display more patchy and clumpy distributions across the galaxy and those would bias the final shape parameters values. Moreover, these components emit at long wavelengths and the associated images have thus lower spatial resolution, which tends to make the objects appear rounder, hence further biasing the ellipticity determinations.

Despite these precautions, the largest irregularities of our spiral galaxies (i.e. the bulges and bars) still potentially impact the results of our PA and/or ϵ computations. As this happens for some specific observing bands, we simply decided to discard the associated determinations in our final averages. Hence, as the NIR domain principally probe the older stellar populations of the galaxies, bars and bulges can be highlighted in images taken at such wavelengths. In our sample, NGC2403 is classified as a "partially barred" galaxy and its central bar has a visible impact on its shape parameters determination. Its NIR images were thus discarded from its PA and ϵ determinations. Despite the fact that it is the only galaxy of our sample to be clearly classified as a barred spiral, the NIR images of NGC3198 did not produced biased values of its shape parameters. They were thus kept in the global PA and ϵ determinations.

For the galaxies with more prominent bulges, a bias is also expected to occur with NIR images but only during the ellipticity computation. Indeed, the presence of the bulge with a spherical symmetry should not significantly impact the orientation of the galaxy but it could lower its ϵ estimate. Out of the three galaxies expected to have the largest bulges (NGC2841, NGC5055 and NGC7331), this effect was important only for NGC7331 for which the NIR and even the visible images had to be ruled out from the global ϵ

Table 3.1: Shape parameters of our sample of galaxies

Galaxy	Excl. bands†	PA‡ [deg]	Excl. bands†	ϵ‡
NGC2403	NIR, HI	-51.20 ± 2.05	NIR	0.44 ± 0.05
NGC2841		-30.26 ± 1.32	HI	0.58 ± 0.03
NGC2976		-37.81 ± 3.09		0.58 ± 0.05
NGC3198		39.24 ± 0.70		0.64 ± 0.04
NGC5055	HI	-78.31 ± 1.41	HI	0.48 ± 0.05
NGC7331	UV	-12.32 ± 1.36	VIS, NIR	0.74 ± 0.10

† Bands excluded when computing the final averaged PA or ϵ. By default, the used bands are the UV, visible, NIR and HI bands.
‡ The uncertainties associated to the shape parameters result from the dispersion of the individual determinations (in the different bands).

determination.

NGC7331 also has another peculiarity: due to its high inclination, its prominent bulge hides a portion of its disk. The light of the hidden disk stars is thus more absorbed by the bulge dust than the light emitted from the front side of the galaxy, resulting in a global inhomogeneity in UV images. This impacts the PA computation but not the ellipticity one, due to the differences in shape and size of the masks used for the two determinations. We thus also excluded these images from the global PA computation.

Finally, a particular attention should be drawn to the HI gas. Indeed, due to its large radial extension, this component is more likely to display deformations and warps due to interactions with the galaxy neighborhood. This situation occurring for some of our galaxies (NGC2403, NGC2841 and NGC5055), we did not used the PA and/or ϵ from the HI image to estimate the averaged shape parameters.

The images, excluded in the final shape parameters computations, as well as the averaged PA and ϵ values for each galaxy are given in Table 3.1. The PA values are in global agreement with values given by previous works on single images, measured at 21cm (de Blok et al. 2008) or in the visible domain (and converted to B band values by the HyperLEDA database; Paturel et al. 2003).

Improvement

An improvement of the computation developed here would be to allow for the variation of these shape parameters within the galaxy. Such variations are very common and indicate a disk deformation (such as a warp) or the presence of a central bar or bulge. In the sample of galaxies studied in this work, de Blok et al. (2008) showed that important variations are found from emissions of HI gas[1] in NGC2841 (ϵ), NGC2976 (PA), NGC3198 (PA) and NGC5055 (PA and ϵ). An adaptation of our shape parameters determination would then be interesting to implement in order to better characterize and isolate the different isophotes of the galaxies with evident deformations, bars or bulges. This would also allow us to use currently discarded images.

3.1.2 Surface brightness profiles

Once our galaxies' shape parameters are known, we azimuthally averaged each of their images to compute their surface brightness radial profiles, each profile being associated to an observing band. To do so, we created concentric elliptical annulus masks (with the PA and ϵ given in Table 3.1) with increasing semi-major axes. The edges of these annulus masks were taken as ellipses of the same ellipticity in order to properly isolate each projected circular annuli. This resulted in masks of varying apparent thickness with the azimuth angle.

For each galactocentric distance, we determined the mean value of the pixels in the annulus via a sigma-clipping method with a 3σ threshold. This allowed to reduce any remaining foreground contamination and to smooth localized inhomogeneities in the galaxy, mainly the star-forming regions within the spiral arms. Once these averaged flux densities f_ν were computed, we divided them by the solid angle corresponding to one pixel area to obtain the surface brightness I_ν profiles of our galaxies.

For the IRAC images, we applied correction factors to our surface brightness profiles as the photometric calibration of these images has ini-

[1]The variations of the shape parameters with the galactocentric distance are very often given by works computing RCs as they are byproducts of the method used to derive RCs from 2D velocity fields (i.e. the tilted-ring model).

tially been performed for point sources. The corrections factors we used in this work can be found in the IRAC Instrument Handbook (2021)[2].

For some observing bands, the largest annuli extended farther than the images themselves. For a given annulus, if the number of pixels "outside of the image" exceeded a certain percentage of the whole number of pixels (here chosen to be 30%), we discarded the annulus and truncated the surface brightness profile at the corresponding galactocentric distance.

In the same way, we also noticed artifacts in the background of some images of our galaxies. These had not been removed during the preprocessing stages performed either by us or by the DustPedia's and the different facilities' teams from which our images come. These artifacts biased the surface brightness profiles, resulting in stagnating or even increasing profiles. This occurred for the images in MIR for which the background signal is mainly due to the temperature of the instrument and is thus particularly challenging to model and to remove. For these images, we chose to truncate the galactic profiles before the artifacts to avoid any contamination.

Once computed, some of our profiles quickly fell to negative values, sign that we slightly overvalued the sky background during our preprocessing stage (most probably because of extended low surface brightness outskirts of the galaxies). In these cases, a fit of the expected form of such profiles in the exteriors of spiral galaxies (i.e. the sum of the overestimated background constant and of a decreasing exponential function) allowed us to correct from our previous background determinations and to retrieve only the galaxy profiles.

Finally, we corrected the profiles from the galaxy inclination i with respect to the plane of sky. This allowed us to compute face-on profiles as $I_{\nu,\text{face-on}} = I_{\nu,\text{inclined}} \cos(i)$, the cosine term resulting from the deprojection of a unit area in the galactic plane onto a plane perpendicular to the observer line-of-sight. In principle, the inclination can be computed from the apparent ellipticity of the galaxy. Nevertheless, these geometric determinations are subject to simplifying hypotheses. Thus, as proposed by Aaronson et al. (1980), we favored computations of the inclination from high-resolution HI velocity fields (Lelli et al. 2016a), the values being given in Table 2.1 of the previous chapter (on page 42).

To compute the errors on our surface brightness profiles, we took into

[2] `https://irsa.ipac.caltech.edu/data/SPITZER/docs/irac/iracinstrumenthandbook/`

account and propagated various sources of errors: the error images, the error on the mean flux density f_ν in each annulus, the errors on the PA and on the ϵ of the galaxy, the errors on the IRAC calibration factors (evaluated to around 10% of the factors themselves, according to the IRAC Instrument Handbook 2021), the photometric calibrations uncertainties associated to each band (gathered by Clark et al. (2018) and given in Table 2.3 on page 53) and finally, the errors on the galactic inclination. As they are independent from each other, these various uncertainties were added in quadrature to estimate the total errors on profiles.

3.2 Corrections from dust effects

Despite being a marginal component of spiral galaxies, dust has a major impact on their chemistry, their thermodynamics, their star formation history and, most importantly here, their observed SED. As seen in Section 1.3.1, the dust grains absorb and scatter UV and optical light from stars and re-radiate it in the MIR, FIR and sub-mm wavelength ranges. In normal galaxies, dust is estimated to extinct around one third of all stellar radiations (Popescu & Tuffs 2002).

Therefore the short-wavelength surface brightness profiles of our galaxies have to be corrected from effects associated to the presence of dust within the MW as well as within the studied galaxies themselves. In both cases, the stellar light absorption and scattering (out of the line-of-sight) will depend on the dust grains quantity, chemical composition, and physical properties (size distribution, shape, internal structure, ...). It will also vary with the wavelength of the incident light, globally increasing with decreasing wavelengths, resulting in a reddening of the observed objects. Mathematically speaking, the correction from dust extinction can be computed by

$$I_{\nu,0} = I_\nu \; 10^{0.4 A_\nu} \tag{3.1}$$

where $I_{\nu,0}$ and I_ν are respectively the intrinsic and the observed (reddened by dust) surface brightness profiles while A_ν, expressed in magnitudes, quantifies the extinction by dust at a frequency ν.

3.2.1 Correction from extinction by Milky Way dust

To evaluate the quantity of MW dust in the line-of-sight of the galaxies, we used the Schlegel et al. (1998) dust map recalibrated according to Schlafly

Table 3.2: Reddening values associated to the MW dust in the direction of the galaxies in our sample. The E(B − V) values are the averages of the Schlegel et al. (1998) dust map recalibrated by Schlafly & Finkbeiner (2011) over 5 arcmin radius circles centered on each galaxy.

Galaxy	$E(B-V)$
NGC2403	$3.44 \pm 0.01\ 10^{-2}$
NGC2841	$1.31 \pm 0.04\ 10^{-2}$
NGC2976	$6.42 \pm 0.65\ 10^{-2}$
NGC3198	$1.05 \pm 0.03\ 10^{-2}$
NGC5055	$1.53 \pm 0.03\ 10^{-2}$
NGC7331	$7.83 \pm 0.07\ 10^{-2}$

& Finkbeiner (2011) recommendations. This map gives the values of the reddening (or color excess) $E(B-V)$ due to the extinction by the MW dust for all directions of observation. The values associated to the line-of-sight of our sample galaxies were retrieved from this map through the use of the NASA/IPAC Infrared Science Archive[3]. They can be found in Table 3.2.

This reddening $E(B-V)$ is linked to the extinction A_ν via the relation $A_\nu = R_\nu\ E(B-V)$. R_ν describes the dust extinction curve, that is to say, the evolution with the light frequency ν of the extinction by the galactic dust. The extinction curve R_ν of our Galaxy is well described by a Fitzpatrick (1999) law (with a small correction in the IR domain; Indebetouw et al. 2005) whose V band value is fixed at $R_V = 3.1$.

In order to correct our galaxies surface brightness profiles from the MW dust, we evaluated this IR-corrected Fitzpatrick (1999) law for our different observing bands. In fact, the R_ν values were retrieved from the same NASA/IPAC archive and are gathered in Table 3.3. Unfortunately, this law is not defined for the whole frequency range of our study. Indeed, the R_ν values are not given for GALEX and *Herschel* bands. As extinction by dust decreases with increasing wavelength, we do not need to compute R_ν for the long-wavelength bands but an evaluation of the extinction in the UV is necessary to properly correct our surface brightness profiles in these bands. We thus had to extrapolate the IR-corrected Fitzpatrick (1999) law to higher frequencies. To do so, we used a model of our Galaxy dust pop-

[3] `https://irsa.ipac.caltech.edu/applications/DUST/`

Table 3.3: MW extinction curve for the short wavelength bands used in this work

Band name	R_ν	Ref.
FUV	6.79 ± 0.30	(3)
NUV	6.96 ± 0.30	(3)
u	4.239	(1)
g	3.303	(1)
r	2.285	(1)
i	1.698	(1)
z	1.263	(1)
IRAC-3.6	0.178	(2)
IRAC-4.5	0.148	(2)
IRAC-5.8	0.130	(2)
IRAC-8.0	0.122	(2)

References: (1) NASA/IPAC Infrared Science Archive from Fitzpatrick (1999) extinction law; (2) NASA/IPAC Infrared Science Archive from Indebetouw et al. (2005); (3) Computed in this work from Draine (2003) MW dust populations model

ulations by Draine (2003). This model represents the dust grains found in diffuse clouds of the MW and consists in a mixture of silicate and amorphous carbonaceous grains of various sizes (from a few Å to a few μm), supplemented by a component of very small PAH molecules. The extinction curve computed on these grains populations is given for wavelengths between 1 Å and 1 cm, largely covering our observing bands range.

In practice, for the bands for which the R_ν values were given in the archive, we computed the corresponding extinction A_ν. From that, we evaluated, for each band, the column density of MW hydrogen nucleon N_H on the line-of-sight of the galaxy. Indeed, in the ISM of galaxies, the amount of dust (and thus the associated extinction) is highly correlated to the amount of gas (and thus of hydrogen atoms and molecules). Hence, it is possible to compute one from the other and inversely with

$$N_\mathrm{H} = 0.4 \ \ln 10 \ \frac{A_\nu}{C_{\mathrm{ext},\nu}} \tag{3.2}$$

where $C_{\mathrm{ext},\nu}$ is the extinction cross-section by hydrogen nucleon, given by theoretical dust populations models like the Draine (2003) model used in

Table 3.4: Comparison between this work and previous estimates of the MW extinction curve R_ν for the two GALEX bands

Band name	This work	Bianchi (2011)	Yuan et al. (2013)†	Wall et al. (2019)‡
FUV	6.79 ± 0.30	8.06	$4.37 - 4.89$	8.01 ± 0.07
NUV	6.96 ± 0.30	7.95	$7.06 - 7.24$	6.79 ± 0.04

† Yuan et al. (2013) advise to use these values with caution due to large measurement uncertainties.
‡ The error bars correspond to errors on the mean. In fact, R_ν values are particularly spread out depending on the line-of-sight on which they are evaluated. The standard deviations of the R_ν distributions are estimated to be ~ 3.

this work.

By averaging all our determinations of column densities N_H for our different images, we estimated the mean quantity of MW hydrogen nucleon on the line-of-sight of our galaxies. In this average, we excluded the *Spitzer* bands for which the intrinsic emission by dust is not negligible and can bias the A_ν and N_H determinations. From this estimate of the MW N_H, we computed the extinction in magnitude A_ν and the extinction curve R_ν for the two GALEX bands, using here again Draine (2003) dust model. The associated errors were estimated by propagating the error due to the dispersion of the computed $N_{\rm H}$ values and the one on the MW reddening $E(B-V)$ associated to the line-of-sight of the galaxy. As for the R_ν given by Fitzpatrick (1999) and Indebetouw et al. (2005) extinction curve, the R_ν we found for the two GALEX bands are given in Table 3.3.

The latter have been previously computed both theoretically (Bianchi 2011) and observationally (Yuan et al. 2013; Wall et al. 2019). Compiled in Table 3.4, these other estimates differ from our values, particularly for the FUV band. However, Bianchi (2011) theoretical values were computed from Cardelli et al. (1989) MW extinction curve which has been shown to be less favored by the observations than the Fitzpatrick (1999) law (e.g. Schlafly et al. 2010). Moreover, the observational GALEX R_ν estimates show a very large scatter (with standard deviations of around 3; see figure 3 of Wall et al. 2019). In fact, each R_ν value greatly depends on the line-of-sight[4] used to evaluate it. The R_ν values found in this work fall in between

[4]This dependency is the sign that a single extinction law cannot correctly represent

the previous determinations.

3.2.2 Correction from attenuation by galaxy dust

Similarly, we had to correct our surface brightness profiles from effects of dust within the studied galaxies. The problem is slightly different from the correction from MW dust. Indeed, while all the MW dust is located between the galaxy and the observer, the geometry here is completely different with dust and stars mixed all together within the galaxies. In addition to the already known dust extinction (i.e. the absorption and the scattering of the galaxy light out of the line-of-sight), we have to take into account the possible scattering of light back into the line-of-sight as well as the contribution of stars located in front of the dust clouds. Hence, for galaxies other than ours, we do not talk of 'extinction' but rather of 'attenuation' to highlight these additional impacts of dust grains on starlight.

Despite this difference, the correction of the surface brightness profiles followed the same steps as previously: (i) the estimate of the quantities of galactic dust at different galactocentric distances using, here, the thermal emission of dust and (ii) their transformation into A_ν values via, here, an attenuation curve.

3.2.2.1 Dust properties

As previously mentioned, the SED of spiral galaxies is largely dominated at long wavelengths by the thermal emission of the galactic dust. In first approximation, this thermal emission can be modeled by different black body spectra (i.e. Planck laws B_ν parametrized with T_d, the temperatures of the different dust populations) multiplied by a factor taking into account the possible interaction of the emitted radiation with the dust grains themselves. This factor Q_ν, called the efficiency factor for emission, is equal to the unity at all frequencies for a black body but is lower for a medium which scatters and absorbs the light it emits. For the interstellar dust grains, the dependency of Q_ν with the frequency ν of the radiated light can be approximated by a power-law $Q_\nu \propto \nu^\beta$ with β, the emissivity index, characterizing

the dust extinction within the MW. Thus, to properly correct luminosity profiles from this extinction, the R_ν values should be independently evaluated for each galaxy. This being out of the scope of this work, we limited ourselves to a single estimate of $R_{\rm FUV}$ and of $R_{\rm NUV}$ whatever the studied galaxy.

the chemical composition of the dust grains ($\beta \approx 1$ for amorphous materials, $\beta \approx 2$ for crystals and metals; Cimatti et al. 2020). Recent estimates of β for various nearby galaxies indicate values comprised between 1 and 2 ($\beta \approx 1.6$ for the Milky Way or M31; Planck Collaboration 2014, 2015), galaxies with lower metallicities showing lower β values ($\beta < 1.5$; Boselli et al. 2012). Hence the thermal emission of a dust population, made of identical grains, heated to a single temperature T_d can be described by a 3-parameter function, called a modified black body (MBB) or a grey body spectrum

$$I_{\nu,\mathrm{MBB}} = B_\nu(T_d)\ Q_\nu = I_0\ \frac{\nu^{3+\beta}}{e^{h\nu/k_B T_d} - 1} \tag{3.3}$$

with h and k_B the Planck and Boltzmann constants and I_0 a proportionality constant.

According to their size, the dust grains will not react in the same way to highly energetic radiation from nearby hot stars. They will thus not be described by MBB functions of the same temperature. Indeed very small grains (of size $\lesssim 0.02$ μm; Galliano et al. 2018) are highly impacted by individual UV photons and are thus stochastically heated to various temperatures of the order of a few hundreds Kelvin. This out of thermal equilibrium situation results in a broad and complex emission spectrum in the MIR-FIR range (below $\sim$70 μm; Galliano et al. 2018; Mosenkov et al. 2019). Conversely, larger grains (of size $\gtrsim 0.02$ μm) are in thermal equilibrium with the ambient radiation field, resulting in a simpler spectrum peaking around 100–200 μm, well approximated by two MBB of temperatures of a few tens of Kelvin. The colder grains population is heated by old stars to temperatures around 10–30 K while the warmer one ($T_d \approx 20$–60 K) is found around AGNs and regions of recent star formation (Popescu & Tuffs 2002; Stevens et al. 2005; Bendo et al. 2010, 2015).

This MBB approach is a simplification to model the emission of galactic dust. Other methods exist such as the parametrization of the galactic interstellar radiation fields coupled with a multi-component model of dust grains (e.g. Dale et al. 2001; Draine & Li 2007) or the computation of the radiation transfer of starlight through a 3D model of the galactic dust (Galliano et al. 2018). Nevertheless, these more sophisticated methods are beyond the scope of this work. Indeed, here, a simple estimate of the properties and of the quantity of galactic dust is needed in order to correct our surface brightness profiles as well as to evaluate the total dust mass (as

we will see it later in Section 5.1.1). For these particular purposes, various studies found that using a simple MBB method or more sophisticated ones give similar results, particularly for the spiral galaxies that are the subjects of this work (Berta et al. 2016; Nersesian et al. 2019).

Similarly, we limited our fits the FIR and sub-mm observations as the MIR wavelengths display strong emission bands due to the presence of PAH, silicates, and gas lines. This domain is also more strongly impacted by the stellar emission than the FIR (e.g. Meidt et al. 2012; Galliano et al. 2018). The fitting of the MIR galactic SED is thus also beyond the scope of this work.

Practically, we fitted a single-temperature MBB spectrum (described by Equation 3.3) on the surface brightness profiles derived from the FIR and sub-mm (*Herschel*) images of our galaxies. We chose to only model one population of large dust grains, the colder one. Besides constituting the bulk of the total dust quantity in the galaxy, this population also heavily dominates the very long wavelengths emissions of the galaxies. The addition of a (slightly) warmer dust component into the model does not significantly improve the global fit or constrain the cold dust properties (Bendo et al. 2010; Smith et al. 2010; Dale et al. 2012). Thus, we excluded from our fit the PACS-70 images as the emissions in this observing band are heavily impacted by the non-modeled warmer part of the dust component (Bendo et al. 2010; Smith et al. 2010; Bendo et al. 2012). In practice, the wavelength at which the galaxy SED changes from being dominated by the warm to the cold dust population varies from one galaxy to the other (Bendo et al. 2015) but the vast majority of studies modeling dust emissions with a single-temperature MBB exclude observations at wavelengths smaller or equal to 70 μm (e.g. Dale et al. 2012; Bianchi 2013; Hunt et al. 2015; Nersesian et al. 2019).

As mentioned, we will later derive from these fits the mass profiles of the dust within each galaxy. In order to do this properly (more details will be given in Section 5.1.1), we had to fix the emissivity index β to a value of 2.08 as the dust models we will use afterwards have been computed with this particular value (Draine 2003; Bianchi 2013). This restriction is beneficial to this work as the dust grain temperature and the emissivity index derived from the fit of a MBB spectrum are in fact degenerated parameters, hence difficult to estimate separately (Hunt et al. 2015; Galliano et al. 2018).

Finally, with the fit performed here, one has to keep in mind that the

best-fit MBB parameters often[5] do not correspond to the real physical properties of the galactic dust component. Rather, they are effective values, resulting from a mixture of different physical conditions.

Results

For each of our galaxies, we characterized their cold dust population by performing fits of single-temperature MBB spectra on the photometric SEDs built from our FIR and sub-mm ($\lambda \geq 100$ μm) surface brightness profiles. We thus obtained, for each galaxy, profiles of the two MBB parameters, T_d and I_0 (β being fixed to a value of 2.08), characterizing the cold dust population. These profiles are given in Figure 3.1 and show global decreases of the temperature and of the quantity (directly related to the MBB amplitude I_0) of cold dust over the galactic disks.

Three galaxies in our sample possess a molecular ring whose position is highlighted in grey on the figure. For two of them (NGC2841 and NGC7331), this ring corresponds to slightly warmer dust grains. This indicates the presence of more intense radiation fields in these areas and can be explained by the fact that molecular rings are often associated with numerous star-forming regions, as will be shown when studying the stellar content of these galaxies in Section 4.1.5.1.

For NGC2976, the situation is different as its ring (localized around the grey line) is not associated with a warmer population of dust grains. The dust quantity seems relatively constant over the whole inner half of the galaxy with a breaking point around 80 arcsec (90 arcsec for the T_d profile). This kind of breaking point is typical of this galaxy and is also observed in its visible (∼70 arcsec) and NIR (∼100 arcsec) luminosity profiles (Simon et al. 2003) as well as on optical images (see the insert in panel (c) of Figure 2.1 of page 44). In fact, it is the result of an important modification of the composition and of the physical conditions within this galaxy. It is therefore not surprising to find it in the properties of its dust component.

Finally, the central regions of NGC2841, NGC3198 and NGC5055 also show an important increase of their dust populations' temperature. For NGC2841 and NGC5055, this could be explained by the presence of their

[5] They are reliable estimates of the grain properties only if the interstellar radiation field in the neighborhood of the grains is uniform (hence, not in star-forming regions) and if long wavelength ($\lambda \geq 100$ μm) measurements are used in the fits (Galliano et al. 2018).

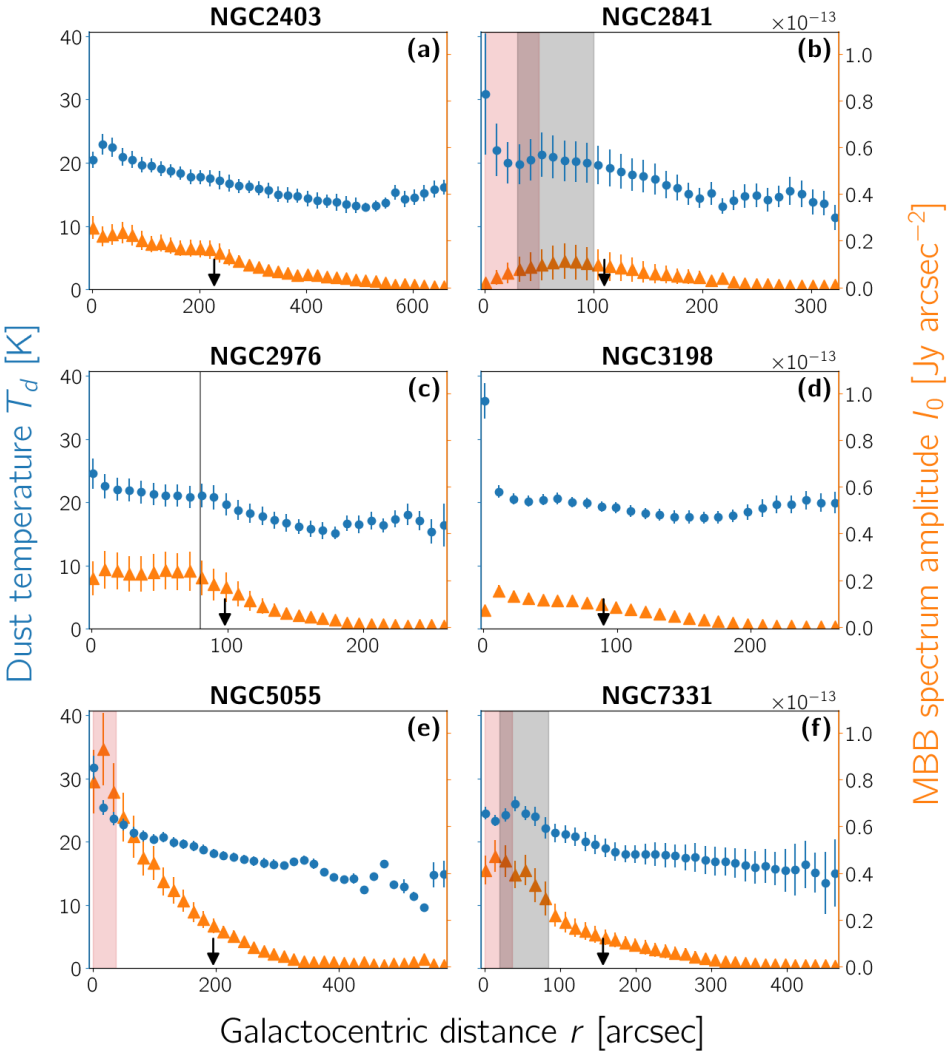

Figure 3.1: Dust properties profiles of the galaxies in our sample. They result from the fits of single-temperature MBB spectra (with a fixed emissivity index $\beta = 2.08$) on FIR/sub-mm SEDs ($\lambda \geq 100$ μm). The two parameters of the fitted MBB function are its temperature (in blue dots) and its amplitude (in orange triangles). For the distances indicated by the black arrows, a visualization of the corresponding fits is given in Figure 3.4 on page 82. Peculiar zones are represented for some galaxies: their molecular ring (in grey) and the regions impacted by the presence of their LINER nucleus (in light red).

Table 3.5: Mean values of the dust temperature profiles of Figure 3.1, compared to Nersesian et al. (2019) values (same methodology for the modeling of the galactic cold dust emissions with a different choice of the emissivity index)

Galaxy	This work ($\beta = 2.08$)	Nersesian et al. (2019) ($\beta = 1.79$)
NGC2403	16.14 ± 0.30	20.0 ± 1.4
NGC2841	15.69 ± 0.31	19.61 ± 0.74
NGC2976	17.97 ± 0.21	22.41 ± 0.67
NGC3198	19.31 ± 0.22	20.89 ± 0.76
NGC5055	15.94 ± 0.33	21.28 ± 0.72
NGC7331	20.75 ± 0.31	22.68 ± 0.87

LINER nucleus (light red zones in the figure) that warm up their surroundings (and incidentally complicates or even prevents the use of their ionized gas emission lines to derive their central RCs). Nevertheless, this explanation does not hold for NGC3198 and its quiet nucleus. Moreover, NGC7331 also has a LINER nucleus but with no associated warming of its dust component. We thus rather think that these central increases are due to the presence of intense star formation in these regions (see Section 4.1.5.1 for a confirmation of this hypothesis).

Comparison with previous works

To compare our results with previous ones, we averaged our dust temperature profiles over the whole galaxies as other works estimating this dust property often deal with observations of the galaxies as a whole. The mean values describing our T_d profiles can be found in Table 3.5 and in Figure 3.2 where they are compared to previous determinations from works with similar methodology as ours (i.e. fits of single-temperature MBB spectra with fixed emissivity indexes on dust thermal emissions). As can be seen, our values (blue dots) are systematically lower than the other estimates. This is mainly due to two effects.

On the one hand, the older estimates (green crosses) have been realized when the FIR and sub-mm domains were not as accessible as they have recently been, particularly with *Herschel*. Hence, they rely on emissions at

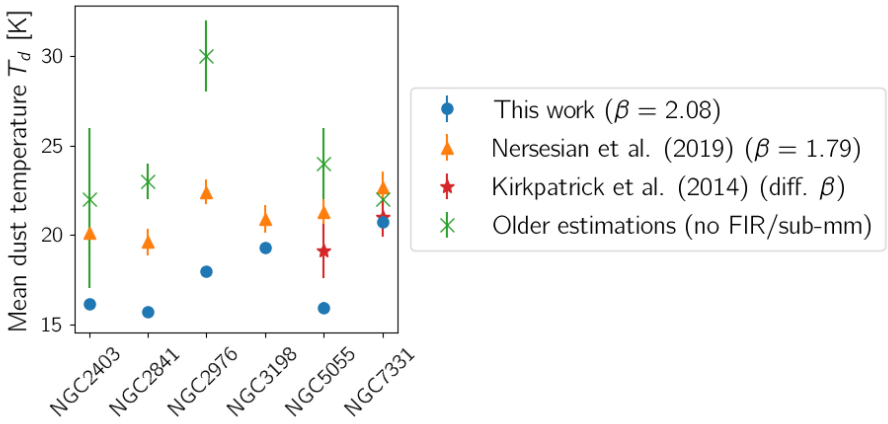

Figure 3.2: Comparison between the mean value of the dust temperature profiles of Figure 3.1 and previous estimates from the literature. The latter are systematically higher than our values (blue dots) due to differences in modeled SED wavelength coverage and/or chosen emissivity index values. Kirkpatrick et al. 2014 (red stars) values for β vary from one galaxy to the other (NGC5055: $\beta = 2.04$, NGC7331: $\beta = 1.81$). The older estimates of T_d (green crosses) are from Bendo et al. (2010) (NGC2403), Kaneda et al. (2007) (NGC2841 and NGC2976), Bendo et al. (2003) (NGC5055) and Regan et al. (2004) (NGC7331).

short FIR wavelength ($\lambda < 100\ \mu$m), a domain that is impacted by the warm dust populations, as already mentioned. Fitting a single-temperature MBB spectrum on this domain then biases the results towards high temperatures (e.g. Popescu & Tuffs 2002). When using these wavelengths, two MBB spectra must, at least, be fitted. Kirkpatrick et al. (2014) work, for example, performed such double-temperature MBB fits on photometric SEDs built on observations from 70 to 500 μm for two of our galaxies (NGC5055 and NGC7331) and ended up with T_d estimates (red stars) closer to ours.

On the other hand, the choice of the emissivity index β, fixed during the MBB spectrum fit, also impacts the final dust temperature. Indeed, as already explained, these two parameters are not independent from each other, lower values of β being associated to warmer dust populations and inversely (Pollack et al. 1994; Paradis et al. 2009). This well-known anti-

correlation is even observed in astrophysical dust laboratory analogs (e.g. Mennella et al. 1998; Boudet et al. 2005). Hence, as Nersesian et al. (2019) values (orange triangles) have been computed from fits with β fixed to a value of 1.79 given by the THEMIS dust model (Jones et al. 2013; Köhler et al. 2014; Ysard et al. 2015), they are expectedly higher than our evaluations (for which we took β equal to 2.08 to match the Draine (2003) dust model). Using the anti-correlation measured on nearby galaxies by Galametz et al. (2012) (see their figure 7) and Hunt et al. (2015) (see the left panel of their figure 12), we estimate that an increase of β from 1.79 to 2.08 should translate in a decrease of T_d of about 2 K but with a large variation from one galaxy to the other.

In conclusion, our dust temperatures are consistent with the temperature range (15–30 K; Bendo et al. 2010) probed by our methodology (fits of single-temperature MBB spectra with fixed β at long wavelengths, $\lambda \geq 100$ μm) and they are in agreement within the error bars with similar previous works.

3.2.2.2 Attenuation law(s)

For galaxies other than the MW, we need to use attenuation (instead of extinction) curves to account for the spatial distribution of stars and dust within the galaxies. When estimated from observations, these curves happen to vary strongly from one galaxy to another. The most salient differences are associated to the UV slope as well as to the strength of the 2175 Å bump (Salim et al. 2018). By varying the assumed dust/stars distributions, this observed wide range of attenuation curves' shape is reproduced by theoretical models, whatever their degree of complexity (from simple analytical ones to complete hydrodynamic simulations of galaxy evolution; see for example Narayanan et al. 2018).

Hence, the exact attenuation curve must ideally be determined individually on each galaxy. Nevertheless, these determinations often require to model the whole galactic SED (stars + dust emissions). As explained in Section 1.3.1.1, such modelings are complex and computationally expensive with a lot of free parameters and numerous degeneracies. We thus preferred to adopt a semi-individual approach where the attenuation curves were fixed for different groups of galaxies. To do so, we based our study on the work of Salim et al. (2018) that has modeled the whole SEDs of 230,000 nearby galaxies, derived their attenuation curves and classified them into

different categories. A particularity of their work is that, during the modeling of the SEDs, the emissions from dust (in the IR domain) and from stars (in the UV and optical domains) have been decoupled. This provides robust results regardless the galactic SED and is the recommended way to evaluate properly the UV attenuation curves (Burgarella et al. 2005).

The galaxies in Salim et al. (2018) were grouped in categories depending on their stellar masses and on their specific star formation rates (sSFR). The latter is defined as the ratio between the current star formation rate (SFR) of a galaxy and its stellar mass. Regarding this sSFR, two main categories of galaxies are defined by Salim et al. (2018): the quiescent and the star-forming galaxies whose log(sSFR) are respectively lower or larger than -11. Among star-forming galaxies, another subgroup is defined and called the high-redshift analogs. It is composed of galaxies with a very high sSFR (whose log(sSFR) is higher by 0.5 dex or more than the median log(sSFR) of all star-forming galaxies).

Each category is then associated to an analytical attenuation curve, defined between the wavelength of 912 Å and a maximal wavelength $\lambda_{\rm max}$. They are modeled by a third-degree polynomial in λ^{-1} with a Drude profile $D_\lambda(B)$ to represent the UV bump at $\lambda_{\rm B} = 2175$ Å with a width $w_{\rm B}$ =350 Å:

$$R_\lambda = a_0 + a_1\lambda^{-1} + a_2\lambda^{-2} + a_3\lambda^{-3} + D_\lambda(B) + R_{\rm V} \tag{3.4}$$

with

$$D_\lambda(B) = \frac{B\lambda^2 w_{\rm B}^2}{(\lambda^2 - \lambda_{\rm B}^2)^2 + \lambda^2 w_{\rm B}^2}.$$

The parameters sets (a_0, a_1, a_2, a_3, B, $R_{\rm V}$, $\lambda_{\rm max}$) for each category of galaxies are given by Salim et al. (2018) and summarized in Table 3.6.

Practically, we roughly evaluated the M_* and the sSFR of each galaxy in our sample, following Leroy et al. (2008) prescriptions, that is to say, using and integrating the surface brightness profiles derived from the IRAC-3.6 band for the stellar mass and from the FUV and MIPS-24 bands for the sSFR. With the two latter, we thus tracked the direct emission from young hot stars as well as the thermal emission from small dust grains heated by these stars. Thanks to this quick galaxy categorization, we could assign a semi-individualized attenuation curve to each galaxy of our sample. The masses and SFRs we obtained with this methodology can be found respectively in Tables 4.5 and 4.3 (on pages 118 and 106) where they are compared with values from Leroy et al. (2008).

Table 3.6: Salim et al. (2018) parameters of the analytical form (Equation 3.4) of dust attenuation curves for different categories of galaxies (based on their specific star formation rate and on their stellar mass M_*)

Galaxy category	a_0	$a_1{}^\dagger$	$a_2{}^\dagger$	$a_3{}^\dagger$	$B^\dagger$	R_V	$\lambda_{max}{}^\ddagger$
Star-forming galaxies							
$\log(M_*) \in]8.5; 9.5]$	-3.66	2.13	-0.043	0.0086	2.62	2.61	2.01
$\log(M_*) \in]9.5; 10.5]$	-4.13	2.56	-0.153	0.0105	1.73	2.99	2.18
$\log(M_*) \in]10.5; 11.5]$	-4.66	3.03	-0.271	0.0147	1.09	3.47	2.45
High-redshift analogs							
$\log(M_*) \leq 10$	-3.80	2.25	-0.073	0.0092	2.74	2.72	2.05
$\log(M_*) > 10$	-4.12	2.56	-0.152	0.0104	2.11	2.93	2.09
Quiescent galaxies	-3.72	2.20	-0.062	0.0080	2.21	2.61	1.95

† Parameters values if the wavelength λ in Equation 3.4 as well as λ_B and w_B are given in μm

‡ Given in μm. At $\lambda > \lambda_{max}$, the Equation 3.4 gives negative values and the attenuation curves are fixed to zero.

All the galaxies in our sample are classified as star-forming galaxies and are differentiated by their mass: NGC2976 belonging to the low-mass category defined by Salim et al. (2018), NGC2403 and NGC3198 to the medium-mass category and NGC2841, NGC5055 and NGC7331 to the high-mass category. As expected, they constitute the same three groups as when the classification is based on their RC shape.

Finally, one may wonder about the effects of the galaxy inclination on the attenuation curve. If it has an impact on the quantity of dust on the line-of-sight of the observer, it also changes the general shape of the attenuation curve. Indeed, Salim et al. (2018) found a small correlation between the inclination on the galaxy and the UV slope of its attenuation curve, more face-on galaxies having steeper attenuation curves. This trend is in fact the footprint of another correlation between the UV slope and the optical attenuation A_V. Indeed, at same A_V value, a very inclined galaxy with little dust has the same attenuation curve shape as a face-on dusty one. Taking the optical attenuation into account thus cancels the correlation between the UV slope and the inclination. Luckily for us, Salim et al. (2018) already reckoned with this trend in their analytical forms of attenuation curves for the different categories of galaxies defined

on M_*. Indeed, the A_V parameter also correlates with the stellar mass of the galaxy, more massive galaxies having higher A_V values and thus shallower attenuation curves.

3.2.2.3 Profiles corrections

Given the attenuation curve of our galaxies and the properties of their dust populations, we corrected our short-wavelength surface brightness profiles from the effect of the galactic dust.

For that, we made an energy-balance hypothesis: all the energy absorbed by dust grains in the UV, visible and NIR domains heats the grains and is thus totally radiated at long wavelengths. With our MBB fits, we only considered and modeled emissions in FIR and sub-mm. We thus completely neglected the MIR domain and its warm dust populations in our energy-balance. This underestimates the absorption of starlight in the UV to NIR domains. However, the emission by dust at wavelengths smaller than $\sim$50 μm is found to be approximately half of the one at longer wavelengths (Draine 2003). The total energy radiated by dust grains of all sizes at all wavelengths can then be directly estimated from our best-fit MBB spectra. Mathematically, this translates as

$$1.5 \int_{\text{FIR/sub-mm}} I_{\nu,\text{MBB}}\, d\nu \approx \int_{\text{UV/VIS/NIR}} (I_{\nu,0} - I_\nu)\, d\nu \qquad (3.5)$$

where $I_{\nu,0}$ and I_ν are respectively the intrinsic and the attenuated (after correction from MW dust) surface brightness profiles. $I_{\nu,\text{MBB}}$ is the surface brightness profile associated to the MBB spectrum determined via Equation 3.3. Using Equation 3.1 and the definition of A_ν, we can rewrite this as

$$1.5 \int_{\text{FIR/sub-mm}} I_{\nu,\text{MBB}}\, d\nu \approx \int_{\text{UV/VIS/NIR}} I_\nu\, (10^{0.4 R_\nu E(B-V)} - 1)\, d\nu \qquad (3.6)$$

where R_ν is given by Salim et al. (2018) attenuation curves (defined by Equation 3.4 with parameters given in Table 3.6) expressed in frequency terms. Solving this balance of energies at each galactocentric distance allowed us to obtain the reddening $E(B-V)$ profile of each galaxy in our sample and to correct our surface brightness profiles.

Results

The reddening profiles $E(B-V)$ for each of our galaxies are displayed in Figure 3.3. Their shape follows logically the profiles of the MBB spectra parameters, particularly the amplitude one, previously shown in orange triangles in Figure 3.1. The molecular ring of NGC7331 (whose position is highlighted in grey in panel (f) of Figure 3.3) is particularly visible in the reddening profile, confirming the significant impact of dust on the stellar emissions in these regions. Finally, comparing these $E(B-V)$ profiles with the MW reddening values ($\sim 10^{-2}$ from Table 3.2), the main impact of dust on the stellar emissions of our galaxies comes from their own component.

The SEDs of our galaxies at a specific galactocentric distance (corresponding to half of their characteristic radius r_{25}[6]) are shown in Figure 3.4 before (black dots) and after (blue triangles) correction from the MW and from the galactic dust effects. As expected, the shorter the wavelength, the more important the correction.

The MBB spectra fitted on wavelengths longer or equal to 100 μm (on points located at the right of the dotted red vertical lines) are also shown in this figure and it is clear that the emission at shorter wavelengths by warmer dust populations is not modeled by our single-temperature MBB fits. As can be seen, the importance of ignoring these warm dust grains varies greatly from one galaxy to another. For example, this population significantly impacts the SED of NGC2403 but not the one of NGC2841. Nevertheless, this conclusion is only valid at the particular distance at which this figure is drawn. Indeed, as the warm dust is heated in very localized regions, by young stars in star-forming regions and by AGN emissions, its importance strongly depends on the position probed within the galaxy.

3.3 Conclusion

At this point, we have transformed the 2D images of the luminous components of our galaxies into 1D surface brightness profiles to ease their conversion into mass distributions. We also corrected the short-wavelength profiles for the reddening effect of the dust on the line-of-sight, that is to

[6]For our sample of galaxies, we determined their r_{25} values on the surface brightness profiles associated to the SDSS g band (the closest from the B band that we have at our disposal) after correction for the dust effects. Our estimates for each galaxy are given in Table 2.1 on page 42.

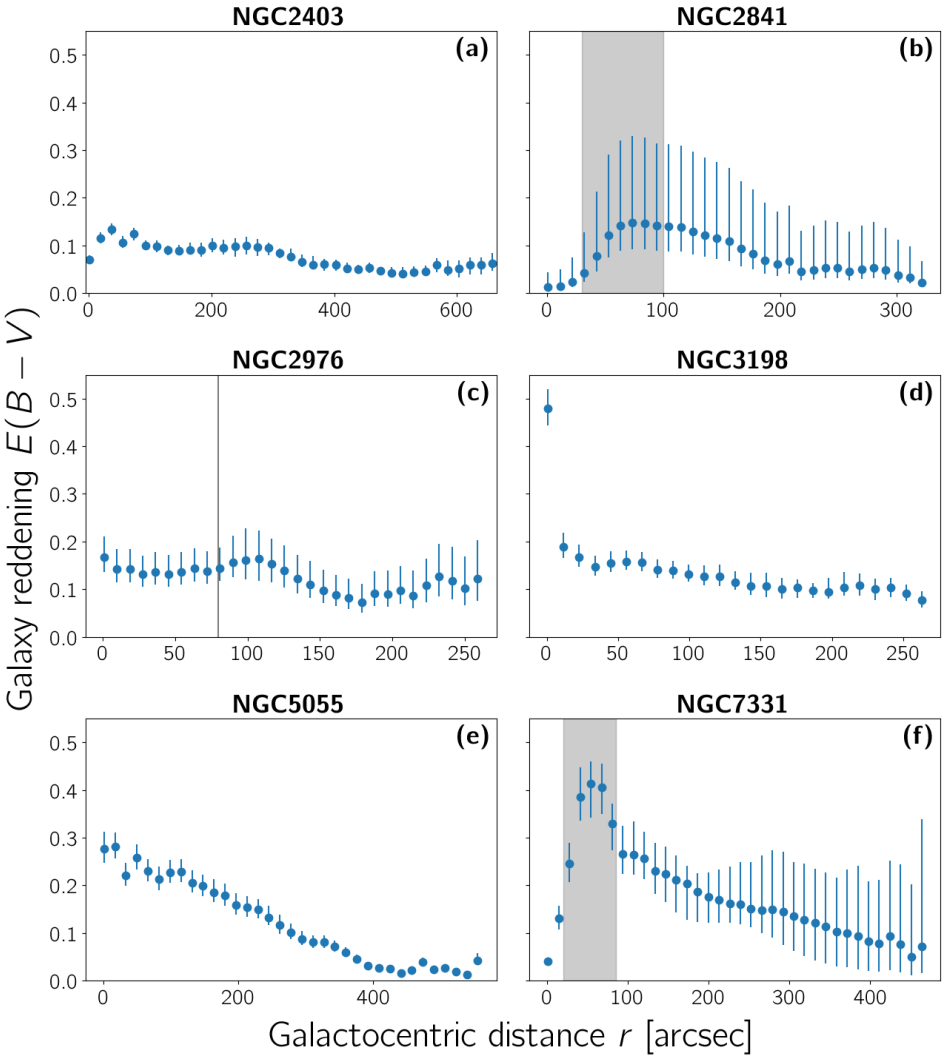

Figure 3.3: Reddening E(B – V) profiles due to the dust component of each galaxy in our sample. If present, the position of the molecular ring is shown in grey.

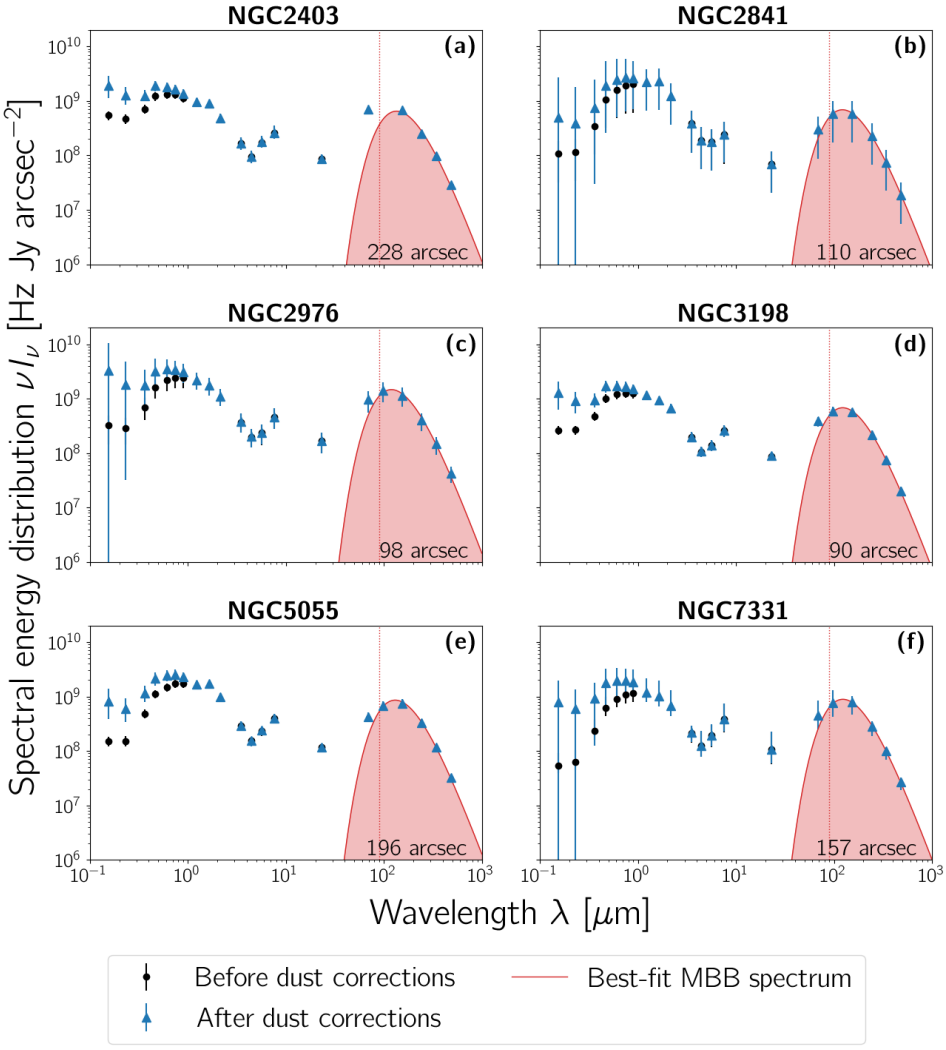

Figure 3.4: Examples of galactic SEDs before (black dots) and after (blue triangles) correction from the effects of dust (from both the MW and the galaxy itself). The galactocentric distance corresponding to the SED is written in the lower right corner of each panel. The red regions show the emissions from the single-temperature MBB spectra fitted on all the FIR/sub-mm points located at the right of the dotted red lines (i.e. $\lambda \geq 100$ μm).

say, of the extinction in the MW and, more importantly, of the attenuation in the galaxy itself. These corrected profiles now correspond to the intrinsic emissions of all the stars[7] in the different galaxies. During the course of these computations, we characterized the properties of the cold dust content of these galaxies. With our stars and dust emissions disentangled, the mass modeling of all the galactic luminous components is now possible.

[7]Strictly speaking, these profiles also display specific gaseous emission lines. Nevertheless, as we use broad bands in this work, we can safely consider that this pollution of stellar emissions is negligible.

Chapter 4

Stellar content
Effect of a global SED modeling on the mass distribution

Among the luminous components of a spiral galaxy, the one with the largest impact on its global rotation is its stellar content. Its modeling is thus a decisive step that should not be overlooked. In this work, we perform a complete modeling of the galaxy stellar photometric SED from the FUV to the NIR domains. We hence depart from the usual mass conversion of a unique NIR luminosity profile, conversion that does not allow to probe all the stellar populations of the galaxy.

In this chapter, we present our modeling of stellar SEDs, apply it to the six galaxies in our sample in order to derive their stellar mass distributions (Section 4.1). Through a comparison with the distribution resulting from the usual NIR conversion, we then assess the correctness of this simplification – and its pertinence in a RC context (Section 4.2). Along the way, we also describe the stellar content of these galaxies through interesting and valuable byproducts of our methodology, such as the evolution of their metallicity or of their stellar formation within the galaxies as well as along their lives.

4.1 Characterizing the stellar component from SED modeling

The principle behind the modeling of a galactic stellar photometric SED is relatively simple in theory. Synthetic spectra of stellar populations are combined to match the observed SED of a given galaxy. Assuming models for the evolution of the star formation and of the chemical enrichment of the galaxy, we can then deduce from this fit the actual stellar content of the galaxy. Nevertheless, in practice, such a fitting is particularly challenging as it is an inverse problem with a large number of free parameters and many degeneracies, without even mentioning the fact that the stellar emission of a galaxy is also largely impacted by another of its components, the dust. To derive reliable information on the galaxies in our universe, an interesting approach is to use Bayesian inference techniques, which necessitate the creation of grids of theoretical SEDs to be compared with the observed one. This allows to compute and marginalize the probability distribution functions (pdfs) describing the evolution within the galaxy of a certain number of physical quantities such as the star formation, the metallicity or, more interestingly in the context of this work, the total stellar mass.

It should be noted that, usually, studies aiming at modeling the SED of a galaxy work on the observed (i.e. attenuated by dust) luminosity profiles (see Walcher et al. (2011), Conroy (2013) or Baes (2020) for recent review papers). They hence have to directly parametrize the dust attenuation curve along with the SED fitting. This technique increases the number of degeneracies associated to the fit and makes it extremely challenging to retrieve reliable results. The recent advent of FIR/sub-mm telescopes (such as WISE, *Spitzer* and particularly *Herschel*) made it possible to take into account the dust thermal emissions, which remarkably improved the modelings. In such global FUV-to-sub-mm SED fitting codes (such as in the well-known MAGPHYS or the CIGALE codes; by da Cunha et al. 2008, 2015 and Noll et al. 2009; Boquien et al. 2019 respectively), the impact of dust is estimated through an energy-balance assumption, where all the energy emitted by the dust in the FIR/sub-mm domains is equal to the energy absorbed at shorter wavelengths. In Section 3.2.2, when disentangling our stellar and dust luminosity profiles, this is exactly the hypothesis we made. In this way, the methodology developed in this work is in fact similar to the modeling of attenuated galactic SEDs usually performed in SED fitting studies. The only difference stands in the treatment of the dust attenuation curve parametrization. Indeed, rather than letting the

parameters of this curve free during the fitting, we preferred to fix them to six different possible sets, previously computed by Salim et al. (2018). As also explained in Section 3.2.2, we chose this slightly more constrained approach in order to limit the complexity and the resources necessary to perform the SED modeling.

4.1.1 Composite stellar populations

To model a stellar SED, the galaxy[1] has to be considered as constituted of multiple populations of stars, each population (called simple stellar population; SSP) having a given age and a given metallicity. All the stars of one SSP are taken as born exactly at the same time in a (non-physical) instantaneous burst of star formation. The assumption of an IMF as well as the use of stellar evolution theories and of spectral libraries makes it possible to compute the synthetic spectrum associated to each SSP as well as its evolution with time as the galaxy ages. In this work, we used the SSPs computed by Maraston (2005)[2] for a Kroupa IMF (Kroupa 2001). These SSPs are given for 67 stellar ages (going from 10^3 yr to 15 Gyr) and 4 metallicity values ($Z \in \{0.001; 0.01; 0.02; 0.04\}$ where Z is the fraction in mass of metals in the ISM gas at the origin of the stellar population, $Z = M_{\text{metals}}/M_{\text{gas}}$). With these SSPs, a particular attention has been drawn to the modeling of a late stage of the stellar evolution, the TP-AGB phase. This modeling is of great importance as the populations of stars in this phase have been shown to significantly contribute to the NIR emission of galaxies (e.g. Maraston 2005; Meidt et al. 2012; Melbourne & Boyer 2013; Gerke & Kochanek 2013). They are hence critical to include when modeling the stellar SED and mass distributions (Walcher et al. 2011).

The combination of synthetic spectra of SSPs of various ages and metallicities, called a composite stellar population (CSP), is then used to reproduce the observed stellar SED (for this work, the SED for observing bands

[1] In this work, as explained in Chapter 3, we did not model the galaxy as a whole but we rather decomposed it into different annuli of increasing radii and modeled the individual SEDs of each annuli. Nevertheless, for readability reasons, we chose to not specify this technical detail when describing the general idea behind our stellar SED modelings (i.e. in the next three sections).

[2] `http://www.icg.port.ac.uk/~maraston/Claudia%27s_Stellar_Population_Model.html`

of frequency ν in the UV, visible and NIR domains) with

$$I_{\nu,\mathrm{CSP}}(t_0) = \int_{t'=0}^{t'=t_0} \mathrm{SFR}(t_0 - t')\ I_{\nu,\mathrm{SSP}}\big(t', Z(t_0 - t')\big)\ dt' \tag{4.1}$$

where t_0 corresponds to the current age of the galaxy (in other words, the star formation has started t_0 years ago) while t' represents the age of the stellar populations found in the galaxy. This integral is then evaluated over all possible ages of the SSPs, the oldest stars being as old as the galaxy itself. In this work, the maximal age of the galaxy has been fixed to 13.4 Gyr, corresponding to the age of the oldest observed galaxy in our universe (whose redshift is ∼11; Oesch et al. 2016), assuming a cosmological model given by the latest results from the *Planck* telescope (Planck Collaboration 2020).

In addition, the distribution of SSPs of different ages in a galaxy is defined by its star formation history (SFH), that is to say, the evolution with time of its SFR. Hence, $\mathrm{SFR}(t_0)$ is the current SFR of a galaxy (roughly evaluated for each galaxy of our sample in Section 3.2.2.2 and gathered in Table 4.3 on page 106). The term appearing in Equation 4.1, $\mathrm{SFR}(t_0 - t')$, is then the SFR of the galaxy when the stars of age t' have been created.

Finally, $I_{\nu,\mathrm{SSP}}(t', Z(t_0 - t'))$ represents the surface brightness profile of a SSP of age t' and of metallicity $Z(t_0 - t')$, the ISM metallicity of the galaxy when the stars have been created, t' years ago. We have made here a simplifying hypothesis when assuming that, at one moment in the life of the galaxy corresponds one ISM metallicity Z. If one wants to assume a certain distribution of metallicities with the age of the galaxy, Equation 4.1 should be modified and an additional integral on the metallicity should be added (see Conroy 2013, for example).

To summarize, to compute Equation 4.1, one has to use SSP synthetic spectra, representing various populations of stars of different ages and metallicities and to assume the SFH of the galaxy to model as well as the evolution of its metallicity with time, called its metallicity history (ZH).

4.1.2 Star formation history

The SFH of all types of galaxies are expected to show some stochasticity with various bursts of star formation due principally to interactions between the galaxy and its neighborhood (e.g. Walcher et al. 2011). Because

of that, the most accurate way to represent the real evolution of a galaxy with time is to use non-parametric functions as they offer more flexibility and as they result in less biased SFHs (Pacifici et al. 2015; Carnall et al. 2019; Leja et al. 2019; Lower et al. 2020). However, the degeneracies between the stars populations of different ages (principally the old ones whose SSP do not significantly vary with age) make it very challenging to retrieve this stochasticity from observations. To have satisfying results, the non-parametric approach requires very high-quality (photometric and spectroscopic) data and implies a lot of computation time.

Since this work aims at developing a new RC decomposition methodology that could be applied on a large number of galaxies, the necessity of high-quality data prevents us to use such an approach. We thus preferred parametric modelings of the SFHs, which are in fact very reasonable approximations due to the degeneracy we just mentioned. We assumed that all the stars in a galaxy have been created in one or two well-separated bursts of star formation, using two different parametrizations to model these bursts:

- an exponentially declining burst (represented by the blue dashed line on Figure 4.1):

$$\mathrm{SFR}_b(t) = \begin{cases} \mathrm{SFR}_{b,0} \ \exp\left(-\frac{t-t_{b,0}}{\tau_b}\right) & \text{if } t \geq t_{b,0} \\ 0 & \text{otherwise.} \end{cases}$$

  Three parameters per burst have to be determined: (i) $\mathrm{SFR}_{b,0}$ the amplitude of the burst, (ii) $t_{b,0}$ the time at which the burst occurred and, (iii) τ_b the time scale of the burst. This kind of evolution, among the most used in modern literature (Robotham et al. 2020), is typical of a situation where the SFR is proportional to the gas density in a galaxy where no matter is exchanged with the environment, that is to say, in a closed-box model (Schmidt 1959).

- a skewed normal burst, truncated such that the SFR is null at the beginning of the life of the galaxy (blue solid lines on Figure 4.1 and on its inset; Bellstedt et al. 2020):

$$\mathrm{SFR}_b(t) = \mathrm{SFR}_{b,0} \ \exp\left(0.5X(t)^2\right) \ \left[1 - \frac{1}{2} \ \mathrm{erf}\left(\frac{t - t_{b,0}}{\sqrt{2}\sigma_b} + \frac{2}{\sqrt{2}}\right)\right]$$

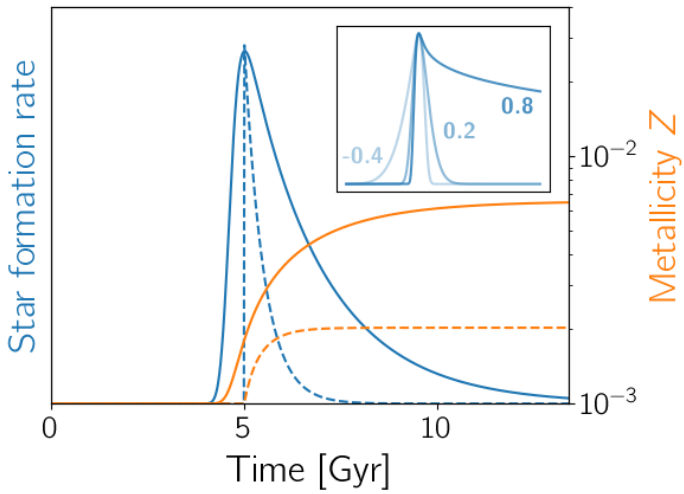

Figure 4.1: Parametrizations of a burst of star formation (in blue) and resulting evolution of the ISM metallicity (assuming a closed-box model representation of the galaxy; in orange). Two mathematical functions describing the burst are used in this work: (i) an exponentially declining burst (dashed lines) and (ii) a truncated skewed normal one (solid lines). Here, the two functions have the same burst amplitude $\mathrm{SFR_{b,0}}$, peak time $\mathrm{t_{b,0}}$ and time scale τ_b. *Inset panel:* Examples of truncated skewed bursts with different $\mathrm{s_b}$ parameter values (the main graph SFH is constructed with a $\mathrm{s_b}$ of 0.5).

where the skewness of the normal burst is associated to

$$X(t) = \left(\frac{t - t_{b,0}}{\tau_b}\right) \exp\left(s_b \operatorname{asinh}\left(\frac{t - t_{b,0}}{\tau_b}\right)\right)$$

and its truncation results from the last factor where

$$\sigma_b = \frac{|t_{\max} - t_{b,0}|}{2t_{\mathrm{trunc}}}.$$

In this expression, the parameter τ_b is the standard deviation of the non-truncated symmetric Gaussian centered on $t_{b,0}$. If it does not represent exactly the same physical quantity as for the exponential

model, we will nevertheless still designate it as the "time scale parameter" in the rest of this work. Formally, this is a misuse of language but it will facilitate the reading without impacting the comprehension.

Compared to the exponentially declining burst model, we have one additional parameter: s_b which characterizes the skewness of the burst. The burst is a simple Gaussian for a $s_b = 0$ and has a large early (resp. late) tail for negative (resp. positive) s_b values. Different examples of these asymmetric bursts (with associated s_b values) are shown in the inset of Figure 4.1. The two other new parameters, $t_{\rm max}$ and $t_{\rm trunc}$, are usually fixed. $t_{\rm max}$ is the maximal age of the galaxy (already fixed at 13.4 Gyr) and $t_{\rm trunc}$ characterizes the sharpness of the early-time truncation (0 corresponding to no truncation). Here, a value of $t_{\rm trunc} = 2$ Gyr, associated to a strong truncation, is fixed in oder to ensure a physically sound null SFR at the beginning of the life of the galaxy (Bellstedt et al. 2020).

The advantages of the first model is its relative simplicity but it has recently been shown that it is not capable to reproduce the observations of the cosmic SFH (i.e. the evolution with redshift of the global SFR of the universe; Carnall et al. 2019) while the second one (when combined with a particular metallicity history, that we will describe in the next section) gives good results (Bellstedt et al. 2020). Moreover, the truncated skewed normal burst helps to get rid of the intrinsic discontinuity inherent to exponentially declining bursts as the s_b parameter adjusts the steepness of the rising (and of the decreasing) portion(s) of the burst.

As mentioned earlier, assuming one or two star-forming bursts of such a simple form is clearly not realistic and such SFHs should thus not be considered as the true SFHs of the galaxy but just as a simple way to model them, sufficiently accurate for our purpose.

4.1.3 Metallicity history

Usually, when performing SED fitting, the metallicity history of the galaxy is simplified at the maximum with Z taken as a constant (either fixed or left as a free parameter) all along the life of the galaxy (see da Cunha et al. 2008; Noll et al. 2009; Han & Han 2014, for examples from important SED fitting codes). This non-physical hypothesis has been called into question

by recent works which showed that allowing Z to vary with time better reproduces observations such as the cosmic SFH (when associated with a particular model of star-forming bursts, the truncated skewed normal) or the diversity of scenarios described by semi-analytic models of galaxy formation (Chevallard & Charlot 2016; Robotham et al. 2020; Bellstedt et al. 2020).

The most recent implementation of ZH in SED fitting computations, and the one used in this work, is the closed-box model. In this model, the galaxy starts as a cloud of baryonic gas, transforms it gradually into stars following a given SFH and, importantly, does not exchange any matter with its environment. To compute the evolution of Z with time in this situation, two other assumptions have to be made: (i) the instantaneous recycling approximation, stating that metals produced by the stars are instantaneously rejected in the galactic ISM when the stars are formed and, (ii) the instantaneous mixing, implying that, when released in the ISM, these metals are homogeneously distributed within the whole galaxy. The instantaneous recycling approximation has the advantage to allow an analytical representation of the ZH of the galaxy while being quite reasonable in the case of SED fitting. Indeed, the time scales associated to the release of metals in the ISM (Myr to Gyr[3]) are short compared to the characteristic times of spiral galaxies evolution (several Gyr). Thus, at each episode of star creation, a certain portion of a given mass of gas is directly converted into metals that are injected in the ISM while the rest of the mass is transformed and locked-up in long-life stars. Concerning the instantaneous mixing, this is also a reasonable approximation in the context of this study as we work with galaxies that are azimuthally averaged.

With all these hypotheses in mind, the evolution of Z in a closed-box galaxy is modeled by

$$Z(t) = -p \ \ln\left(\frac{M_i - M_*(t)}{M_i}\right) + Z_i \tag{4.2}$$

where $M_*(t)$ is the evolution with time of the galactic stellar mass (directly given by the SFH) and M_i is the initial mass of the pregalactic gas cloud.

[3]For the main contributors to the metallicity of the galaxy (type II supernovae that explode after a few Myr), this approximation holds much better than for type Ia supernovae (time scales of hundreds Myr to a Gyr) or AGB stars (time scales of a Gyr or more) (Peeples et al. 2014; Cimatti et al. 2020).

As the galaxy is supposed to have no exchange with its environment, the total mass of the galaxy (distributed between the gas and the stars) remains equal to this initial mass at any time ($M_i = M_{\rm tot} = M_*(t) + M_{\rm gas}(t),\ \forall t$). Hence, the ratio of masses in Equation 4.2 is equivalent to the gas fraction $M_{\rm gas}/M_{\rm tot}$ of the galaxy, the lower the gas fraction, the higher the metallicity.

Z_i is the initial metallicity of the galaxy. Before the formation of the present spiral galaxies, the universe had been enriched by the first populations of stars, the population III stars, to a metallicity of $\sim 10^{-4}$ (e.g. Fumagalli et al. 2011). Unfortunately, as the SSPs used in this work are not computed for this value of Z, we fixed Z_i to 10^{-3}, the lowest of all the SSPs metallicities.

Finally, the factor p in the equation is called the effective metallicity yield and is defined as the ratio between the mass of metals added in the ISM when the stars form and the mass locked up in long-live stars. If this yield value is influenced by the stellar nucleosynthesis, it also depends on the IMF (i.e. on the amount of high-mass stars producing metals compared to the long-live low-mass stars). When computing Equation 4.2, this yield is usually taken as a constant independent of time or of the galaxy metallicity. This simplification allows for an analytical evolution of Z with time. The value of p should rather decrease as the galaxy ages. As times passes and as generations of stars are formed, the metallicities of the ISM and hence of the new-born stars increase. Nevertheless, this does not impact the metal production as the supernovae always produce the same quantity of metals whatever the metallicity of their progenitors. Hence, the mass of newly produced metals added to the ISM declines with time (Robotham et al. 2020). To model that, the yield p value should decrease with the evolution of the galaxy. To account for this while still assuming a constant value of p, we fixed it to 0.02 (Bellstedt et al. 2020), a value slightly lower than the typically assumed 0.03, derived from nucleosynthesis models (Peeples et al. 2014; Lagos et al. 2018).

To go one step further, one could also decide to take into account the interactions between the galaxy and its environment (multiple gas infalls and/or outflows due to the stellar winds and the supernovae explosions). Indeed, if the galaxy accretes huge amounts of low-metallicity gas or if it expels a significant part of the metal production from its stars, the evolution of its metallicity will not follow the one of a closed-box model. Nevertheless, at first sight, it is not necessary to go into such a level of details. Indeed,

taking the outflows into account only results in a reduction of the value of the fixed yield p by a factor representing the rate at which the gas leaves the galaxy. Moreover, simulations have shown that it is more probable for the infall gas to be recycled 'metallic' gas previously ejected by winds and explosions than pristine gas, thus not decreasing too much the galaxy metallicity (Übler et al. 2014; Christensen et al. 2016).

The closed-box model is therefore a good analytical and physically motivated representation of galactic ZHs. Moreover, this model has the non-negligible advantage to be parsimonious with its parametrization as it only adds one parameter to our SED fitting: the total baryonic mass M_i, a parameter which directly defines the current metallicity of the galaxy.

Finally, the methodology we developed here to model stellar SEDs should help to lift the well-known degeneracy between the stellar ages and their metallicities. Indeed, using photometric SED observations, it is very challenging, if not impossible, to distinguish a low-Z old population of stars from a young highly metallic one. With our approach linking the metallicity evolution of galaxies with their SFH (as clearly illustrated in Figure 4.1), we should be able to better constrain these different populations.

4.1.4 SED modeling

To model the stellar FUV-to-NIR SEDs of the galaxies in our sample, we followed a Bayesian methodology first formally introduced by Kauffmann et al. (2003) and implemented in practice by Salim et al. (2007), since then gaining in efficiency and growing in popularity (Baes 2020). The idea here is (i) to create a library of theoretical CSP models, each model being associated to one set of parameters, and (ii) to compare these models with the observations in order to build the associated posterior pdf. The best-fit values and uncertainties of each of the SFH and ZH parameters can then be estimated via the marginalization of this posterior pdf. Additionally, other pdfs can also be constructed for the observables themselves and for other derived quantities (such as the stellar mass associated to each model, as will be explained in Section 4.1.6). For this work, each computed library corresponded to a specific combination of SFH and ZH parametrizations. A summary of these libraries can be found in Table 4.1.

An important step to build these libraries is the choice of the prior pdfs of each parameter. The ones used for this work are given in Table 4.2. To sum up, the restrictions on the parameters were chosen to be as

Table 4.1: Libraries of theoretical CSP models computed for this work. For each library, the ZH chosen is the closed-box model (1 parameter).

Library name	SFH burst model	Number of bursts	Number of parameters	Number of models
Exp-1pop	Decl. exponential	1	4	$1.5\ 10^5$
Exp-2pop	Decl. exponential	2	7	$1.6\ 10^6$
Skewed	Trunc. skewed normal	1	5	$5.5\ 10^5$

loose as possible, with uniform or log-uniform distributions, depending on the ranges of the parameters values. Hence, the bursts of star formation were chosen to occur at any moment of the life of the galaxy, the galaxy itself being potentially as old as the oldest observed galaxy in our universe (Oesch et al. 2016). We also allowed the SFH to be described by anything from rapidly evolving, well-defined peaks (with widths of a fraction of a billion years) to a nearly constant SFR all along the galaxy life (a "peak" with a time scale several times the age of the galaxy). For the amplitude of the bursts, the prior was taken to allow moments of intense star formation, typical of what is currently found in starbursts galaxies (Bellstedt et al. 2020). For Skewed library, the burst asymmetry was left variable with less chance to have a larger early tail than a larger late one (Bellstedt et al. 2020). The latter even had the possibility to be wider than the age of the galaxy, resulting in a nearly constant SFR after the beginning of star formation.

The case of the ZH parameter M_i, the mass of pregalactic gas cloud, is particular. This parameter value directly depends on the SFH parameters. Indeed, these parameters define the mass of stars created during the life of the galaxy, which in fact corresponds to the lower bound of M_i. Moreover, models leading to the formation of more stars than the upper bound of the M_i parameter (conservatively chosen as the maximum total galactic mass estimated from current star-forming galaxies; Cimatti et al. 2020) were discarded from our libraries.

This dependency of the ZH parameter on the SFH ones thus resulted in various modifications of the initial uniform and log-uniform prior distributions. The final distributions are shown in Figure 4.2, where one can notice that high, large and/or highly asymmetric bursts with large late tails are disfavored due to the too large quantity of stars they create. Similarly, the

Table 4.2: Priors on the SFH and ZH parameters used for the computation of the libraries of CSP models (see Table 4.1)

FIXED PARAMETERS					
Parameter	Description	Value	Unit		Ref.
$t_{\rm max}$	Maximal age of the galaxy	13.4	Gyr		(1)
$t_{\rm trunc}$	Truncation time at the beginning of the life of the galaxy	2	Gyr		(2)
VARIABLE PARAMETERS					
Parameter	Description	Range	Unit	Initial* dist.	Ref.
	SFH parameters				
$\mathrm{SFR}_{b,0}$†	Amplitude of the burst b	$10^{-4} - 10^{2}$	yr^{-1}	Log-uniform	(2)
$t_{b,0}$	Time at which the (peak of the) burst b occurs	$0 - t_{\rm max}$	Gyr	Uniform	(2,3)
τ_b	Time scale of the burst b	$10^{-1} - 10^{2}$	Gyr	Log-uniform	(2,3)
s_b	Skewness of the burst b	-0.5 – 1		Uniform	(2)
	ZH parameters				
M_i†	Initial mass of gas	$M_*(\infty)$‡ -10^{11}	$\mathrm{M}_\odot$	Log-uniform	(4)

† Ring values, the whole galaxy being divided in ∼50 rings for the computation of the stellar mass profiles
‡ The initial mass of gas, which will create all the stars of the galaxy, should at least be equal to $M_*(\infty)$, the mass of stars created along the complete life of the galaxy. The latter directly results from the values of the parameters of the associated SFH.
* The initial uniform and log-uniform distributions are directly impacted by the correlation between the SFH and the ZH parameters and result in distributions illustrated in Figure 4.2.
References: (1) Oesch et al. (2016); (2) Bellstedt et al. (2020); (3) Maraston (2005); (4) Cimatti et al. (2020)

ZH prior distribution ends up not being log-uniform at all but rather displays a strong asymmetry towards the most massive galaxies, as its minimal bound changes for each set of parameters. In other words, from all the sets of parameters randomly drawn from the initial uniform and log-uniform priors, we discarded the ones for which the SFH parameters produce a stellar mass larger than the M_i parameter.

Once all the models of a library have been computed, they had to be compared with the FUV-to-NIR surface brightness values at each galactocentric distance for each galaxy in our sample. As this step is time consuming, we decided to bin our luminosity profiles. The centers of spiral galaxies being crucial to probe the DM halo shape, we binned the profiles finely near the centers and more coarsely in the outskirts, stopping at a distance considered as large enough to encompass the majority of the stellar component of the galaxies (i.e. for $r \approx 1.5\ r_{25}$).

Practically, we convolved each CSP theoretical spectra with the transmission curves of our observing bands. This gave us theoretical luminosities that we converted into surface brightness values by taking into account the distance of the galaxy. We compared these theoretical values at each galactocentric distance with the observations and evaluated the goodness-of-fit for each model i via the computation of a χ_i^2. We then used these values to estimate the weights $w_i = \exp(-\chi_i^2/2)$ associated to each model and we built the associated posterior pdf. Finally, we marginalized this pdf over the SFH and ZH parameters in order to evaluate their best-fit values (taken as the averages of the marginalized pdfs) and their associated uncertainties (defined by the 16^{th} and 84^{th} percentiles of the pdfs).

4.1.4.1 Considerations on results representation and usage

For each galaxy of our sample and for each combination of SFH and ZH (given in Table 4.1), we computed the parameters profiles describing the evolution of the star formation and of the associated metallicity during the life of the galaxy. These are displayed in Figures 4.3, 4.4, and 4.5 respectively for the Exp-1pop, Exp-2pop, and Skewed library models.

As they give the average values of the marginalized posterior pdfs and their associated 1σ error bars, these profile representations are not exempt of bias and should be considered with caution, especially when the pdf is not well represented by a (skewed) Gaussian. This is the case for the burst peak time parameters $t_{b,0}$ of our three libraries for which the marginalized

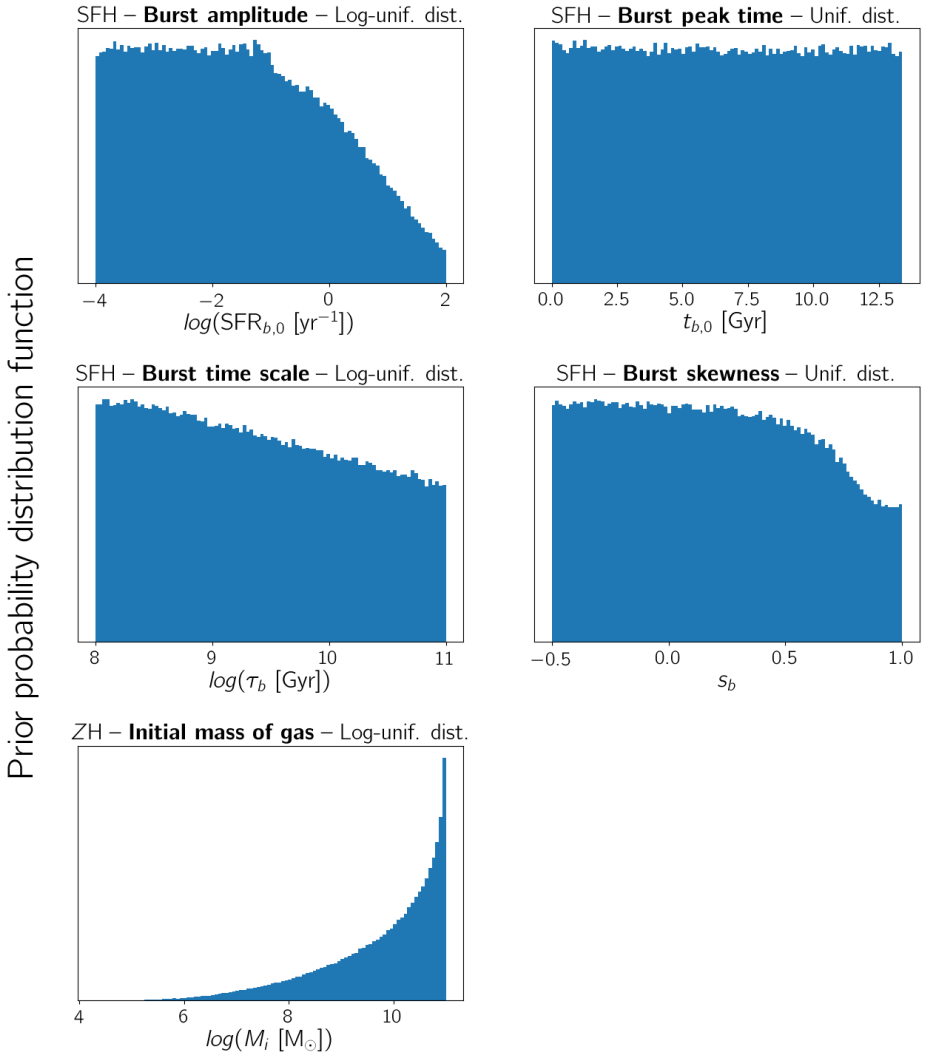

Figure 4.2: Prior pdfs of the SFH and ZH parameters described in Table 4.2. The correlation between the SFH parameters and the ZH one modifies the initial uniform and log-uniform distributions, resulting in less bursts of high amplitude, long time scale and/or large late tail. Equivalently, the ZH parameter prior is completely modified by this correlation with a resulting strong asymmetric prior towards massive galaxies.

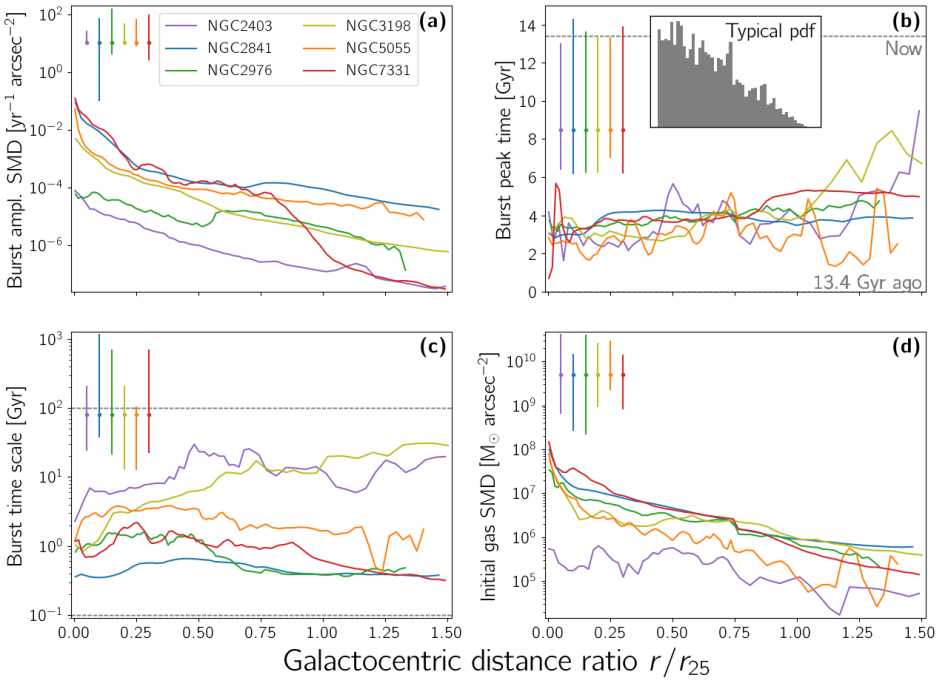

Figure 4.3: Profiles of the SFH and ZH parameters from the Exp-1pop library for all the galaxies in our sample. The typical errorbars for each galaxy are given in the upper right corner of each panel. The horizontal dashed lines in panels (b,c) correspond to the parameters' maximal and minimal limits (assumed when creating the library and given in Table 4.2).

posterior pdf typically look like the inset on panel (b) of Figure 4.3, where the earlier the peak, the better the fit. Equivalently, bimodality is observed in the burst amplitude $\mathrm{SFR}_{b,0}$ and in the skewness parameter s_b distributions for some galactocentric distances of some galaxies. Such shapes are not correctly described by the representations with the best-fit parameters profiles displayed in these three figures.

Hence, we want to emphasize again that these profiles and the parameters values should not be taken as exact representations of the SFH and of the ZH of galaxies. They are only given to retrieve some general tendencies. This is not a problem here as the goal of this work is not to describe

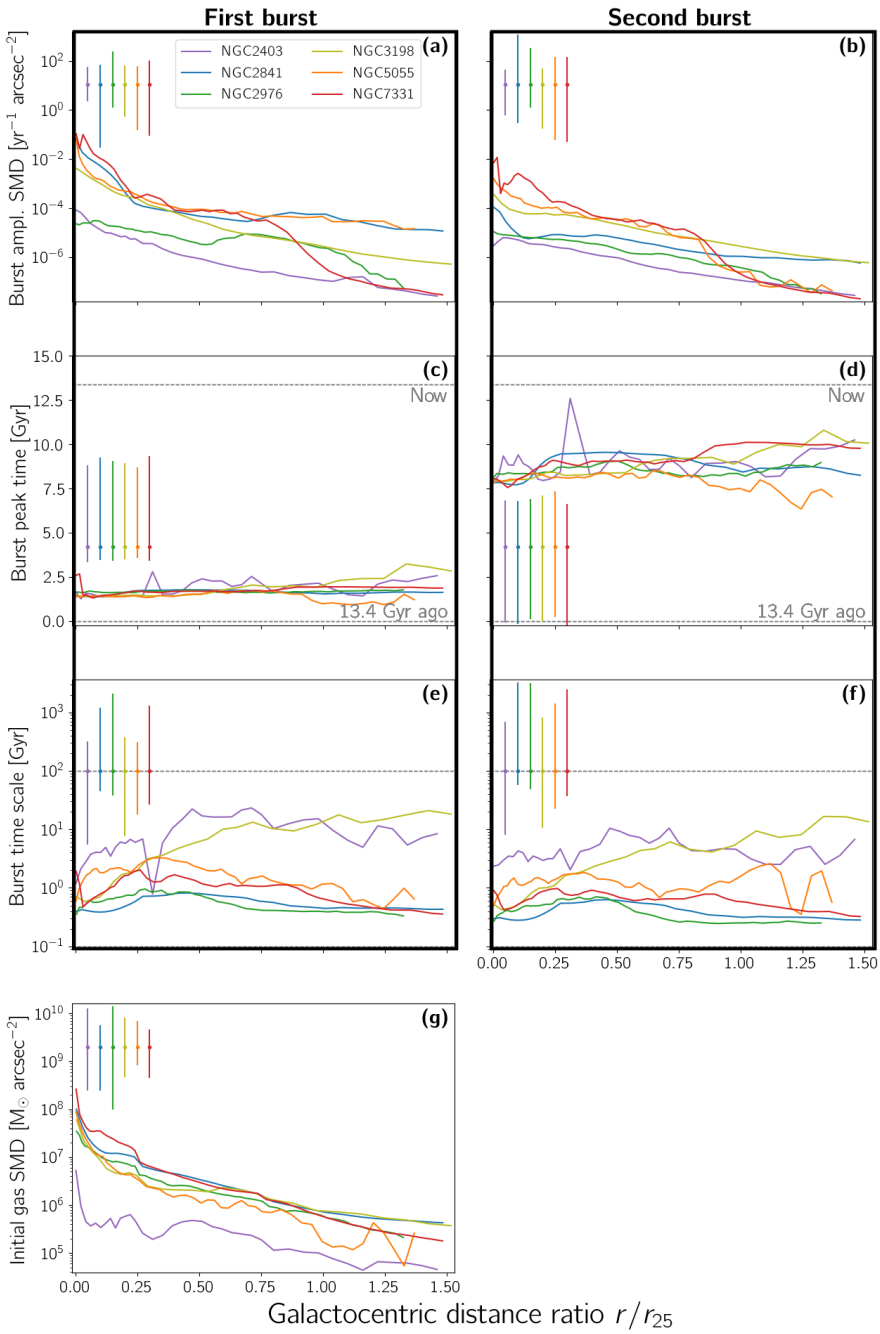

Figure 4.4: Same as Figure 4.3 for the parameters of the Exp-2pop library.

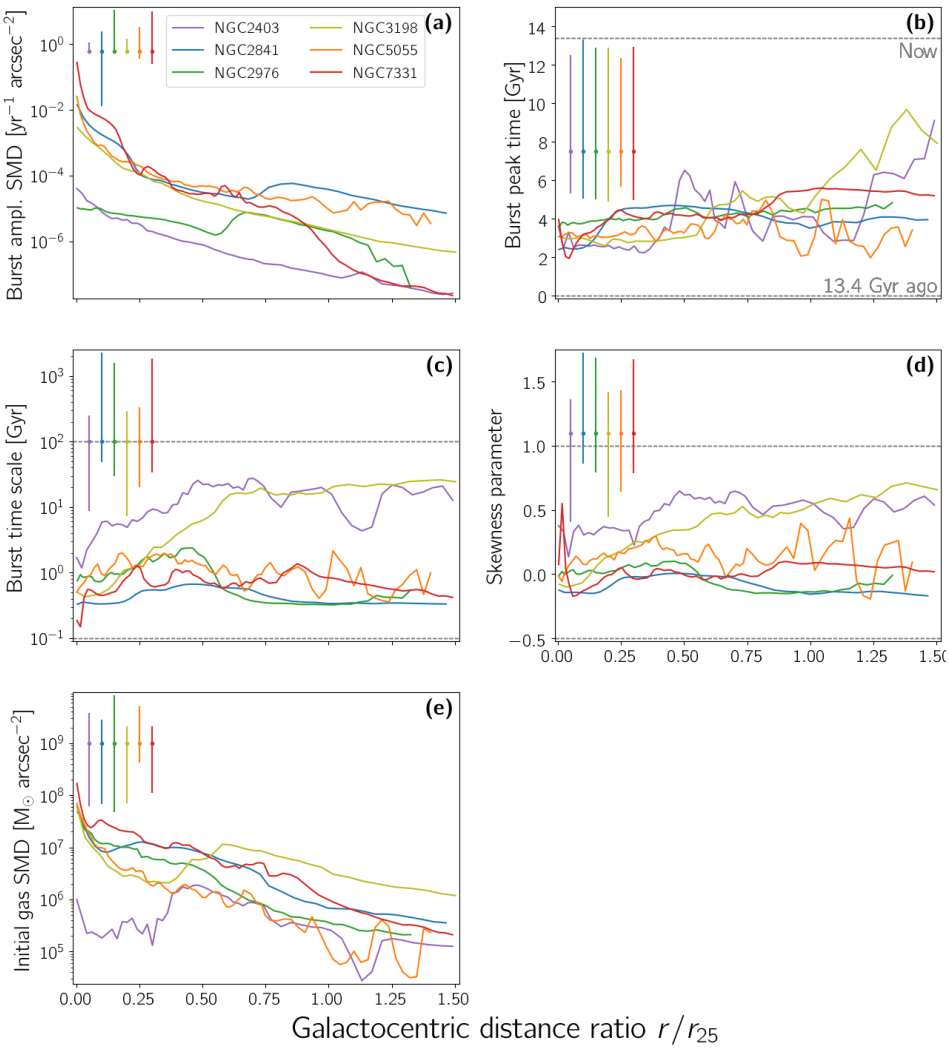

Figure 4.5: Same as Figure 4.3 for the parameters of the Skewed library.

in details the galactic SFH and ZH but only to use them to compute the stellar mass profiles. To do so in a proper way without being impacted by the (not always representative) best-fit parameters profiles, one has to be careful to always derive this mass profile from its associated posterior pdf in order to draw unbiased conclusions on the current stellar content of the studied galaxies. Similarly, this methodology should also be used for any other galactic physical quantity such as the current SFR or the ISM metallicity, as will be done in the rest of this chapter.

4.1.4.2 Global tendencies of the SFH/ZH parameters

Keeping these considerations in mind, we can still derive some global conclusions from the best-fit parameters profiles shown in Figures 4.3, 4.4, and 4.5. These conclusions are in agreement with the expected SFH/ZH of spiral galaxies.

First, for all libraries, the galaxies which currently have the smallest stellar mass (NGC2403 in purple and NGC2976 in green on the figures; see Table 4.5 on page 118 for the exact values) are logically the ones that created the smallest number of stars during their lifetime (i.e. the galaxies with the lowest burst amplitudes; see panels (a) in all the three figures). The opposite is also true for the most massive galaxies (NGC2841 in blue, NGC5055 in orange and NGC7331 in red).

Moreover, the stellar content of all the galaxies formed relatively early in their lifetime with a burst occurring 9–10 Gyr ago (for libraries with only one burst; panel (b) in Figures 4.3 and 4.5) or an early burst ∼11 Gyr ago with a later one 4–5 Gyr ago (for the two-bursts library; see panels (c,d) in Figure 4.4). For all scenarios, it is notable that the star formation started concurrently over the whole galaxy. If they exist, the global differences observed nowadays in stellar populations across the galaxies are thus not associated to differences in the moment at which the first stars appeared.

Explanations are rather to be found in the burst time scale parameter τ_b. The latter shows an important diversity from one galaxy to the other (see panels (c) of Figure 4.3 and 4.5 as well as panels (e,f) of Figure 4.4). Two extreme cases are NGC2841 (in blue) that has very short burts (with $\tau_b \sim 0.3$ Gyr, which is typical of elliptical galaxies and high-mass/early-type spirals) and NGC2403/3198 (in purple/yellow) with bursts of star formation that are so wide that the resulting SFRs end up being nearly constant with time, a classical behavior of intermediate and lower mass/late-type spirals.

This incidentally explains why NGC2403, despite its notably low burst amplitude (even lower that the quasi-dwarf galaxy, NGC2976; in green) is still relatively massive. On top of that, a great diversity of behavior of this time scale parameter within the galaxies can also be observed. Hence, all over NGC2841 (in blue) or NGC5055 (in orange), the burst time scales are similar while they ten-fold increase from the center of NGC3198 (in yellow) to its outskirts.

NGC2976 (in green) is another example of SFH and time scale variations across the disk. As explained when introducing this galaxy in Section 2.2.2, the star formation in NGC2976 seems to be shutting down from the outside-in: its inner half shows signs of recent star formation while it does not occur anymore in its outskirts. For all our libraries, we can clearly distinguish two regimes. In the center of the galaxy, the star-forming bursts have low amplitudes with long time scales and inversely in its outskirts. Such a situation is consistent with the star formation occurring currently in the inner but not in the outer regions of the galaxy. The limit at which this change happens varies depending on the observable. Williams et al. (2010), using color-magnitude diagrams, found a limit at ∼3 kpc (or a ratio of r/r_{25} of 0.9) while the break observed in optical and NIR luminosity profiles is located around respectively 70 and 100 arcsec (resp. ratios of 0.35 and 0.50; Simon et al. 2003). For our modeling, the transition between the two star-forming regimes falls in between these estimates range with a ratio r/r_{25} of ∼0.6 (corresponding to 2 kpc or 115 arcsec).

Concerning the case of the Skewed library models, the width of the star-forming burst is impacted both by the time scale τ_b and by the skewness parameter s_b. At high value, these two parameters degenerate: a flat SFH is equivalently described by a very large burst or by a burst with an prominent late tail (as shown by the inner panel in Figure 4.1 on page 90 for $s_b = 0.8$). In our sample, the skewness parameter profiles (panel (d) of Figure 4.5) reflect the inter- and intra-galaxy diversities observed in the time scale profiles. The correlation between these two parameters seems direct: if a burst has a large time scale, it is also highly asymmetric (with a large late tail) while symmetric bursts have shorter width. Nevertheless, it should be noted that the error bars associated to the skewness parameters are particularly important (corresponding to more than 50% of the allowed range, represented by the two horizontal dashed lines in panel (d) of Figure 4.5). This parameter is thus nearly unconstrained by our SED fitting. Hence, for the modelings performed in this work, this kind of burst models,

that is more physical on paper, does not bring additional useful information compared to the simple exponentially declining bursts.

4.1.5 Byproducts

In addition to the product that particularly interest us in this work, namely the mass distributions of stars within the galaxy, our global SED modeling also provides interesting byproducts to understand and further describe spiral galaxies.

4.1.5.1 Current star formation

Besides their old populations of stars, the galaxies in our sample are still actively creating stars, like all other spiral galaxies. This is not a surprise for NGC2403 (in purple) and NGC3198 (in yellow), which both have a relatively flat SFH (with τ_b of approximately their age, $\sim$ 10 Gyr). However, it is also the case for the four other galaxies whose star-forming peaks are way shorter ($\tau_b \leq$ 1–2 Gyr).

The method to evaluate the current star formation of a galaxy is to compute its present SFR, SFR(t_0). For our sample of galaxies, they have already been roughly estimated from each galaxy FUV and MIR luminosity profiles in Section 3.2.2.2 (in order to select the most appropriate dust attenuation curve). Doing so but this time using our SED modeling, we computed the present SFR posterior pdfs at each galactocentric distance of each galaxy, resulting in SFR profiles (whose surface density can be visualized in Figure 4.6). These profiles were then integrated to determine the present global SFRs. For each library, these values are gathered in Table 4.3 along with our first rough estimates (from luminosity profiles) and an estimate from literature (following the same luminosity methodology; Leroy et al. 2008). For both teh figure and the table, the SFR values given by the SED modeling have been converted in solar mass units assuming a Kroupa IMF (Kroupa 2001) to correspond to the IMF used by Maraston (2005) when building the SSPs used in this work.

From this, it is clear that all the galaxies in our sample have similar present SFRs. NGC5055 and NGC7331 are even more active than the two galaxies with the flat SFHs (NGC2403 and NGC3198). This *a priori* paradoxical situation highlights the problems of drawing conclusions from the SFH/ZH parameters profiles instead of from the whole posterior dis-

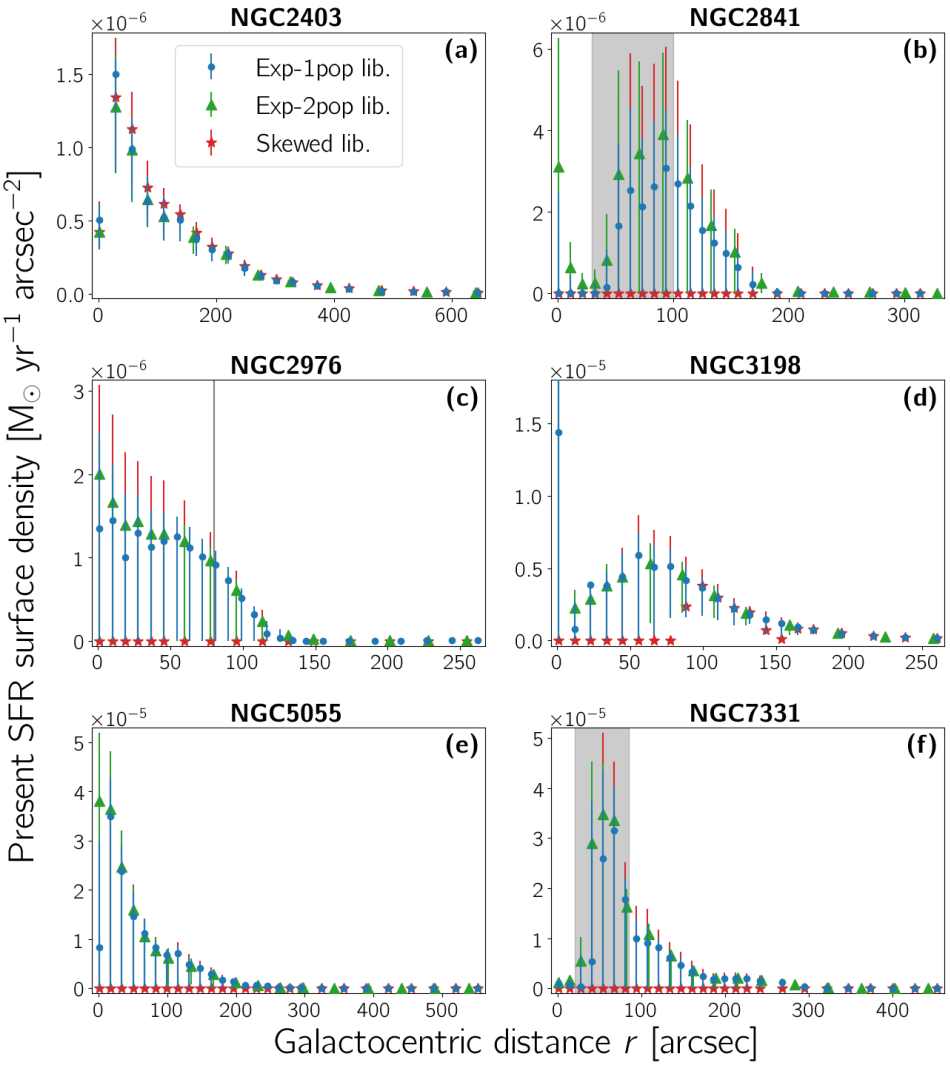

Figure 4.6: Present SFR surface density profiles of each galaxy in our sample. The values given by the SED modeling have been converted in solar mass units assuming a Kroupa IMF (Kroupa 2001). If present, the location of the molecular ring is shown in grey.

Table 4.3: Present SFR[†] (expressed in $M_\odot$ yr^{-1}) of all the galaxies in our sample

	From lum. profiles		From stellar SED mod.		
Galaxy	Leroy et al. (2008)	First est.[‡]	Exp-1pop	Exp-2pop	Skewed
NGC2403	0.382	0.217	$0.36^{+0.07}_{-0.11}$	$0.35^{+0.07}_{-0.12}$	$0.37^{+0.09}_{-0.08}$
NGC2841	0.741	0.409	$0.39^{+0.28}_{-0.39}$	$0.57^{+0.35}_{-0.57}$	$0.00^{+0.87}$
NGC2976	0.087	0.069	$0.10^{+0.03}_{-0.10}$	$0.11^{+0.02}_{-0.11}$	$0.00^{+0.16}$
NGC3198	0.931	0.601	$0.85^{+0.22}_{-0.56}$	$0.88^{+0.22}_{-0.54}$	$0.49^{+0.69}_{-0.05}$
NGC5055	2.123	1.917	$2.36^{+0.62}_{-2.36}$	$2.40^{+0.75}_{-2.26}$	$0.00^{+3.12}$
NGC7331	2.987	2.872	$3.19^{+1.48}_{-3.19}$	$3.91^{+1.05}_{-3.89}$	$0.00^{+5.36}$

[†] Resulting from the integration of the SFR surface density profiles of Figure 4.6 up to a galactocentric distance of 1.5 r_{25} (1.0 r_{25} for NGC5055); converted in solar mass units assuming a Kroupa IMF (Kroupa 2001)

[‡] Our first estimates of the galaxies' present SFR have been obtained from their FUV and MIR luminosity profiles, following Leroy et al. (2008) methodology. They have been used to choose the dust attenuation curve of each galaxy in Section 3.2.2.2. The differences between Leroy et al. (2008) values and ours are related to the way each of us corrected the galactic FUV profiles from the extinction by the MW dust.

tributions, as explained earlier. The difference between the two categories of galaxies (the ones with flat SFH and the others) is nevertheless visible in the SFR uncertainties. Indeed, if NGC2403 and NGC3198 have well defined SFRs and associated surface density profiles, this is not the case for the other four galaxies which all have profiles and global SFR values with important uncertainties (of the order of the values themselves). For the computations with the Skewed library, it is even worse, with null SFR values and very large positive error bars. Hence, on top of not being more constraining than the simple exponentially declining bursts, the truncated skewed normal model also leads to problematic results for the galactic SFR estimates. For completeness, we will continue in this chapter to show the results from our SED modeling with this library but we will not use it to

perform additional analyses.

Comparing our present SFR determinations from stellar SED modeling to those performed by Leroy et al. (2008) from FUV and MIR luminosity profiles, the values are in agreement with each other. Moreover, analyzing the galactic profiles, we can clearly see the regions of intense star formation in the inner half of NGC2976, associated to the molecular rings of NGC2841 and NGC7331 or in the centers of NGC2841, NGC3198 and NGC5055 (as previously seen in a different indicator, the dust temperature profiles of Figure 3.1 on page 73).

4.1.5.2 Metallicity profiles

As for the SFR, the profile of the present galactic metallicity is a byproduct of our stellar SED modeling. Computed from their pdfs, the $Z(t_0)$ averages and associated uncertainties are plotted in Figure 4.7 (blue, green and red points) as a function of the galactocentric distance for all the galaxies in our sample. The two dashed horizontal lines show the range of metallicity used by Maraston (2005) to compute the SPSs at the basis of our work (between 10^{-3} and $4\ 10^{-2}$) and the solid line corresponds to the solar metallicity ($Z_{\odot} = 0.0139$; Asplund et al. 2021).

In our sample, the most massive galaxies (NGC7331, NGC5055 and, to a lesser extend, NGC2841[4]) are also the most metallic ones. This is in accordance with the classic mass-metallicity relation (Lequeux et al. 1979) that is particularly tight in our local neighborhood (Tremonti et al. 2004). As shown in Equation 4.2, with the closed-box approximation assumed in this work, the present metallicity Z is a measure of the ratio between the mass of stars created during the life of the galaxy and the mass of the pregalactic gas cloud. As the star formation is fixed by the SFH parameters, the metallicity value is directly dictated by the M_i parameter whose evolution within the galaxy has been shown in panels (d), (g) and (e) of Figures 4.3, 4.4 and 4.5. In those three figures, whatever the library (or equivalently, the SFH parametrization), the M_i parameter has an evolution similar to the burst amplitude, either within a given galaxy or within the sample itself. Hence, the galaxies whose bursts have the lowest/highest amplitudes are the galaxies which were initially the least/most massive.

[4]This galaxy in fact presents high metallicity values in its central regions, followed by a very steep decrease starting at ∼30 arcsec, a curious feature on which we will come back.

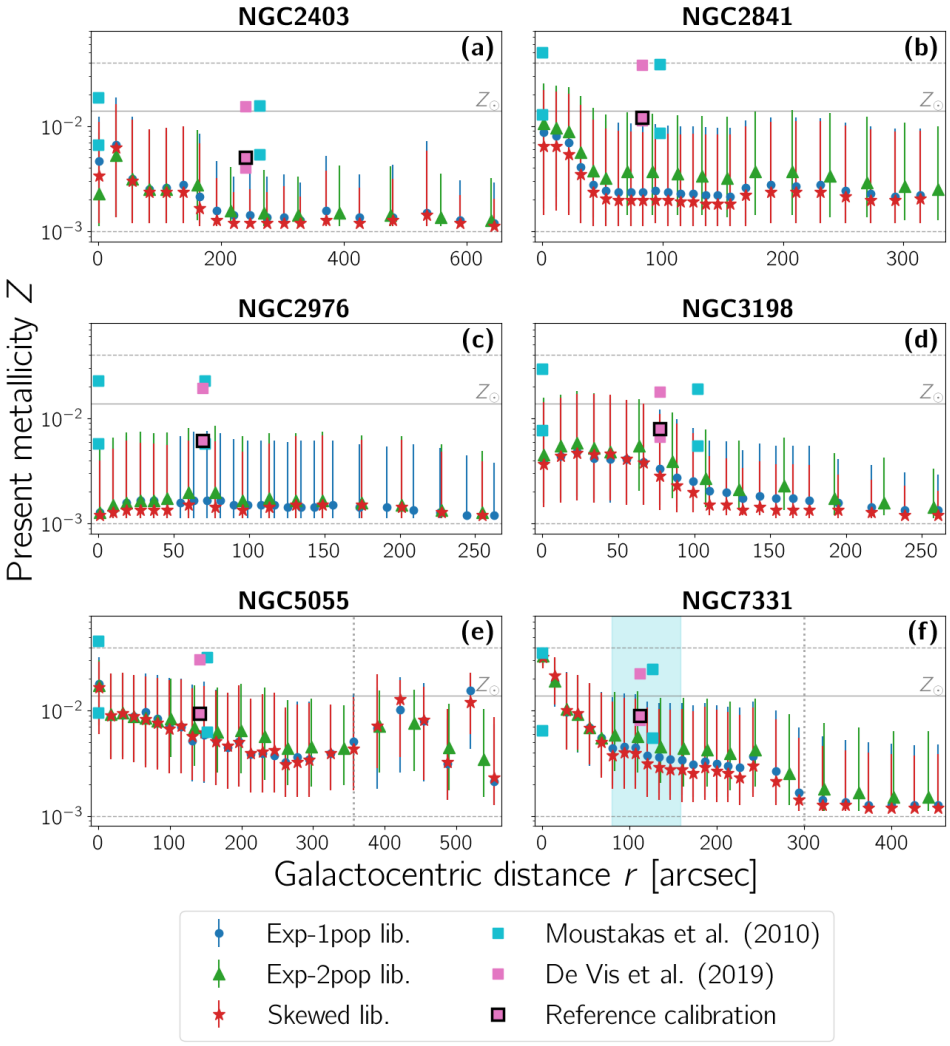

Figure 4.7: Present ISM metallicity profiles (blue, green and red points) of each galaxy in our sample. The range of metallicities accessible through our methodology ($Z \in \{10^{-3}; 4\ 10^{-2}\}$; Maraston 2005) as well as the solar metallicity ($Z_\odot = 0.0139$; Asplund et al. 2021) are respectively represented by the dashed and the solid horizontal lines. Our profiles are compared with independent estimates based on oxygen abundances from strong emission lines observations (cyan and pink squares; resp. Moustakas et al. 2010 and De Vis et al. 2019). Depending on the type of calibration assumed by these methods,

Figure 4.7 (continued): higher (theoretical calib.) and lower (empirical calib.) values are found. The black border square highlights the calibration considered as a reference by De Vis et al. (2019) (the Pilyugin & Grebel 2016 calibration). The vertical dotted lines depict the radial limits outside which the profiles are considered as unreliable. For NGC7331 in panel (f), the cyan region highlights the zone on which Moustakas et al. (2010) estimated the slope of the metallicity profile of the galaxy.

A notable exception exists with the least massive galaxy of our sample, NGC2976. Indeed, its pregalactic gas cloud has a SMD profile slightly below the ones of the very massive NGC7331 and NGC2841 while its star-forming burst(s) have the second smallest amplitudes. This combination makes NGC2976 the least metallic of the sample, its profile being barely higher than our low bound on Z (10^{-3}). Contrary to its SFR or its SFH/ZH parameters profiles, the modification of stellar populations in NGC2976 does not appear in its Z profile. This is consistent with a very recent shutdown ($\lesssim$ 500 Myr) of the star formation in its outskirts, as suggested by Williams et al. (2010). Indeed, as the metallicity profile depends on the total mass of stars formed during the whole life of the galaxy and as the current SFR in the inner half of NGC2976 is not that high, a very recent shutting down of the star-formation in its outskirts should not leave a detectable mark on its present Z profile.

Two steep and large decreases of Z can be observed in the profiles of NGC2841 and of NGC7331. This is due a problem with the prior that we imposed for the M_i parameter during the stellar SED fitting. As explained earlier, the lower limit on this parameter is modified for each model of each library so that it is equal to the total mass of stars formed during the whole life of the galaxy. Nevertheless, when computing this minimum bound, we did not take into account the fact that the stars would eventually release a portion of their initial material into the ISM, allowing other generations to be created from the same initial quantity of gas. This error has significant consequences on the lower bound of the M_i prior which is in fact systematically overestimated. This thus forbids the SED fitting to reach smaller values that would have resulted in higher present metallicities.

A careful inspection of the prior and posterior pdfs of M_i revealed that this effect impacted the fit, and hence the Z computation, of both NGC2841

and NGC7331 (but not of the other galaxies in our sample). The posterior pdfs of these two galaxies are clearly limited by the imposed overestimated prior. For NGC7331, this does not affect all the galaxy but only its outskirts (at distances larger than ∼300 arcsec; at the right of the vertical dotted line on panel (f) of Figure 4.7). We thus discarded this portion of the profile (and of the corresponding stellar mass profile) in our future analyses. For completeness, we will nevertheless still display them in the rest of this chapter. Concerning NGC2841, the effects of the incorrect prior are more global and affect, at least slightly, the SED fittings at all distances. As is, the metallicity profile of this galaxy is thus not reliable and should be recomputed with a corrected M_i prior.

Finally, it can be noted that whatever the library we used, the associated metallicity profiles of the studied galaxies are all compatible with each other. There is nevertheless a systematic trend: the Exp-2pop models give galaxies more metallic than the Exp-1pop ones, both followed by the Skewed models.

Comparison with strong emission lines estimates

To estimate the ISM metallicity of galaxies, the modeling of their stellar photometric SED is not a usual methodology. More commonly, this estimate is performed via observation and comparison between some specific emission lines such as Hα, Hβ or forbidden lines of oxygen or nitrogen. To emit these lines, the ISM gas has to be ionized either by young massive stars or by AGNs. Such types of estimates are thus only possible in certain parts of the galaxies, in their HII regions or in their very center.

Moreover, direct metallicity estimates are often very complicated to perform as the used lines are very faint (Maiolino & Mannucci 2019). Hence, indirect methods requiring calibrations using strong nebular emission lines have been developed. With such methods, a calibration is necessary to derive the metallicity values. Depending on the chosen type of calibration, these values vary strongly. Typically, the theoretical calibrations (based on stellar populations synthesis and photoionisation models) end up with estimates of Z several times higher than the empirical ones (∼4 times higher; Moustakas et al. 2010).

In Figure 4.7, we plotted such estimates of the metallicities of our sample of galaxies (cyan and pink squares; resp. Moustakas et al. 2010 and De

Table 4.4: Galactic present ISM metallicity in oxygen abundance (12+log(O/H)) at the galactocentric distance corresponding to values from De Vis et al. (2019)

Galaxy	De Vis et al. (2019)†	Exp-1pop	Exp-2pop	Skewed
NGC2403	$8.297^{+0.025}_{-0.026}$	$7.73^{+0.65}_{-0.11}$	$7.77^{+0.72}_{-0.12}$	$7.65^{+0.48}_{-0.06}$
NGC2841	$8.695^{+0.036}_{-0.035}$	$7.96^{+1.56}_{-0.24}$	$8.16^{+1.18}_{-0.28}$	$7.87^{+1.58}_{-0.20}$
NGC2976	$8.390^{+0.027}_{-0.027}$	$7.80^{+1.57}_{-0.16}$	$7.86^{+1.47}_{-0.18}$	$7.73^{+1.41}_{-0.11}$
NGC3198	$8.506^{+0.025}_{-0.027}$	$8.11^{+1.21}_{-0.25}$	$8.27^{+0.81}_{-0.28}$	$8.04^{+1.31}_{-0.29}$
NGC5055	$8.581^{+0.054}_{-0.053}$	$8.32^{+1.08}_{-0.28}$	$8.44^{+0.69}_{-0.26}$	$8.37^{+0.83}_{-0.29}$
NGC7331	$8.562^{+0.033}_{-0.031}$	$8.24^{+1.01}_{-0.27}$	$8.36^{+0.77}_{-0.25}$	$8.18^{+1.07}_{-0.24}$

† Values derived from strong emission lines flux measurements assuming the Pilyugin & Grebel (2016) calibration (corresponding to the black border squares in Figure 4.7)

Vis et al. 2019). At each given distance, the lowest estimate corresponds to an empirical calibration and the highest to a theoretical one, illustrating the two possible values of the metallicities and their rough variation across the galaxy. The black border squares represent the calibration of reference recommended by De Vis et al. (2019) (the Pilyugin & Grebel 2016 calibration) because of its high reliability on low-Z galaxies. For quantitative comparison, this reference values are given in Table 4.4 and compared to our Z profiles values at the same galactocentric distance. Here, the metallicity values have been converted into oxygen abundances (12 + log(O/H)), as it is done in works estimating metallicities from strong emission lines. For this conversion, we assumed that all the metals in our galaxies have the same relative abundance as in the Sun (as also done by Maraston (2005) when computing its SPSs) and we fixed the value of the Sun oxygen abundance to 8.69 ± 0.04 (Asplund et al. 2021).

As can be seen in the table, our methodology results in uncertainties higher than the usual observations of strong emission lines. This is expected as the latter method is more direct than ours and as the age/metallicity degeneracy is inevitably associated to any photometric SED modeling. For

all the galaxies, we retrieve Z values that are compatible, given their uncertainties, but systematically lower[5] than the estimates based on empirically calibrated strong emission lines (represented by the lower squares in the figure).

This systematic discrepancy can be explained by the intrinsic differences between the two methods compared here. Indeed, our Z values take into account all the metal content of galaxies while the strong emission lines method is principally based on observations of one atom, the oxygen. Hence, if the proportion of oxygen compared to the other metallic elements is enhanced compared to the solar abundance (taken as reference in this work and in Maraston 2005), the comparison between our Z values and the oxygen abundance of De Vis et al. (2019) could be biased.

Such a situation is common in metal-poor galaxies in which oxygen atoms are overrepresented (e.g. Mateo 1998; Kunth & Östlin 2000; Nomoto et al. 2013). Hence, if such a difference of abundance is not taken into account, methods using characterizations of the whole metal content of these galaxies will give systematically lower estimates compared to metallicity values derived from oxygen emission lines. Moreover, the metallicity determinations from strong emission lines methods are based on individual measures in the zones of the galaxies where the gas is ionized. Recent and on-going star formation[6] is thus necessary, increasing locally the oxygen content (due to type II supernovae explosions; Peeples et al. 2014; Cimatti et al. 2020) and the corresponding metallicity estimates.

Both these effects could explain the discrepancy observed between our metallicity values, Z being converted into $12 + \log(\mathrm{O/H})$ values without taking into account the potential modification of relative abundance, and the ones from De Vis et al. (2019) and Moustakas et al. (2010).

[5]For NGC2841, the discrepancy is larger than for the other galaxies of our sample. Indeed, its strong emission lines metallicity qualifies it as the most metallic spiral while our Z values, at the galactocentric distance considered here, are comparable to the ones of the quasi-dwarf metal-poor NGC2976. This contradictory situation is explained by the incorrect M_i prior imposed during the SED fitting. When our Z determinations are performed, the correction of this prior should thus give back to NGC2841 its rank of highly metallic galaxy.

[6]The presence of a neighboring AGN is also a source of possible ionization but such regions are less used than HII regions in the metallicity determinations (Moustakas et al. 2010; De Vis et al. 2019).

Radial evolution of metallicity

An important feature of our methodology is that it naturally produces profiles of metallicity. While such profiles are of extreme importance to constrain the models of galaxy evolution, they are not easily derived from the strong emission lines method. Indeed, in this case, it is necessary to have observations of many HII (or AGN ionized) regions distributed in a large enough fraction of the galactic disk (Zaritsky et al. 1994; Dutil & Roy 2001). For example, in Moustakas et al. (2010) work, this constraint divided the number of analyzable galaxies by a factor of 3. Moreover, such works usually model the radial metallicity profiles as simple analytical functions (i.e. decreasing exponentials for Z or straight lines for oxygen abundances) despite the evidence of strong dependency of the ISM metallicity with local conditions (see Maiolino & Mannucci 2019 and references within). On the contrary, our methodology and its individual modelings at each galactocentric distance does not have such constraint and thus give more realistic profiles.

Comparing the global decrease of our profiles with the ones derived by Moustakas et al. (2010), we find very good agreements. Despite having lower absolute values, our metallicities evolve similarly within the galaxies. This can be visualized in Figure 4.8. The slopes of the oxygen abundance profiles of Moustakas et al. (2010) (with the empirical[7] calibration of Pilyugin & Thuan 2005) are given in ordinate and are compared to the slopes of the linear regressions fitted on our profiles (the three libraries results are shown with three different symbols). As NGC2976 had not enough regions for which the metallicity could be measured through the strong line method, its radial Z profile has not been computed by Moustakas et al. (2010) and thus does not appear in the figure.

For three galaxies (NGC2403 in purple, NGC2841 in blue and NGC3198 in yellow), our profiles' slopes are perfectly compatible with the ones from Moustakas et al. (2010). For the other two galaxies, we have either very steep (NGC7331 in red) or very shallow (NGC5055 in orange) profiles.

In NGC7331, our very negative slope values are principally due to the steep decrease of metallicity in the center of the galaxy (which corresponds to the zone impacted by the presence of the central LINER). The differ-

[7]We compare our metallicity gradients with the results from this calibration as our absolute values are closer to this calibration results than to the theoretical ones.

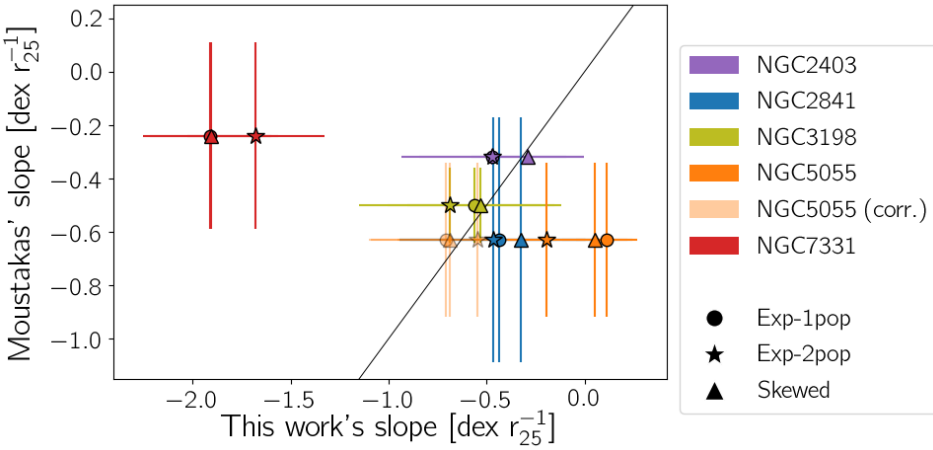

Figure 4.8: Comparison between the slopes of the metallicity profiles from Moustakas et al. (2010) (empirical calibration of Pilyugin & Thuan 2005) and the ones of our profiles for the galaxies studied in both works. All the slopes have been computed on oxygen abundances profiles (12+log(O/H)), normalized in radius by the r_{25} values from Moustakas et al. (2010). For NGC5055, we show the profile slopes computed on the whole profile (dark orange) and on the corrected profile (light orange) after exclusion of the unreliable outskirts regions (at the right of the dotted vertical lines in panel (e) of Figure 4.7). For NGC7331 (red), the unreliable portions of the profiles have also been excluded.

ence between our slope values and the one from Moustakas et al. (2010) can be explained by the regions of the galaxy on which these slopes have been evaluated. Indeed, the HII regions used by Moustakas et al. (2010) were all localized in a very restricted zone of the galaxy (between 79 and 158 arcsec; highlighted in cyan on panel (f) of Figure 4.7). The profile of NGC7331 being locally shallower in this zone, this explains the discrepancy between Moustakas et al. (2010) value and ours. Using complete profiles of metallicity, as provided by our methodology, is thus extremely important in such case, the spatially restricted measures biasing the results of strong emission lines methods.

For NGC5055, our slope values are impacted by the metallicities in the outskirts of the galaxy (at galactocentric distances larger than ∼354 arcsec; at the right of the vertical dotted line in panel (e) of Figure 4.7). Indeed,

when performing a linear regression on the profiles of NGC5055 while excluding these regions, we found slopes values (in light orange on Figure 4.8) completely in agreement with the independent estimates of Moustakas et al. (2010). This suggests that the important variations of Z far from the center of this galaxy are artifacts rather than real physical variations. After a visual inspection of the images of this galaxy, it appears that these variations are in fact due to our preprocessing of the SDSS-u and SDSS-i images. As explained in Section 2.3.2.2 on page 52, these two images are both strongly impacted by an artifact associated to the presence of a saturated star close to the line-of-sight of the galaxy (visible in the inset in panel (e) of Figure 2.1 on page 44). Hence, to clean from this artifact, we decided to erase the impacted pixels. However, the non-physical variations of the Z profile (when $r \gtrsim 354$ arcsec) appear when these cleaned pixels (and the ones nearby) are considered in the elliptical masks to compute the surface brightness profiles. Another cleaning procedure should thus be implemented to correct from this artifact in a future work. For now, our SED modelings of NGC5055 in these regions will be considered as unreliable and will not be used for the RC analysis of Chapter 6. As for NGC7331 previously, the profiles of this galaxy will not be truncated in its outskirts and the limit of $\sim$354 arcsec (corresponding to its r_{25} value) will be depicted as a vertical dotted line in all the subsequent figures of the rest of this chapter.

Considerations on future use of metallicity profiles

The agreement between the general evolution of our metallicity profiles and the one derived by the strong emission lines method goes along with the idea that the discrepancy between our values and the independent ones could only be due to a conversion that does not take into account the abundance specificities of the galaxies.

When using the metallicity profiles produced by our methodology to compute other quantities through relations that have been calibrated on metallicity estimates from strong emission lines methods, an empirical correction can be implemented. A simple rescaling of our Z profiles is sufficient, in order to match the absolute values given by strong emission lines methods. To match the reference calibration values (of Pilyugin & Grebel (2016), as recommended by De Vis et al. 2019), our profiles have to be multiplied by factors from 1.4 to 4.3 for all the galaxies except for NGC2841

and its prior problem (factors of 3 to 6, depending on the library).

4.1.6 Mass profiles

Once the SFH of a galaxy is known, the associated stellar mass at the moment of the observation $M_*(t_0)$ can be evaluated. Mathematically, this is given by

$$M_*(t_0) = \int_{t'=0}^{t'=t_0} \mathrm{SFR}(t_0 - t')\ M_{*,\mathrm{SSP}}\left(t', Z(t_0 - t')\right) dt'$$

where, as for the CSP definition (Equation 4.1), t_0 corresponds to the current age of the galaxy and t' to the age of the stellar populations. $M_{*,\mathrm{SSP}}$ represents the proportion of the initial mass of the stellar population of age t' and metallicity $Z(t_0 - t')$ that has not been reinjected into the ISM by stars explosions and that is thus currently locked into stellar remnants. These remnant mass values have been determined by Maraston (2005) for each SSP and they are based on a relation between the initial and the remnant stellar masses from Renzini & Ciotti (1993).

Computing the posterior pdfs and extracting our stellar mass values and associated error bars from them, we ended up with profiles of the stellar surface mass density (SMD) as a function of the galactocentric distance for each galaxy in our sample and for each of the SFH/ZH parametrizations studied in this work. These profiles are shown in Figure 4.9. By integrating them up to galactocentric distances equal to 1.5 r_{25} (1.0 r_{25} for NGC5055 and NGC7331), we also computed the total stellar mass of each galaxy, given in Table 4.5.

Both the table and the figure show that for every library, the resulting mass distributions within the galaxy as well as the total mass are equivalent. This is even true for the models that have been shown to produce non-realistic estimates of other galactic physical quantities (the Skewed models for the present SFR). Hence, the modeling of the stellar SED is very robust when used to estimate the stellar mass of the galaxy, whatever the assumed star-forming burst(s) parametrization. In the next chapters of this work, we will thus only present the results based on one of these libraries, the Exp-1pop one.

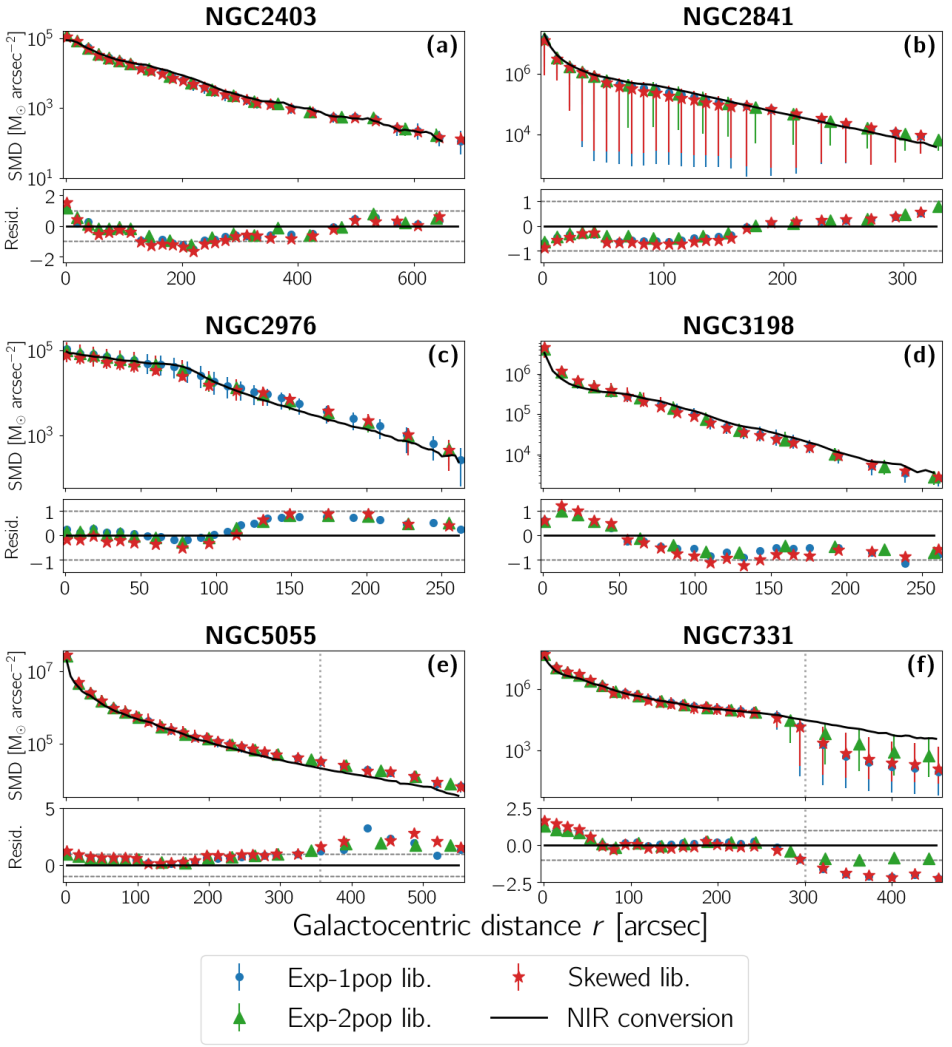

Figure 4.9: Stellar SMD profiles of each galaxy in our sample. The profiles resulting from our SED modeling (colored points) are compared with the one obtained from the simple conversion of NIR luminosity profiles (3.6 μm profiles, assuming a constant stellar mass-to-light ratio of 0.5, as recommended by Lelli et al. (2016a); black line). The "Residuals" panels are given by the difference between our profiles and the NIR ones, divided by the error bars associated to our profiles. The dashed horizontal lines thus correspond to deviations of 1σ

Figure 4.9 (continued): between our SED modeling profiles and the NIR converted one. The vertical dotted lines depict the radial limits outside which the profiles are considered as unreliable.

Table 4.5: Logarithm of the total[†] stellar mass ($\log(M_*)$; expressed in $M_\odot$) of all the galaxies in our sample

	From 3.6 μm lum. prof.		From stellar SED mod.		
Galaxy	Leroy et al. (2008)	First est.[‡]	Exp-1pop	Exp-2pop	Skewed
NGC2403	9.7	$9.61^{+0.09}_{-0.11}$	$9.56^{+0.10}_{-0.13}$	$9.57^{+0.12}_{-0.12}$	$9.54^{+0.11}_{-0.07}$
NGC2841	10.8	$10.68^{+0.11}_{-0.14}$	$10.60^{+0.17}_{-1.40}$	$10.61^{+0.20}_{-0.91}$	$10.56^{+0.22}_{-1.38}$
NGC2976	9.1	$9.28^{+0.09}_{-0.11}$	$9.33^{+0.19}_{-0.28}$	$9.31^{+0.18}_{-0.25}$	$9.23^{+0.28}_{-0.18}$
NGC3198	10.1	$10.13^{+0.11}_{-0.15}$	$10.12^{+0.15}_{-0.16}$	$10.13^{+0.15}_{-0.16}$	$10.11^{+0.16}_{-0.12}$
NGC5055	10.8	$10.92^{+0.08}_{-0.10}$	$10.96^{+0.13}_{-0.14}$	$10.97^{+0.12}_{-0.14}$	$10.97^{+0.15}_{-0.12}$
NGC7331	10.9	$11.01^{+0.11}_{-0.15}$	$11.08^{+0.17}_{-0.24}$	$11.08^{+0.17}_{-0.23}$	$11.07^{+0.20}_{-0.20}$

[†] Resulting from the integration of the stellar SMD profiles of Figure 4.9 up to a galactocentric distance of 1.5 r_{25} (1.0 r_{25} for NGC5055 and NGC7331)

[‡] Our first estimates of the total stellar masses have been obtained from the conversion of their 3.6 μm luminosity profiles, assuming a constant mass-to-light ratio of 0.5±0.1 (Lelli et al. 2016a). They have been used to determine the category of the dust attenuation curve to use to correct the observed SEDs (as explained in Section 3.2.2.2).

4.2 Comparison with NIR stellar modeling

RC studies usually model the stellar component of the galaxies via a simple methodology consisting in using a single image and assuming a mass-to-light ratio value to convert the observed luminosity into stellar mass. For that, NIR images (and particularly 3.6 μm ones) are well-suited as the ratios associated to these wavelengths are known to vary less than in other spectral domains with respect to the age or to the metallicity of stars populations. Hence, this ratio is often taken as constant across the galaxy and even as independent from one galaxy to another. As explained in details in Section 1.3.1.2, its value is estimated from different independent observations (models of stellar populations, observations of resolved stars, analyses of galaxy kinematics...). This stellar modeling is thus subject to three main assumptions: (i) the mass of stars in a galaxy is well described by its luminosity in only one NIR band, (ii) the ratio to transform this NIR luminosity into mass does not change with the position within the galaxy and, (iii) its value is the same whatever the galaxy (and equal to 0.5 ± 0.1; Lelli et al. 2016a).

With the global stellar SED modeling performed in this work, we are able to test all these hypotheses and to quantify the associated biases on the resulting stellar mass distributions as well as their impacts on the galactic RC and DM content. Indeed, by using the FUV-to-NIR photometric SED of a galaxy, we can model its all-age stellar populations while the NIR conversion neglect the young massive populations. Admittedly this portion is not significant when considered in mass terms but still this simple methodology is missing a whole part of the stars present in the galaxies. Moreover, the product of our modeling (the stellar mass profiles) can be used to evaluate the mass-to-light ratios in the 3.6 μm band of each galaxy and thus to assess the validity of the simplifying approximations usually performed in RC studies concerning these ratios.

4.2.1 Stellar mass profiles

In Figure 4.9, we show a direct comparison of the mass profiles resulting from both our SED modeling (colored points) and from the conversion of 3.6 μm luminosity profiles, assuming a constant stellar mass-to-light ratio of 0.5 (black line; Lelli et al. 2016a). The comparison is made easier through the "Residuals" panels. These are created by computing the difference

between each of our profiles and the NIR one and by dividing this difference by the error bars associated to our profiles. The ordinate of each colored point is thus expressed in error bar units, the two dashed horizontal lines indicating the location of the points distant from the NIR profile by exactly 1σ.

Only for two galaxies in our sample (NGC5055 and NGC7331), we found differences larger than 1σ between the profiles derived by the two methodologies. These differences are always located in the outskirts of the galaxies, in zones where the profiles have been characterized as unreliable for both galaxies. The important discrepancies between our profiles and the NIR ones in the outskirts of these galaxies should thus not be considered.

Discarding these two outskirts profiles, nearly all our points are located between the two horizontal 1σ limits, indicating that the usually used and very simple NIR luminosity-to-mass conversion is a very good approximation of the stellar mass distributions. This is also visible in Table 4.5 where the total mass values never differ by more than 0.75σ from one methodology to the other. Hence, we confirm that the massive stars in the young stellar populations, neglected by the NIR methodology but modeled by ours, do not contribute significantly to the mass of the galaxies and the use of only one NIR band to evaluate the total mass of stars in the galaxy does not bias the results.

Nevertheless, a few features should be noticed. First of all, even if we only focus on the inner regions of NGC5055, we can clearly see that there is a global vertical shift between the profiles: the 3.6 μm luminosity of NGC5055 systematically predicts masses lower than the ones derived from our SED modelings. Secondly, the global slope of the profiles in the outskirts of the galaxies, are slightly different. These differences are particularly visible for NGC2841, NGC2976 or NGC5055 (even before the discarded regions). Finally, small systematic differences between the profiles also exist in the central regions of the galaxies. This could have non-negligible consequences on the RC and DM content as these regions are particularly important to characterize the shape of the DM halo (e.g. Portinari & Salucci 2010; Frank et al. 2016; Katz et al. 2017; Korsaga et al. 2018). In Chapter 6, we will thus evaluate the significance of the impact of these *a priori* slight variations of the stellar mass distributions on the RCs of our galaxies.

4.2.2 Mass-to-light ratios in the 3.6 μm band

From our stellar SMD and our 3.6 μm surface brightness profiles, we can compute the mass-to-light ratios in that band. To express them in solar units, we derived the luminosity $L_{\odot}^{3.6\mu m}$ from the zero magnitude flux of the 3.6 μm band ($F_0^{3.6\mu m} = 280.9 \pm 4.1$ Jy; IRAC Instrument Handbook 2021) and from the absolute magnitude of the Sun in this band ($M_{\odot}^{3.6\mu m} = 3.24$; Oh et al. 2008), finding a value of 1.69 10^{18} erg s^{-1} Hz^{-1}.

Our $\Upsilon_*^{3.6\mu m}$ profiles are shown in Figure 4.10 (colored points). Their radial variations indicate modifications of the stellar populations such as the one in NGC2976 that we already described several times. In the centers of NGC3198, NGC5055, NGC7331 or (to a lesser extend) NGC2403, we can also see the increase of the ratio due to the presence of the galactic bulge composed of older stellar populations. These radial variations are slight, as expected from the NIR domain used to compute them (such variations would be significantly more important in the optical; e.g. Meidt et al. 2014; Norris et al. 2014; Korsaga et al. 2019).

All our profiles are compatible with a constant mass-to-light ratio across the whole galaxy and with the recommended value of 0.5±0.1 (Lelli et al. 2016a), represented with the solid black line and the associated shaded regions. For a quantitative comparison, the averages and standard deviations associated to each of our profiles are given in corresponding colors at the top of each panel. One may note that, as expected from the analysis of the stellar SMD profiles, the ratio profiles of NGC5055 (panel (e) of the figure) are higher than the 0.5 value (even when the outskirts regions of this galaxies are excluded as recommended; values in lighter colors in panel (e) of the figure). For this particular galaxy, the 3.6 μm mass-to-light ratio used when computing stellar mass profiles directly from NIR images thus has to be slightly increased compared to the 0.5 value recommended by Lelli et al. (2016a).

We also compare our results with profiles from de Blok et al. (2008), computed from the NIR J-K color profiles of each galaxy. These color values are converted into 3.6 μm mass-to-light ratios following empirical relations derived from synthetic stellar populations by Bell & de Jong (2001) and Oh et al. (2008). These profiles are schematically[8] represented in dashed black lines on Figure 4.10. As can be seen, some of their $\Upsilon_*^{3.6\mu m}$ values are

[8]The exact profiles can be found in the figures 24, 27, 32, 36, 47 and 51 of de Blok et al. (2008).

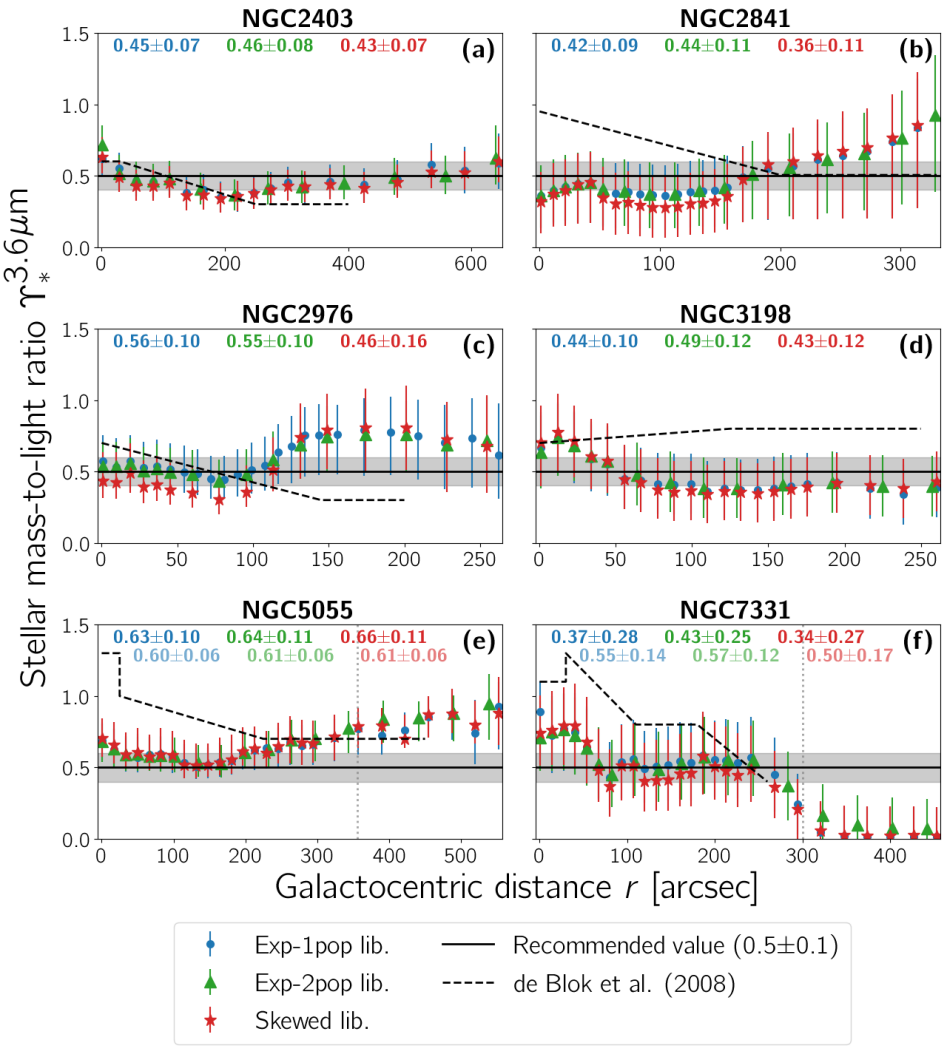

Figure 4.10: Stellar mass-to-light ratios in the 3.6 μm band of each galaxy in our sample. The profiles computed by our SED modelings (colored points) are compared with profiles from de Blok et al. (2008) (derived from NIR *J-K* color; black dashed lines) and from the recommended value when converting stellar masses from 3.6 μm luminosity profiles (0.5±0.1; Lelli et al. (2016a); solid black lines and associated shaded regions). The mean values of our profiles are written in corresponding colors at the top of each panel. For NGC5055 and NGC7331, the mean values excluding the unreliable points of profiles (at the right of the dotted vertical lines) are also given beneath, in lighter colors.

relatively high, particularly at the center of the galaxies where they can reach values larger than 1, and they vary greatly within the galaxy. These results encouraged the idea that drove the present work: to allow for the possibility of more complex modelings of the stellar component and avoid the simplifying hypotheses concerning the mass-to-light ratios underlying the usual NIR conversion. Nevertheless, as can be seen in the figure, with a global modeling of the stellar component rather than with empirical color relations, we do not reproduce at all de Blok et al. (2008) profiles, either in terms of absolute value or of variation across the galactic disk. The only two galaxies for which our profiles give consistent descriptions are NGC2403 and NGC7331 (but with an offset).

Consequently, if de Blok et al. (2008) results were a hint towards the necessity to develop stellar mass modeling with more freedom in the luminosity-to-mass conversion, our computations using global SED modelings do not go into that direction. Rather, they confirm the pertinence and the correctness of using constant mass-to-light ratios with the recommended value of 0.5. The validity of the empirical relations used by de Blok et al. (2008) should thus be called into question, as already pointed out by de Denus-Baillargeon et al. (2013).

4.3 Conclusion

At this point, we have developed a methodology to model the stellar content of spiral galaxies by reproducing their FUV-to-NIR photometric SEDs. This provides a general description of this component and of its evolution with cosmic time. Along the way, we derived very interesting byproducts and retrieved information about the dust component[9] of the galaxy, its present SFR as well as its metallicity profile (which will be useful when estimating the mass of molecular gas, as will be done in Section 5.1.2.2).

For RC studies, however, the only interesting physical quantity related to the stellar components of galaxies is their mass distributions. In this context, we have shown that the usual NIR conversion provides very good estimates of the stellar mass distributions within the galaxies. We thus confirmed the correctness of this simple method. The stellar SED modeling

[9]Technically, this is obtained not by the SED modeling itself but by the mandatory step occurring before it, a step that allows the stellar and the dust emissions to be disentangle.

developed and performed here improves this approximation but at first sight, it does not seem to balance the inherent complexity and uncertainties it brings.

Nevertheless, the effects of these two different stellar modelings on the RCs of galaxies still have to be investigated. Indeed, despite their small amplitudes, the observed differences between the two stellar mass profiles could impact significantly the DM characterization, particularly at the center of the galaxies where the baryonic matter distribution has to be accurately determined to distinguish between cored and cuspy halos (Portinari & Salucci 2010). This will thus be studied in Chapter 6, where the RCs expected from the modelings of all the luminous components of our galaxies will be computed and compared to the observed ones. However, before this final analysis, the mass distributions of the other two luminous components have still to be determined.

Chapter 5

Dust, gas and 3D distributions
Final stages of the luminous mass modelings

Having modeled the stellar content of spiral galaxies in the previous chapter, we are now left with the other two luminous components: dust and gas. Additionally, the galaxies themselves have to be modeled as 3D objects in hydrostatic equilibrium in order to compute their RCs as accurately as possible. During this whole process, we get rid of some widely used assumptions to analyze their impacts on the global modeling of galaxies and on the discrepancy between their predicted and observed RCs. This way, our methodology estimates the usually neglected molecular gas of spiral galaxies, systematically decomposes their stellar content into two dynamical structures (a bulge and a disk) and allows the gaseous components to be distributed out of the galactic plane.

In this chapter, we thus describe the final modelings before the RC derivation. In Section 5.1, we finalize the estimates of the projected mass profiles of the galaxies in our sample, by computing the SMD profiles of their last two luminous components. We then decompose, in Section 5.2, their stellar content into two structures with different out-of-plane distributions before performing a complete 3D modeling of the galaxies in Section 5.3.

5.1 Final modeling of the luminous components

5.1.1 Dust component

From the fits of MBB spectra performed in Section 3.2.2.1 to correct the galactic SEDs from the effect of their dust component, we can determine the total mass of the latter. Indeed, the dust SMD profile $\Sigma_{d,\nu}$ for a given FIR/sub-mm band is given by (e.g. Berta et al. 2016)

$$\Sigma_{d,\nu}(r) = \frac{I_\nu(r)\ D^2}{B_\nu(T_d(r))\ \kappa_\nu}$$

where I_ν is the surface brightness associated to the band and D is the distance of the galaxy. B_ν is the Planck function (parametrized with the dust temperature T_d previously fitted) convolved with the band associated transmission curve. The κ_ν term represents the absorption cross-section of dust per unit of mass at the frequency ν. Its evolution with the frequency is well approximated by a power law

$$\kappa_\nu = \kappa_0 \left(\frac{\nu}{\nu_0}\right)^\alpha$$

where the normalization constant κ_0 and the spectral index α values depend on the modeling of the dust grain populations within the galaxy.

As dust absorption and emission are the two faces of the same coin, the two spectral indexes used in this work (α for the absorption and β for the emission; see Section 3.2.2.1) are in fact equal to each other. As pointed out by Bianchi (2013), this equality is particularly important to take into account as inconsistent assumptions of the spectral indexes lead to underestimations of dust masses up to a factor 2–4 (e.g. Regan et al. 2004; Magdis et al. 2012; Dale et al. 2012; Magnelli et al. 2012). At first, these underestimations were wrongly attributed to the simplicity of the single-temperature MBB approach, that was viewed as unable to reproduce the complex landscape of dust temperatures. However, with consistent assumptions on the spectral indexes, the MBB methodology has been proved to perform equally well than more complex models such as Dale & Helou (2002) or Draine & Li (2007), both modeling the dust spatial distributions along with the radiation field of the galaxy. The dust masses derived by these two kinds of method, using consistent values of the spectral indexes for the MBB approach, are shown to be in good agreement, especially for

the spiral galaxies that are the subject of this work (see Magrini et al. 2011; Berta et al. 2016; Nersesian et al. 2019, for examples). This robustness of the dust mass estimate thus also explains why we chose to implement this simple one-temperature MBB approach when modeling the galactic dust content in Section 3.2.2.1.

To evaluate the absorption cross-sections κ_ν, we used a model of dust populations in the MW. Indeed, the final dust mass determination is relatively independent from the detailed composition of modeled grain populations (Draine et al. 2007). This model has been computed by Draine (2003) and gives $\kappa_0 = 27.1$ cm^2 g^{-1} at a frequency $\nu_0 = 3\ 10^{12}$ Hz (or $\lambda_0 = 100\ \mu$m) and a value of $\alpha = 2.08$ (that thus fixed the β value used in Section 3.2.2.1) (Draine 2003; Bianchi 2013). We then calculated, for each galactocentric distance of each galaxy, the mean value of the SMDs $\Sigma_{d,\nu}$ of the 5 FIR/sub-mm bands at our disposal (i.e. with wavelengths larger than 100 μm).

The resulting dust SMD profiles of all the galaxies in our sample are depicted with red squares in Figure 5.2 (on page 135) which shows the SMD profiles of all the galactic luminous components. The corresponding total mass values can be found in Table 5.1 (on page 136).

We can compare these results with the ones from Nersesian et al. (2019) which modeled the galactic dust using two methodologies: (i) a single fit of MBB spectra on FIR and sub-mm emissions of galaxies (as the one performed in this work) and (ii) a global modeling of the FUV-to-sub-mm SEDs of the galaxies via the use of the fitting code CIGALE (Noll et al. 2009; Boquien et al. 2019) assuming different state-of-the-art models of dust grains. Comparing our values of total dust mass with theirs, we found that their MBB values are systematically lower than ours. This is expected as we assumed dust grain models with different spectral indexes β. This is in fact the same phenomenon as the one observed when comparing the dust temperatures of our MBBs in Section 3.2.2.1. However, when computed with CIGALE while assuming a dust model by Draine et al. (2014) (which is an updated version of the models by Draine (2003) used in this work), the Nersesian et al. (2019) values and ours are compatible. This confirms the results from Bianchi (2013): a particular attention has to be drawn towards the choice of the spectral indexes α and β. If their values are consistent during the whole modeling, the resulting computation of dust mass is very robust independently from the methodology (simple MBB or complex global SED fitting).

5.1.2 Gaseous components

Of all the luminous components of a galaxy, the gaseous ones are the easiest to model thanks to their specific emission lines. Hence, with a single image of the galaxy, the luminosity of its gas content can be directly converted in mass values.

More precisely, as explained when describing the images used in this work in Section 2.4, the images probing the gaseous content of a galaxy are in fact velocity-integrated, or moment 1, maps. Created to cancel the Doppler effect associated to the rotation of the galaxy itself, these maps gather the emission of all the gas of the galaxy in a single image. From such images, the velocity-integrated surface brightness profiles of galaxies can be obtained through the azimuthal averaging process described in Section 3.1. Afterwards, the mass profiles of hydrogen-only gas are derivable via luminosity-to-mass conversion factors specific to each type of gas (atomic or molecular). A multiplication by a factor 1.4, to take into account the mass of helium and metals synthesized during primordial nucleosynthesis (e.g. Aver et al. 2015; Planck Collaboration 2020), then allows to compute the mass distributions of atomic and molecular gases in galaxies.

5.1.2.1 Atomic hydrogen

The derivation of the atomic hydrogen SMD $\Sigma_{\rm HI}$ from the velocity-integrated profile $I_{\rm int,HI}$ of a galaxy is given by

$$\Sigma_{\rm HI}(r) = 2.36\ 10^5\ D^2\ I_{\rm int,HI}(r)$$

where the multiplicative factor is given for values of $I_{\rm int,HI}$ in Jy arcsec^{-2} km s^{-1} and of the galaxy's distance D in Mpc. The resulting $\Sigma_{\rm HI}$ values are then expressed in M$_\odot$ arcsec^{-2} (see for example Walter et al. 2008; Casasola et al. 2020).

This relation is only valid if we assume an optically thin medium. For atomic hydrogen, it is a good approximation up to column densities of a few 10^{21} cm^{-2} (Cimatti et al. 2020), extreme conditions that can be found in highly inclined galaxies. Estimates on large samples of galaxies showed that ignoring the self-absorption by atomic hydrogen can lead to underestimate the total mass of this gas by 10 to 20 % (Zwaan et al. 1997). To estimate the quantity of self-absorption in an individual galaxy, we computed the correcting factor $f_{\rm HI}$ by which the mass profile has to be multiplied to

recover the genuine profile. This factor has been found to depend on the inclination i of the studied galaxy and to be given by $f_{\rm HI} = (\cos i)^{-e}$ where the exponent e depends on the Hubble type of the studied galaxy ($e = 0.04$ for Sa galaxies, 0.16 for Sb, 0.14 for Sbc-Sc and 0 for all other types; Haynes & Giovanelli 1984). Hence, for our sample of galaxies, this self-absorption correction increases the mass profiles by 8 to 25 %.

As for the dust component, the atomic gas SMD profiles of the galaxies in our sample are shown in Figure 5.2 (on page 135; dark green upward triangles) and the associated total masses are given in Table 5.1 (on page 136). With no surprise, these masses are in agreement with estimates of previous studies (Walter et al. 2008; Leroy et al. 2008; Casasola et al. 2020, to cite a few works on large samples of galaxies). A direct comparison can be realized with the results from Leroy et al. (2008) whose values are given in Table 2.1 (on page 42) of the present work.

5.1.2.2 Molecular hydrogen

For the molecular hydrogen, the conversion from the galactic velocity-integrated CO (J=2→1) luminosity profile $I_{\rm int,CO21}$ (given in Jy arcsec^{-2} km s^{-1}) into the H_2 SMD profile Σ_{H_2} (in $M_\odot$ arcsec^{-2}) requires the evaluation of additional factors as

$$\Sigma_{H_2}(r) = 9.94\ 10^{-17}\ D^2\ X_{\rm CO}\ \frac{I_{\rm int,CO21}(r)}{R_{21}}$$

where the multiplicative factor is also valid if the distance D of the galaxy is expressed in Mpc.

In this equation, $X_{\rm CO}$ is the conversion factor between the velocity-integrated CO (J=1→0) brightness temperature and the column density of H_2. Contrary to atomic hydrogen, CO gas is optically thick (except in very low density environments). The transformation from luminosity to mass profiles is thus not as direct as for the 21 cm emission line as the received CO light only comes from the exteriors (as opposed to the totality) of the molecular clouds. Hence, the $X_{\rm CO}$ factor cannot be theoretically calculated but has to be empirically determined. For normal spiral galaxies, the assumed $X_{\rm CO}$ value is generally the one estimated in the solar neighborhood, $X_{\rm CO,\odot} = 2\ 10^{20}$ cm^{-2} (K km s^{-1})$^{-1}$ with a factor 2 of uncertainty (Bolatto et al. 2013).

Finally, the last factor in the equation, R_{21}, allows to convert profiles associated to the J=2→1 line (used in this work) into profiles associated

to the J=1→0 line for which the $X_{\rm CO}$ factor is estimated. We adopted here a value $R_{21} = I_{\rm int,\,CO21} \,/\, I_{\rm int,\,CO10} = 0.7$, as recommended[1] by the HERACLES team at the origin of the images used in this work (Leroy et al. 2009, 2013).

Recently, observations and theoretical models showed that $X_{\rm CO}$ depends on various parameters and particularly on the metallicity and on the dust quantity within the galaxy (see references within Amorín et al. 2016 or Accurso et al. 2017). Indeed, dust has a high impact on the relative abundance of CO and H_2 molecules as (i) H_2 molecules are created at the surface of dust grains and (ii) dust grains prevent the destruction of the CO molecules by the FUV radiations, which have weak shelf-shielding compared to the H_2 ones (Bolatto et al. 2013). Hence, in low metallicity (thus low dust) environments, the clouds of molecular hydrogen are associated to lower quantities of CO, leading to increases of the $X_{\rm CO}$ factor.

Thanks to the stellar SED modeling developed in Chapter 4, we have access to the radial evolution of the ISM metallicity of all the galaxies in our sample. We thus used these profiles to more accurately estimate the conversion factor $X_{\rm CO}$ across the galaxies through the relation determined by Amorín et al. (2016):

$$X_{\rm CO}(Z) = X_{\rm CO,\odot} \left(\frac{Z}{Z_\odot} \right)^{-\gamma} \tag{5.1}$$

where $\gamma = 1.5 \pm 0.3$. Evaluated on blue compact dwarf galaxies, this relation is nevertheless is consistent with measurements in more massive local galaxies (Leroy et al. 2011; Genzel et al. 2012) and with model predictions (Wolfire et al. 2010; Sandstrom et al. 2013).

Effect of a metallicity-dependent $X_{\rm CO}$

The resulting SMDs of molecular hydrogen of the galaxies in our sample are shown in Figure 5.1. On this figure, the profiles obtained with a metallicity-dependent $X_{\rm CO}$ factor (blue dots and green triangles) are compared with the profile resulting from the assumption that this conversion

[1] This value slightly differs from the value of 0.8 originally published by Leroy et al. (2009). This is due to the fact that the main beam efficiency of the IRAM 30-m telescope used to create the HERACLES maps has been revised by Leroy et al. (2013).

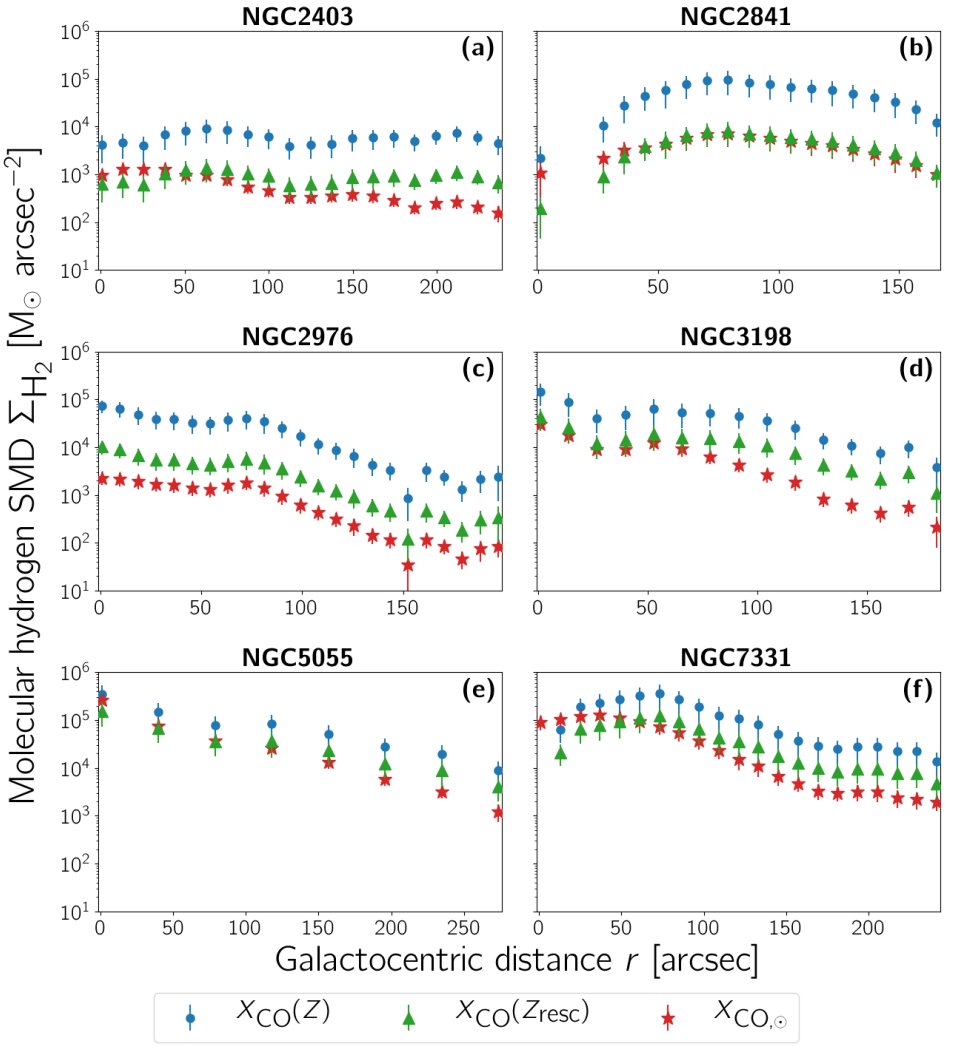

Figure 5.1: Molecular hydrogen SMD profiles of all the galaxies in our sample. Different assumptions on the conversion factor X_{CO} have been realized with either a constant value ($X_{CO,\odot}$; red stars) or a value following the metallicity evolution within the galaxy. To do so, the metallicity profiles from the stellar SED modelings of Chapter 4 (for the Exp-1pop library) have been used: (i) the Z profiles directly retrieved from the modelings (resulting in the profiles shown with blue dots) or (ii) the profiles rescaled to match strong emission lines estimates of metallicities (green triangles).

factor is constant over the whole galaxy and that its value is equal to the one estimated in the solar neighborhood, $X_{\mathrm{CO},\odot}$ (red stars).

As explained in Section 4.1.5.2, the Z profiles provided by the stellar SED modeling developed in this work give galactic metallicity values lower than strong emission lines estimates. When using our metallicity determinations with relations that have been calibrated on strong emission lines estimates (as it has been done by Amorín et al. (2016) for the relation 5.1 we use in this work), we advised to rescale our results in order to match the independent Z measurements by De Vis et al. (2019). Figure 5.1 displays the effects on the final H_2 mass profiles of using the original Z profiles (blue dots) or the rescaled ones (green triangles). The lower the metallicity, the higher the conversion factor X_{CO} and hence, the more massive the molecular gas component. This can also be seen when comparing the last two columns of Table 5.1 (on page 136).

For all except two galaxies in our sample (NGC2403 and NGC3198), using directly our Z profiles results in galaxies whose gas mass budgets are dominated by their molecular component. For this kind of galaxies, this situation is unlikely. If such a mass budget is frequently observed in the central regions of spiral galaxies (for galactocentric distances smaller than their characteristic radius r_{25}; Casasola et al. 2020), it does not hold anymore if we compute the whole content of the galaxy. Indeed, while the molecular gas is very localized in the central regions of spiral galaxies (in the visible disks and in their spiral arms), the atomic gas radially extends way beyond these regions. This can be visualized in Figure 5.2 where the stellar (blue dots), atomic gas (dark green upward triangles) and molecular gas (light green downward triangles) SMD profiles are compared. Hence, even if the gas mass budget of the galaxy is dominated by its molecular form in the inner regions, the balance will eventually fall towards the side of the atomic one if the total masses are evaluated (e.g. Catinella et al. 2018). Taking this into account, we thus confirm the necessity to rescale the metallicity profiles when the relation used has been calibrated with strong emission lines estimates.

With this rescaling accepted, the usefulness of a metallicity-dependent X_{CO} factor can be demonstrated, in the context of RC studies in general and of the present work in particular. First, as can be seen in Table 5.1, neglecting the dependence on Z of X_{CO} results in underestimations of molecular gas masses (as the metallicities of the galaxies in our sample are globally lower than the solar metallicity; see Figure 4.7 on page 108). This

non-modeled mass could thus be wrongly attributed to the galactic DM component. Moreover, as the present work is performed with profiles of metallicity (and not only a mean metallicity value), the radial distribution of mass within the galactic disk is impacted. In Figure 5.1, we can compare the H_2 SMDs derived by our rescaled Z profile (green triangles) and the ones that assume a constant X_{CO} (red stars). For all the galaxies (except NGC2976 and its very flat Z profile), significant differences can be seen, notably in the central regions, crucial for the characterization of the DM component.

When modeling the molecular gas of spiral galaxies, metallicity-dependent conversion factors should thus be favored to the generic $X_{CO,\odot}$ value. Moreover, if Z profiles are available, they should also be used as they allow for a finer and more accurate description of this component.

For each galaxy of our sample, the corresponding molecular gas SMD profiles , computed from $X_{CO}(Z_{resc})$, are showed with light green downward triangles in Figure 5.2 and are compared to the profiles of the other luminous components. The associated total masses are given in the last column of Table 5.1. As expected, these values are higher than what is usually derived in literature studies which use a $X_{CO,\odot}$ value to convert from CO emission to H_2 mass (for examples, see Casasola et al. 2020 or Leroy et al. 2008, whose values are gathered in Table 2.1 on page 42).

Molecular gas modeling in the context of RC studies

In RC studies, the molecular gas is usually either not modeled or considered as distributed like the stellar component (and hence incorporated into the uncertainties associated to the assumed stellar mass-to-light ratio). Nevertheless, as can be seen in Figure 5.2 where we compare among other profiles, the molecular gas (light green downward triangles) with the stellar (blue dots) SMD profiles, this simplifying hypothesis is not valid and the molecular gas should thus be modeled by itself.

This has already been recommended by Frank et al. (2016) and used in a few recent works (Richards et al. 2018; Relatores et al. 2019). However, with the usual modelings of the luminous components, it is not easy to consider a conversion factor X_{CO} whose value (i) is different from the generic $X_{CO,\odot}$ and, if so, (ii) varies with the position within the galaxy. Indeed, when the stellar component is modeled through the simple NIR conversion, it does

not provide the information necessary to perform the metallicity-dependent molecular gas modeling we recommend. Hence, Richards et al. (2018) and Relatores et al. (2019) simply considered $X_{\rm CO}$ to be equal to $X_{\rm CO,\odot}$. More realistically, Frank et al. (2016) used radially-varying conversion factors that had been previously determined by Sandstrom et al. (2013) from high-resolution maps of the dust, HI and CO emissions for a given sample of 26 nearby galaxies. Nevertheless, due to this reliance on a previous work, it has not been possible for Frank et al. (2016) to model the molecular gas of all their galaxies with their initial methodology. Indeed, the conversion factors for 2 of their 12 galaxies (one of them being NGC2403) had not been previously computed and they then had to assume a $X_{\rm CO,\odot}$ value.

On the contrary, thanks to the SED modeling performed when estimating the stellar mass distributions, we directly and effortlessly end up with molecular gas mass distributions that take into account the radial evolution of the $X_{\rm CO}$ conversion factors, and that, for all the galaxies in our sample.

5.1.3 Discussion

For the six galaxies in our sample, the total masses of their dust, gas and stellar components are gathered in Table 5.1 and the corresponding SMD profiles are shown in Figure 5.2.

As expected, dust (red squares) plays a negligible role in the mass budget of spiral galaxies. Concerning the gas component, it is preferentially found under its molecular form (light green downward triangles) in the centers of the galaxies and under its atomic form (dark green upward triangles) in their outskirts with a radial extension 2.7 to 4.8 times larger than the characteristic radius r_{25} of (the stellar content of) galaxies. The molecular rings of NGC2841 and NGC7331 (highlighted in grey on Figure 5.2) are visible in the mass profiles of both the molecular gas and the dust components.

For all except one galaxy (the quasi-dwarf NGC2976), the gas mass budget is strongly dominated by the atomic component, which is consistent with both observations and simulations of spiral galaxies (e.g. Lagos et al. 2015; Davé et al. 2016; Saintonge et al. 2017; Catinella et al. 2018). Low-mass galaxies such as NGC2976 are expected to contain a small quantity ($\sim$10%) of molecular gas when compared to the atomic one but these results often do not consider the dependence on the metallicity of the conversion factor $X_{\rm CO}$.

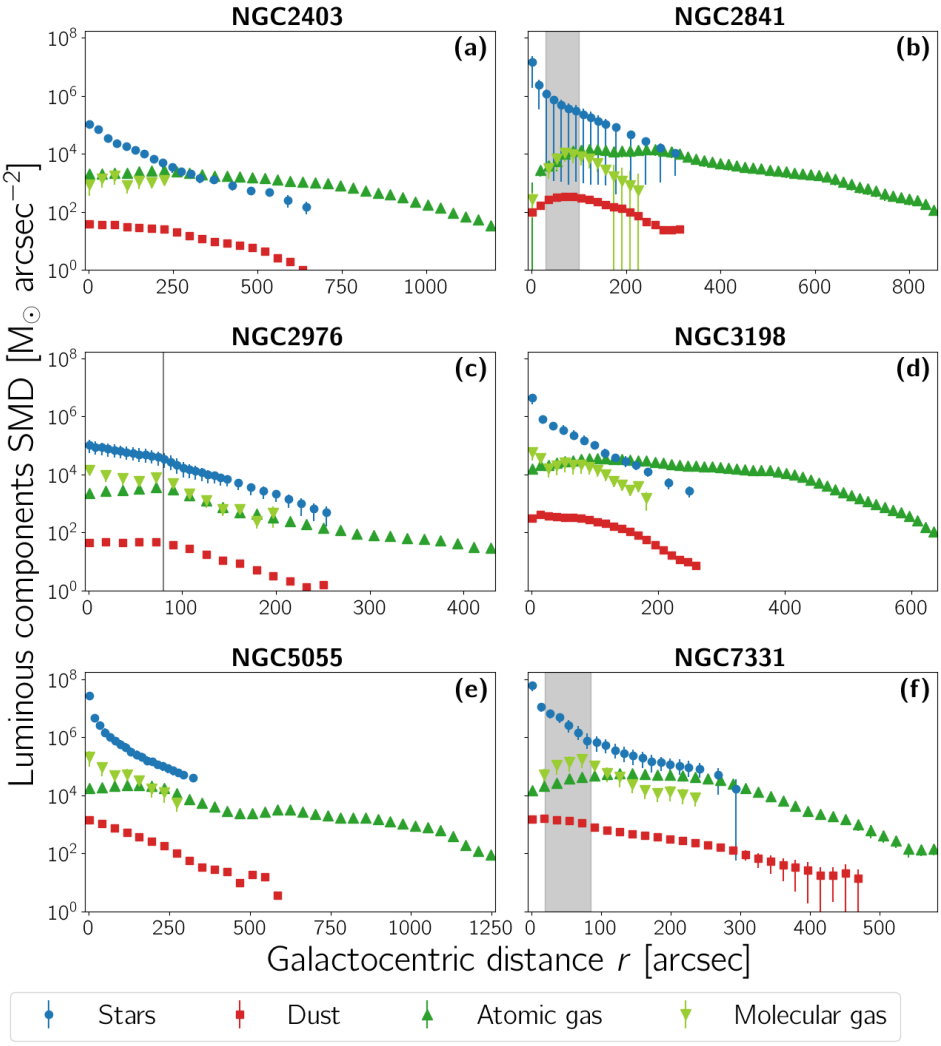

Figure 5.2: SMD profiles of all the luminous components (*stars:* blue dots – *atomic gas:* dark green upward triangles – *molecular gas:* light green downward triangles – *dust:* red squares) of the galaxies in our sample. If present, the location of the molecular ring is shown in grey. The profiles of the stellar component have been derived from SED modelings performed with the Exp-1pop library. The profiles of molecular gas are computed through a metallicity-dependent conversion factor X_{CO} with the rescaled metallicity profile from the same library.

Table 5.1: Logarithm of the total stellar, dust and gas masses ($\log(M_X)$; expressed in $M_\odot$) of all the galaxies in our sample

Galaxy	Stars†	Dust‡	Atomic gas*	Molecular gas*		
				$X_{CO,\odot}$	$X_{CO}(Z)$**	$X_{CO}(Z_{resc})$**
NGC2403	$9.56^{+0.10}_{-0.13}$	$7.12^{+0.04}_{-0.04}$	$9.54^{+0.04}_{-0.05}$	$8.06^{+0.11}_{-0.14}$	$9.19^{+0.15}_{-0.24}$	$8.37^{+0.15}_{-0.24}$
NGC2841	$10.60^{+0.17}_{-1.40}$	$7.58^{+0.08}_{-0.10}$	$9.90^{+0.14}_{-0.21}$	$8.74^{+0.18}_{-0.27}$	$9.87^{+0.23}_{-0.53}$	$8.80^{+0.23}_{-0.53}$
NGC2976	$9.33^{+0.19}_{-0.28}$	$6.42^{+0.05}_{-0.05}$	$8.34^{+0.07}_{-0.09}$	$7.91^{+0.13}_{-0.18}$	$9.30^{+0.15}_{-0.23}$	$8.45^{+0.15}_{-0.23}$
NGC3198	$10.12^{+0.15}_{-0.16}$	$7.36^{+0.04}_{-0.05}$	$10.10^{+0.06}_{-0.07}$	$8.67^{+0.12}_{-0.17}$	$9.59^{+0.17}_{-0.28}$	$9.06^{+0.17}_{-1.04}$
NGC5055	$10.96^{+0.13}_{-0.14}$	$8.05^{+0.03}_{-0.03}$	$10.10^{+0.04}_{-0.05}$	$9.72^{+0.11}_{-0.14}$	$10.21^{+0.18}_{-0.32}$	$9.86^{+0.18}_{-0.32}$
NGC7331	$11.08^{+0.17}_{-0.24}$	$8.10^{+0.07}_{-0.09}$	$10.17^{+0.09}_{-0.11}$	$9.69^{+0.12}_{-0.17}$	$10.33^{+0.18}_{-0.32}$	$9.86^{+0.18}_{-0.32}$

† Copied from Table 4.5 (on page 118) for the Exp-1pop librairy

‡ Integration of the dust SMD profiles of Figure 5.2 up to a galactocentric distance of 1.5 r_{25}

* Integration over the whole hydrogen-only gas SMD profiles of Figures 5.2 and 5.1, multiplied by a factor 1.4 to take into account the helium and metals produced by the primordial nucleosynthesis

** The two metallicity profiles used are either the one directly given by the stellar SED modeling implemented in this work (Z) or the one rescaled to match the metallicity value estimated by independent observations (Z_{resc}). In both cases, the values correspond to the computations based on the Exp-1pop library.

Indeed, the relatively high content of molecular gas in NGC2976 that we found is directly due to the correction we applied on $X_{\rm CO}$ due to the low metallicity value of NGC2976. Roughly speaking, this correction corresponds to a multiplication by a factor of $\sim$3.5 of the H_2 mass profile. This value is consistent with a previous study by Bolatto et al. (2008) (who found a similar factor of 4.5) and with the modeling of this galaxy performed by Simon et al. (2003). Nevertheless, other works found that the $X_{\rm CO}$ factor of NGC2976 should not be modified compared to the $X_{\rm CO,\odot}$ value (Sandstrom et al. 2013; Hatakeyama et al. 2017). For Hatakeyama et al. (2017), we have tracked down the reason of this surprising non-impact of the very low metallicity of NGC2976. This is due to an error in the assumed metallicity of the galaxy that has been wrongly transformed in a value close to the solar metallicity by Schruba et al. (2011) when gathering the results of Moustakas et al. (2010).

Concerning the study by Sandstrom et al. (2013), they estimated conversion factors in different HII regions of, among other galaxies, NGC2976. By averaging on all the factor estimates[2], they found a mean value that implies a galactic metallicity higher than the solar one. Such a high value is relatively surprising regarding the relatively low stellar formation that occurred during the life of this dwarf galaxy. It is nevertheless in agreement with Moustakas et al. (2010) and De Vis et al. (2019) ones if theoretical calibrations (of the nebular emission lines) are used. As we rather based the computations of our conversion factors on metallicity values derived from empirical calibration, it explains the difference between our results and those from Sandstrom et al. (2013).

The case of NGC2976 should then be investigated in further details as the molecular gas that is derived from its metallicity profile can have significant consequences on the mass budget in the very center of this galaxy, usually thought to be heavily dominated by its DM content. Hence, if a significant portion of its luminous mass budget is in fact constituted of molecular gas, this well-known property of NGC2976 (and of other late-type spirals of its kind) could be completely called into question.

[2]This galaxy is incidentally the one among all their sample with the largest discrepancies between the different values, hence the one with the average value with the highest uncertainty.

5.2 Bulge/disk decomposition of the stellar component

In spiral galaxies, the stellar component is divided between a central bulge, an outer disk and a surrounding halo. If, as mentioned in Chapter 1, the halo can be ignored in this work, it is nevertheless important to correctly decompose our stellar populations, and their SMD profiles, into the two other structures. Indeed, as they are gravitationally supported by very different mechanisms, the 3D distributions of their constitutive stars have not the same effect on the expected RC (as will be detailed in Chapter 6).

A correct separation of the stellar component into bulge and disk structures is thus particularly important (Korsaga et al. 2018, 2019). Nevertheless, in RC studies, this separation is usually relatively limited. By default, all the stars are distributed only within the disk. If any, the central structure (of a given fixed distribution) is only modeled if it significantly improves the RC description (e.g. de Blok et al. 2008; de Denus-Baillargeon et al. 2013; Lelli et al. 2016a; Richards et al. 2018). In contrast, in this work, we systematically modeled the bulge of galaxies, whatever the result on the RC decomposition. Furthermore, we allowed each bulge to be described with different types of distributions, adding more freedom in the decomposition of the stellar content of spiral galaxies.

5.2.1 Classical decomposition

To separate the mass profiles into both a bulge and a disk, we modeled these two structures via their expected mathematical form. Indeed, the surface brightness, and thereby the SMD profile $\Sigma_{*,\mathrm{disk}}$, of a (face-on) galactic disk is well modeled by a decreasing exponential (Patterson 1940; de Vaucouleurs 1957, 1958; Freeman 1970) with

$$\Sigma_{*,\mathrm{disk}}(r) = \Sigma_{0,\mathrm{disk}} \ \exp\left(-\frac{r}{r_{\mathrm{disk}}}\right). \tag{5.2}$$

This function is parametrized by $\Sigma_{0,\mathrm{disk}}$, the disk central SMD, and by r_{disk}, the disk scalelength.

On the contrary, the stellar bulges present more diversity, going from the classical bulges which look like mini elliptical galaxies to pseudobulges which present disk-like features (flatter shape, younger stars, rotation dominated kinematics...) (Andredakis et al. 1995; Kormendy & Kennicutt 2004). For these reasons, it is more common to use a function with more degrees of

freedom to describe the bulges, that is to say, a Sérsic profile (Sérsic 1968):

$$\Sigma_{*,\mathrm{bulge}}(r) = \Sigma_{\mathrm{eff,bulge}} \ \exp\left(-b_{n_S}\left[\left(\frac{r}{r_{\mathrm{eff,bulge}}}\right)^{1/n_S} - 1\right]\right) \tag{5.3}$$

where b_{n_S} is a function of n_S and is approximated by $b_{n_S} \approx 2n_S - 1/3 + 4/(405n_S)$ (Ciotti & Bertin 1999). Here, $\Sigma_{\mathrm{eff,bulge}}$ is the bulge SMD estimated at the bulge effective radius $r_{\mathrm{eff,bulge}}$. The latter is the radius of the isodensity contour containing half of the total mass[3] of the bulge. In addition to these two usual parameters, the Sérsic index n_S controls the shape of the function, allowing it to be a good representation of either classical bulges or pseudobulges (respectively when $n_S \gtrless 2$; Kormendy & Kennicutt 2004; Fisher & Drory 2008, 2010). If this limit of 2 has been determined from decompositions of NIR luminosity profiles, it is nevertheless also valid for the decompositions performed here (on mass profiles). Indeed, this domain is a good proxy for the stellar mass of spiral galaxies, as shown in Chapter 4. In Figure 5.3, examples of Sérsic bulges with different values of the index n_S are shown in orange tones. The higher the index value, the more peaked the profile and the more massive the bulge.

When decomposing the SMD profiles into a bulge and a disk, we tried to reduce the degeneracies between the parameters of the two structures. Indeed, for the galaxies in our sample (intermediate to late-type spirals), these degeneracies can be relatively strong as their bulges, even for the largest ones, are not very prominent and extended. Hence, very few (if any) central points are helpful to constrain the bulge modeling. The decomposition of the galaxy via one single fit is thus very hazardous, especially if the Sérsic index is left free (de Blok et al. 2008). To avoid this, we decoupled the bulge and the disk fits.

We started by fitting an exponential profile (Equation 5.2) on the outer parts of the galaxies (at galactocentric distances chosen such as $r > 0.25\, r_{25}$) where the bulge does not impact the total SMD. We extrapolated this model to the central parts ($r < 0.25\ r_{25}$) of the galaxy and subtracted it from the total SMD profile in order to isolate the mass associated to the bulge only. The latter was then fitted with a Sérsic function (Equation 5.3).

[3] Usually, the effective radius is defined in term of luminosity. In this work, we adopted a mass definition as we fitted the Sérsic function on the galactic SMD profiles and not on their surface brightness profiles. In the case where the mass-to-light ratio of the bulge does not radially vary, these two definitions are equivalent.

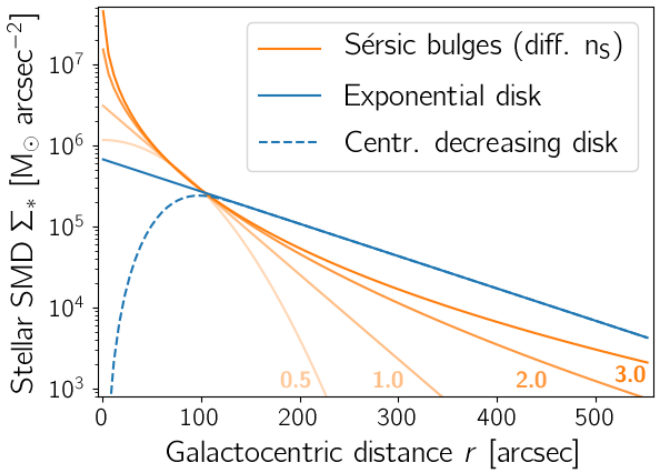

Figure 5.3: Analytical functions describing the distribution of stars in spiral galaxies and decomposing it into two structures. The bulge (orange lines) is modeled by a Sérsic function (Equation 5.3) with different index n_S values. The disk is classically represented as an exponential (Equation 5.2; solid blue line) but new observational evidence point out towards a possible decrease of the disk mass within the zone dominated by the bulge (Equation 5.4; dashed blue line).

By default, we fixed the Sérsic indexes to values determined by previous articles (from bulge/disk decompositions of NIR luminosity profiles; Fisher & Drory 2010; Jovanović 2017). For two of our galaxies (NGC2841 and NGC7331), these literature values are flagged as not reliable due to a combination of important dust lanes in their central regions and of the galaxy high inclination (NGC7331) or central compact structure (NGC2841) (Fisher & Drory 2010). As the fit performed in this work is realized on mass, rather than on the usual luminosity, profiles, we tried to let the Sérsic index free for these two galaxies to check if such a mass decomposition improves the determination. Coincidentally, these two spirals are both of an earlier type and are hence the most appropriate for decompositions with free indexes.

With these two decoupled fits, we had a rough estimate of the bulge and disk parameters that we finally refined (allowing a modification of

the parameters values up to 10%) thanks to a global fit (the sum of an exponential disk and of a Sérsic bulge) on the whole profile. Once these fits were performed and the best parameters were estimated (their values can be found in the upper panel of Table 5.2), we kept the Sérsic profile as the bulge profile. For high values of Sérsic indexes, the SMD profiles of the bulges stabilize at high galactocentric distances as can be seen in Figure 5.3. This thus results in density values unrealistically higher for the bulge than for the disk in the outskirts of the galaxies. This nonphysical situation is avoided by limiting the bulge radial extension. We thus cut the bulge profile at a distance where 95% of the total mass of the bulge was reached. Finally, we subtracted the bulge profile from the total SMD to define the disk profile.

It is worth noting that two of the galaxies studied in this work (the two late-type spirals, NGC2403 and NGC2976) could not be modeled with a bulge as their mass profile did not show any signs of the presence of this structure. Thus, we represented them only with a disk.

5.2.2 "Centrally decreasing disk" decomposition

Recently, observational and theoretical studies on the formation and evolution of spiral galaxies have questioned the widely used assumption that the disk keeps its exponential profile in the center of the galaxy, that is to say, in the zone dominated by the bulge (Obreja et al. 2013; Breda et al. 2020; Du et al. 2020; Papaderos et al. 2022). The reason of this reassessment is that this hypothesis implies that, since their creation, there has not been any interaction or mass exchange between these two structures. The discussion about the formation of spiral galaxies is still widely open as contradictory observations exist but two scenarios prevail: either the bulge has been created at first and the disk latter assembled around it, or they both appeared simultaneously and evolved together (see Breda et al. 2020 and the references within). In any case, from a physical point of view, the hypothesis of a central disk that keeps its outskirts' exponential behavior in its central regions does not hold. If confirmed, this could have important consequences on the estimates of the bulge properties of spiral galaxies and all studies based on that, notably for the DM halo characterization.

We thus decided to perform another bulge/disk decomposition, assuming a centrally decreasing disk (CDD) profile in the bulge-dominated region of the galaxy. For that, we modified the exponential fits we obtained during

Table 5.2: Bulge/disk decompositions of the stellar component (derived from the Exp-1pop library) of the appropriate galaxies of our sample

Galaxy	Previous works		n_S	$r_{\rm eff,bulge}$	$\log M_{*,\rm bulge}{}^{\dagger}$	$r_{\rm bulge}$	$r_{\rm disk}$	$\log M_{*,\rm disk}{}^{\ddagger}$
	n_S	Ref.		[kpc]	[$M_\odot$]	[kpc]	[kpc]	[$M_\odot$]
CLASSICAL DECOMPOSITION								
NGC2841	$3.6 \pm 0.27^*$	(1)	$1.7^{+2.3}_{-1.7}$	$1.35^{+2.45}_{-1.35}$	$9.92^{+0.40}_{-9.92}$	-	4.35 ± 0.76	$10.50^{+0.27}_{-10.50}$
NGC3198	1.3 ± 0.56	(1)	$1.4^{+1.5}_{-1.4}$	$0.69^{+0.74}_{-0.69}$	$9.05^{+0.28}_{-0.94}$	-	2.82 ± 0.12	$10.08^{+0.18}_{-0.21}$
NGC5055	2.059	(2)	1.87 ± 0.59	2.27 ± 1.00	$10.60^{+0.18}_{-0.32}$	-	5.48 ± 0.44	$10.79^{+0.22}_{-0.39}$
NGC7331	$5.73 \pm 0.34^*$	(1)	2.12 ± 0.76	1.63 ± 0.73	$10.36^{+0.11}_{-0.15}$	-	2.66 ± 0.16	$10.99^{+0.21}_{-0.34}$
CENTRALLY DECLINING DISK DECOMPOSITION								
NGC2841	-		1.4 ± 1.4	$1.4^{+1.5}_{-1.4}$	$10.06^{+0.40}_{-10.06}$	2.18	4.40 ± 0.75	$10.46^{+0.28}_{-10.46}$
NGC3198	-		0.92 ± 0.55	0.58 ± 0.23	$9.20^{+0.23}_{-0.50}$	0.79	2.81 ± 0.11	$10.06^{+0.18}_{-0.22}$
NGC5055	-		2.60 ± 0.72	3.35 ± 1.72	$10.75^{+0.18}_{-0.32}$	3.69	5.23 ± 0.44	$10.65^{+0.27}_{-0.66}$
NGC7331	-		1.53 ± 0.93	1.73 ± 1.32	$10.65^{+0.27}_{-0.91}$	2.58	2.71 ± 0.12	$10.88^{+0.29}_{-0.81}$

† Integration over the bulge SMD profiles of Figure 5.4

‡ Integration of the disk SMD profiles of Figure 5.4 up to a galactocentric distance of 1.5 r_{25} (1.0 r_{25} for NGC5055 and NGC7331)

* Unreliable values due to the galaxy dust lanes as well as high inclination (NGC7331) or central structure (NGC2841) (Fisher & Drory 2010). For these two galaxies, the Sérsic index is let free during the first part of the decomposition.

References: (1) Fisher & Drory (2010); (2) Jovanović (2017)

the classical decomposition so that the SMD of the disk is null at the very center of the galaxy. An analytic form of this kind of profile has been given by Papaderos et al. (1996):

$$\Sigma^{\rm dec}_{*,\rm disk}(r) = \Sigma_{*,\rm disk}(r) \left[1 - \exp\left(\frac{r}{r_{\rm bulge}}\right)^3\right] \tag{5.4}$$

where $\Sigma_{*,\rm disk}(r)$ is the usual exponential disk profile (given by Equation 5.2) and where $r_{\rm bulge}$ is the distance defining the bulge-dominated zone inside which the disk profile begins to decrease. An example of this profile (dashed blue line) is shown in Figure 5.3 and compared with the associated classical disk (solid blue line).

Practically, we defined the bulge radius $r_{\rm bulge}$ as the distance inside which the majority (here arbitrary chosen as more than 75%) of the total mass of the classical bulge is located. The values for each galaxies can be found in the lower panel of Table 5.2. We then followed the same methodology as for the classical decomposition, starting by a first estimate of the bulge and disk parameters with separated fits on the inner and outer portions of the galactic profiles, followed by a refining of the parameters values through a global fit. As previously, the latter can be also found in Table 5.2.

5.2.3 Effect of the decompositions

In Figure 5.4, we show the SMD profiles resulting from the two bulge/disk decompositions performed in this work. As expected, the decomposition for which the disk decreases in the bulge-dominated region results in larger bulges (orange downward triangles) than their classical counterparts (red upward triangles). This is also visible in Table 5.2 where the total masses of the disk and bulge structures can be compared.

With the classical decomposition, all the galaxies are disk-dominated while the situation is not so obvious with the other decomposition, NGC5055 even having a bulge more massive than its disk. For NGC7331, the two structures have similar masses, which goes into the same direction as previous RC decompositions where the galaxy rotation was found to be dominated by its stellar bulge (and DM halo Bottema 1999; Bottema & Pestaña 2015). Incidentally, well before the recent interest on CDD models, these works had already noticed that the RC of NGC7331 is better fitted by a disk model that is thinner, and hence less massive, in the bulge region.

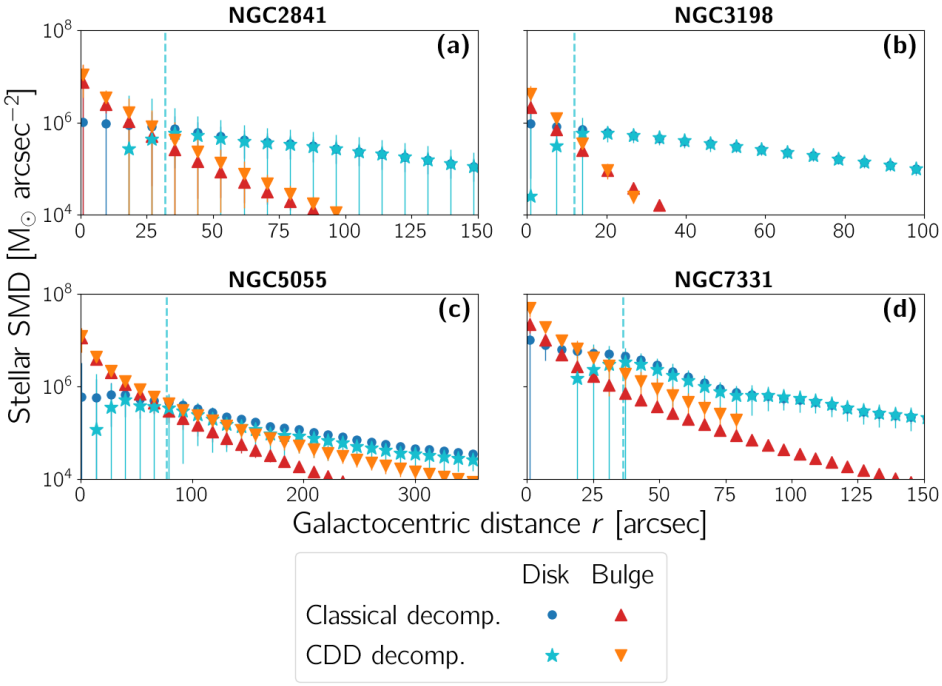

Figure 5.4: Bulge/disk decompositions of the stellar content (derived from the Exp-1pop library) of the appropriate galaxies of our sample. Two types of decompositions are compared, differing by their disk modeling with (i) a classical exponential disk (blue dots) or (ii) a disk that decreases in the bulge-dominated region (at the left of the vertical dashed cyan line; cyan stars). The bulges of this CDD decomposition (orange downward triangles) are thus more peaked and massive than their classical counterparts (red upward triangles).

On top of increasing the bulge mass, the CDD decomposition also modifies its shape via the Sérsic index n_S. For each decomposition, our sample of galaxies counts more pseudobulges than classical ones, a situation that is in agreement with studies estimating the proportions of these two kinds of bulges as a function of the type of the spiral galaxies (e.g. Andredakis et al. 1995; Graham 2001; Kormendy & Kennicutt 2004). Furthermore, looking individually at each galaxy, we find that going from the classical to the CDD decomposition, the bulge index of NGC3198 decreases to reach a value lower than 1, the limit indicative of the presence of a central bar (Cimatti et al. 2020), consistent with this galaxy being the only one in our sample formally identified as a barred spiral.

Concerning NGC5055 and NGC7331, their bulges change between a pseudo ($n_S \lesssim 2$) and a classical ($n_S \gtrsim 2$) nature depending on the methodology used. In fact, in literature, there is no census to classify these galaxies' bulges. The bulge of NGC5055 is seen as a pseudobulge by Fisher & Drory (2008) and Fisher & Drory (2010) but as a classical one by Jovanović (2017). The possibility for this galaxy to have two central structures, each one with different bulge characteristics, is even proposed by Fisher & Drory (2008). For NGC7331, as already said, its high inclination and the large quantity of obscuring dust in its center make it challenging to determine its bulge type. For that reason, Fisher & Drory (2010) consider untrustworthy their classification as classical bulge while Fabricius et al. (2012) did not even attempt to provide such categorization. Comparing our modeling with previous studies based on RC decompositions and stellar radial velocities observations (Bottema 1999; Bottema & Pestaña 2015), we find that our decompositions are in agreement when regarded in term of total masses of bulge and disk. We thus estimated that our use of mass (instead of luminosity) profiles improves the bulge/disk decomposition, for this galaxy at least.

Concerning the other free-index galaxy, NGC2841, the situation may *a priori* not seem as promising as for NGC7331. Indeed, the uncertainties on our decompositions are particularly important for this galaxy, with error bars larger than the values themselves for the parameters of the Sérsic function. These large uncertainties thus impact the associated mass profiles of both the bulge and the disk. With its central large amounts of dust and compact structure, this galaxy is known for its challenging decomposition, as already stated. Recently, by combining photometric and kinematic data, Peters & Kuzio de Naray (2017) showed the existence, besides the central

bulge, of a bar, invisible in the images of the galaxy. This great complexity of the inner region of NGC2841 thus explains the poor results of our decompositions. Nevertheless, when analyzed in term of mass, which is the interest of this work, our results are plausible and consistent with literature decompositions. Indeed, whatever the decomposition, we can see in Table 5.2 that the associated bulges are significantly less massive than the disks with $M_{*,\mathrm{bulge}} = 0.26 - 0.40\ M_{*,\mathrm{disk}}$. In theory, as NGC2841 is the spiral of our sample with the earliest type, it should have a bulge relatively massive compared to its disk, more so than the ones of NGC5055 and NGC7331 (e.g. Andredakis et al. 1995; Graham 2001; Kormendy & Kennicutt 2004). However, the fact that we found a smaller bulge, what's more, in the same proportions as previous studies (Bottema & Pestaña 2015; Peters & Kuzio de Naray 2017), comforts us in the use of our own decompositions for the future computations of this galaxy RC.

5.3 Luminous components 3D distributions

The final information required to compute the RCs of galaxies is their 3D structure in order to include the impact of the out-of-plane components on their rotation. Usually in RC studies, only the stellar component is considered as distributed in 3D. The atomic gas (and the molecular one, when modeled separately from the stars) is commonly approximated by an infinitely thin disk (e.g. Verheijen 1997; de Blok et al. 2008; Bottema & Pestaña 2015; Richards et al. 2018). Nevertheless, this does not correspond to the observations of gas in edge-on galaxies as performed by Sancisi & Allen 1979, van der Kruit 1981 and many after them. In this work, we therefore departed from this simplification and decided to model the vertical distribution of all the luminous components of spiral galaxies.

To do so, we made a few classical hypotheses concerning the galaxies symmetries. In addition to the axisymmetry assumed since the beginning of this work, we also considered that the galaxies are symmetric with regard to their mid-plane. To mathematically describe such symmetries, the most appropriate set of coordinates are the cylindrical ones, where r and θ are defined into the galactic mid-plane and z is in the direction perpendicular to it, the mid-plane being characterized by $z = 0$.

In addition, each luminous component i of the galaxy (the disk/bulge stars, the dust, the atomic/molecular gases) was restricted to two possible

Table 5.3: 3D distributions assumed or computed in this work for each luminous component of spiral galaxies

		Distrib.	Flaring†	Scaleheight	Ref.
Stars	Disk	Exp. disk	No	$z_{0,\mathrm{disk}} \approx 0.137\ R_{\mathrm{disk}}$	(1)
	Class. bulge	Sphere	-	-	
	Pseudobulge	Exp. disk	No	Same as stellar disk	(2)
Dust		Exp. disk	No	$z_{0,\mathrm{dust}} \approx 0.33\ z_{0,\mathrm{disk}}$	(3)
Gas	Atomic	Exp. disk	Yes	Global modeling	(4)
	Molecular	Exp. disk	Yes	$z_{0,\mathrm{H_2}}(r) \approx 0.5\ z_{0,\mathrm{HI}}(r)$	(5)

† Increase with the galactocentric distance of the disk vertical scaleheight
References: (1) Kregel et al. (2002); (2) Kormendy & Kennicutt (2004); (3) Bianchi (2007); (4) Das et al. (2020); (5) Bacchini et al. (2019)

vertical distributions, either a sphere or a thin disk whose density $\rho_i(r,z)$ decreases exponentially[4] as

$$\rho_i(r,z) = \rho_{0,i}(r)\ \exp\left(\frac{-|z|}{z_{0,i}(r)}\right) \tag{5.5}$$

where $z_{0,i}(r)$ is the disk scaleheight profile and $\rho_{0,i}(r)$ the density value at this specific height. To estimate this last quantity, we relied on the SMD profiles $\Sigma_i(r)$ computed in this chapter as well as in Chapter 4. Indeed, the latter are simply the projections onto the galactic mid-plane of the densities (i.e. $\Sigma_i(r) = \int_{-\infty}^{+\infty} \rho_i(r,z)dz$). Hence, $\rho_{0,i}(r)$ can be written as

$$\rho_{0,i}(r) = \frac{\Sigma_i(r)}{2z_{0,i}(r)}. \tag{5.6}$$

Depending on the nature of the component, different assumptions were made on their associated scaleheights. Further details will be given in the following sections but we briefly summarize these hypotheses here and in Table 5.3. On the one hand, the scaleheights of the stellar and dust components have been estimated from empirical relations between the vertical and the radial distributions of the stellar disks. On the other hand, for the gaseous components, we performed a complete modeling of the galaxy's gravitational potential and derived from it their out-of-plane distributions.

[4]The choice of this particular form is discussed in more details for each individual component in the next sections.

5.3.1 Stellar disk

Vertical distribution of stars in disks of edge-on galaxies are described either by (i) a sech^2 function (resulting from the modeling of this component as a self-gravitating isothermal sheet; Camm 1950; van der Kruit 1981), (ii) a decreasing exponential (mathematically described by Equation 5.5; Fuchs & Wielen 1987) or (iii) an intermediate sech form (van der Kruit 1988). Indeed, these three functions are equivalent far away from the mid-plane, in zones where the stellar component of edge-on galaxies are more reliably studied (as the effects of the attenuation by dust lanes and the uncertainties on the galaxy inclination have a lower influence; Kregel et al. 2002). If the exponential and the sech^2 models are equivalently used when modeling the stellar disk in RC studies, the first one is slightly more realistic as it allows the disk to be not perfectly isothermal (van der Kruit & Freeman 2011) and it seems favored by observations closer to the galaxy mid-plane (van der Kruit 1988). We thus chose to use this form in this work but it is worth noting that we checked that our choice of one model or the other did not significantly impact the derived RCs.

Regardless of the exact mathematical form of the vertical distribution, the important feature here is that the associated scaleheight of the disks does not radially vary for late-type galaxies, as seen observationally (van der Kruit 1981; de Grijs & Peletier 1997) and explained theoretically (Minchev et al. 2015). Moreover, the scaleheight value depends on the size of the galaxy. Hence, we used Kregel et al. (2002) results that showed, from a study on edge-on galaxies, that the exponential scaleheight of old stars populations is correlated to the exponential scalelength of the disk r_{disk} (as defined in Equation 5.2) with

$$z_{0,\mathrm{disk}} = 0.137^{+0.059}_{-0.032}\, r_{\mathrm{disk}}. \tag{5.7}$$

Thus, from the disk/bulge decompositions performed in Section 5.2 whose r_{disk} values are given in Table 5.2, we fixed the vertical scaleheight of our stellar galactic disks.

Assuming that all the disk stars constitute only one homogeneous population is a rough approximation. Indeed, observations in the Milky Way (Gilmore & Reid 1983) and in other spiral galaxies (Burstein 1979; Tsikoudi 1979; van der Kruit 1981; van der Kruit & Searle 1981) showed evidence of two interlocked disks, one thicker, larger, older, kinematically hotter and more metal-poor than the other. We stress that the Equation 5.7 used

in this work has been determined on old populations of stars in edge-on galaxies and thus, gives globally the scaleheight of this thick disk. However, in massive galaxies (which is the case for all but one galaxy of our sample, NGC2976), the majority of the disk mass is located in the thin disk (Yoachim & Dalcanton 2006), hence closer to the galactic mid-plane than what is given by Equation 5.7. In term of associated RC, our use of this equation will thus results in slightly underestimated rotation velocities.

5.3.2 Stellar bulge

As seen in Section 5.2, galactic bulges are divided in two categories: (i) the classical bulges, very similar to mini elliptical galaxies, and (ii) pseudo-bulges, considered as small versions of spiral galaxies (Kormendy & Kennicutt 2004). We thus modeled the bulges of our galaxies accordingly, assuming (i) a spherical distribution for the classical bulges (for whom the fitted Sérsic index in Table 5.2 have been found to be larger than 2) and (ii) a disk distribution, described by Equation 5.5, for the others. For the latter case, we performed the same modeling as for the stellar disk and hence used the same relation (Equation 5.7) to estimate their scaleheights. For the classical bulges and their spherical symmetry, the deprojection of their SMD profiles into 3D densities is slightly more complex.

Due to the bulge/disk decompositions performed in Section 5.2, the SMDs of classical bulges are exact Sérsic profiles whose parameters are given in Table 5.2. If analytical deprojections of such functions do not exist for all values of the Sérsic index, good approximations nevertheless exist, each with their own limitations (see Vitral & Mamon 2020, and the references within for more information). In this work, we chose to use the analytical approximation presented by Prugniel & Simien (1997) and corrected by Lima Neto et al. (1999). Despite not being the most precise, it was chosen for its robustness, the approximation holding for a wide range of Sérsic indexes (between $n_S = 0.55$ and 10; Lima Neto et al. 1999).

Hence, the density profile of a classical bulge modeled in 2D by a Sérsic function (Equation 5.3 on page 139) can be approximated by

$$\rho_{*,\mathrm{bulge}}(r) \approx \rho_{0,\mathrm{bulge}} \left[\frac{r}{r_{\mathrm{eff,\ bulge}}}\right]^{-p_{n_S}} \exp\left(-b_{n_S}\left[\frac{r}{r_{\mathrm{eff,\ bulge}}}\right]^{1/n_S}\right). \quad (5.8)$$

As for b_{n_S}, the exponent p_{n_S} is a function of the Sérsic index. Its value is fitted so that the projected profile of the approximated 3D density effectively

corresponds to a Sérsic profile in 2D ($p_n = 1 - 0.6097\ n_S^{-1} + 0.05463\ n_S^{-2}$; Lima Neto et al. 1999). Moreover, the central density $\rho_{0,\mathrm{bulge}}$ can be directly computed as it is given by

$$\rho_{0,\mathrm{bulge}} = \Sigma_{\mathrm{eff,bulge}}\ \exp(-b_{n_S})\ b_{n_S}^{(1-p_{n_S})n_S}\ \frac{\Gamma(2n_S)}{\Gamma[(3-p_{n_S})n_S]}$$

where Γ is the gamma function defined by $\Gamma(x) = \int_0^\infty t^{x-1}\mathrm{e}^t dt$.

5.3.3 Dust

The hypothesis that dust is vertically distributed in the galactic disk as an exponential is very commonly used when modeling the attenuation by dust of galactic emissions at short wavelengths (e.g. Xilouris et al. 1999; Bianchi 2007; Muñoz-Mateos et al. 2009; Popescu et al. 2011). Recently, the validity of this assumption has been confirmed on images of dust thermal emission (e.g. Verstappen et al. 2013; Hughes et al. 2014; Hunt et al. 2015). Applications of radiative transfer models on optical images of edge-on galaxies showed that, as for the stellar disk, the dust disk does not flare (its scale-height remains constant with the galactocentric distance). Moreover, the dust is located closer to the galaxy mid-plane than the stellar component with a correlation

$$z_{0,\mathrm{d}} \approx 0.33\ z_{0,\mathrm{disk}} \tag{5.9}$$

between the dust $z_{0,\mathrm{d}}$ and the stellar disk $z_{0,\mathrm{disk}}$ scaleheights (Xilouris et al. 1999; Bianchi 2007).

5.3.4 Atomic and molecular gases

The description of the vertical distribution of the last of the three luminous components, the gaseous one, cannot be derived through the use of convenient empirical relations as for the other two. Hence, we had to completely model the galaxy and its gravitational potential in 3D in order to retrieve the vertical extension of its gas content.

5.3.4.1 Methodology

To model the entire galaxy in 3D, it is necessary to solve a system composed of a global Poisson equation coupled with hydrostatic equilibrium (HE) equations, each one associated to a component of the galaxy (Narayan &

Jog 2002a,b; Patra 2020). Applying the different symmetries assumed in this work, these equations can be written in cylindrical coordinates as

$$\begin{cases} \dfrac{1}{r}\dfrac{\partial}{\partial r}\left(r\,\dfrac{\partial \Phi}{\partial r}\right) + \dfrac{\partial^2 \Phi}{\partial z^2} = 4\pi G \rho_{\rm tot} \\ \dfrac{\partial \Phi}{\partial z} = \dfrac{-1}{\rho_i}\dfrac{\partial(\rho_i\ \sigma_{z,i}^2)}{\partial z} \end{cases} \tag{5.10}$$

where Φ is the gravitational potential of the whole galaxy, G is the gravitational constant and $\rho_{\rm tot}$ is the total density of the galaxy. It is thus given by the sum of all the individual densities ρ_i of each component i (the disk/bulge stars, the dust, the atomic/molecular gases[5]). Finally, $\sigma_{z,i}$ is the velocity dispersion along the vertical axis associated to each component. Indeed, the HE equations express the fact that the vertical pressure $\rho_i\ \sigma_{z,i}^2$ of each component balances the vertical gravitational force exerted by the whole galaxy. A widely used simplifying hypothesis when solving this system of equations is to model each component as isothermal in the vertical direction, or in other words, to assume that the velocity dispersion is independent of the z coordinate (e.g. Narayan & Jog 2002b; Bacchini et al. 2019; Patra 2020). Recent high-quality observations showed that this hypothesis is not correct for the stellar disks of galaxies (see Sarkar & Jog 2020, and references therein) but relaxing this approximation would be out of the scope of this paper. We thus kept the components isothermal.

The System 5.10 thus consists in 6 coupled partial differential equations with 11 unknowns: the gravitational potential Φ, the 5 individuals densities $\rho_i(r, z)$ and the 5 vertical velocity dispersion profiles $\sigma_{z,i}(r)$. Assuming a decreasing exponential disk[6] (Equation 5.5) for all components (except for

[5]Formally speaking, the DM component of the galaxy should evidently also be taken into account in the total galactic density. Nevertheless, as the goal of this work is to model the galaxy without any prior assumption on the DM distribution, we neglected, for now, its impact on the galactic gravitational potential close to the mid-plane. Such a simplifying hypothesis should not have a strong impact on the final RC decomposition and can be corrected *a posteriori* through an iterative process (as we explain it in Section 5.3.4.3).

[6]One may notice that this exponential disk is not often used when describing the vertical distribution of the gaseous components of galaxies, a Gaussian function being usually preferred (Bacchini et al. 2019; Cimatti et al. 2020). Nevertheless, we used it in this work (as done by Das et al. 2020, for example) because it allowed to find simple solutions for the scaleheight profiles, while still being a good approximation of the distributions.

the classical bulge), the unknown $\rho_i(r, z)$ can be replaced by the scaleheight profiles $z_{0,i}(r)$. Moreover, as we fixed the scaleheights of the stellar and dust components via the empirical relations described in the previous sections, we could get rid of the HE equations for these two components.

The existence of these empirical relations that simplify the System 5.10 is fortunate. Indeed, to solve the HE equations, it is necessary to have direct measurements of vertical velocity dispersion profiles $\sigma_{z,i}(r)$. However, such measurements for the stellar and dust components are very challenging to perform, even for recent telescopes on nearby galaxies, as they necessitate very high resolution observations (e.g. Leroy et al. 2008; Bacchini et al. 2019; Patra 2020). The relations described by Equations 5.7 and 5.9 are thus necessary to model a large amount of spirals.

Concerning the gas components, such measurements are also particularly difficult to obtain for the molecular gas (Bacchini et al. 2019) but not for the atomic one. It is thus possible to link these two types of gases in order to solve the System 5.10. Only a small sample of 12 nearby galaxies have currently been observed with sufficiently high resolution to estimate their molecular gas velocity dispersions but a correlation between the two gases profiles has still been determined (Caldú-Primo et al. 2013; Mogotsi et al. 2016). Converted in terms of scaleheight (Bacchini et al. 2019), it is given by

$$z_{0,\mathrm{H_2}}(r) \approx 0.5\ z_{0,\mathrm{HI}}(r).$$

Hence, the System 5.10 could be simplified in a system of two equations (the Poisson equation and the atomic gas HE one):

$$\begin{cases} \dfrac{1}{r}\dfrac{\partial}{\partial r}\left(r\ \dfrac{\partial \Phi}{\partial r}\right) + \dfrac{\partial^2 \Phi}{\partial z^2} = 4\pi G\left(\rho_* + \rho_\mathrm{d} + \rho_\mathrm{HI} + \rho_{\mathrm{H_2}}\right) \\ \dfrac{\partial \Phi}{\partial z} = -\sigma_{z,\mathrm{HI}}^2\ \dfrac{1}{\rho_\mathrm{HI}}\dfrac{\partial \rho_\mathrm{HI}}{\partial z}. \end{cases} \tag{5.11}$$

In the Poisson equation, one may notice that we did not differentiate between the stars of the bulge and the stars of the disk. For the resolution of this system and the determination of the atomic gas scaleheight, we chose to consider that all the stars of our galaxies are distributed in their stellar disks. This was done for simplicity reasons and does not significantly influence the resulting scaleheight and density profiles of atomic gas. Indeed, the central regions of galaxies, in which this approximation has the highest impact, are also the regions with the smallest quantity of atomic gas.

Moreover, we would like to stress out that this "no bulge" approximation[7] is only performed when deriving the gas scaleheights. When computing the RCs in Chapter 6, the bulge and the disk will be separated and modeled as previously explained.

The combination of the two equations of System 5.11 results in

$$\sigma_{z,\mathrm{HI}}^2 \frac{1}{\rho_{\mathrm{HI}}} \frac{\partial \rho_{\mathrm{HI}}}{\partial z} = -\int_0^z 4\pi G \left(\rho_* + \rho_{\mathrm{HI}} + \rho_{\mathrm{H_2}}\right) - \frac{1}{r}\frac{\partial}{\partial r}\left(r \frac{\partial \Phi}{\partial r}\right) dz \quad (5.12)$$

where ρ_{d} is neglected as dust is largely outweighed by the stellar and the gaseous components in spiral galaxies.

In this last equation, the radial derivative of the gravitational potential can be estimated from the observed RC of the galaxy. Indeed, in the mid-plane of the galaxy (at $z = 0$), the velocity v_{c} of a test particle on a circular orbit of radius r is given by this derivative as

$$\frac{v_{\mathrm{c}}^2(r)}{r} = \left.\frac{\partial \Phi(r,z)}{\partial r}\right|_{z=0}.$$

As stated in Chapter 1, this circular velocity can be approximated by the rotational velocity of any dynamically cold component of the galaxy, which is the case for the atomic hydrogen. Hence, using RCs derived from HI observations allows to estimate the derivative of Φ in the mid-plane of our galaxies. To determine this derivative at any height z, we made the widespread assumption that the RCs do not significantly change as we probe farther away from the galactic mid-plane (see Patra 2020, for example). If high-latitude lagging HI clouds have been observed for some edge-on galaxies (e.g. Matthews & Wood 2003; Heald et al. 2007; Zschaechner & Rand 2015), these only constitute a small fraction of the total mass of HI and should thus not significantly affect the observed RC. It is then reasonable to consider that the second term in the integral of the Equation 5.12 can be estimated thanks to the galactic global RC and does not depend on z.

Developing the densities for the stars, as well as for the atomic and

[7] For NGC2403 and NGC2976, this is not even an approximation as we already modeled these galaxies without a bulge in Section 5.2.

molecular gases with Equation 5.5, Equation 5.12 can be transformed into

$$\sigma^2_{z,\mathrm{HI}} \frac{1}{\rho_{\mathrm{HI}}} \frac{\partial \rho_{\mathrm{HI}}}{\partial z} = -2\pi G\, \Sigma_* \left[1 - \exp\left(-\frac{|z|}{z_{0,*}}\right)\right] - 2\pi G\, \Sigma_{\mathrm{HI}} \left[1 - \exp\left(-\frac{|z|}{z_{0,\mathrm{HI}}}\right)\right] - 2\pi G\, \Sigma_{\mathrm{H_2}} \left[1 - \exp\left(-\frac{2|z|}{z_{0,\mathrm{HI}}}\right)\right] + \frac{1}{r}\frac{\partial v^2_{\mathrm{rot}}}{\partial r} z.$$

By integrating both sides of this last equation between $z = 0$ and $z = +\infty$, the whole initial system finally takes the form of a simple third-degree equation

$$z^3_{0,\mathrm{HI}} \left(\frac{-1}{r}\right) \frac{\partial v^2_{\mathrm{rot}}}{\partial r} + z^2_{0,\mathrm{HI}} \left(2\pi G\Sigma_* + \pi G\Sigma_{\mathrm{HI}} + \frac{4\pi G}{3}\Sigma_{\mathrm{H_2}} - \frac{1}{r}\frac{\partial v^2_{\mathrm{rot}}}{\partial r} z_{0,*}\right) + z_{0,\mathrm{HI}} \left(\pi G\Sigma_{\mathrm{HI}} z_{0,*} + \frac{4\pi G}{3}\Sigma_{\mathrm{H_2}} z_{0,*} - \sigma^2_{z,\mathrm{HI}}\right) - \sigma^2_{z,\mathrm{HI}} z_{0,*} = 0.$$

Solved at each galactocentric distance r, this equation gives the scale-height profile of the atomic gas component $z_{0,\mathrm{HI}}(r)$ for each of our galaxies. This methodology thus allowed us to model galaxies with flaring HI disks (i.e. with a vertical scaleheight increasing with the distance to the center of the galaxy), a well-known property of gaseous disks, observed in edge-on galaxies (e.g. Sancisi & Allen 1979; van der Kruit 1981) and consistent with measurements of gas velocity dispersions in all the galaxies in our sample (Bacchini et al. 2019; Patra 2020).

5.3.4.2 Inputs

The necessary inputs to compute the vertical scaleheight profiles of atomic hydrogen $z_{0,\mathrm{HI}}(r)$ are (i) the SMD profiles of the stellar, atomic, and molecular gas components, (ii) the assumed scaleheight of the stellar (disk) component $z_{0,*}$, (iii) the vertical velocity dispersion of the atomic gas $\sigma_{z,\mathrm{HI}}(r)$, and (iv) the variation of the observed rotation velocity with the galactocentric distance $\frac{\partial v^2_{\mathrm{rot}}}{\partial r}$. While the first two were directly available given the previous products of this work, the last two inputs still had to be computed.

For the vertical velocity dispersion of atomic gas, we used the results of Bacchini et al. (2019) from observations of the 21cm line. Using the datacubes provided by the THINGS team (Walter et al. 2008) and described in

Section 2.4.1, they were able to compute these profiles with the ^{3D}BAROLO software (Di Teodoro & Fraternali 2015), taking into account the various beam-smearing effects that can bias the estimates of the dispersions. These effects can be particularly important for the galaxies with the highest inclinations, observed with the lowest resolutions and/or whose central rotations curves are the most strongly varying (Patra 2020). In our sample of galaxies, NGC2841, NGC7331 and, to a lesser extent, NGC3198 are particularly subject to this problem. A processing of the original datacubes such as the one performed by Bacchini et al. (2019) is thus necessary to correctly estimate the intrinsic vertical velocity dispersions of our galaxies. Nevertheless, as this work is outside the scope of this study, we chose to directly use the results of Bacchini et al. (2019) under the form of analytical models fitted on their profiles $\sigma_{z,\mathrm{HI}}(r)$

$$\sigma_{z,\mathrm{HI}}(r) = \sigma_{0,\mathrm{HI}} \ \exp\left(\frac{-r}{r_{\sigma,\mathrm{HI}}}\right) \tag{5.13}$$

where $\sigma_{0,\mathrm{HI}}$ is the vertical velocity dispersion (of the atomic hydrogen) at the galaxy center and $r_{\sigma,\mathrm{HI}}$ is the scalelength of the profile. These parameters' best-fitting values are given by Bacchini et al. (2019) and gathered in the first two columns of Table 5.4.

For the term associated to the derivative of the RCs, we did not compute it directly on the observed RCs at our disposal (Lelli et al. 2016a). Indeed, we wanted to avoid any nonphysical values due to the intrinsic stochastic variations associated to real observations (Patra 2020). We thus preferred to model the RCs with a Brandt function (Brandt 1960)

$$v_{\mathrm{rot}}(r) = \frac{r}{r_{\mathrm{max}}} \ \frac{v_{\mathrm{max}}}{\left[\frac{1}{3} + \frac{2}{3}\left(\frac{r}{r_{\mathrm{max}}}\right)^{n_B}\right]^{3/2n_B}} \tag{5.14}$$

where v_{max} is the maximum velocity of the RC, r_{max} is the distance from the center of the galaxy at which $v_{\mathrm{rot}} = v_{\mathrm{max}}$ and n_B is an index associated to the rising part of the RC. The best-fit parameters for each of our galaxies are given in the last three columns of Table 5.4. This modeling thus transformed the observed RCs and their derivatives into continuous, slowly evolving functions.

Table 5.4: Best-fit parameters for the modeling of the two inputs (the atomic gas vertical velocity dispersion profile and the RC) necessary to compute the scaleheight of atomic gas $z_{0,\mathrm{HI}}(r)$ in all the galaxies of our sample

Galaxy	Velocity disp.†		Rotation curve‡		
	$\sigma_{0,\mathrm{HI}}$ [km s^{-1}]	$r_{\sigma,\mathrm{HI}}$ [kpc]	v_{max} [km s^{-1}]	r_{max} [kpc]	n_B
NGC2403	14.7	22.5	130.6 ± 0.2	14.7 ± 0.4	0.42 ± 0.01
NGC2841	15.2	84.4	313.7 ± 1.7	6.4 ± 1.1	0.19 ± 0.03
NGC2976	14.2	12.4	87.6 ± 3.9	2.3 ± 0.3	5.0 ± 1.9
NGC3198	17.9	42.6	156.9 ± 0.6	16.4 ± 0.3	0.72 ± 0.03
NGC5055	18.7	36.7	206.4 ± 0.3	10.3 ± 0.1	0.46 ± 0.01
NGC7331	32.6	21.4	250.6 ± 4.8	2.7 ± 3.2	0.07 ± 0.05

† Best-fit parameters from Bacchini et al. (2019) for an exponential profile described by Equation 5.13
‡ Fitted on the observed RCs (Lelli et al. 2016a) with Brandt profiles (Equation 5.14)

5.3.4.3 Results

The resulting scaleheight profiles of the disk-distributed luminous components are shown in Figure 5.5.

The modeled disks of atomic (dark green upward triangles) and molecular (light green downward triangles) are both flaring with increases of their scaleheights of 2–3 orders of magnitude. As they are supposed to be considerably less extended than the stars, these gaseous components are usually described as infinitely thin disks in RC studies. With regards to our 3D modelings, this assumption is valid in the inner regions of the galaxies where the stars' scaleheights (solid and dashed blue lines) are significantly larger than the gaseous ones. Nevertheless, as we begin to move away from the galactic centers (in regions sometimes as close as $\sim 0.4\ r_{25}$ in the case of NGC2403), this approximation does not hold anymore.

When compared to other 3D modelings of galaxies in literature (e.g. Bacchini et al. 2019; Patra 2020), our results are of the same order of magnitude but systematically higher than their scaleheight estimates (in the galactic inner regions, common to both their and our analyses). This is expected as such studies also modeled the DM component of the galaxies,

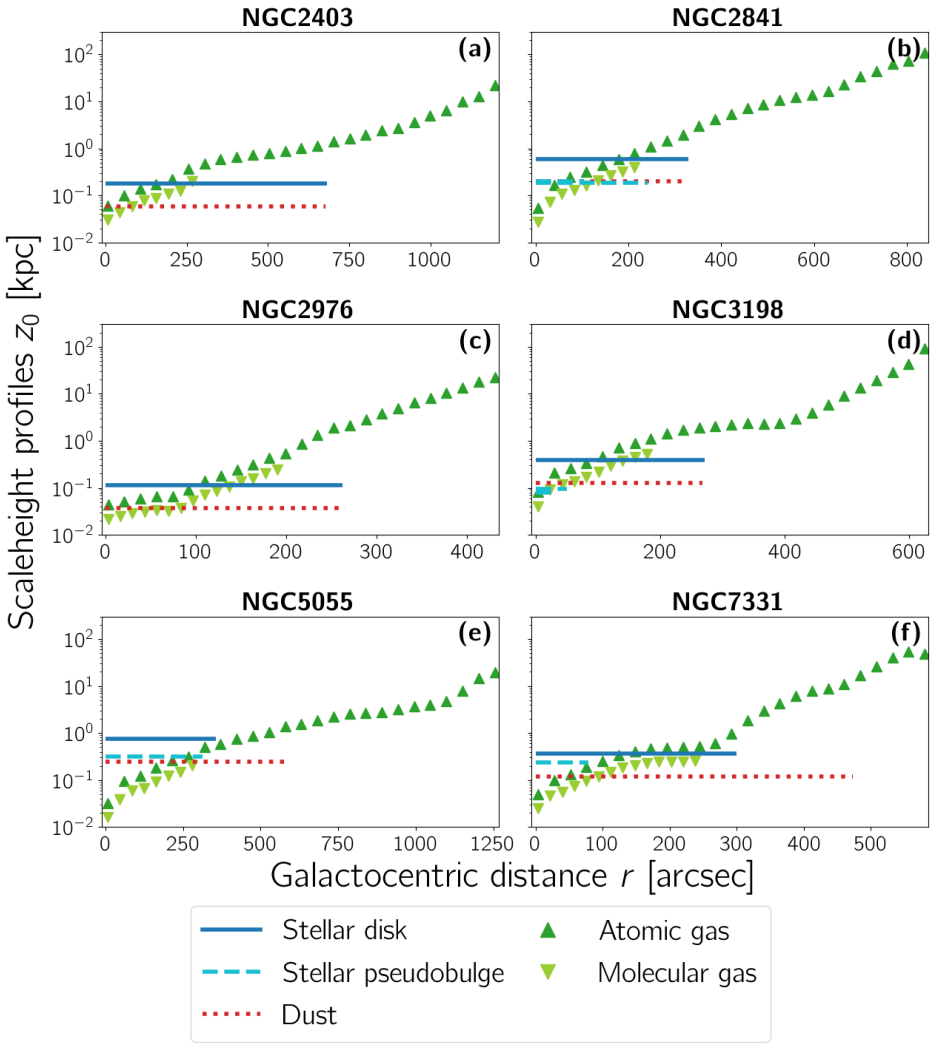

Figure 5.5: Scaleheight profiles of the appropriate luminous components (*stellar disk:* solid dark blue lines – *stellar pseudobulge:* dashed cyan blue lines – *atomic gas:* dark green upward triangles – *molecular gas:* light green downward triangles – *dust:* dotted red lines) of all the galaxies in our sample. For the pseudobulges, the scaleheight values vary with the chosen decomposition but they have not been differentiated in the figure.

which we neglected here. Indeed, with additional DM mass, the balance, between the gravitational force exerted by the whole galaxy and the pressure associated to the velocity dispersion of the gaseous components, occurs closer to the mid-plane, resulting in a flattening[8] of the gaseous disks.

Hence, not taking into account the DM component in the 3D modeling of the galaxies results in thicker disks of gas or, in other words, in disk whose mass is located farther away from the galactic mid-plane. Interpreted in term of RC, the rotation velocities associated to the luminous components' distribution will be smaller. This will increase the discrepancy between the observed and the modeled RCs and thus the necessity for a DM component. This situation with opposite effects is beneficial for us as it makes it possible to model the 3D distributions of galaxies without assuming DM halo models (Narayan & Jog 2002b; Bacchini et al. 2019; Patra 2020). Indeed, after the computation of the RC of our thick gas disk and the characterization of the DM content, an iterative process could be implemented with multiple steps, each composed of a determination of the gas scaleheight profile (this time, taking into account the DM component) followed by a new DM characterization. Once converged, these iterations would end up with the final characterization of DM as well as the associated gas scaleheight profiles.

5.4 Conclusion

At this point, we have performed a complete 3D modeling of all the galaxies in our sample. For that, we have followed the work initiated in Chapter 4 and have determined the SMD profiles of the dust, atomic, and – more uniquely – molecular gas components. We have also systematically separated their stellar content into two dynamical structures associated to different vertical distributions. Finally, we have deprojected all these SMDs in order to describe the galaxies as 3D objects in hydrostatic equilibrium and allow thick flaring disk distributions for their gas components. If all these steps have been implemented in some individual works studying RCs of spirals, they are rarely combined altogether, and not with the level of complexity developed here.

[8] It is worth noting that, even when the DM component is modeled, the flaring of the gas is still important enough to invalidate the approximation of an infinitely thin disk (Bacchini et al. 2019).

All the ingredients are now gathered to reach the primary goal of this work, describing the RCs associated to the luminous components of spiral galaxies and comparing them to their observational counterparts. Nevertheless, with all the products and byproducts computed along the way, the methodology developed here is an indubitably versatile tool. Indeed, the galaxies in our sample can now be studied in numerous different ways by computing a multitude of relations between their modeled components (gas vs dust, molecular gas vs stars, gas vs present SFR, to name but a few of the most famous examples; e.g. Leroy et al. 2008; Mosenkov et al. 2019; Nersesian et al. 2019; Casasola et al. 2020). By increasing the number of studied galaxies (with a wider range of masses and of types), statistics could then be drawn to bring additional constraints not only on the kinematics of spiral galaxies but also on models of formation and evolution of these objects.

Chapter 6

Rotation curves
Characterizing mass discrepancies and dark matter contents

The mass modeling of all the luminous components of spiral galaxies being complete, the ultimate step of the methodology developed in this work can be performed. Through the discrepancies between the observed RCs and the ones expected from these modelings, the last of the galactic components, the non-luminous or DM one, is now accessible. In this last modeling, we continue to avoid as much as possible assumptions commonly used in RC studies. With the aim of independently characterizing and constraining this still unknown component, we limit the hypotheses on the DM distribution to their strict minimum, assuming only disk or spherical symmetries.

In this chapter, we thus convert the 3D densities of all the galactic luminous components into RCs in Section 6.1. Comparing them with the observed RCs, we then characterize the DM content of galaxies in Section 6.2. Along the way, we also analyze the pertinence of the methodology developed in this work by comparing the impacts of our more realistic alternative modelings with respect to the simplifying hypotheses usually performed in RC studies.

6.1 RCs of luminous components

From the 3D densities of the different luminous components of our galaxies, it is possible to compute the individual contributions of each of these components to the global RC. These contributions are defined as the evolution, with the galactocentric distance, of the circular velocity of a particle of negligible mass orbiting in the gravitational potential associated to the considered component. Depending on the 3D structure of the component, this computation is more or less straightforward. For a spherical distribution, the resulting RC is analytical and hence very easily computable. For other distributions, a numerical derivation of the RC is often the only possible solution.

6.1.1 Deriving RCs from spherical mass distributions

For a spherically symmetric distribution, the situation is quite simple. The motion of a test particle is only impacted by the total amount of matter embedded in its orbit. The gravitational potential Φ associated to a spherical distribution is given by

$$\Phi(r) = -\frac{GM(r)}{r}$$

where G is the gravitational constant and $M(r)$ is the total mass embedded inside the sphere of radius r. Hence, computing the gravitational acceleration and equalizing it to the centripetal one, we have

$$\left|\frac{d\Phi}{dr}\right| = \frac{GM(r)}{r^2} = \frac{v_c^2(r)}{r}, \tag{6.1}$$

allowing for an easy calculation of the circular velocity of test particles at various distances r if the masses inside their orbits are known.

In this work, the only luminous component of spiral galaxies that is assumed to be distributed with a spherical symmetry is the classical bulge. Its associated density $\rho_{*,\mathrm{bulge}}$ derives from the deprojection in 3D of its Sérsic SMD profile (given by Equation 5.8). Integrating this density over spheres of increasing radii, the embedded mass $M(r)$ is given as a function of the parameters of the Sérsic function that models the bulge (Lima Neto et al. 1999):

$$M(r) = 2\pi n_S \frac{\Sigma_{\mathrm{eff,bulge}}\ r_{\mathrm{eff,bulge}}^2}{\exp(b_{n_S})\ b_{n_S}^{2n_S}}\ \frac{\Gamma(2n_S)\ \gamma(a, x(r))}{\Gamma[(3-p_{n_S})n_S]}$$

where γ is the lower incomplete gamma function defined by $\gamma(a,x) = \int_0^x t^{a-1}\mathrm{e}^t dt$. Here, its arguments a and $x(r)$ are also only functions of the Sérsic parameters and of the galactocentric distance as $a = (3-p_{n_S})n_S$ and $x(r) = b_{n_S}(r/r_{\mathrm{eff,bulge}})^{1/n_S}$.

Hence, the embedded masses and the associated RCs of the classical bulges of the galaxies in our sample can be directly computed after their bulge/disk decomposition.

6.1.2 Deriving RCs from non-spherical mass distributions

For the non-spherically distributed components, the computation is generally not that straightforward. Simple ways to calculate the RC of a galaxy exist but only if its SMD is described by a certain number of analytical models (Binney & Tremaine 2008). As we wanted to directly use the profiles computed in the previous chapters and not some analytical approximations of them, we had to numerically compute the RCs associated to the components without spherical symmetry (i.e. every component with the exception of the classical bulges).

Similarly to the mathematical developments performed for a spherical distribution, the derivation of the RC associated to a particular component results from the equality on a test particle of (i) the gravitational acceleration created by the total mass distribution of this component and (ii) the centripetal acceleration that makes it orbit in the galactic mid-plane. Using once again cylindrical coordinates, we distributed various test particles in the mid-plane of the galaxy (for which $z = 0$) and on the same line (for which $\theta = 0$) at different distances r.

On each test particle, we computed the element of gravitational acceleration $d\vec{a}_g$ associated to the presence of an infinitesimal element of mass dM located at coordinates (r', θ', z') with

$$d\vec{a}_g(r) = -\frac{G\ dM(r',\theta',z')}{d^{3/2}}\ \vec{d}$$

where the vector $\vec{d}$ connects the element dM and the test particle. Its norm is symbolized by d and it components are $(r - r'\cos\theta', -r'\sin\theta', -z')$. Then, an integration on all the elements dM (or equivalently $\rho(r',\theta',z')dV$) of the galaxy provides the total gravitational acceleration on the given test particle. Due to the assumed axisymmetry and symmetry with respect to the galactic mid-plane, the transverse and the vertical components of the

acceleration are both null, leaving only the radial component whose norm is given by

$$a_{g,r}(r) = \int_0^{+\infty} \int_0^{2\pi} \int_{-\infty}^{+\infty} \frac{G\ (r - r'\cos\theta')\rho(r', \theta', z')}{(r^2 + r'^2 - 2rr'\cos\theta' + z'^2)^{3/2}}\ r' dz' d\theta' dr'.$$

Aa all the non-spherical components studied in this work are disk-distributed with densities $\rho(r', \theta', z')$ described by Equation 5.5, this expression can be substituted in the last equation. The RC associated to each disk-distributed component is then given by the integral

$$v_c^2(r) = r \int_0^{+\infty} \Sigma(r') K_{3\mathrm{D}}(r, r') dr' \tag{6.2}$$

where the kernel $K_{3\mathrm{D}}$ is expressed as

$$K_{3\mathrm{D}}(r, r') = \frac{2Gr'}{z_0(r')} \int_0^{\pi} \int_0^{+\infty} \frac{(r - r'\cos\theta')\ \mathrm{e}^{-z/z_0(r')}}{(r^2 + r'^2 - 2rr'\cos\theta' + z'^2)^{3/2}} dz' d\theta'. \tag{6.3}$$

6.1.3 RCs of luminous components

The RCs associated to each luminous component of all the galaxies in our sample are shown in Figure 6.1. We represented with different colors and symbols the rotation velocity of a test particle orbiting in the gravitational potential created by each individual component (dark blue dots for the stellar disk, cyan blue stars for the bulge, dark green upward triangles for the atomic gas, light green downward triangles for the molecular one and red squares for the dust).

To compare the results of our modelings with the effectively observed RCs (brown plus signs; Lelli et al. 2016a), all the individual velocities have been combined through a quadratic sum to determine the rotation velocities expected from the global mass distribution of all the galactic luminous components:

$$v_{\mathrm{lum}}^2 = v_{*,\mathrm{disk}}^2 + v_{*,\mathrm{bulge}}^2 + v_{\mathrm{at.\ gas}}^2 + v_{\mathrm{mol.\ gas}}^2 + v_{\mathrm{dust}}^2.$$

It is worth noting that if the mass distribution of a galactic component presents a central depression (which is often the case for the atomic gas), the gravitational acceleration on test particles located in this region will be directed outwards instead of inwards. Mathematically, this translates

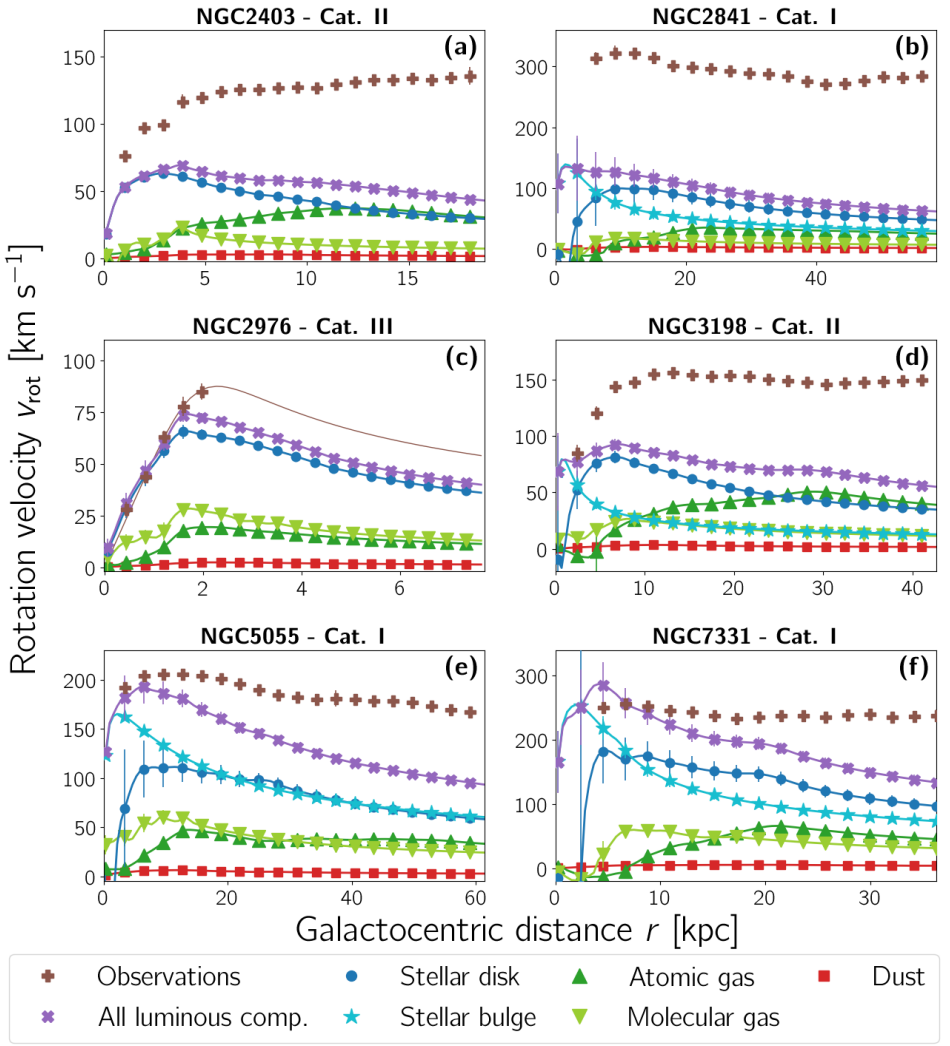

Figure 6.1: RCs of all the galaxies in our sample. The individual RCs associated to each luminous components (*stellar disk:* dark blue dots – *stellar bulge:* cyan blue stars – *atomic gas:* dark green upward triangles – *molecular gas:* light green downward triangles – *dust:* red squares) are combined to give the expected RC (purple crosses) that can then be compared to the effectively observed one (brown plus signs; Lelli et al. 2016a). The portions of RCs associated to gravitational accelerations directed towards the outskirts of the galaxies are artificially depicted with negative velocities values. The stellar

Figure 6.1 (continued): RCs result from modelings with the Exp-1pop library and from CDD bulge/disk decompositions. The molecular gas RC derive from the mass profiles computed with $X_{CO}(Z_{resc})$ factors. For NGC2976 (panel (c)), we also show the best-fit Brandt function (Equation 5.14; brown thin line) that could be used to extrapolate the observed RC to the whole region on which luminous components are observed.

---

into negative values of squared velocities (or complex values of velocities), not displayable in RC representations. To not lose this information when using and showing RCs, a negative sign is assigned by convention to the rotation velocities of these regions. In Figure 6.1, this has been done for the innermost data points of the gaseous and stellar disks RCs of NGC2841, NGC3198 and NGC7331. Hence, when computing the quadratic sum to determine the global RC of a galaxy, this convention, and the artificial negative signs it implies, should not be overlooked.

6.2 RC discrepancy and DM content

The discrepancy, displayed in Figure 6.1, between the observed RCs (brown plus signs) and the ones expected from the mass modelings of the galactic luminous components (purple crosses) is typical of spiral galaxies. For half a century, this has been interpreted as the sign of the existence of a massive non-luminous component within the galaxy, the DM. The rotation velocity associated to this component is easily obtained as

$$v_{\rm DM}(r) = \sqrt{v_{\rm obs}^2 - v_{\rm lum}^2}.$$

From it, the gravitational field, and hence the mass distribution, of this component can be deduced and compared with other indirect observations of DM in order to understand the nature of this still unknown constituent of our universe.

In RC studies, the DM component of is usually described with specific analytic models derived not from the RCs themselves but from theoretical considerations or cosmological simulations of our universe. The two most widespread models, the cored pseudo isothermal (PIS) and the Navarro-Frenk-White (NFW) ones, have been presented in Chapter 1. In this work,

nevertheless, we wanted to characterize the non-luminous component of spiral galaxies with the smallest possible number of hypotheses. We thus decided to get rid of these models and to only describe the quantity of additional matter so that the resulting expected RC of the galaxy matches the observed one. After having performed this independent characterization, it will then still be possible to fit the DM models derived from other constraints. This will be realized in Section 6.2.5.

6.2.1 Deriving mass distributions from RCs

To derive the mass distribution of DM from its RC, it is necessary to reverse the conversion realized at the beginning of this chapter. Similarly to what has been done then, an assumption has to be made on the 3D structure of the DM component. In the overwhelming majority of recent studies, galactic DM is taken as distributed in a spherical halo. However, in this work, we also wanted to test the possibility to have DM distributed as luminous matter (hence, in a disk). This idea has been proposed a few decades ago by works such as the ones by Pfenniger et al. (1994), Gerhard & Silk (1996) or Read et al. (2008). We thus decided to also model the galactic DM as disks, that we assumed here to be infinitely thin. While this no-thickness hypothesis is non-physical, it has the advantage to represent an extreme case of DM disk-distribution and thus to provide a lower limit for thick-disk profiles.

For both distributions, it is necessary to inverse the Equations 6.1 and 6.2 established to associate the velocity of test particles to the mass profiles of the galaxies. The spherical symmetry greatly facilitating the computations, the inversion of Equation 6.1 is straightforward. For the disk distributions, however, things are more complicated as we face an inverse problem. Indeed, knowing the effects (here, the velocity profile $v_{\rm DM}(r)$), it is necessary to determine the causes (the SMD $\Sigma_{\rm DM}(r)$ of the galaxy). The equation to inverse is then a slightly modified version of Equation 6.2,

$$v_{\rm DM}^2(r) = r \int_0^{+\infty} \Sigma_{\rm DM}(r'), K_{\rm 2D}(r, r') dr'$$

where, due to the modeling of DM as an infinitely thin disk, the kernel is now given by

$$K_{\rm 2D}(r, r') = 2Gr' \int_0^{+\infty} \frac{r - r' \cos\theta'}{(r^2 + r'^2 - 2rr' \cos\theta')^{3/2}} d\theta'.$$

This inverse problem can be solved through an iterative process, starting from a rough estimate of the SMD profile $\Sigma_{\rm est}(r)$ (here chosen as the $\Sigma_{\rm DM}(r)$ if a spherical symmetry is assumed). To determine the "real" DM SMD $\Sigma_{\rm DM}(r)$, the corrections $\delta\Sigma(r)$ to apply to our rough estimate ($\Sigma_{\rm DM}(r) = \Sigma_{\rm est}(r) + \delta\Sigma(r)$) are computed by solving the integral equation rewritten as

$$\delta v^2(r) = v^2_{\rm DM} - v^2_{\rm est} = r \int_0^{+\infty} \delta\Sigma(r') K_{\rm 2D}(r, r') dr'$$

where $v_{\rm est}(r)$ is the rotational velocity associated to the SMD profile $\Sigma_{\rm est}(r)$ assuming a 2D disk distribution.

Discretizing this equation for each galactocentric distance r_i ($i = 1...N$) results in a system of N equations with N unknowns

$$\delta v_i^2 = r_i \sum_{j=1}^{N} \delta\Sigma_j \; K_{ij} \; dr_j$$

with $\delta v_i^2 = \delta v^2(r_i)$, $\delta\Sigma_j = \delta\Sigma(r'_j)$ and $K_{ij} = K(r_i, r'_j)$. A minimization of a least-square estimator can then be used to solve the system. Unfortunately, as is often the case for inverse problems such as this one, it is ill-posed and its solution is not stable (small modifications of the data produce very different solutions). A regularization term has thus to be added to the least-square estimator to impose some constraints (often on the smoothness) of the solution. With this restriction, it is then necessary to work iteratively to come closer and closer to the final solution as the amplitude of the corrections at each step is limited. In this work, we chose to use the relatively simple and common Tikhonov regularization, consisting in minimizing the norm of the solution or, in other words, in imposing the corrections $\delta\Sigma_j$ to be as small as possible. With this regularization, the sum

$$S = \sum_{i=1}^{N} \left(r_i \sum_{j=1}^{N} \delta\Sigma_j K_{ij} dr_j - \delta v_i^2 \right)^2 + \eta \sum_{j=1}^{N} \left(\delta\Sigma_j\right)^2$$

has to be minimized, the parameter η controlling the importance of the regularization term. Its value is arbitrary chosen to make a compromise between the stability of the solution and the rapidity of the convergence (as higher values of η impose smaller corrections, hence more iterations).

To find the corrections $\delta\Sigma_j$ minimizing S, it is necessary to build the system of N equations that express the canceling of the N derivatives of S with respect to each of these corrections:

$$\frac{\partial S}{\partial \delta\Sigma_k} = 0 \quad (k = 1...N).$$

The latter can then be written more compactly as a matrix equation

$$\mathcal{V} = \delta\Sigma \, (\mathcal{K} + \eta\mathcal{I})$$

where $\mathcal{I}$ is the identity matrix $(N \times N)$ and where the elements of the vector $\mathcal{V}$ $(N \times 1)$ and of the matrix $\mathcal{K}$ $(N \times N)$ are given by

$$\mathcal{V}_k = \sum_{i=1}^{N} K_{ik} \delta v_i^2 \quad \text{and} \quad \mathcal{K}_{jk} = \sum_{i=1}^{N} K_{ij} K_{ik}.$$

The inversion of this matrix equation then allows to determine the vector of corrections $\delta\Sigma$. Applying these corrections on Σ_{est} gives a better estimate of the DM SMD, that can then be used to compute a new estimate of the RC and iteratively converge towards the SMD profile that finally produces the RC associated to the DM content of the galaxy. The iteration is then stopped when the corrections to apply are too small to have any visible impact on the RC.

One may note that nothing here forbids the final SMD profile to have negative values, a non physical situation that is a natural consequence of our numerical computations in the centers of the galaxies, where the RC associated to all the galactic luminous matter can be higher than the observed RC. It is the case, mainly for NGC7331 as can be seen in panel (f) of Figure 6.1. At each iteration, we thus restricted the estimated mass profiles to positive values (by canceling all the non-physical negative masses) before computing the associated RC.

6.2.2 Characterizing the DM component

In Table 6.1, we present the resulting total masses of non-luminous matter that should be added in the galactic disk (second and third columns) or as a spherical halo (fourth and fifth columns). As expected, when distributed within the galactic disk, less DM is necessary to explain the observed velocity discrepancies than for a spherical distribution.

Table 6.1: Comparison between the total mass (in the region probed by the observed RCs) of the luminous and DM components for all the galaxies in our sample

	Lum. comp.†	DM disk dist.		DM sphere dist.	
Galaxy	$\log(M_{\rm lum})$	$\log(M_{\rm DM})$	$\frac{M_{\rm DM}}{M_{\rm lum}}$	$\log(M_{\rm DM})$	$\frac{M_{\rm DM}}{M_{\rm lum}}$
NGC2403	$9.87^{+0.34}_{-0.82}$	10.61 ± 0.01	5.5	$10.84^{+0.05}_{-0.06}$	9.4
NGC2841	$10.69^{+0.39}_{-0.50}$	11.81 ± 0.01	13.2	$12.03^{+0.02}_{-0.03}$	21.8
NGC2976	$9.42^{+0.40}_{+0.48}$	9.25 ± 0.02	0.2	$9.09^{+0.09}_{-0.11}$	0.5
NGC3198	$10.43^{+0.36}_{-0.66}$	11.06 ± 0.01	4.2	$11.28^{+0.02}_{-0.02}$	7.1
NGC5055	$11.05^{+0.37}_{-0.61}$	11.22 ± 0.01	1.5	$11.43^{+0.03}_{-0.03}$	2.4
NGC7331	$11.10^{+0.36}_{-0.65}$	11.24 ± 0.01	1.4	$11.51^{+0.05}_{-0.05}$	2.6

† Sum of total masses of the stellar (for the Exp-1pop library; from Table 4.5), gaseous and dust (from Table 5.1; the mass of molecular gas is computed with the conversion factor $X_{\rm CO}(Z_{\rm resc})$) components

It has to be noted that with our modeling, we can only probe the region on which the RCs have been observed. Hence, this limits the spatial extension of the DM component of each galaxy to the one of its atomic gas disk. However, according to actual models of DM, this component should be considerably more extended than the region we are able to probe here. The DM masses given in the table are thus minimum bounds on the total DM mass of each galaxy.

When compared to the total mass of luminous components (first column of Table 6.1), we can separate the galaxies into different categories that also correspond to the ones based on their RC shape (defined in Chapter 2). Galaxies with a RC of category I (the spirals of early type: NGC5055, and NGC7331) require less DM ($M_{\rm DM} \approx 2M_{\rm lum}$) than the ones of category II (the spirals of intermediate type: NGC2403 and NGC3198; $M_{\rm DM} \approx 5 - 8M_{\rm lum}$, depending on the assumed DM 3D distribution). This increase of DM quantity as we study spirals of later type is expected and well known (e.g. Persic et al. 1996). Nevertheless, two galaxies in our sample, NGC2841 and NGC2976, do not match this tendency.

NGC2976

NGC2976 is the only representative of the category III RCs. The galaxies with such a RC shape are late-type, dwarf and/or low-surface brightness spirals that are commonly described as heavily dominated by their DM halo, even in their very inner regions (e.g. Carignan & Beaulieu 1989; de Blok & McGaugh 1997; Côté et al. 2000). This property makes these galaxies an ideal laboratory to understand DM as the modeling of the galactic luminous matter seems less crucial. *A priori*, NGC2976 is not an exception as its RC has already been decomposed by Simon et al. (2003) or Saburova et al. (2016) to find a domination of DM at all galactocentric distances.

However, in the regions probed in this work, our results do not go in this direction. Indeed, with our galactic modeling, nearly all the observed RC of NGC2976 (brown plus signs in panel (c) of Figure 6.1) is explainable by its luminous (and particularly by its stellar) components (respectively in purple crosses and in blue dots). In this case, the DM total mass corresponds to only 20 to 50% of the total luminous mass. As the RC at our disposal is only built on Hα and CO observations, it is limited to the central regions of NGC2976. Nevertheless, even if we extrapolate it with the Brandt profile fitted in Section 5.3.4.2 (shown with the thin brown line in the same figure), the DM mass ratio slightly increases (reaching values of 70 to 90% of the mass of the other components) but not enough to dominate the mass budget.

Here, the key to understand this situation lies in the modeling of the stellar populations of NGC2976. Indeed, studies predicting a domination by DM base their stellar modeling on NIR images with free mass-to-light ratios, leading to very low best-fit values (0.19 for Simon et al. (2003); 0.23 for de Blok et al. (2008); 0.16 or 0.20 for Saburova et al. (2016)). On the contrary, when these ratios are fixed to higher values (around 0.5 as done by Lelli et al. 2016a or by de Blok et al. 2008 and Saburova et al. 2016 for some of their decompositions), the stellar component is always found to be dominant across the region where the observed RC is derived. Such behavior is also found in other late-type dwarf and LSB spirals (Swaters et al. 2011).

The value of the stellar mass-to-light ratio is therefore extremely important to correctly characterize the quantity of DM in the inner regions of NGC2976 (and probably of the other galaxies of this category). Contrary to what is usually thought, the luminous components of such types

of galaxies are primordial to model accurately in order to study their DM content. A RC decomposition like the one developed in this work, where the stellar mass-to-light ratio is not derived from the RC itself but is rather computed independently via the modeling of the populations of stars, is thus particularly important to study such galaxies.

NGC2841

The case of NGC2841, the spiral with the earliest type in all our sample, is more enigmatic. Indeed, the rotation of the inner regions of such galaxies should be heavily dominated by their luminous (and particularly stellar) components, as it is the case for NGC5055 and NGC7331. Concerning NGC2841 in particular, the contribution of its luminous components is known to be smaller than for usual early-type spirals but it is nevertheless expected to be relatively important, with stellar maximum velocities of 150–200 km/s (de Blok et al. 2008; Samurović et al. 2015; Lelli et al. 2016a). Our stellar RCs never reach such high values, with maximum velocities of respectively ∼140 km/s and ∼100 km/s for the bulge and disk of this galaxy (see curves with cyan blue stars and dark blue dots in panel (b) of Figure 6.1). Even if NGC2841 suffers from a too restrictive prior pdf when fitting its stellar SED (as explained in Section 4.1.5.2), the discrepancy observed in these two determinations of RCs is unlikely to be due to an underestimation of our stellar mass profile. Indeed, when compared with a classical NIR converted profile (see panel (b) of Figure 4.9 on page 117), we find similar results.

Moreover, these seemingly underestimated rotation velocities also occur for the RC associated to atomic gas, a component whose modeling is completely[1] uncorrelated with the stellar one. Indeed, at high galactocentric distances, our RC stabilizes around values of ∼30 km/s (see curve with dark green upward triangles in panel (b) of Figure 6.1). Here again, our values are lower than the 40–50 km/s found by other studies (de Blok et al. 2008; Samurović et al. 2015; Lelli et al. 2016a).

[1]Strictly speaking, the description in 3D of this gaseous component is impacted by the stellar modeling performed in this work. Nevertheless, as we will show it in the next sections, the thickness of the gas components has a very small, nearly negligible, impact on their RC. Hence, the RC of atomic gas we derive in this work can be considered as independent of the stellar modeling.

The underestimations of these two uncorrelated RCs hints towards a reason related to one of the general properties of the galaxy used for all our modelings. As the distance of this galaxy is computed via the reliable relation between the magnitude and the period of Cepheids, the other possible galactic property that could have such an impact is the inclination of the galaxy. In this work, we used this property to transform the profiles of the observed inclined galaxies into face-on profiles. An error in the estimate of this property would thus impact all our luminosity and mass profiles as well as the associated rotation curves.

As explained in Section 3.1.2 (page 63), we used in this work the inclinations computed by Lelli et al. (2016a) on HI velocity-field maps and averaged in the outskirts of the galaxies. Nevertheless, if the galactic disk is warped, the inclination may vary with the galactocentric distance and the corrections of the luminosity profiles determined in the outskirts of the galaxies could then be incorrect in their inner regions. This could thus explain the puzzling large discrepancy between the expected and the observed RCs of NGC2841. Analyzing the inclination profile of its HI disk (de Blok et al. 2008), we can clearly see a monotonic increase from 70° in the stellar disk of the galaxy (up to galactocentric distances of ∼200 arcsec or 13 kpc, corresponding to approximately the characteristic radius r_{25} of NGC2841) to ∼ 80° in the outskirts of its HI disk. When estimated on optical images from the determinations of apparent ellipticities that we performed in Chapter 3 or from the HyperLEDA database (Makarov et al. 2014), the inclinations of the stellar disk of NGC2841 have values similar to the ones found in the central regions of the HI disk with ∼65°.

Hence, a significant bias could originate from the use of the outer determination of the inclination of NGC2841 (76°; Lelli et al. 2016a) in its centers instead of more realistic values (∼65°). As the face-on correction on the profiles depend on the cosine of the inclination, this bias can be roughly estimated to reductions by 40% of the luminosity and mass profiles of NGC2841 in its central regions. Translated in term of rotation velocities, this gives RCs that have to be multiplied by a factor ∼1.3 to take this incorrect inclination into account, strongly decreasing the discrepancy we found between the results from in this work and from previous studies.

Hence, the results shown in the next sections, on the characterization of the DM content of NGC2841, should be taken with caution. Indeed, neglecting the monotonic evolution of the galactic disk inclination increases the RC discrepancy and thus the need for DM. This evolution should thus be

directly taken into account and incorporated in our modelings to effectively draw conclusions on warped galaxies such as NGC2841. One may note that in our sample, NGC5055 also exhibit a strong warp of its HI disk. Nevertheless, this warp does not translates into a monotonic variation of its inclination, resulting in an inclination in the outskirts of the HI disk (given by Lelli et al. 2016a and used in this work) similar to the one in the stellar disk that we probed. The RCs we derived for NGC5055 are thus reliable.

6.2.3 Effects of the usual simplifying hypotheses on the DM mass

In this work, we developed a more realistic modeling of all the luminous components of spiral galaxies by getting rid of many widely used simplifying approximations in order to accurately characterize their DM content. In the previous section, the given values of DM mass were derived when all these approximations had been replaced by our alternatives. In this section, we study the individual impact of each approximation.

By default, we modeled the galaxies with all our alternative hypotheses (highlighted in blue in Table 6.2). We then computed the resulting DM quantity to add in the galaxy in order to explain the RC discrepancies. The other rows of this table show the supplementary modelings, performed to isolate the effects of each individual hypothesis.

The results are shown in Figures 6.2 and 6.3 where we display, for each galaxy and for each individual hypothesis, the value of the ratio between the DM mass resulting from the modeling with our alternative hypothesis and the mass from the modeling with its usual counterpart. Hence, a point located at an abscissa of 1 (highlighted by the black vertical lines) corresponds to a DM component whose mass does not change if we model the galaxy with the usual simplifying hypothesis or with our more realistic alternative. The figures also show the DM mass ratios combining all the hypotheses (purple crosses), hence comparing directly the effect of RC decompositions in usual RC studies ("all-in-one" modeling in Table 6.2) with our complete methodology (default modeling, highlighted in blue in the same table).

As expected from the mass budget of spiral galaxies, taking into account the mass distribution of the dust component (red squares in Figures 6.2 and 6.3) does not modify the DM quantity in the galaxy, or equivalently the global RC associated to its luminous components. Concerning the gaseous

Table 6.2: Different modelings implemented in this work to evaluate the impacts of the simplifying hypotheses usually assumed in RC studies on the DM content of spiral galaxies

	Stel. mod.[†]	Bulge/disk dec.	Gas thick.	Mol. gas	Dust
Modelings with usual simplifying hypotheses:					
Stellar modeling	NIR	✗	✓	$X_{\rm CO}(Z_{\rm resc})$	✓
Bulge/disk decomposition	SED	✗	✓	$X_{\rm CO}(Z_{\rm resc})$	✓
Gas thickness	SED	CDD	✗	$X_{\rm CO}(Z_{\rm resc})$	✓
Molecular gas modeling	SED	CDD	✓	✗	✓
Dust modeling	SED	CDD	✓	$X_{\rm CO}(Z_{\rm resc})$	✗
All-in-one	NIR	✗	✗	✗	✗
Modelings with this work alternatives:					
Default modeling	**SED**	**CDD**	✓	$\boldsymbol{X_{\rm CO}(Z_{\rm resc})}$	✓
Stellar modeling	SED	✗	✓	$X_{\rm CO}(Z_{\rm resc})$	✓
Bulge/disk decomposition[‡]	SED	Classical	✓	$X_{\rm CO}(Z_{\rm resc})$	✓
Molecular gas modeling[‡]	SED	CDD	✓	$X_{\rm CO,\odot}$	✓

[†] NIR: modeling of the stellar component through a conversion of 3.6 μm images assuming a constant stellar mass-to-light ratio of 0.5 – SED: modeling of the stellar component through a global photometric SED fitting

[‡] Performed in addition to the default modeling (hence the two different cyan stars and light green downward triangles for each galaxy in Figures 6.2, 6.3 and 6.6)

components, their modeling as a thick disk (dark green upward triangles) does not modify significantly the quantity of DM in the galaxy. At the maximum, the DM mass increases by ∼2% for NGC3198, a galaxy known to be gas-rich compared to other galaxies of its size and mass (Bottema & Pestaña 2015).

Similarly, the decomposition of the stellar component into a bulge and a disk structure (cyan stars) does not significantly affect the total mass of DM in the galaxy. Only NGC5055 is significantly impacted with an increase of DM mass of ∼3%. This is *a priori* not a surprise as this decomposition affects only the very center of the galaxy. Hence, it should not impact the indicator analyzed here (i.e. the total mass of DM in the whole region probed by the RC). Nevertheless, such decomposition could affect the shape of the DM distribution and be important to discriminate between core and cusp halos (e.g. Korsaga et al. 2018, 2019). We thus discuss this hypothesis in more details in Section 6.2.6 where we compute a more appropriate indicator to study the shape of this halo.

If the effects of these three hypotheses are similar (and small) for all the galaxies analyzed in this work, this is not the case for the two remaining ones. Indeed, the fact that we modeled the usually neglected molecular gas (light green downward triangles) impacts NGC2976, NGC5055, NGC7331 but not NGC2403, NGC2841 or NGC3198. If the effect is rather low on NGC5055 and NGC7331 (<5 %), it is particularly important for NGC2976 with a DM mass reduction of ∼20 % if its low metallicity is taken into account. This result contradicts the ones from Frank et al. (2016) for this galaxy, as they found that the molecular gas of NGC2976 does not contribute greatly to its global rotation. Nevertheless, Frank et al. (2016) is based on the determination of the conversion factor $X_{\rm CO}$ by Sandstrom et al. (2013) that considered a galaxy metallicity higher – and hence a total mass of molecular gas lower – than ours (see Section 5.1.3).

The most impacting of all the simplifying hypotheses tested in this work is the use of NIR images to model the stellar component of spiral galaxies. For all except one galaxy (NGC2403), the SED modelings resulted in reductions of DM masses by a few to a few tens of percents. Once again, the most affected galaxy is NGC2976 (∼ 30%), followed by NGC5055 and NGC7331 (∼ 10%), then NGC3198 and NGC2841 (∼ 3%). This situation is relatively surprising due to the good correspondence between the mass profiles derived from simple conversion of 3.6 μm images and from complete SED fitting (as shown in Figure 4.9 on page 117). To understand this result,

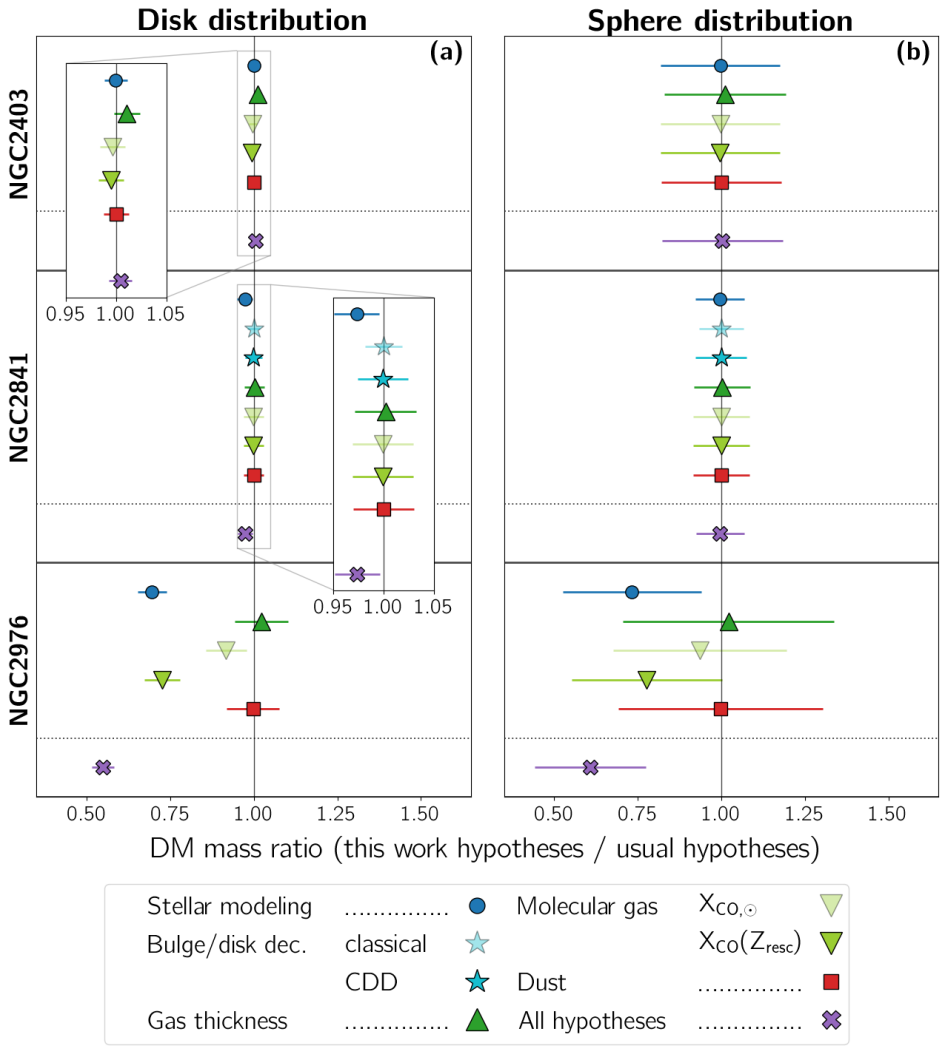

Figure 6.2: Effects of the different simplifying hypotheses tested in this work (see Table 6.2) on the DM mass derived from the RC discrepancies for NGC2403, NGC2841 and NGC2976. The DM component of the galaxies is either modeled as a thin disk (panel (a)) or as a sphere (panel (b)). Each point corresponds to the test of one hypothesis, its abscissa giving the ratio between the DM mass derived with our alternative hypothesis and the mass derived with its usual counterpart. The horizontal dotted lines separate the tests of individual hypotheses and the one which combines them all (purple crosses). Results for NGC2841 should be considered with caution.

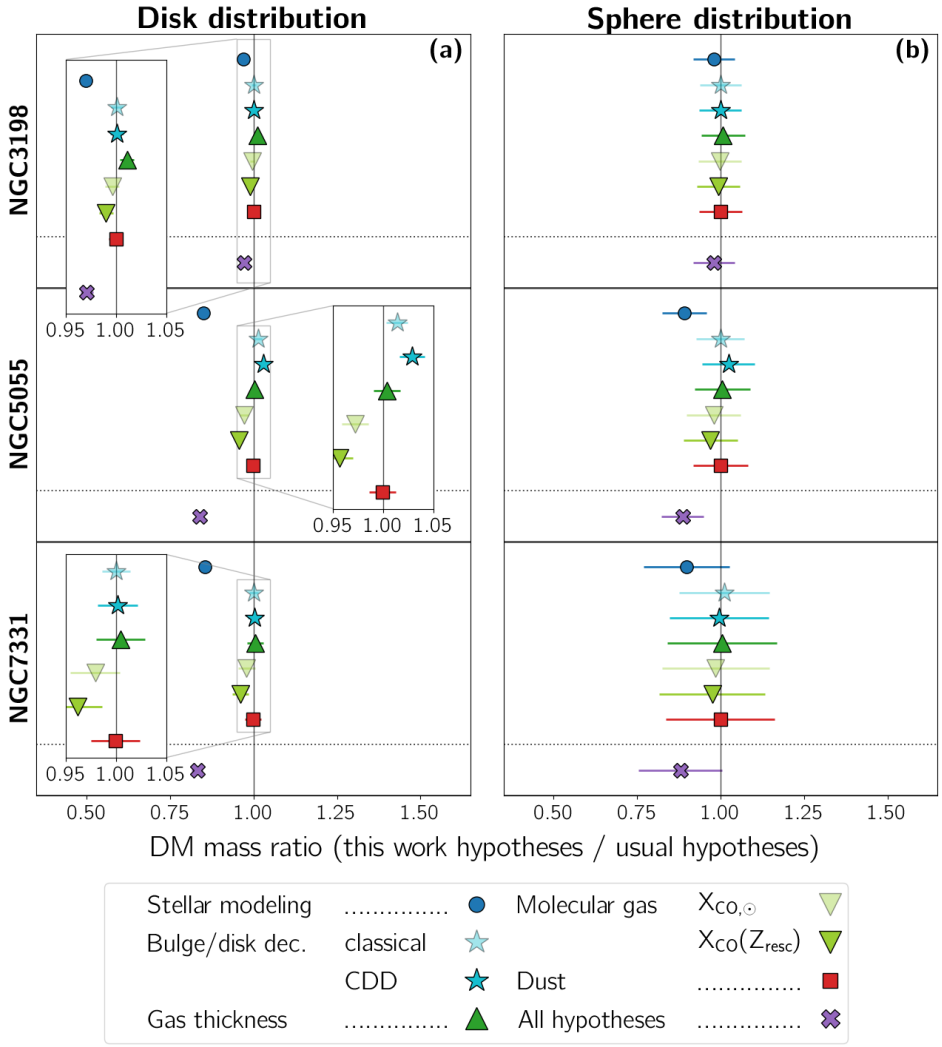

Figure 6.3: Same as Figure 6.2 for NGC3198, NGC5055 and NGC7331.

one has to pay attention to the difference between the two profiles' global slope, particularly in the outskirts of the galaxies. Indeed, to make the most of the data at our disposal during the RC analysis, we extrapolated the luminous components' mass profiles on the whole range of galactocentric distances probed by the observed RCs. Doing so, we amplified the differences between the two mass profiles in the outskirts of the galaxies (where DM dominates the mass budget). This therefore explains the large impact of the stellar modelings on the DM mass of galaxies.

In conclusion, while the simplifying hypotheses usually assumed in RC studies do not have dramatic impacts on the mass budgets, they can nevertheless change the content of DM in the regions probed by the observed RC by up to ∼30%, our more realistic analysis reducing the RC and mass discrepancies.

6.2.4 DM distributed as a disk

Modeling the DM component of spiral galaxies as a thin disk allowed to test an old suggestion by Pfenniger et al. (1994) or Gerhard & Silk (1996) that DM could be constituted of very cold gas. Indeed, since Bosma (1978), the atomic gas SMDs have been observed to scale with the DM ones in the outskirts of spiral galaxies. Assuming a correlation between these two components, the RCs of many spiral galaxies have been successfully decomposed (e.g. Hoekstra et al. 2001; Hessman & Ziebart 2011; Swaters et al. 2012). Among other things, such works found that the factor by which the atomic gas SMDs have to be multiplied to explain the RC discrepancies varies with the type of galaxies (with values of ∼10 for Sa to Sbc spirals, ∼5 for Sc and ∼3 for irregular spirals; Swaters et al. 2012).

If some papers attribute this correlation to a simple consequence of the way the galaxies formed (Zasov & Terekhova 2013; Meurer et al. 2013), other estimate that this could be the sign of the existence of significant amounts of baryonic DM localized in the galactic disk (Hessman & Ziebart 2011). The existence of this kind of matter, very challenging to detect due to its low emissions, is also supported by recent observations of dark clouds of very cold atomic and molecular gas in the MW and in its neighborhood (e.g. Grenier et al. 2005; Walker et al. 2017; De Paolis et al. 2019; Busch et al. 2021; Seifried et al. 2022; Guo et al. 2022). Moreover, the possibility of disk-distributed DM and the stability of such structures (contrary to what had been found with the 1970s simulations) have been found by

both cosmological simulations and dynamical studies (e.g. Read et al. 2008; Revaz et al. 2009; Das et al. 2020).

With the methodology developed in this work, testing the idea of a disk of baryonic gaseous DM is straightforward as we directly have all the necessary modelings at our disposal. In Figure 6.4, we thus show the SMD profiles of all the galaxies in our sample and we particularly compare the atomic gas (dark green upward triangles) and the DM (black diamonds) ones. We also show the atomic profiles rescaled to match the DM ones (dark green line). The factor by which each profile has been multiplied is given in the lower right corner of each panel. These values, while slightly higher than what is expected from Swaters et al. (2012) results, are still consistent with the global tendency, a decrease with the Hubble type of the galaxy (given in Table 2.1 on page 42). The only exception, here, is NGC2403 which is associated to a relatively high factor compared to the one expected from its late type. Nevertheless, this discrepancy seems due to the object itself rather than to our methodology as our results are in agreement with previous works assuming disk-distributed DM for this particular galaxy (Hoekstra et al. 2001; Hessman & Ziebart 2011).

As can be seen in the figure, the rescaled atomic gas profiles do not match exactly the DM ones in the outskirts of the galaxies as well as in their very centers. In the inner regions, this is due to the fact that the atomic gas is replaced by its molecular form as well as by stellar populations in regions of star formation. This can be taken into account during the RC decomposition (Hessman & Ziebart 2011). However, in the outskirts of the galaxies, this explanation does not hold anymore.

Hence, further investigation should be performed to understand if the apparent correlation between the atomic gas and the dark component of the galaxies is real and if all the DM necessary to explain the RC discrepancies could be located within the disks. In any case, it is highly probable that at least a part of it is in fact hidden in the disk. To perform such a study, the methodology developed in this work is an ideal tool thanks to its very small number of assumptions when computing the DM distributions.

6.2.5 DM distributed as a spherical halo

DM distributions with spherical symmetries are more common in RC studies and, in general, in all studies involving this component. Indeed, theoretical considerations and cosmological simulations predict such symme-

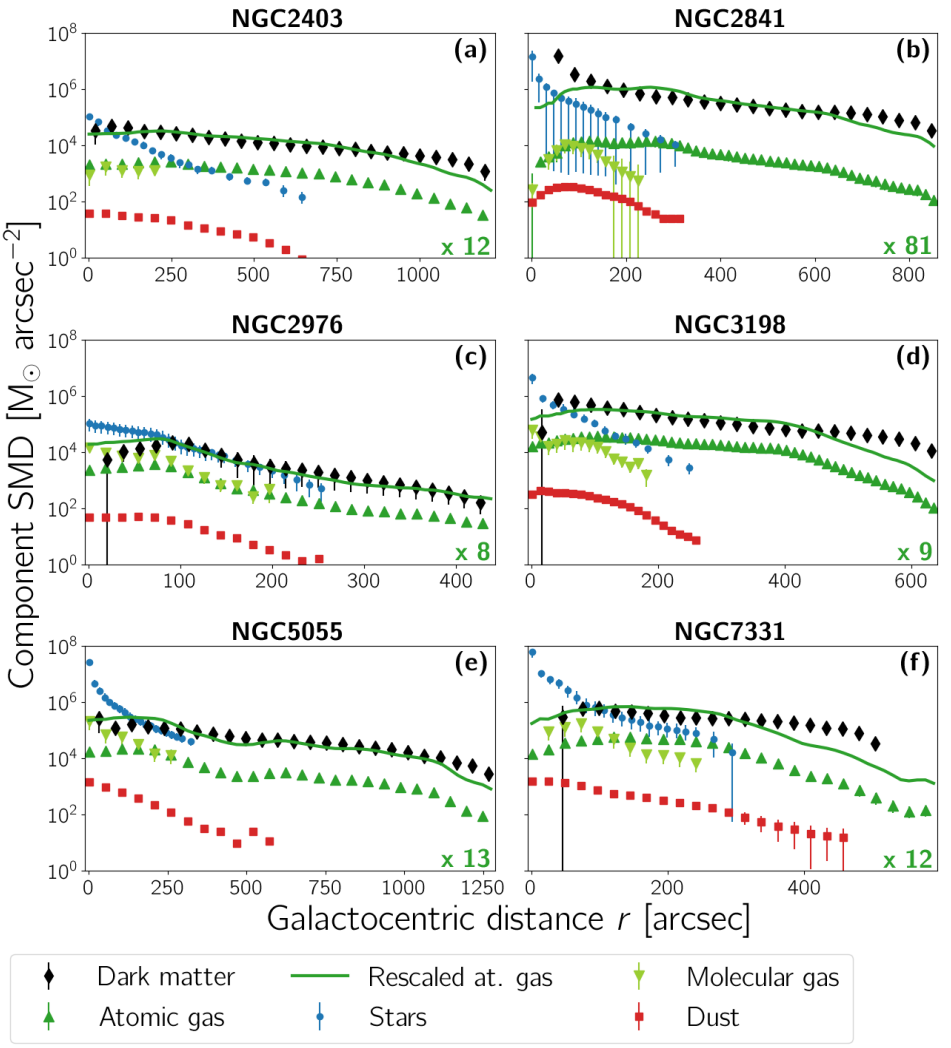

Figure 6.4: SMD profiles of all the components (*stars:* blue dots – *atomic gas:* dark green upward triangles – *molecular gas:* light green downward triangles – *dust:* red squares – *DM:* black diamonds) of the galaxies in our sample. The details for the luminous components profiles are the same as for Figure 5.2 on page 135. The DM component distribution is assumed to be an infinitely thin disk and is limited to the region probed by the observed RC (Lelli et al. 2016a). The thick green lines represent the SMD profiles of atomic hydrogen multiplied to match the DM profiles (the multiplying constant is given in the lower right

Figure 6.4 (continued): corner of each panel). For the regions where v^2_{DM} is negative (in the very centers of the galaxies), the corresponding SMD values are set to zero. Results for NGC2841 should be considered with caution.

---

tries for the DM halos of galaxies. Different halo models nevertheless exist. Constraining them with observations is thus particularly important to understand this still mysterious component.

As explained in Chapter 1, the two main categories of DM halos around galaxies are spherical distributions with either a central core (of which the most famous representative is the PIS model) or a central cusp (such as the NFW model). If the last ones are predicted by simulations of the evolution of the universe in a ΛCDM context, the first seem favored by RCs. The main difference between these two categories of models lies in the radial evolution of their density in the inner regions of the galaxies. The cored models have constant densities ($\rho \propto R^{-0}$) in their centers while the cusp models' densities increase with decreasing distance ($\rho \propto R^{-1}$).

The modeling of the luminous components of spiral galaxies is particularly important to determine the central shape of the DM halo. Indeed, modeling the stellar content of spiral galaxies with either fixed or free mass-to-light ratio values modifies the associated best-fitting model of halo (passing from cusp to core models or inversely; e.g. de Blok et al. 2008; Saburova et al. 2016). Neglecting the molecular gas or the bulge contribution when computing the global RC can also give rise to similar biases (Frank et al. 2016; Korsaga et al. 2018, 2019). By determining the value of the mass-to-light ratios, performing systematic bulge/disk decompositions and modeling the molecular gas of all the galaxies in our sample, our methodology results in less uncertain descriptions of the DM content of spiral galaxies.

To determine which category of model better describes the galaxies of our sample, we fitted general power laws $\rho \propto R^{-\delta}$ on the spherically symmetric density profiles of their DM component. These profiles are given in Figure 6.5 (black diamonds) along with their best-fit power laws (blue lines). By default, two different power laws have to be assumed as the density evolves differently in the center or in the outskirts of galaxies. The transition between the two regimes of power laws is then highlighted with a vertical dashed blue line. Nevertheless, half of the galaxies in our sample did not depict such a two-regime behavior. This is due to the fact that the

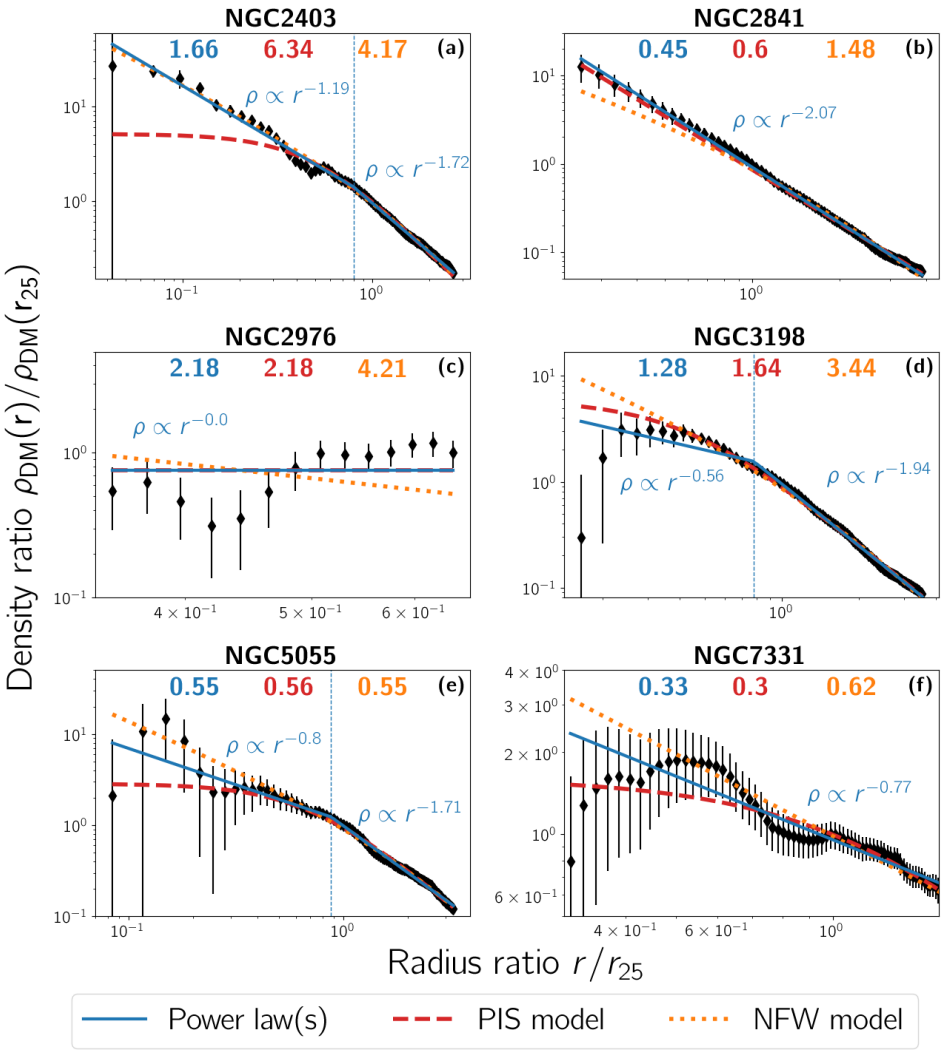

Figure 6.5: DM density profiles of the galaxies in our sample. A spherically symmetric distribution is assumed. Several models are fitted: (i) general power law(s) (solid blue lines; when appropriate, the vertical dashed line shows the transition between the two regimes of power laws), (ii) a PIS model (dashed red lines), and (iii) a NFW model (dotted orange lines). For each model, the associated reduced χ^2 is given in corresponding color at the top of each panel. Results for NGC2841 should be considered with caution.

DM profiles are either restricted to only one region of the halo (the central one for NGC2976 and the outer one for NGC2841) or too oscillating to confidently fit a double power law on it (NGC7331). We thus restricted the fits of these three galaxies to a single power law.

In all cases, in the outskirts of the galaxies, the power law index is always consistent with $\delta \sim 2$, the index value expected from the flatness of observed RCs. In the central regions, the density profile flattens with three different behaviors: (i) a core model evolution (NGC2976 and, to a lesser extent, NGC3198), (ii) a cusp model evolution (NGC2403) or (iii) an intermediate regime (NGC5055 and NGC7331). The case of NGC2841 differs from the other with a DM halo evolution similar in the inner regions of the galaxy than in its outskirts. This uncommon behavior directly results from the overestimation of its DM component due to the warp of its disk and should thus be taken with caution.

From these general descriptions of DM content, it is also possible to assess the validity of the DM halo models that are extensively used in literature, particularly in RC studies. In this work, we only give preliminary results for the PIS and the NFW halo models but a deeper analysis could be easily implemented with the test of different models of halos (such as the Einasto, the Burkert or the "Lucky" profiles; Einasto 1965; Burkert 1995; Li et al. 2020). More exotic forms of halos could also be tested as the ones predicted by models of new forms of DM (like the self-interacting DM; Spergel & Steinhardt 2000; Kaplinghat et al. 2000) or by simulations of the universe that take into account the effect of the baryonic matter on the DM component (e.g. Di Cintio et al. 2014; Read et al. 2016a,b).

The radial evolution of the PIS and NFW densities are given in Chapter 1 by Equations 1.2 and 1.3 (pages 30 and 31). We fitted them on our DM profiles, the results being displayed in Figure 6.5 (PIS: dashed red lines – NFW: dotted orange lines). The reduced χ^2 values associated to each fit (including ours and its general power laws) are given in corresponding colors at the top of each panel. As expected, our fits better reproduce the data as power laws are less constrained than the usual halo models. As for our own fits, the galaxies exhibit more central cores than cusps (with only NGC2403 better described by a NFW model than by a PIS one and NGC5055 equally well fitted by both models). If some models are strongly disfavored by the data (NGC2403 with PIS or NGC2976 and NGC3198 with NFW), the galaxies for which we found intermediary behavior between the cored and cusp models (NGC5055 and NGC7331) are described equivalently by both

PIS and NFW profiles.

6.2.6 Effects of the usual simplifying hypotheses on the halo shape

As done in Section 6.2.3 on the DM masses in the regions probed by the observed RCs, it is also possible to analyze the impact of the simplifying hypotheses usually performed in RC studies on the shape of the resulting DM halo. Similarly to what we did then, we fitted power laws on the spherically symmetric DM profiles derived from different modelings of the luminous components of galaxies, hence isolating each individual hypothesis studied in this work (see Table 6.2 for the computed modelings).

The DM halo shape modifications are shown in Figure 6.6. In this figure, we display the values of the indexes δ of the power law fitted in the inner regions of the galaxies. The empty symbols corresponds to the modeling for which the usual hypotheses are assumed and the filled ones to the modelings with our alternatives. The two symbols overlay, the filled one hiding the empty one, if the tested hypothesis does not modify the DM halo shape. The typical value of cored (resp. cusp) models is also displayed with the vertical solid (resp. dashed) line.

Significant impacts of the hypotheses used to model the galaxies are observed, particularly for the stellar populations processing, with the modeling in itself (dark blue dots) and the decomposition into bulge and disk structures (cyan blue stars). These two hypotheses seem to have opposite effects. Even if exceptions exist in our sample (for NGC2403 and NGC3198), the stellar modeling tends to flatten the DM profile while the bulge/disk decomposition steepens it. Similarly, neglecting the molecular content of galaxies (light green downward triangles) produces cuspier halos while neglecting the 3D distribution of their gaseous content (dark green upward triangles) results in cored ones. Once again, NGC3198 with its very high content in atomic gas is the one for which the simplifying hypothesis on the gas thickness has the highest impact.

For some galaxies in this sample, the effect of our more realistic alternative hypotheses is particularly important with a clear transformation of the nature of the DM halo for the CDD bulge/disk decomposition of both NGC3198 and NGC5055. One may note that in RC studies implying a large number of galaxies, the bulge/disk decompositions are usually limited to early-type galaxies (e.g. de Blok et al. 2008; Lelli et al. 2016a). They are

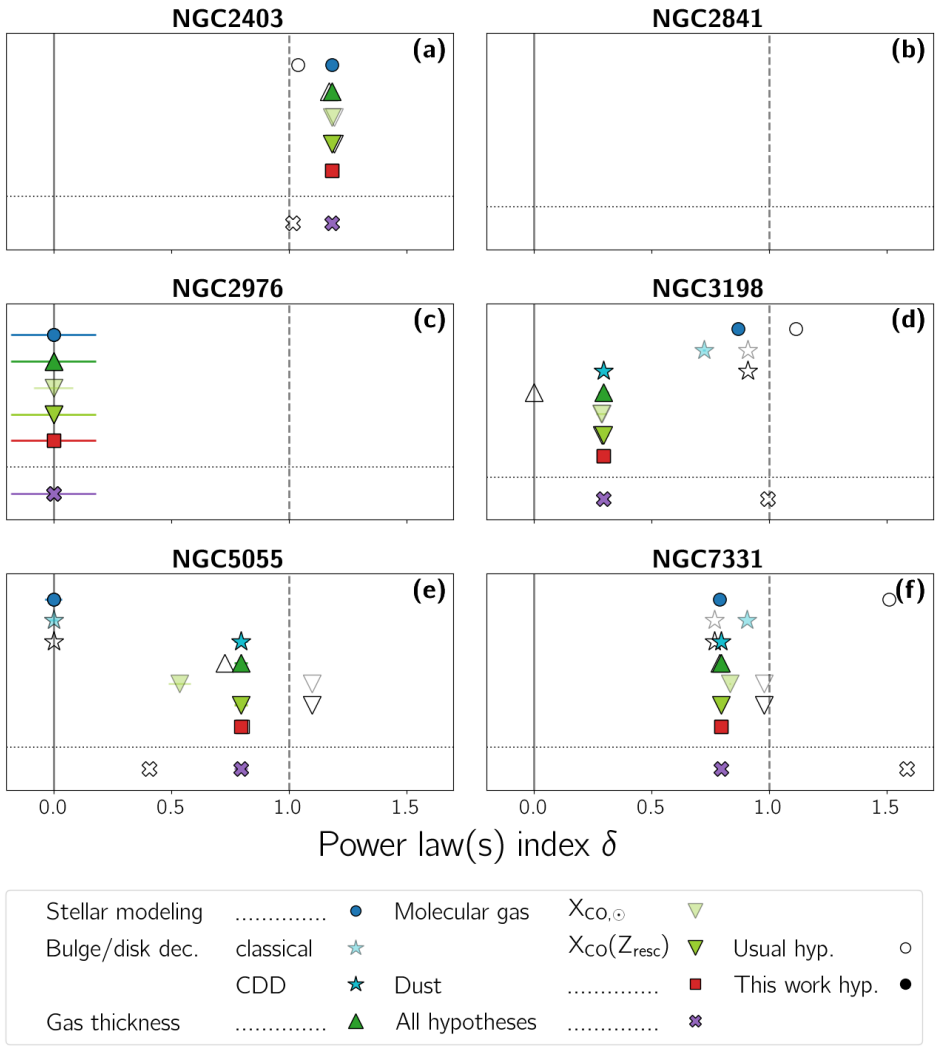

Figure 6.6: Effects of the different simplifying hypotheses tested in this work (see Table 6.2) on the shape of the DM spherical halo derived from the RC discrepancies. The abscissa of each point corresponds to the index δ of the power law fitted on the DM inner density profiles derived when the luminous components are modeled either with a usual hypothesis (empty symbols) or with our more realistic alternative (filled symbols). The vertical solid (resp. dashed) lines correspond to indexes associated to cored (resp. cusp) halo models. In panel (b), there is no data point for NGC2841 as the inner evolution of DM halo of this galaxy cannot be probed due to its disk warp.

thus not performed on NGC3198 and NGC5055, the two galaxies of our sample for which this decomposition is, in fact, of the highest importance.

Finally, while NGC2976 is the galaxy in our sample with the most important impact of the different simplifying hypotheses on its DM mass, it shows here no sign of shape modification. For all the tested hypotheses, this galaxy is particularly well described by a purely cored model and a central constant DM density.

6.3 Conclusion

In this final chapter, we completed the methodology developed along this work with the computations of the RCs of all the luminous components of spiral galaxies, the determination of the resulting discrepancies with the observed RCs and the characterization (in mass as well as in shape) of their DM content. We also quantified the impacts of the simplifying hypotheses commonly used in RC studies on the final galactic modelings.

In the last part of this work, we will give an overview of the pertinence of the method implemented here to model spiral galaxies, and their RCs, in a more realistic way.

Part II

Dark energy & Type Ia supernovae

II

Based on

Hauret, C., Magain, P. & Biernaux, J. (2018). A cosmology-independent calibration of type Ia supernovae data. *MNRAS*, 479(3)

Chapter 7

Type Ia supernovae
Characterization through a cosmology-independent calibration

Revolutionizing cosmology, the discovery of the accelerated expansion of the universe has been made possible thanks to the observation of a certain type of stars, the type Ia supernovae (SNe Ia). From the observed relation between two of their properties, their distance and their redshift, cosmologists at the end of the 1990s deduced that, on top of the unknown DM, the universe is also constituted of an even more elusive and even more dominant component, the dark energy (DE). Over the years, this composition of the universe has been corroborated by various other observations, leading to an overwhelming domination of the ΛCDM model on the whole cosmological field. Hence, nowadays, the methodologies developed to analyze, among others, the SNe Ia data, often incorporate at their heart this particular cosmological model, at the risk of making the data biased towards the model they are supposed to test.

Similarly to what we did in the first part of this work on RCs of spiral galaxies, we developed an alternative methodology to analyze the SNe Ia data by getting rid of this cosmological assumption. In this chapter, we thus describe in Section 7.1 why SNe Ia observations became one of the best cosmological tools to understand the content and the evolution of the universe. We then explain the current (potentially problematic) entangle-

ment between the ΛCDM model and these data in Section 7.2. Finally, we present our model-independent methodology in Section 7.3.

7.1 Characterizing the universe with Hubble diagrams

The idea to use the relation between the distance and the redshift of celestial objects in order to characterize the dynamical evolution of the universe is as old as (modern) cosmology itself. Indeed, the works of Lemaître (1927) and Hubble (1929), computing this relation for spiral nebulae, settled the extragalactic nature of these objects and hence opened this field of Science. Incidentally, the graphical representations of the distance-redshift relations are nowadays referred as Hubble diagrams.

At low redshift, such diagrams only allow to retrieve the velocity at which the universe is presently expanding (characterized by the Hubble constant). However, if more and more distant objects are observed and added, the acceleration of the expansion itself can be constrained. Such observations are nevertheless difficult to gather as these objects have to be luminous enough to be visible at very large distances. Moreover, their distance has obviously to be determined independently from their redshift. A way to do so is to use objects whose intrinsic luminosity is known or is correlated with another of their properties. The distance of such objects can thus be deduced directly from the observations of their apparent magnitude, giving them the name of standard candles.

Since the 1960s, different types of galaxies have been used as standard candles, with relative success (e.g. Sandage 1968; Lilly & Longair 1984). If the low redshift[1] ($z \lesssim 0.5$) diagrams were possible to build, the inclusion of more distant objects were (and are still) particularly hazardous. Indeed, the intrinsic properties of galaxies significantly change as they evolve. Hence, Hubble diagrams comparing nearby and distant galaxies were more interesting to understand the astrophysics of these objects than the cosmological model of the universe (Longair 2006).

The revolution in this field came from a particular type of supernovae, the SNe Ia. These objects arise from the thermonuclear explosions of white dwarfs in binary systems (Hoyle & Fowler 1960). As they accrete mat-

[1] In this chapter, the symbol z will not be used anymore to designate the direction perpendicular to the plane of spiral galaxies but will now represent the redshift of cosmological objects.

ter from their companions, they grow and reach explosion conditions when their mass approaches the Chandrasekhar limit (Hillebrandt & Niemeyer 2000). If the details of this scenario are still a matter of debate, it is reasonable to assume that all SNe Ia present similar intrinsic luminosities as the explosions of white dwarfs of similar masses should release the same amount of energy. This property thus makes of SNe Ia the Holy Grail of standard candles, the small dispersion of their intrinsic luminosities having been observationally confirmed for decades (Kowal 1968; Branch & Tammann 1992).

In the 1990s, hence, extensive surveys dedicated to the detection and to the analysis of low- and high-redshift SNe Ia have been set up (Norgaard-Nielsen et al. 1989; Hamuy et al. 1993; Perlmutter et al. 1995; Schmidt et al. 1998). And quickly after the first observations of distant objects, the results were unequivocally pointing towards an accelerated expansion of the universe (Perlmutter et al. 1997a; Riess et al. 1998; Perlmutter et al. 1999). At that time, these results completely disrupted cosmology and our view of the universe, transforming it into a object whose 95% of the content was (and still is) unknown to our theories. On top of the DM necessary to describe, among others, the RC of spiral galaxies, it was then necessary to add in the models of the universe a non-null cosmological constant, its action countering and even outperforming the expected decelerating effect due to gravity. If a similar cosmological constant had been postulated a few years before in order to explain the observations of some celestial objects older than the estimated age of the universe (see references in Longair 2006 or in Frieman et al. 2008), SNe Ia observations were the first direct evidence pointing towards the ΛCDM model, that then quickly set up to become the standard model in cosmology.

7.2 Building Hubble diagrams with SNe Ia data

In reality, SNe Ia are not perfect standard candles as a certain diversity exists in their intrinsic luminosities. Fortunately, this can be considerably reduced as some correlations between the SN Ia luminosity and other of its properties have been discovered. The main of these correlations, first suggested by Pskovskii (1977) and formally implemented by Phillips (1993), is the relation between the peak luminosity of SNe Ia and the shape of their light curves. Similarly, further correlations have been discovered, taking

into account the effects of the SN Ia color (Riess et al. 1996; Tripp 1998) and of its host-galaxy environment (Neill et al. 2009; Kelly et al. 2010; Sullivan et al. 2010; Lampeitl et al. 2010). The brighter objects experience slower decreases of their luminosity with time, are bluer, and are found in more massive galaxies. Thanks to these correlations, the standardizable candles that are the SNe Ia are now considered as the best and the most mature of all cosmological tools to characterize the DE content of the universe (Frieman et al. 2008).

The methodology to deal with these light-curve shape, color and host galaxy corrections (called hereafter the standardization corrections) is extremely important in order to accurately describe our universe via cosmological models. Mathematically speaking, applying these corrections to retrieve the SN Ia intrinsic peak absolute magnitude can be written as

$$M_{B,\mathrm{corr}} = M_B - \alpha x_1 + \beta c + \delta P \left(M_{\mathrm{stellar}} < 10^{10} M_\odot\right) \tag{7.1}$$

where M_B is the absolute B band magnitude of a SN Ia with x_1, c and $P = 0$ while $M_{B,\mathrm{corr}}$ is the same magnitude for a SN Ia of given x_1, c and P. The latter are parameters linked respectively to the SN Ia light-curve shape, its color and its host galaxy mass, while α, β and δ are parameters that describe the correlations of the peak magnitude to the three aforementioned properties.

First, x_1 is a measurement of the light-curve shape, related to the so-called *stretch correction* as the differences in light-curve shape can also be seen as the stretching of the light-curve time axis (Perlmutter et al. 1997a,b). Second, c is the $B - V$ color of the object at its maximum luminosity (Tripp 1998). Finally, P is the probability that the SN Ia host galaxy is less massive than a threshold fixed at $10^{10} M_\odot$ (Sullivan et al. 2010). One will notice that the relation between host mass and absolute magnitude presented in Equation 7.1 can be implemented differently than with the probability P defined in this work or in others, such as Suzuki et al. (2012) or Mohlabeng & Ralston (2014). For example, it can be computed as a step function of the host mass as it has been done in Betoule et al. (2014) or in Calcino & Davis (2017).

Initially, M_B as well as the α and β coefficients[2] were calibrated on nearby SNe Ia (e.g. Phillips 1993; Hamuy et al. 1995; Tripp 1997, 1998 as

[2]One can notice that the δ coefficient was not yet introduced at that time but it can nevertheless be calibrated the same way.

well as papers based on the MLCS light-curve fitter introduced by Riess et al. 1996) and the relations were applied to more distant objects. However, since Perlmutter et al. (1999), another determination of these standardization corrections has been introduced and developed around the SALT and SALT2 light-curve fitters (Guy et al. 2005, 2007). Nowadays, this methodology is the most common way to transform SNe Ia into standard candles. M_B, α, β, and δ are seen as nuisance parameters and are determined together with the cosmological parameters by fitting an assumed model (generally the ΛCDM model) on the Hubble diagram (Suzuki et al. 2012; Betoule et al. 2014; Calcino & Davis 2017).

Unfortunately, while it gives better fits if this chosen model model is in fact the best representation of our universe, this technique can lead to a bias in its favor (Gopal Vishwakarma & Narlikar 2010; Marriner et al. 2011; Melia 2012; Wei et al. 2015b). Indeed, when the cosmology and the standardization corrections are fitted simultaneously, their respective parameters are no longer independent from each other. In theory, this could skew the observational data towards the assumed cosmology, at the expense of any other one. This will especially be true if the standardization corrections are correlated with the redshift. With such corrections, the SNe Ia data could no longer be used to test cosmological models as they would always favor the assumed one. In order to correctly compare the ability of various cosmological models to fit the SNe Ia data, the standardization parameters should be redetermined for each non-ΛCDM cosmologies (as it has been done for example by Wei et al. 2015b), leading to possible time-consuming calculations.

Nowadays the ΛCDM model is widely favored by various observations. Hence, most of the present observational works, including SNe Ia analyses, are not aimed at testing which cosmological model is the most representative of our universe anymore but they are instead designed to increase the precision on the determination of its density parameters. In this case, the methodology currently used for SNe Ia is perfectly well-suited. However, its possible collateral effect on data and on model comparison raises important philosophical questions. Should we approve of a way of processing the data that can potentially make them compliant to a certain theoretical model? Should we not prefer a cosmology-independent approach to avoid this possible problematic effect?

7.3 Developing a cosmology-independent calibration of SNe Ia

To answer these questions and check if this potential compliance of data is effectively present in the SNe Ia compilations, we developed an alternative cosmology-independent calibration to process the standardization corrections. Different cosmological models could then be fitted on the recalibrated SNe Ia data in order to determine the most representative model of our universe, as it has been done by Xu & Zhang (2016) for example. The decisive advantage of the standardization parameters values we determined is that they can be directly used when working with non-ΛCDM cosmologies instead of having to be re-evaluated for each studied cosmological model.

7.3.1 Calibration principles

Apart from developing a precise model able to determine the standardization parameters directly from the physics of the SNe Ia thermonuclear explosions, the only way to evaluate these parameters is through the Hubble diagram. Indeed, on the one hand, one can express the distance modulus μ of each SN Ia as a difference between its apparent and absolute magnitude (respectively m_B and $M_{B,\mathrm{corr}}$) and, using Equation 7.1, we have

$$\mu = m_B - M_B + \alpha x_1 - \beta c - \delta P \left(M_{\mathrm{stellar}} < 10^{10} M_\odot\right). \tag{7.2}$$

On the other hand, this distance modulus can also be derived from the SN Ia redshift z via the luminosity distance $d_\mathrm{L}(z)$:

$$\mu = 5 \log\left(d_\mathrm{L}(z)\right) - 5. \tag{7.3}$$

Unfortunately, the $d_\mathrm{L}(z)$ relation cannot be found exactly without assuming a particular cosmological model. Hence, as previously said, the recent SNe Ia compilations have been primarily processed assuming a ΛCDM model but one can use another cosmology (such as the $R_\mathrm{h} = ct$ model, for example; Wei et al. 2015b). However, this prior choice of a model can lead to the already-pointed-out problem of data compliance.

To put this possibility to the test, we decided to get rid of any assumption on the cosmology at the cost of loosing the exact dependency of luminosity distance with redshift. To do so, we expanded the $d_\mathrm{L}(z)$ relation as a Taylor series around the observer (for whom $z = 0$). We tested two different Taylor expansions, imposing for both a null luminosity distance

at a zero redshift: (i) one of the redshift (hereafter called the z-series):

$$d_{\mathrm{L}}(z) = d_{0,z}\left[z + d_{1,z}z^2 + d_{2,z}z^3 + d_{3,z}z^4 + \mathrm{O}(z^5)\right] \tag{7.4}$$

and (ii) one of a function f of the redshift ($f(z) = z/1+z$) (hereafter called the f-series):

$$d_{\mathrm{L}}(z) = d_{0,f}\left[f(z) + d_{1,f}f^2(z) + d_{2,f}f^3(z) + d_{3,f}f^4(z) + \mathrm{O}\left(f^5(z)\right)\right]. \tag{7.5}$$

In Section 7.3.3, we will choose between these two kinds of series, limited to different orders, so as to minimize the number of Taylor parameters while optimizing the representation of SNe Ia data.

Our specific choice of the $f(z)$ function can be explained as follows. As SNe Ia with redshifts larger than unity have been observed, the high-order terms of the z-series could quickly become non-negligible if their associated parameters $\{d_{i,z}\}$ are non-null. The $d_{\mathrm{L}}(z)$ relation would then not be well approximated by a limited series and our calibration would be useless. This is why we also considered the f-series with the f function such that it stays low as z goes high. We would then *a priori* neglect high-order terms more easily than in the z-series. Furthermore, one can notice that in a model based on the Friedmann-Lemaître-Robertson-Walker (FLRW) metric, this f-series is in fact the luminosity distance expanded as a Taylor series of the scale factor R of the universe around its actual value $R(t_0)$ as $z + 1 = R(t_0)/R$. Our particular choice of the function $f(z)$ is thus quite natural in a FLRW context.

To sum up, with these two Taylor series, all the information about cosmology is exclusively included in the Taylor parameters $\{d_{i,z/f}\}$. We would like to point out that in neither of our series, do we suppose a specific form of the metric. We do not even assume General Relativity. Nonetheless, for cosmological models based on General Relativity and on the FLRW metric, these parameters are directly related to the well-known present Hubble H_0 and deceleration q_0 parameters defined by

$$H_0 \equiv H(t_0) = \frac{\dot{R}(t_0)}{R(t_0)} \quad \text{and} \quad q_0 \equiv q(t_0) = -\frac{\ddot{R}(t_0)}{R(t_0)}\left[\frac{\dot{R}(t_0)}{R(t_0)}\right]^{-2}.$$

Fixing the present value of the scale factor $R(t_0)$ to unity, the first two[3]

[3]The expressions of the next two Taylor parameters of this same series can be found in Visser (2004).

Taylor parameters of the z-series have a very simple form:

$$d_{0,z} = \frac{c_{\text{light}}}{H_0} \quad \text{and} \quad d_{1,z} = \frac{1 - q_0}{2}$$

where c_{light} is the speed of light.

Going back to our estimate of the standardization parameters through the Hubble diagram, we combined Equations 7.2, 7.3 and 7.4 or 7.5 (limiting here the series to the third order) to have

$$m_B - M_B + \alpha x_1 - \beta c - \delta P \left(M_{\text{stellar}} < 10^{10} M_\odot\right) \simeq 5 \log(d_{0,z}) + 5 \log\left(z + d_{1,z} z^2 + d_{2,z} z^3\right) - 5 \quad (7.6)$$

or

$$m_B - M_B + \alpha x_1 - \beta c - \delta P \left(M_{\text{stellar}} < 10^{10} M_\odot\right) \simeq 5 \log(d_{0,f}) + 5 \log\left(f(z) + d_{1,f} f^2(z) + d_{2,f} f^3(z)\right) - 5. \quad (7.7)$$

The terms appearing in these equations are divided in two categories: (i) the SN Ia observable properties (m_B, x_1, c, P and z) and (ii) the standardization and Taylor parameters (α, β, δ, $d_{i\neq 0,z/f}$ as well as a combination[4] of M_B and $d_{0,z/f}$). The latter can be determined by minimizing a χ^2 statistics (as made in Suzuki et al. 2012 and Betoule et al. 2014) or, in a more rigorous approach, by using a Bayesian framework (such as the one first developed by March et al. 2011 and its extensions applied to the JLA compilation by Shariff et al. 2016, for example).

7.3.2 Dataset and intrinsic dispersion

In this work, we used SNe Ia data released in the Joint Light-curve Analysis (JLA) compilation[5] from Betoule et al. (2014), containing 740 objects with redshifts ranging from around 0.01 to 1.3. When working with SNe Ia data, one has to evaluate a parameter besides the standardization parameters: the intrinsic dispersion of the SNe Ia magnitudes. It may include both a true intrinsic scattering component and any uncharacterized sources of errors.

[4] For models based on the FLRW metric, we find the well-known degeneracy between M_B and H_0.

[5] `http://supernovae.in2p3.fr/sdss_snls_jla/ReadMe.html`

Table 7.1: Intrinsic dispersions in magnitude, evaluated separately on each sample of SNe Ia through the methodology developed by Betoule et al. (2014)

Sample	Intrinsic dispersion
low-z	0.116
SDSS-II	0.045
SNLS	0.128
HST	0.060

To determine its value, we could not use the usual methodology (Conley et al. 2011; Sullivan et al. 2011; Suzuki et al. 2012, for examples), which consists in adding an error to that of the SNe Ia apparent magnitudes until the best-fitting χ^2 reaches a value of one per degree of freedom. This procedure obviously forbids any comparison between models as all fits end up with equally good (artificial) χ^2 values. This problem is not new and has been pointed out by many authors such as Conley et al. (2011). Nevertheless, it is particularly an issue for our work as we eventually have to choose between the different Taylor series presented previously.

Fortunately, Betoule et al. (2014) developed a technique to avoid this problem and to evaluate this dispersion more properly. Basically, they divide the SNe Ia into different redshift bins and evaluate the intrinsic dispersion in each bin via a restricted log-likelihood criterion. Our resulting intrinsic dispersions can be found in Table 7.1 and are compatible with previous determinations (Conley et al. 2011; Betoule et al. 2014). Similarly to these works, we determined different dispersions for each sample of objects at our disposal: the low-z, the Sloane Digital Sky Survey-II (SDSS-II), the Supernova Legacy Survey (SNLS), and the *Hubble* Space Telescope (HST) samples. Indeed, the dispersion we evaluate includes a true intrinsic component as well as a component coming from the remaining unexplained sources of errors, which could vary from one survey program to another. For each sample, the dispersion values given in Table 7.1 are the weighted means of the dispersions evaluated on the different redshift bins defined by Betoule et al. (2014).

7.3.3 Cosmology-independent calibration

To calibrate the SNIe data, we had to choose between the $d_{\rm L}$ z- and f-series (Equations 7.4 or 7.5) and limit them to a particular order, so that we minimize the number of Taylor parameters while optimizing the representation of our data.

We calibrated the standardization and Taylor parameters on SNe Ia data for these two series limited to five increasing orders. To determine the optimal of these 10 calibrations, we did not use the usual minimization of a χ^2 statistics as this criterion does not take into account the complexity (i.e. the number of parameters) of the series. Hence, at equivalent agreement, we wanted to favor a model with fewer parameters. This also had the advantage to avoid an overtraining of our methodology. Other statistical criteria, called information criteria, have been developed to consider this idea of complexity. Among them, the Akaike information criterion (AIC; Akaike 1974) and the Bayesian information criterion (BIC; Schwarz 1978) are widely used. They are defined by

$$\mathrm{AIC} = -2\ln\mathcal{L}_{\max} + 2k \quad \text{and} \quad \mathrm{BIC} = -2\ln\mathcal{L}_{\max} + k\ln N$$

where $\mathcal{L}_{\max}$ is the maximum likelihood ($-2\ln\mathcal{L}_{\max} = \chi^2_{\min}$ if we assume that the errors on the data are normally distributed, as it is generally the case in cosmology), k is the number of parameters of the model considered and N is the number of data points.

The model with the lowest AIC and BIC are then preferred and, for comparison with other models, only the relative values between models are important. Thus, to quantify the goodness of a given model i compared to the one with the minimum AIC or BIC, one has to compute the differences $\Delta\mathrm{AIC}_i = \mathrm{AIC}_i - \mathrm{AIC}_{\min}$ or $\Delta\mathrm{BIC}_i = \mathrm{BIC}_i - \mathrm{BIC}_{\min}$. The larger these differences, the stronger the empirical evidence against the given model with defined categories (Liddle 2004; Shi et al. 2012). For example, a model with $\Delta\mathrm{AIC}_i$ or $\Delta\mathrm{BIC}_i < 2$ is considered as substantially supported by the data while one with $\Delta\mathrm{AIC}_i$ or $\Delta\mathrm{BIC}_i > 10$ is very strongly rejected by them.

Our resulting standardization and Taylor parameters can be found in Table 7.2. Each set of parameters has been determined using a simulated annealing algorithm implementing a χ^2 minimization on the whole SNe Ia population, that is to say on the 740 objects. For each of these sets, the covariance matrix had been calculated, yielding the one-sigma error bars.

Table 7.3 displays the corresponding χ^2 for these best-fitting models and their associated AIC and BIC, so that models can be compared to each other. The $d_{\mathrm{L}}(z)$ series are also plotted on Hubble diagrams and compared to binned data in Figure 7.1.

First of all, it is clear in Table 7.3 and on Figure 7.1 that the z-series represent the data more quickly and more correctly than the f-ones. Even the fifth order of the f-series does not provide a fit as good as the z-series, third order. This result is slightly surprising as one would *a priori* be more confident in the f-series where the values $f(z) = z/1+z$ stay low while z itself can reach relatively high values (there are 9 objects with $z \geqslant 1$ in our dataset). Non-negligible differences between the true $d_{\mathrm{L}}(z)$ relation and its Taylor approximation in z could thus be expected at high redshift. Nevertheless, if the redshift powers of Equation 7.4 can be high for the most distant objects, these powers are multiplied by relatively low Taylor parameters $\{d_{i,z}\}$ as can be seen in Table 7.2. Those have to be compared with the lower powers of $f(z)$, multiplied by the quite high associated $\{d_{i,f}\}$ values, presented in this same table.

This can also be visualized in Figure 7.2 where the z and f Taylor series limited to different orders as a function of the redshift are plotted. One can directly see that adding terms in the z-series has a weaker effect on the approximated $d_{\mathrm{L}}(z)$ function than in the f-one. Hence, even though the z-series seems at first more likely to invalidate the Taylor approximation, it turns out to give better results than the f-ones.

Consequently, having decided which kind of series to use in our calibration, its order is left to be selected. As can be seen in Table 7.3, limiting the z-series to the third order gives optimal values of both the information criteria, AIC and BIC. Furthermore, in Table 7.2, the $d_{3,z}$ and $d_{4,z}$ Taylor parameters associated to the fourth and fifth order series are not significantly different from zero.

On top of that, one can notice, when comparing columns of Table 7.2 or when observing the (unmoving) binned data points on Figure 7.1, that the standardization parameters α, β and δ do not significantly vary starting from the second order of the z-series or from the third one of the f-series. This can be more easily visualized in Figure 7.3 that shows the evolution of these parameters with the order of the Taylor series. For both series, the values of the parameters quickly stabilize, even allowing us to use the standardization parameters values given by the fit of the second order of the z-series. One may notice that even if our calibration had suffered from

Table 7.2: Best-fitting standardization and Taylor parameters for our cosmology-independent methodology, up to different orders of both z and f Taylor series

	1st order	2nd order	3rd order	4th order	5th order
			z TAYLOR SERIES		
α	0.121 ± 0.007	0.149 ± 0.006	$\mathbf{0.149 \pm 0.006}$	0.150 ± 0.006	0.150 ± 0.006
β	4.58 ± 0.11	3.358 ± 0.071	$\mathbf{3.369 \pm 0.071}$	3.370 ± 0.071	3.372 ± 0.071
δ	0.177 ± 0.015	0.085 ± 0.012	$\mathbf{0.084 \pm 0.012}$	0.084 ± 0.012	0.084 ± 0.012
Comb.†	24.300 ± 0.008	24.074 ± 0.009	$\mathbf{24.049 \pm 0.012}$	24.044 ± 0.015	24.041 ± 0.018
$d_{1,z/f}$	-	0.606 ± 0.018	$\mathbf{0.726 \pm 0.044}$	0.761 ± 0.075	0.79 ± 0.13
$d_{2,z/f}$	-	-	$\mathbf{-0.151 \pm 0.050}$	-0.26 ± 0.19	-0.41 ± 0.55
$d_{3,z/f}$	-	-	-	0.08 ± 0.13	0.33 ± 0.84
$d_{4,z/f}$	-	-	-	-	-0.12 ± 0.39
			f TAYLOR SERIES		
α	-0.381 ± 0.065	0.158 ± 0.006	0.148 ± 0.006	0.150 ± 0.006	0.150 ± 0.006
β	33.2 ± 2.8	3.924 ± 0.084	3.393 ± 0.071	3.368 ± 0.071	3.369 ± 0.071
δ	0.68 ± 0.10	0.098 ± 0.013	0.087 ± 0.012	0.084 ± 0.012	0.084 ± 0.012
Comb.†	24.934 ± 0.063	23.822 ± 0.013	24.093 ± 0.016	24.036 ± 0.021	24.038 ± 0.027
$d_{1,z/f}$	-	3.500 ± 0.060	1.118 ± 0.089	1.96 ± 0.22	1.88 ± 0.42
$d_{2,z/f}$	-	-	5.49 ± 0.22	0.3 ± 1.3	1.4 ± 3.8
$d_{3,z/f}$	-	-	-	8.7 ± 2.0	3 ± 13
$d_{4,z/f}$	-	-	-	-	7 ± 14

† Combination of one standardization and one Taylor parameters: $M_B + 5\log(d_{0,z/f}) - 5$
In bold and blue: Calibration minimizing the number of Taylor parameters while optimizing the data representation (see Table 7.3 for the choice of this particular calibration)

Table 7.3: Goodness-of-fit indicators associated to the cosmology-independent calibrations (whose parameters values are given in Table 7.2)

Order	k	χ^2	χ^2/dof†	AIC	ΔAIC	BIC	ΔBIC
***z*-series:**							
1st	4	2555	3.47	2563	1522	2581	1512
2nd	5	1038	1.41	1048	7	1071	2
3rd	**6**	**1029**	**1.40**	**1041**	**0**	**1069**	**0**
4th	7	1029	1.40	1043	2	1075	6
5th	8	1029	1.41	1045	4	1082	13
***f*-series:**							
1st	4	4385	5.96	4393	3352	4411	3342
2nd	5	1556	2.21	1566	525	1589	520
3rd	6	1055	1.44	1067	26	1095	26
4th	7	1031	1.41	1045	4	1077	8
5th	8	1030	1.41	1046	5	1083	14

† χ^2 per degree of freedom (dof), all the fits being performed on the 740 SNe Ia
In bold and blue: Calibration minimizing the number of Taylor parameters while optimizing the data representation (minimum values of both AIC and BIC)

overtraining, the parameters we are interested in (the standardization parameters) would not have been impacted by this issue.

Nevertheless, to be rigorous, our cosmology-independent standardization parameters has been chosen as the ones found through our z-series limited to the third order (highlighted in bold blue in our Tables 7.2 and 7.3). The corresponding covariance matrix is given in Table 7.4. The SNe Ia data can then be properly recalibrated and used to perform fits of various cosmological models. We want to highlight the fact that if using the same SNe Ia dataset to perform the calibration and the cosmological fits, the error propagation between the parameters of these two fits is tricky. For future works, we thus strongly encourage to separate the SNe Ia at disposal into two independent subsets, performing the calibration fit on one group of objects and the cosmological one on the other.

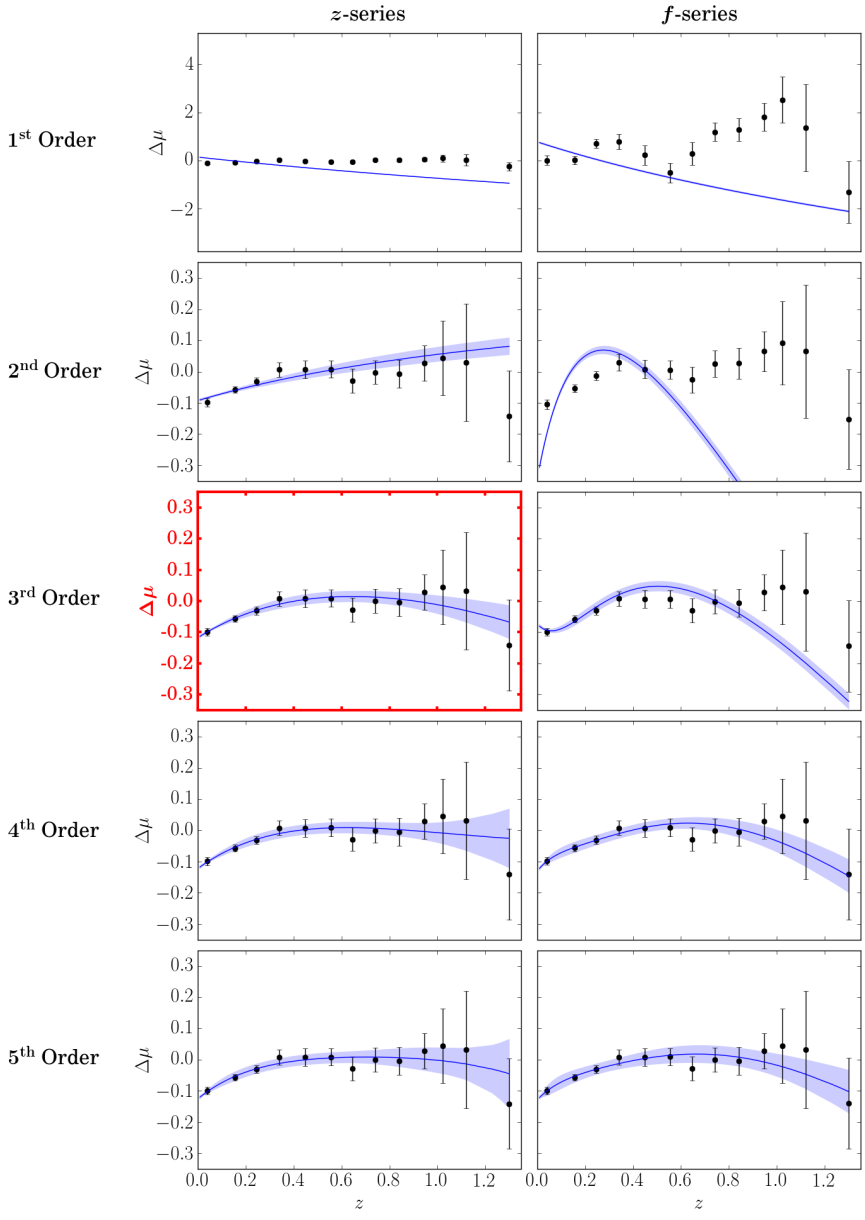

Figure 7.1: Hubble diagram residuals when the distance moduli of an empty cosmological model have been subtracted. Each panel compares the weighted SNe Ia data over 0.1-length redshift bins (built on the standardization parame-

Figure 7.1 (continued): ters presented in Table 7.2; black points) with our calibration distance moduli (built on the Taylor parameters presented in this same Table; blue line with shaded zones corresponding to 1σ errors). *From left to right*: calibration based on the z- or f-series. *From top to bottom*: calibration based on the first to the fifth order of the series. The panel highlighted in red corresponds to the series that minimizes the number of Taylor parameters while optimizing the representation of the data (see Table 7.3 for the choice of the calibration).

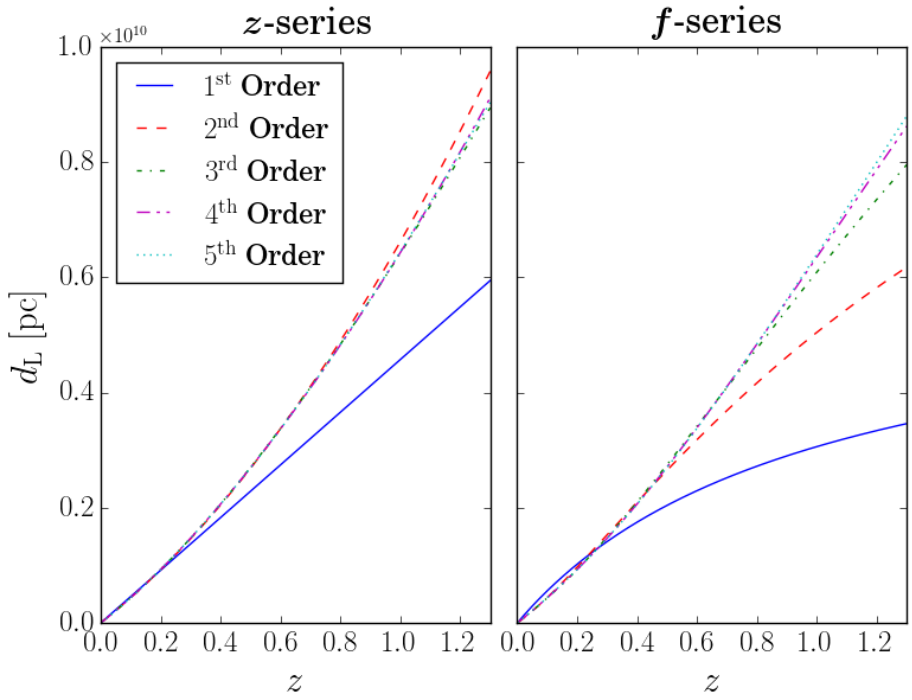

Figure 7.2: Evolution of our best-fitting z- (left panel) and f-(right panel) series limited to different orders as a function of the redshift. These approximated relations are given by Equations 7.4 and 7.5 whose Taylor parameters values can be found in Table 7.2.

Table 7.4: Covariance matrix associated to our best cosmology-independent calibration (z Taylor series limited to the third order). The standardization and Taylor parameters are presented in the same order than in Table 7.2.

$$\mathrm{Cov} = 10^{-6} \times \begin{pmatrix} 32 & -60 & 21 & -13 & 22 & -16 \\ & 5056 & 34 & -45 & 425 & -303 \\ & & 147 & -46 & -32 & 9 \\ & & & 147 & -436 & 410 \\ & & & & 1929 & -1984 \\ & & & & & 2457 \end{pmatrix}$$

7.3.4 Digression about cosmology-dependent calibrations

For the sake of illustration, we also performed cosmology-dependent fits on SNe Ia data. These calibrations simultaneously fit the standardization parameters as well as the cosmological ones as it was done by Suzuki et al. (2012), Betoule et al. (2014) and many others since Perlmutter et al. (1999). These parameters as well as their associated goodness-of-fit indicators are displayed in Table 7.5, along with $\Delta\mathrm{AIC}_{\mathrm{CI}}$ and $\Delta\mathrm{BIC}_{\mathrm{CI}}$, the differences between the AIC/BIC values of the particular cosmology-dependent fit and the ones of our best cosmology-independent (CI) calibration. From these values, one can notice that the cosmology-dependent calibrations have a goodness-of-fit similar to the best independent ones, the ΛCDM fit being marginally favored by the data due to its smallest number of parameters.

With this work, we aimed at testing the possible compliance of the SNe Ia data when fitting standardization and cosmological parameters simultaneously. We thus developed a cosmology-independent calibration to compare results from dependent and independent methods. For the sake of this comparison, a clear distinction has to be made between those two families of calibrations. On one hand, when focusing on finding the best independent calibration, we favored our Taylor expansion, even though the cosmology-dependent calibration results in slightly better fits (as it is the case here for the ΛCDM model). On the other hand, when using SNe Ia data in general cosmological tests (as done by Shi et al. (2012) or Xu & Zhang (2016) for examples) and when a cosmology-dependent calibration leads to a much better fit than an independent one, we would advise to favor the former, despite the philosophical questions raised.

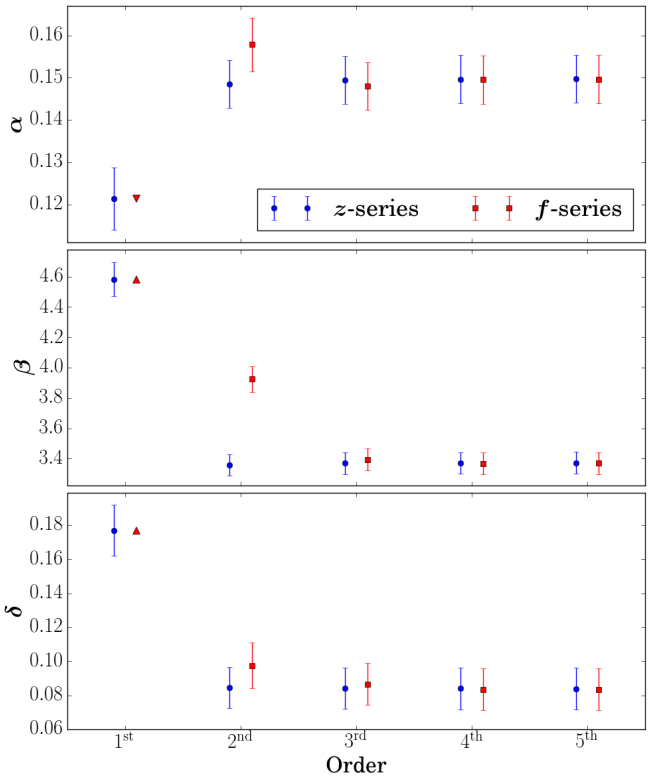

Figure 7.3: Evolution of the standardization parameters (*from top to bottom*: α, β and δ) as a function of the order of the limited z- (blue circles) and f-series (red squares). Exact values can be found in Table 7.2. For purposes of readability, the parameters of the f-series limited to the first order are not depicted on the panels. Red triangles indicate their out-of-graph location.

7.3.5 Discussion

Comparing the values of the standardization parameters highlighted in Table 7.2 and the ones associated to the ΛCDM cosmology in Table 7.5, one can see that we retrieved quasi-identical parameters using either the simultaneous fit methodology or our cosmology-independent one. This means that even though assuming a particular cosmology to standardize the SNe Ia could theoretically lead to data compliance problems, it is not the case in practice for the JLA compilation. JLA data are not significantly skewed towards the ΛCDM model assumed to process them. We thus independently confirm the results from Betoule et al. (2014), where the possible correlation between the cosmological and the standardization parameters was found to be non-existent for this compilation.

This can be explained by the fact that the numerous SNe Ia from the JLA compilation sufficiently populate the space of standardization parameters and redshift. However, if that conclusion is valid for this SNe Ia compilation as well as for the more recent ones (Scolnic et al. 2018, 2021; Brout et al. 2019), which includes hundreds of objects, it might not be valid for other standard candles, for which the sample might not be as large and as independent on redshift. As an example, let us mention the superluminous type Ic supernovae, for which only about 20 are presently known (Inserra & Smartt 2014, 2015; Wei et al. 2015a). In such smaller samples, there is no guarantee that the space of standardization parameters and redshift will be sufficiently filled so that the calibration will be independent of the assumed cosmological model.

Table 7.5: Best-fitting standardization and cosmological parameters along with the goodness-of-fit indicators for simultaneous fits of different basic cosmologies. The present Hubble constant is assumed to be equal to 70 km s^{-1} Mpc^{-1}.

	α	β	δ	M_B
(Flat) ΛCDM	0.150 ± 0.006	3.379 ± 0.071	0.084 ± 0.012	-19.130 ± 0.008
Non-flat ΛCDM	0.149 ± 0.006	3.361 ± 0.071	0.084 ± 0.012	-19.108 ± 0.013
Flat wCDM†	0.149 ± 0.005	3.363 ± 0.061	0.084 ± 0.012	-19.108 ± 0.012
Non-flat wCDM†	0.150 ± 0.005	3.371 ± 0.061	0.084 ± 0.012	-19.124 ± 0.017

	${\Omega_{m,0}}^{\ddagger,*}$	${\Omega_{\Lambda,0}}^{\ddagger,*}$	w^*
(Flat) ΛCDM	0.273 ± 0.018	–	–
Non-flat ΛCDM	0.095 ± 0.095	0.44 ± 0.14	–
Flat wCDM†	$0.01^{+0.17}_{-0.01}$	–	-0.60 ± 0.15
Non-flat wCDM†	0.15 ± 0.21	0.36 ± 0.57	-1.5 ± 2.1

	k	χ^2	χ^2/dof	AIC	${\Delta\text{AIC}_{\text{CI}}}^{**}$	BIC	${\Delta\text{BIC}_{\text{CI}}}^{**}$
(Flat) ΛCDM	5	1030	1.40	1040	−1	1063	−6
Non-flat ΛCDM	6	1030	1.40	1042	+1	1070	+1
Flat wCDM†	6	1030	1.40	1042	+1	1070	+1
Non-flat wCDM†	7	1029	1.40	1043	+2	1075	+6

† Models for which the equation of state (between the pressure p and the energy density ρ) associated to the DE/cosmological constant term is given by $p_\Lambda = w\rho_\Lambda c^2$.

‡ Density parameters describing the content of the universe in ordinary and dark matter ($\Omega_{m,0}$) as well as in DE, represented by the cosmological constant term ($\Omega_{\Lambda,0}$)

* For flat models, the $\Omega_{\Lambda,0}$ are fixed to $1 - \Omega_{m,0}$. For the ΛCDM models, w are fixed to -1.

** Values defined as differences between the AIC (resp. BIC) associated to a given cosmology and the AIC (resp. BIC) of the best cosmology-independent (CI) calibration (built on the z-series limited to the third order; values highlighted in bold blue in Table 7.3)

Part III

Conclusions & Perspectives

Conclusions & Perspectives

In this thesis, we revised the cosmological observations that first imposed DM and DE as constituents of the universe. To do so, we analyzed the methodologies currently implemented to process these data and then characterized the DM content of spiral galaxies through their RCs as well as the DE content of the whole universe through calibrations of SNe Ia. We questioned the simplifications and assumptions inherent to these methodologies, assessing their validity and correctness thanks to comparisons with our more realistic alternatives.

This chapter is thus divided in three sections. The first two present the individual conclusions associated to each of the two key observations studied in this thesis while the last section provides more general considerations.

Dark matter & galactic rotation curves

In the first part of this thesis, we focused on the way the RCs of spiral galaxies are usually modeled from their luminous content and compared to the observed ones in order to characterize the DM component of this type of galaxies. We hence developed a global modeling of all the components of these galaxies, avoiding as many simplifying hypotheses as possible. This alternative RC decomposition has then been applied to a first sample of six galaxies, spanning different types (from early Sb to late Sc), masses (from 10^9 to 10^{11} $M_\odot$) and RC shapes (from the very steeply rising with a late plateau category I RCs to the slowly rigid-body category III ones). Each galaxy having its own peculiarities, we showed that systematic and automatic studies of large samples of galaxies can be hazardous and lead to biased DM characterizations. In-depth studies of each galaxies should rather be preferred.

Stellar component modeling

Our alternative methodology mainly consists in a more realistic modeling of the stellar content of spiral galaxies through complete FUV-to-NIR SED fittings. It has the advantage of modeling the stars populations of all ages, particularly the young and massive ones that are neglected by the usual NIR luminosity conversion.

To do so, we used multiwavelength images of galaxies in a variety of domains going from FUV to sub-mm. Using short wavelength images implied that they had to be corrected from the effects of dust, both in the MW and, more importantly, in the host galaxy. This component, negligible in mass but considerably impacting the light emitted by galaxies, has been evaluated via its thermal emission at long wavelengths ($\lambda \geq 100$ μm). Its impacts on the galactic luminosity profiles have then been estimated with semi-individualized attenuation curves. Dust and stars emissions were disentangled and the resulting FUV-to-NIR stellar SEDs have been fitted with a Bayesian approach. For that, we assumed various parametrizations of the evolution of the star formation along the life of the galaxy, taking into account its associated chemical enrichment. Relatively new in SEDs modeling studies, this approach allows our methodology to produce an interesting and not easily computable byproduct: the metallicity profile of the galaxy. This latter can bring important constraints on models of formation and evolution of galaxies. When used and compared to the more common estimates of galactic metallicity, based on oxygen abundances, our profiles nevertheless require a rescaling conversion as they are associated to the content in all metals of galaxies.

To compute the contribution of the stellar component to the global RC, the only useful product is the stellar mass profile. When comparing our profiles to the ones resulting from the usual NIR conversions (with a fixed and constant value of the mass-to-light ratios), we showed the latter method to be a good approximation to estimate the stellar mass of a spiral galaxy. Nevertheless, to go further into the characterization of the DM content of galaxies and notably to discriminate between cored and cusp halos, this approximation reached its limits for some galaxies in our sample, with systematic differences taking place between the SED-fitted and the approximated profiles. If these differences seem negligible at first sight, they nevertheless impact the shape as well as the quantity of DM necessary to add in the galaxy in order to explain the observed RCs. Using the usual

approximation hence results in more massive and cuspier halos.

From all the simplifying hypotheses tested in this work, we found that the simple NIR conversion is the one with the most important impact on the DM content of galaxies. We also showed that more realistic modelings of stellar populations are crucial for late-type dwarf spirals while their accurate modeling is wrongly neglected in most of RC studies.

Moreover, our global modeling allows to test the recommendations concerning the stellar mass-to-light ratio values to use when performing the usual NIR conversion. When a single constant ratio is assumed, the value of 0.5 ± 0.1 recommended by Lelli et al. (2016a) for the 3.6 μm band was not suitable for one object out of our sample of six galaxies. If this sample should be increased to compute the proportion more accurately, it is not, as is, negligible. It thus raises the question of the validity of applying of this recommended value indiscriminately of the type of galaxy. When this ratio is more realistically considered as varying with the galactocentric distance, its values is often estimated from empirical relations based on NIR or optical colors. However, the ratio profiles derived from our SED fittings did not match with profiles derived from these empirical correlations, thus questioning the validity of such relations.

Bulge/disk decompositions

In the context of the core/cusp problem, the other approximation with the highest impact on the final shape of the galactic DM halo is the decomposition of stars into two different dynamical structures, a bulge and a disk. Indeed, accurate descriptions of the central regions of galaxies are primordial to effectively constrain the DM models.

In this work, we systematically performed such decompositions, whatever the final impact on the RC modeling. We hence only modeled as single disks the very late-type spirals that clearly did not display any sign of a central bulge. By contrast, usually, a bulge is only added in for early-type spirals or if it significantly improves the RC decomposition. With this work, we showed the dangers of this approximation as the two galaxies in our sample on which the bulge/disk decomposition has the highest impact are usually modeled as simple disks (particularly in more automatic studies involving large numbers of galaxies).

Moreover, our decomposition has been performed on the mass profiles and not on the NIR luminosity ones, as it is usually done. For galaxies that

are more challenging to decompose (due to the existence of large quantities of dust or of compact structures in their centers), this choice revealed to be beneficial. This is due to the fact that our mass profiles are corrected from the dust effects and also incorporate any variations of the mass-to-light ratio due to the very different stellar populations within these two galactic structures.

Finally, on top of the classical description of galactic disks as decreasing exponentials, a modeling widely performed in a variety of galactic studies among which the RC ones, our alternative methodology also tested another type of disk. Describing a disk whose mass decreases in the region dominated by the galactic bulge, this recently proposed model is more realistic and consistent with theories of formation and joint evolution of these two structures. Using it to decompose the stellar component of spiral galaxies significantly modified both the mass and the shape of the bulges, and hence of the DM halo surrounding spiral galaxies.

Gas components modeling

The alternative methodology developed in this work was not limited to the stars but also tackled the modeling of the second most massive component of spiral galaxies, the gaseous one. Images in two specific emission lines have been used to estimate the mass distribution of the atomic gas (via the atomic hydrogen line at 21cm) as well as the molecular one (via one of the CO lines). We drew a particular attention to the latter form of gas as it is usually completely neglected in RC studies. Testing this simplification, we found it to be invalid for half of the galaxies in our sample, resulting in a bias towards more massive and cuspier DM halos.

When pushed to its full potential, our global galactic modeling allowed to perform even more realistic estimates of the molecular hydrogen content of galaxies by taking into account the effect of the ISM metallicity on the conversion from CO luminosity to H_2 mass. With such sounder estimates, the bias introduced when neglecting the gas under its molecular form was (often) stronger, particularly for the galaxies with RC of category III that did not formed a lot of stars along their life.

Finally, an additional hypothesis tested in this work was the modeling of the gaseous components of galaxies as 3D disks in hydrostatic equilibrium. Usually, this component is seen as distributed in an infinitely thin disk, an approximation that simplifies the RCs computations. With our

3D modeling, we showed the validity of this simplification, only impacting slightly the gas-rich galaxies.

Dark matter component modeling

For the DM content characterization, we also bypassed the approximations usually used in RC decompositions. With our methodology, this component was thus not constrained by the DM halo models, classically the PIS and NFW models. We rather described it as distributed either spherically or, less commonly assumed, as a disk. This last distribution allows for the possibility of DM to be (partially) made of baryonic matter with very low emission while the spherically symmetric profiles can be easily and independently compared with predictions from various DM models.

Perspectives

Applying our methodology to a larger corpus of galaxies would allow to draw stronger conclusions on the effects of the approximations commonly assumed in RC studies and tested in this work. In particular, this sample enlargement would reduce the remaining doubts about hypotheses that we found to impact only one or two galaxies in our sample. Increasing the number of analyzed galaxies would also allow to assess the validity of the tested hypotheses as a function of some galactic properties and then confirm or refute tendencies that are only hinted by this work. Furthermore, on top of simply testing the usual approximations, we would also end up with a larger number of galaxies, modeled with more realistic and consistent assumptions, that could eventually constrain DM models as well as theories of galaxies formation and evolution.

The main limitation to the enlargement of the sample of galaxies comes from the availability of FIR and sub-mm observations from *Herschel* that we used to estimate the quantity of dust in the galaxy. Replacing these by a combination of observations in MIR/FIR by *Spitzer* and in sub-mm by *Planck* could help increase the number of objects appropriate for our methodology. Opening our sample to galaxies whose distance is less accurately known, possibly with a determination via the Hubble flow, would also significantly enlarge our sample of studied spirals.

Parallel to this increase of sample, one of the very first steps of our methodology should be enhanced by taking into account the variation of the

galactic disk inclination with respect to the galactocentric distance. Such an improvement would then avoid the problem we met with NGC2841. Similarly, an additional effort could be carried on the stellar population modelings. Indeed, the SED fittings performed here are not exempt from approximations and assumptions. Particular choices of the synthetic spectra of stellar populations, of the used IMF or of the models of SFH/ZH have to be made and can then impact the resulting mass modelings (see reviews by Walcher et al. 2011 or Baes 2020). For example, non-parametric models of SFH could be tested as they are more realistic than our exponential bursts (Pacifici et al. 2015; Carnall et al. 2019; Leja et al. 2019; Lower et al. 2020). Accreting box models could also be implemented to represent the chemical enrichment of galaxies as they have been found to better describe the evolution of high-mass spirals (Greener et al. 2021).

Even without these improvements, our methodology, as is, already provides a large variety of products and byproducts that can be used directly to better understand spirals. Indeed, as we have completely modeled all the luminous and non-luminous components of these galaxies, we end up with a very versatile tool, not limited to the study of their global rotation. Correlations between the different components and tendencies with the properties of the galaxies could be easily studied. Even their evolution with cosmic time can be probed. A great diversity of studies could thus be performed, already on the current results of the modelings performed in this work.

Finally, it would also be interesting to push the galactic modelings one step further, getting rid of even more simplifications. One important approximation remaining in our work is the one that associate the modeling of the molecular hydrogen gas mass with the observation of the CO molecule. In that context, only the molecular gas located in zones where the star formation occurred and thus synthesized metals (i.e. in the centers of galaxies) can be probed, completely neglecting the molecular hydrogen formed at the beginning of the universe from primordial gas. Supposedly located in the same regions as the currently observed atomic hydrogen, this primordial molecular gas could impact, if massive enough, the regions where the RC discrepancies are the highest. Already mentioned when postulating the possibility of a disk distributed DM component in Chapter 6, this hypothesis would benefit from a more in-depth study with comparisons between the required DM quantities, observational constraints (e.g. Grenier et al. 2005; Walker et al. 2017; De Paolis et al. 2019; Busch et al. 2021; Seifried

et al. 2022; Guo et al. 2022) and models of formation of this primordial molecular hydrogen (e.g. Sternberg et al. 2021; Maio et al. 2022).

One additional track that would also be particularly interesting to follow is the modeling of the effect of the galactic large-scale magnetic field on the RC. Indeed, such global fields can significantly affect the dynamics of the gas, particularly in the outskirts of the galaxies, resulting in observed rotation velocities wrongly interpreted as simple (gravitational) circular velocities. If they are expected to have a significant impact on the evolution of galaxies and of large-scale structures of the universe, the study of magnetic fields is nevertheless not developed in astrophysics and cosmology as it implies challenging observations and theoretical modelings. However, the idea of magnetic fields to explain the flatness of spirals RCs is not new with field values typical of the MW even removing any need for a DM component (Nelson 1988; Battaner et al. 1992; Battaner & Florido 1995, 2000). While more recent analyses temper these claims with galactic magnetic fields not sufficient to explain the total RC discrepancies, they nevertheless find that these fields cannot be ignored either. In the outskirts of galaxies, the magnetic contribution to the rotation can reach up to $\sim$20 km/s (Sánchez-Salcedo & Reyes-Ruiz 2004) and some features of the observed RCs can only be explained in this context (Ruiz-Granados et al. 2010, 2012; Wulandari & Wulandari 2019). With the recent developments in modelings of spiral galaxies' magnetic fields (Santiago Rodrigues 2018; Shukurov et al. 2019), considering this important, yet not well-known, galactic component constitutes an interesting and promising extension of the present work.

Dark energy & type Ia supernovae

In the second part of this thesis, we switched from extragalactic astrophysics to cosmological observations and took part in the general tendency of the field to develop cosmology-independent analyses. As the development of precision cosmology significantly increases the amount of data available, it currently becomes possible to reduce little by little the assumptions (particularly the use of specific cosmological models) made when retrieving information on the structure and on the evolution of the universe. Hence, various model-independent works have been developed in the last couples of years, in order, among other reasons, to assess the validity of the standard

model of cosmology. To give a few examples of these studies, let us mention the estimates of the expansion rate of the universe via redshift drift determinations (Martins et al. 2016) or via the use of gravitational lenses coupled with standard candles observations (Collett et al. 2019; Wagner & Meyer 2019), the constraints on baryon acoustic oscillations (Marra & Chirinos Isidro 2019) or on cosmic microwave background (Vonlanthen et al. 2010) and the distance-redshift relations derived from gravitational waves and their electromagnetic counterparts (Abbott et al. 2017; Wei 2018).

In this work, we implemented such a cosmology-independent approach for the use of SNe Ia data in the characterization of the dark content of the universe. Here again, we critically analyzed the currently widespread methodology to standardize SNe Ia and proposed a sounder alternative in order to avoid the prior assumption of a particular cosmological model (namely the ΛCDM model). Indeed, such a prior could theoretically bias the data towards the used cosmology and hence nullify all works conducted on model comparison (e.g. Xu & Zhang 2016; Hee et al. 2017). By applying the model-independent calibration developed in this work on the JLA compilation of SNe Ia data, we assessed the validity of such an assumption. Our resulting corrections turned out to be very close to the ΛCDM-based corrections. Therefore, even if a ΛCDM-based calibration is questionable from a theoretical point of view, the potential compliance of SNe Ia data does not happen in practice for the JLA compilation. Previous works of model comparison based on these data do not have to be called into question. However, as this cosmology-independent standardization method has the same degree of complexity than the model-dependent one, it is worth using it in future works, especially if smaller samples are considered, such as the superluminous type Ic supernovae.

The application of our model-independent calibration to such objects would then be a logical and direct extension of this work. In parallel, comprehensive models of the progenitors of SNe Ia as well as of their explosions could replace the use of empirical calibrations, transforming these objects into real standard candles, independent from any cosmology. Recently, a study on pairs of similar SNe Ia showed that the way these data are currently standardized does not take into account all the possible correlations (Fakhouri et al. 2015). There is thus an on-going effort to reduce the dispersion of their intrinsic luminosities to its minimum, particularly focusing on the link with the SN Ia host galaxy, local neighborhood and progenitor (see Rigault et al. (2020) and references within). This effort therefore

brings our understanding of these objects closer to comprehensive models (e.g. Nordin et al. 2018). Moreover, such studies are also necessary to analyze the possible evolution of SNe Ia (and of their progenitors) with redshift (e.g. Milne et al. 2015; Rigault et al. 2020; Foley et al. 2020). This is of vital importance when using distance-redshift relations and Hubble diagrams. Indeed, as these diagrams compare nearby and distant SNe Ia, neglecting their evolution along the life of the universe could severely bias the resulting best-fitting cosmology, potentially to the point of canceling the acceleration of the expansion of the universe (e.g. Podsiadlowski et al. 2006; Rigault et al. 2015; Lee et al. 2021).

Final words

With its tremendous and explosive debut, new-born cosmology has shaken our view of the universe to its core. For a century, its progresses have been in constant acceleration, developing our knowledge and unveiling new challenges to solve. Started in the 1980s with the observations of spiral galaxies rotation curves and magnified only two decades ago with the distance-redshift relation of type Ia supernovae, the understanding of the nature of the puzzling dark content of the universe is nowadays the Holy Grail of cosmology and gathers the whole community towards a common goal. To make the most of the increasingly varied and precise available data, our theories and models have to evolve, constantly re-evaluating the widely accepted approximations and replacing them with more realistic and sounder alternatives.

Your assumptions are your windows on the world.
Scrub them off every once in a while, or the light won't come in.

Alan Alda
Commencement address, Connecticut College, 1980

Used tools and data

This thesis has made use of

- images from the DustPedia project, a collaborative focused research project supported by the European Union under the Seventh Framework Programme (2007-2013) call (proposal no. 606847);
- the SVO Filter Profile Service, supported from the Spanish MINECO through grant AYA2017-84089;
- the NASA/IPAC Infrared Science Archive, funded by the National Aeronautics and Space Administration and operated by the California Institute of Technology;
- the SIMBAD database and the "Aladin sky atlas", operated and developed at CDS, Strasbourg Observatory, France;
- the Astropy, NumPy, SciPy, Matplotlib and sqlite3 Python libraries.

List of publications

Hauret, C., Magain, P. & Biernaux, J. (2018). A cosmology-independent calibration of type Ia supernovae data. *Monthly Notices of the Royal Astronomical Society*, 479(3)

Paper constituting the second part of this thesis

Hauret, C., Magain, P. & Biernaux, J. (2017). Cosmological time, entropy and infinity. *Entropy*, 19(7)

Development of toy cosmological models associating the time of fundamental clocks and the entropy of the region of the universe casually connected to them. In this context, the models describe closed, finite universes in accelerated expansion without recourse to dark energy.

Biernaux, J., Magain, P. & **Hauret, C.** (2017). Analysis of luminosity distributions of strong lensing galaxies: subtraction of diffuse lensed signal. *Astronomy and Astrophysics*, 604

Contribution to the paper via various discussions and manuscript improvements

Bibliography

Aaronson, M., Mould, J., Huchra, J., et al. 1980, The Astrophysical Journal, 239, 12

Abbott, B. P., Abbott, R., Abbott, T. D., et al. 2017, Nature, 551, 85

Accurso, G., Saintonge, A., Catinella, B., et al. 2017, MNRAS, 470, 4750

Afonso, C., Albert, J. N., Andersen, J., et al. 2003, Astronomy and Astrophysics, 400, 951

Akaike, H. 1974, IEEE Transactions on Automatic Control, 19, 716

Alcock, C., Allsman, R. A., Alves, D. R., et al. 2000, The Astrophysical Journal, 542, 281

Amorín, R., Muñoz-Tuñón, C., Aguerri, J. A. L., & Planesas, P. 2016, Astronomy and Astrophysics, 588, A23

Andredakis, Y. C., Peletier, R. F., & Balcells, M. 1995, MNRAS, 275, 874

Angus, G. W., Gentile, G., & Famaey, B. 2016, Astronomy and Astrophysics, 585, A17

Aniyan, S., Freeman, K. C., Gerhard, O. E., Arnaboldi, M., & Flynn, C. 2016, MNRAS, 456, 1484

Appleton, P. N., Davies, R. D., & Stephenson, R. J. 1981, MNRAS, 195, 327

Arp, H. & Kormendy, J. 1972, The Astrophysical Journal Letters, 178, L101

Asplund, M., Amarsi, A. M., & Grevesse, N. 2021, Astronomy and Astrophysics, 653, A141

Aver, E., Olive, K. A., & Skillman, E. D. 2015, Journal of Cosmology and Astroparticle Physics, 2015, 011

Babcock, H. W. 1939, Lick Observatory Bulletin, 498, 41

Bacchini, C., Fraternali, F., Iorio, G., & Pezzulli, G. 2019, Astronomy and Astrophysics, 622, A64

Baes, M. 2020, in Panchromatic Modelling with Next Generation Facilities, ed. M. Boquien, E. Lusso, C. Gruppioni, & P. Tissera, Vol. 341, 26–34

Bahcall, J. N. & Soneira, R. M. 1980, The Astrophysical Journal Supplement Series, 44, 73

Battaglia, G., Fraternali, F., Oosterloo, T., & Sancisi, R. 2006, Astronomy and Astrophysics, 447, 49

Battaner, E. & Florido, E. 1995, MNRAS, 277, 1129

Battaner, E. & Florido, E. 2000, Fundamentals of Cosmic Physics, 21, 1

Battaner, E., Garrido, J. L., Membrado, M., & Florido, E. 1992, Nature, 360, 652

Begeman, K. G., Broeils, A. H., & Sanders, R. H. 1991, MNRAS, 249, 523

Begeman, K. K. G. 1987, PhD thesis, University of Groningen

Bell, E. F. & de Jong, R. S. 2001, The Astrophysical Journal, 550, 212

Bellstedt, S., Robotham, A. S. G., Driver, S. P., et al. 2020, MNRAS

Bendo, G. J., Baes, M., Bianchi, S., et al. 2015, MNRAS, 448, 135

Bendo, G. J., Boselli, A., Dariush, A., et al. 2012, MNRAS, 419, 1833

Bendo, G. J., Joseph, R. D., Wells, M., et al. 2003, The Astronomical Journal, 125, 2361

Bendo, G. J., Wilson, C. D., Pohlen, M., et al. 2010, Astronomy and Astrophysics, 518, L65

Bershady, M. A., Verheijen, M. A. W., Swaters, R. A., et al. 2010, The Astrophysical Journal, 716, 198

Berta, S., Lutz, D., Genzel, R., Förster-Schreiber, N. M., & Tacconi, L. J. 2016, Astronomy and Astrophysics, 587, A73

Betoule, M., Kessler, R., Guy, J., et al. 2014, Astronomy and Astrophysics, 568, A22

Bianchi, L. 2011, Astrophysics and Space Science, 335, 51

Bianchi, S. 2007, Astronomy and Astrophysics, 471, 765

Bianchi, S. 2013, Astronomy and Astrophysics, 552, A89

Biernaux, J., Magain, P., Sluse, D., & Chantry, V. 2016, Astronomy and Astrophysics, 585, A84

Binney, J. & Tremaine, S. 2008, Galactic Dynamics: Second Edition

Blais-Ouellette, S., Amram, P., Carignan, C., & Swaters, R. 2004, Astronomy and Astrophysics, 420, 147

Boch, T. & Fernique, P. 2014, in Astronomical Society of the Pacific Conference Series, Vol. 485, Astronomical Data Analysis Software and Systems XXIII, ed. N. Manset & P. Forshay, 277

Bolatto, A. D., Leroy, A. K., Rosolowsky, E., Walter, F., & Blitz, L. 2008, The Astrophysical Journal, 686, 948

Bolatto, A. D., Wolfire, M., & Leroy, A. K. 2013, Annual Review of Astronomy and Astrophysics, 51, 207

Bolatto, A. D., Wong, T., Utomo, D., et al. 2017, The Astrophysical Journal, 846, 159

Bond, J. R. & Szalay, A. S. 1983, The Astrophysical Journal, 274, 443

Bonnarel, F., Fernique, P., Bienaymé, O., et al. 2000, Astronomy and Astrophysics Supplement, 143, 33

Boquien, M., Burgarella, D., Roehlly, Y., et al. 2019, Astronomy and Astrophysics, 622, A103

Boselli, A., Ciesla, L., Cortese, L., et al. 2012, Astronomy and Astrophysics, 540, A54

Bosma, A. 1978, PhD thesis, University of Groningen

Bosma, A. 1981, The Astronomical Journal, 86, 1791

Bottema, R. 1993, Astronomy and Astrophysics, 275, 16

Bottema, R. 1999, Astronomy and Astrophysics, 348, 77

Bottema, R. & Pestaña, J. L. G. 2015, MNRAS, 448, 2566

Bottema, R., Pestaña, J. L. G., Rothberg, B., & Sanders, R. H. 2002, Astronomy and Astrophysics, 393, 453

Boudet, N., Mutschke, H., Nayral, C., et al. 2005, The Astrophysical Journal, 633, 272

Branch, D. & Tammann, G. A. 1992, Annual Review of Astronomy and Astrophysics, 30, 359

Brandt, J. C. 1960, The Astrophysical Journal, 131, 293

Breda, I., Papaderos, P., & Gomes, J.-M. 2020, Astronomy and Astrophysics, 640, A20

Bregman, J. N. 2007, Annual Review of Astronomy and Astrophysics, 45, 221

Bronkalla, W., Notni, P., & Mutter, A. A. R. 1992, Astronomische

Nachrichten, 313, 1

Brout, D., Sako, M., Scolnic, D., et al. 2019, The Astrophysical Journal, 874, 106

Burgarella, D., Buat, V., & Iglesias-Páramo, J. 2005, MNRAS, 360, 1413

Burkert, A. 1995, The Astrophysical Journal Letters, 447, L25

Burstein, D. 1979, The Astrophysical Journal, 234, 829

Busch, M. P., Engelke, P. D., Allen, R. J., & Hogg, D. E. 2021, The Astrophysical Journal, 914, 72

Calcino, J. & Davis, T. 2017, Journal of Cosmology and Astroparticle Physics, 1, 038

Caldú-Primo, A., Schruba, A., Walter, F., et al. 2013, The Astronomical Journal, 146, 150

Caldwell, J. A. R. & Ostriker, J. P. 1981, The Astrophysical Journal, 251, 61

Camm, G. L. 1950, MNRAS, 110, 305

Cardelli, J. A., Clayton, G. C., & Mathis, J. S. 1989, The Astrophysical Journal, 345, 245

Carignan, C. & Beaulieu, S. 1989, The Astrophysical Journal, 347, 760

Carnall, A. C., Leja, J., Johnson, B. D., et al. 2019, The Astrophysical Journal, 873, 44

Casasola, V., Bianchi, S., De Vis, P., et al. 2020, Astronomy and Astrophysics, 633, A100

Catinella, B., Saintonge, A., Janowiecki, S., et al. 2018, MNRAS, 476, 875

Chevallard, J. & Charlot, S. 2016, MNRAS, 462, 1415

Christensen, C. R., Davé, R., Governato, F., et al. 2016, The Astrophysical Journal, 824, 57

Chynoweth, K. M., Langston, G. I., Yun, M. S., et al. 2008, The Astronomical Journal, 135, 1983

Cimatti, A., Fraternali, F., & Nipoti, C. 2020, Introduction to Galaxy Formation and Evolution: From Primordial Gas to Present-Day Galaxies (Cambridge University Press)

Ciotti, L. & Bertin, G. 1999, Astronomy and Astrophysics, 352, 447

Clark, C. J. R., Verstocken, S., Bianchi, S., et al. 2018, Astronomy and Astrophysics, 609, A37

Collett, T., Montanari, F., & Räsänen, S. 2019, Physical Review Letters, 123, 231101

Combes, F. 2009, Astronomy and Astrophysics, 500, 119

Conley, A., Guy, J., Sullivan, M., et al. 2011, The Astrophysical Journal Supplement, 192, 1

Conroy, C. 2013, Annual Review of Astronomy and Astrophysics, 51, 393

Côté, S., Carignan, C., & Freeman, K. C. 2000, The Astronomical Journal, 120, 3027

Courtes, G. 1982, in Astrophysics and Space Science Library, Vol. 92, IAU Colloq. 67: Instrumentation for Astronomy with Large Optical Telescopes, ed. C. M. Humphries, 123

da Cunha, E., Charlot, S., & Elbaz, D. 2008, MNRAS, 388, 1595

da Cunha, E., Walter, F., Smail, I. R., et al. 2015, The Astrophysical Journal, 806, 110

Daigle, O., Carignan, C., Amram, P., et al. 2006, MNRAS, 367, 469

Dale, D. A., Aniano, G., Engelbracht, C. W., et al. 2012, The Astrophysical Journal, 745, 95

Dale, D. A. & Helou, G. 2002, The Astrophysical Journal, 576, 159

Dale, D. A., Helou, G., Contursi, A., Silbermann, N. A., & Kolhatkar, S. 2001, The Astrophysical Journal, 549, 215

Das, M., McGaugh, S. S., Ianjamasimanana, R., Schombert, J., & Dwarakanath, K. S. 2020, The Astrophysical Journal, 889, 10

Davé, R., Thompson, R., & Hopkins, P. F. 2016, MNRAS, 462, 3265

Davies, J. I., Baes, M., Bianchi, S., et al. 2017, Publications of the Astronomical Society of the Pacific, 129, 044102

de Blok, W. J. G. 2010, Advances in Astronomy, 2010, 789293

de Blok, W. J. G. & McGaugh, S. S. 1997, MNRAS, 290, 533

de Blok, W. J. G., Walter, F., Brinks, E., et al. 2008, The Astronomical Journal, 136, 2648

de Denus-Baillargeon, M. M., Hernandez, O., Boissier, S., Amram, P., & Carignan, C. 2013, The Astrophysical Journal, 773, 173

de Graaff, A., Cai, Y.-C., Heymans, C., & Peacock, J. A. 2019, Astronomy and Astrophysics, 624, A48

de Grijs, R. & Peletier, R. F. 1997, Astronomy and Astrophysics, 320, L21

De Paolis, F., Gurzadyan, A. V., Nucita, A. A., et al. 2019, Astronomy and Astrophysics, 629, A87

de Vaucouleurs, G. 1957, The Astronomical Journal, 62, 69

de Vaucouleurs, G. 1958, The Astrophysical Journal, 128, 465

De Vis, P., Jones, A., Viaene, S., et al. 2019, Astronomy and Astrophysics, 623, A5

den Heijer, M., Oosterloo, T. A., Serra, P., et al. 2015, Astronomy and Astrophysics, 581, A98

Di Cintio, A., Brook, C. B., Dutton, A. A., et al. 2014, MNRAS, 441, 2986

Di Teodoro, E. M. & Fraternali, F. 2015, MNRAS, 451, 3021

Dicaire, I., Carignan, C., Amram, P., et al. 2008, MNRAS, 385, 553

Draine, B. T. 2003, Annual Review of Astronomy and Astrophysics, 41, 241

Draine, B. T., Aniano, G., Krause, O., et al. 2014, The Astrophysical Journal, 780, 172

Draine, B. T., Dale, D. A., Bendo, G., et al. 2007, The Astrophysical Journal, 663, 866

Draine, B. T. & Li, A. 2007, The Astrophysical Journal, 657, 810

Du, M., Ho, L. C., Debattista, V. P., et al. 2020, The Astrophysical Journal, 895, 139

Dubinski, J. & Carlberg, R. G. 1991, The Astrophysical Journal, 378, 496

Dutil, Y. & Roy, J.-R. 2001, The Astronomical Journal, 122, 1644

Einasto, J. 1965, Trudy Astrofizicheskogo Instituta Alma-Ata, 5, 87

Eisenstein, D. J., Weinberg, D. H., Agol, E., et al. 2011, The Astronomical Journal, 142, 72

Eskew, M., Zaritsky, D., & Meidt, S. 2012, The Astronomical Journal, 143, 139

Ewen, H. I. & Purcell, E. M. 1951, Nature, 168, 356

Fabricius, M. H., Saglia, R. P., Fisher, D. B., et al. 2012, The Astrophysical Journal, 754, 67

Fakhouri, H. K., Boone, K., Aldering, G., et al. 2015, The Astrophysical Journal, 815, 58

Filippenko, A. V. & Sargent, W. L. W. 1985, The Astrophysical Journal Supplement Series, 57, 503

Finzi, A. 1963, MNRAS, 127, 21

Fisher, D. B. & Drory, N. 2008, The Astronomical Journal, 136, 773

Fisher, D. B. & Drory, N. 2010, The Astrophysical Journal, 716, 942

Fitzpatrick, E. L. 1999, The Publications of the Astronomical Society of the Pacific, 111, 63

Flagey, N., Boulanger, F., Verstraete, L., et al. 2006, Astronomy and Astrophysics, 453, 969

Flores, R. A. & Primack, J. R. 1994, The Astrophysical Journal Letters, 427, L1

Foley, R. J., Hoffmann, S. L., Macri, L. M., et al. 2020, MNRAS, 491, 5991

Frank, B. S., de Blok, W. J. G., Walter, F., Leroy, A., & Carignan, C. 2016, The Astronomical Journal, 151, 94

Fraternali, F., van Moorsel, G., Sancisi, R., & Oosterloo, T. 2002, The Astrophysical Journal, 123, 3124

Freeman, K. C. 1970, The Astrophysical Journal, 160, 811

Frieman, J. A., Turner, M. S., & Huterer, D. 2008, Annual Review of Astronomy and Astrophysics, 46, 385

Fuchs, B. & Wielen, R. 1987, in NATO Advanced Study Institute (ASI) Series C, Vol. 207, The Galaxy, ed. G. Gilmore & B. Carswell, 375–398

Fumagalli, M., Prochaska, J. X., Kasen, D., et al. 2011, MNRAS, 418, 1796

Gaia Collaboration. 2016, Astronomy and Astrophysics, 595, A1

Gaia Collaboration. 2018, Astronomy and Astrophysics, 616, A1

Galametz, M., Kennicutt, R. C., Albrecht, M., et al. 2012, MNRAS, 425, 763

Galliano, F., Galametz, M., & Jones, A. P. 2018, Annual Review of Astronomy and Astrophysics, 56, 673

Gentile, G., Józsa, G. I. G., Serra, P., et al. 2013, Astronomy and Astrophysics, 554, A125

Genzel, R., Tacconi, L. J., Combes, F., et al. 2012, The Astrophysical Journal, 746, 69

Gerhard, O. & Silk, J. 1996, The Astrophysical Journal, 472, 34

Gerke, J. R. & Kochanek, C. S. 2013, The Astrophysical Journal, 762, 64

Gilmore, G. & Reid, N. 1983, MNRAS, 202, 1025

Gopal Vishwakarma, R. & Narlikar, J. V. 2010, Research in Astronomy and

Astrophysics, 10, 1195

Graham, A. W. 2001, The Astronomical Journal, 121, 820

Greener, M. J., Merrifield, M., Aragón-Salamanca, A., et al. 2021, MNRAS, 502, L95

Grenier, I. A., Casandjian, J.-M., & Terrier, R. 2005, Science, 307, 1292

Gunn, J. E., Lee, B. W., Lerche, I., Schramm, D. N., & Steigman, G. 1978, The Astrophysical Journal, 223, 1015

Guo, H. L., Chen, B. Q., & Liu, X. W. 2022, MNRAS, 511, 2302

Guy, J., Astier, P., Baumont, S., et al. 2007, Astronomy and Astrophysics, 466, 11

Guy, J., Astier, P., Nobili, S., Regnault, N., & Pain, R. 2005, Astronomy and Astrophysics, 443, 781

Hamuy, M., Maza, J., Phillips, M. M., et al. 1993, The Astronomical Journal, 106, 2392

Hamuy, M., Phillips, M. M., Maza, J., et al. 1995, The Astronomical Journal, 109, 1

Han, Y. & Han, Z. 2014, The Astrophysical Journal Supplement Series, 215, 2

Harvey, D., Massey, R., Kitching, T., Taylor, A., & Tittley, E. 2015, Science, 347, 1462

Hatakeyama, T., Kuno, N., Sorai, K., et al. 2017, Publications of the Astronomical Society of Japan, 69, 67

Haynes, M. P. & Giovanelli, R. 1984, The Astronomical Journal, 89, 758

Heald, G., Józsa, G., Serra, P., et al. 2011, Astronomy and Astrophysics, 526, A118

Heald, G. H., Rand, R. J., Benjamin, R. A., & Bershady, M. A. 2007, The Astrophysical Journal, 663, 933

Hee, S., Vázquez, J. A., Handley, W. J., Hobson, M. P., & Lasenby, A. N. 2017, MNRAS, 466, 369

Helfer, T. T., Thornley, M. D., Regan, M. W., et al. 2003, The Astrophysical Journal Supplement Series, 145, 259

Hernandez, O., Carignan, C., Amram, P., Chemin, L., & Daigle, O. 2005, MNRAS, 360, 1201

Herrmann, K. A. & Ciardullo, R. 2009, The Astrophysical Journal, 705, 1686

Hessman, F. V. & Ziebart, M. 2011, Astronomy and Astrophysics, 532, A121

Hillebrandt, W. & Niemeyer, J. C. 2000, Annual Review of Astronomy and Astrophysics, 38, 191

Ho, L. C., Filippenko, A. V., & Sargent, W. L. W. 1997, The Astrophysical Journal Supplement Series, 112, 315

Hoekstra, H., van Albada, T. S., & Sancisi, R. 2001, MNRAS, 323, 453

Hoyle, F. & Fowler, W. A. 1960, The Astrophysical Journal, 132, 565

Hubble, E. 1929, Proceedings of the National Academy of Science, 15, 168

Hughes, T. M., Baes, M., Fritz, J., et al. 2014, Astronomy and Astrophysics, 565, A4

Hunt, L. K., Draine, B. T., Bianchi, S., et al. 2015, Astronomy and Astrophysics, 576, A33

Indebetouw, R., Mathis, J. S., Babler, B. L., et al. 2005, The Astrophysical Journal, 619, 931

Inserra, C. & Smartt, S. J. 2014, The Astrophysical Journal, 796, 87

Inserra, C. & Smartt, S. J. 2015, The Astrophysical Journal, 807, 112

IRAC Instrument Handbook. 2021, Version 3.0.1

Israel, F. P. & Baas, F. 1999, Astronomy and Astrophysics, 351, 10

Jones, A. P., Fanciullo, L., Köhler, M., et al. 2013, Astronomy and Astrophysics, 558, A62

Jovanović, M. 2017, MNRAS, 469, 3564

Just, A., Fuchs, B., Jahreiß, H., et al. 2015, MNRAS, 451, 149

Kalnajs, A. 1983, in Internal Kinematics and Dynamics of Galaxies, ed. E. Athanassoula, Vol. 100, 87–88

Kaneda, H., Suzuki, T., Onaka, T., et al. 2007, Publications of the Astronomical Society of Japan, 59, S463

Kaplinghat, M., Knox, L., & Turner, M. S. 2000, Physical Review Letters, 85, 3335

Kaplinghat, M., Ren, T., & Yu, H.-B. 2020, Journal of Cosmology and Astroparticle Physics, 2020, 027

Kassin, S. A., de Jong, R. S., & Weiner, B. J. 2006, The Astrophysical Journal, 643, 804

Katz, H., Lelli, F., McGaugh, S. S., et al. 2017, MNRAS, 466, 1648

Kauffmann, G., Heckman, T. M., White, S. D. M., et al. 2003, MNRAS, 341, 33

Kelly, P. L., Hicken, M., Burke, D. L., Mandel, K. S., & Kirshner, R. P. 2010, The Astrophysical Journal, 715, 743

Kent, S. M. 1986, The Astronomical Journal, 91, 1301

Kirkpatrick, A., Calzetti, D., Kennicutt, R., et al. 2014, The Astrophysical Journal, 789, 130

Köhler, M., Jones, A., & Ysard, N. 2014, Astronomy and Astrophysics, 565, L9

Kormendy, J. & Kennicutt, Robert C., J. 2004, Annual Review of Astronomy and Astrophysics, 42, 603

Korsaga, M., Amram, P., Carignan, C., & Epinat, B. 2019, MNRAS, 482, 154

Korsaga, M., Carignan, C., Amram, P., Epinat, B., & Jarrett, T. H. 2018, MNRAS, 478, 50

Kowal, C. T. 1968, The Astronomical Journal, 73, 1021

Kranz, T., Slyz, A., & Rix, H.-W. 2003, The Astrophysical Journal, 586, 143

Kregel, M., van der Kruit, P. C., & de Grijs, R. 2002, MNRAS, 334, 646

Kroupa, P. 2001, MNRAS, 322, 231

Kunth, D. & Östlin, G. 2000, The Astronomy and Astrophysics Review, 10, 1

Lagos, C. d. P., Crain, R. A., Schaye, J., et al. 2015, MNRAS, 452, 3815

Lagos, C. d. P., Tobar, R. J., Robotham, A. S. G., et al. 2018, MNRAS, 481, 3573

Lampeitl, H., Smith, M., Nichol, R. C., et al. 2010, The Astrophysical Journal, 722, 566

Lee, Y.-W., Chung, C., Demarque, P., et al. 2021, arXiv e-prints, arXiv:2107.06288

Leitherer, C., Li, I. H., Calzetti, D., & Heckman, T. M. 2002, The Astrophysical Journal Supplement Series, 140, 303

Leja, J., Carnall, A. C., Johnson, B. D., Conroy, C., & Speagle, J. S. 2019, The Astrophysical Journal, 876, 3

Lelli, F., McGaugh, S. S., & Schombert, J. M. 2016a, The Astrophysical Journal, 152, 157

Lelli, F., McGaugh, S. S., & Schombert, J. M. 2016b, The Astrophysical Journal Letters, 816, L14

Lemaître, G. 1927, Annales de la Société Scientifique de Bruxelles, 47, 49

Lequeux, J., Peimbert, M., Rayo, J. F., Serrano, A., & Torres-Peimbert, S. 1979, Astronomy and Astrophysics, 80, 155

Leroy, A. K., Bolatto, A., Gordon, K., et al. 2011, The Astrophysical Journal, 737, 12

Leroy, A. K., Walter, F., Bigiel, F., et al. 2009, The Astronomical Journal, 137, 4670

Leroy, A. K., Walter, F., Brinks, E., et al. 2008, The Astronomical Journal, 136, 2782

Leroy, A. K., Walter, F., Sandstrom, K., et al. 2013, The Astronomical Journal, 146, 19

Li, P., Lelli, F., McGaugh, S., & Schombert, J. 2020, The Astrophysical Supplement Series, 247, 31

Liddle, A. R. 2004, MNRAS, 351, L49

Lilly, S. J. & Longair, M. S. 1984, MNRAS, 211, 833

Lima Neto, G. B., Gerbal, D., & Márquez, I. 1999, MNRAS, 309, 481

Longair, M. S. 2006, The Cosmic Century

López Fune, E., Salucci, P., & Corbelli, E. 2017, MNRAS, 468, 147

Lower, S., Narayanan, D., Leja, J., et al. 2020, The Astrophysical Journal, 904, 33

Magdis, G. E., Daddi, E., Béthermin, M., et al. 2012, The Astrophysical Journal, 760, 6

Magnelli, B., Saintonge, A., Lutz, D., et al. 2012, Astronomy and Astrophysics, 548, A22

Magrini, L., Bianchi, S., Corbelli, E., et al. 2011, Astronomy and Astrophysics, 535, A13

Maio, U., Péroux, C., & Ciardi, B. 2022, Astronomy and Astrophysics, 657, A47

Maiolino, R. & Mannucci, F. 2019, The Astronomy and Astrophysics Review, 27, 3

Makarov, D., Prugniel, P., Terekhova, N., Courtois, H., & Vauglin, I. 2014, Astronomy and Astrophysics, 570, A13

Marasco, A., Fraternali, F., Heald, G., et al. 2019, Astronomy and Astro-

physics, 631, A50

Maraston, C. 1998, MNRAS, 300, 872

Maraston, C. 2005, MNRAS, 362, 799

March, M. C., Trotta, R., Berkes, P., Starkman, G. D., & Vaudrevange, P. M. 2011, MNRAS, 418, 2308

Marra, V. & Chirinos Isidro, E. G. 2019, MNRAS, 487, 3419

Marriner, J., Bernstein, J. P., Kessler, R., et al. 2011, The Astrophysical Journal, 740, 72

Martins, C. J. A. P., Martinelli, M., Calabrese, E., & Ramos, M. P. L. P. 2016, Physical Review D, 94, 043001

Martinsson, T. P. K., Verheijen, M. A. W., Westfall, K. B., et al. 2013, Astronomy and Astrophysics, 557, A131

Mateo, M. L. 1998, Annual Review of Astronomy and Astrophysics, 36, 435

Matthews, L. D. & Wood, K. 2003, The Astrophysical Journal, 593, 721

McGaugh, S. S. & de Blok, W. J. G. 1998, The Astrophysical Journal, 499, 41

McGaugh, S. S. & Schombert, J. M. 2014, The Astronomical Journal, 148, 77

McGaugh, S. S. & Schombert, J. M. 2015, The Astrophysical Journal, 802, 18

McGaugh, S. S., Schombert, J. M., Bothun, G. D., & de Blok, W. J. G. 2000, The Astrophysical Journal, 533, L99

Mediavilla, E., Arribas, S., García-Lorenzo, B., & del Burgo, C. 1997, The Astrophysical Journal, 488, 682

Meidt, S. E., Schinnerer, E., Knapen, J. H., et al. 2012, The Astrophysical Journal, 744, 17

Meidt, S. E., Schinnerer, E., van de Ven, G., et al. 2014, The Astrophysical Journal, 788, 144

Melbourne, J. & Boyer, M. L. 2013, The Astrophysical Journal, 764, 30

Melia, F. 2012, The Astronomical Journal, 144, 110

Mennella, V., Brucato, J. R., Colangeli, L., et al. 1998, The Astrophysical Journal, 496, 1058

Meurer, G. R., Zheng, Z., & de Blok, W. J. G. 2013, MNRAS, 429, 2537

Michelson, A. A. & Pease, F. G. 1921, The Astrophysical Journal, 53, 249

Milne, P. A., Foley, R. J., Brown, P. J., & Narayan, G. 2015, The Astrophysical Journal, 803, 20

Minchev, I., Martig, M., Streich, D., et al. 2015, The Astrophysical Journal Letters, 804, L9

Mogotsi, K. M., de Blok, W. J. G., Caldú-Primo, A., et al. 2016, The Astronomical Journal, 151, 15

Mohlabeng, G. M. & Ralston, J. P. 2014, MNRAS, 439, L16

Moore, B. 1994, Nature, 370, 629

Morrissey, P., Conrow, T., Barlow, T. A., et al. 2007, The Astrophysical Journal Supplement Series, 173, 682

Mosenkov, A. V., Baes, M., Bianchi, S., et al. 2019, Astronomy and Astrophysics, 622, A132

Moustakas, J., Kennicutt, Robert C., J., Tremonti, C. A., et al. 2010, The Astrophysical Journal Supplement, 190, 233

Muñoz-Mateos, J. C., Gil de Paz, A., Zamorano, J., et al. 2009, The Astrophysical Journal, 703, 1569

Muller, C. A. & Oort, J. H. 1951, Nature, 168, 357

Narayan, C. A. & Jog, C. J. 2002a, Astronomy and Astrophysics, 390, L35

Narayan, C. A. & Jog, C. J. 2002b, Astronomy and Astrophysics, 394, 89

Narayanan, D., Conroy, C., Davé, R., Johnson, B. D., & Popping, G. 2018, The Astrophysical Journal, 869, 70

Navarro, J. F., Frenk, C. S., & White, S. D. M. 1996, The Astrophysical Journal, 462, 563

Navarro, J. F., Frenk, C. S., & White, S. D. M. 1997, The Astrophysical Journal, 490, 493

Neill, J. D., Sullivan, M., Howell, D. A., et al. 2009, The Astrophysical Journal, 707, 1449

Nelson, A. H. 1988, MNRAS, 233, 115

Nersesian, A., Xilouris, E. M., Bianchi, S., et al. 2019, Astronomy and Astrophysics, 624, A80

Noll, S., Burgarella, D., Giovannoli, E., et al. 2009, Astronomy and Astrophysics, 507, 1793

Nomoto, K., Kobayashi, C., & Tominaga, N. 2013, Annual Review of Astronomy and Astrophysics, 51, 457

Nordin, J., Aldering, G., Antilogus, P., et al. 2018, Astronomy and Astro-

physics, 614, A71

Norgaard-Nielsen, H. U., Hansen, L., Jorgensen, H. E., Aragon Salamanca, A., & Ellis, R. S. 1989, Nature, 339, 523

Norris, M. A., Meidt, S., Van de Ven, G., et al. 2014, The Astrophysical Journal, 797, 55

Norris, M. A., Van de Ven, G., Schinnerer, E., et al. 2016, The Astrophysical Journal, 832, 198

Obreja, A., Domínguez-Tenreiro, R., Brook, C., et al. 2013, The Astrophysical Journal, 763, 26

Oesch, P. A., Brammer, G., van Dokkum, P. G., et al. 2016, The Astrophysical Journal, 819, 129

Oh, S.-H., de Blok, W. J. G., Walter, F., Brinks, E., & Kennicutt, Robert C., J. 2008, The Astronomical Journal, 136, 2761

Ostriker, J. P. & Peebles, P. J. E. 1973, The Astrophysical Journal, 186, 467

Ostriker, J. P., Peebles, P. J. E., & Yahil, A. 1974, The Astrophysical Journal Letters, 193, L1

Pacifici, C., da Cunha, E., Charlot, S., et al. 2015, MNRAS, 447, 786

Papaderos, P., Breda, I., Humphrey, A., et al. 2022, Astronomy and Astrophysics, 658, A74

Papaderos, P., Loose, H. H., Thuan, T. X., & Fricke, K. J. 1996, Astronomy and Astrophysics Supplement, 120, 207

Paradis, D., Bernard, J. P., & Mény, C. 2009, Astronomy and Astrophysics, 506, 745

Patra, N. N. 2020, MNRAS, 499, 2063

Patterson, F. S. 1940, Harvard College Observatory Bulletin, 914, 9

Paturel, G., Petit, C., Prugniel, P., et al. 2003, Astronomy and Astrophysics, 412, 45

Pawsey, J. L., Payne-Scott, R., & McCready, L. L. 1946, Nature, 157, 158

Peebles, P. J. E. 1982, The Astrophysical Journal Letters, 263, L1

Peeples, M. S., Werk, J. K., Tumlinson, J., et al. 2014, The Astrophysical Journal, 786, 54

Perlmutter, S., Aldering, G., Goldhaber, G., et al. 1999, The Astrophysical Journal, 517, 565

Perlmutter, S., Gabi, S., Goldhaber, G., et al. 1997a, The Astrophysical

Journal, 483, 565

Perlmutter, S., Pennypacker, C. R., Goldhaber, G., et al. 1995, The Astrophysical Journal Letters, 440, L41

Perlmutter, S. A. et al. 1997b, in NATO Advanced Science Institutes (ASI) Series C, Vol. 486, NATO Advanced Science Institutes (ASI) Series C, ed. P. Ruiz-Lapuente, R. Canal, & J. Isern, 749

Persic, M. & Salucci, P. 1991, The Astrophysical Journal, 368, 60

Persic, M., Salucci, P., & Stel, F. 1996, MNRAS, 281, 27

Peters, W. & Kuzio de Naray, R. 2017, MNRAS, 469, 3541

Pfenniger, D., Combes, F., & Martinet, L. 1994, Astronomy and Astrophysics, 285, 79

Phillips, M. M. 1993, The Astrophysical Journal Letters, 413, L105

Pilbratt, G. L., Riedinger, J. R., Passvogel, T., et al. 2010, Astronomy and Astrophysics, 518, L1

Pilyugin, L. S. & Grebel, E. K. 2016, MNRAS, 457, 3678

Pilyugin, L. S. & Thuan, T. X. 2005, The Astrophysical Journal, 631, 231

Planck Collaboration. 2014, Astronomy and Astrophysics, 571, A11

Planck Collaboration. 2015, Astronomy and Astrophysics, 582, A28

Planck Collaboration. 2020, Astronomy and Astrophysics, 641, A1

Podsiadlowski, P., Mazzali, P. A., Lesaffre, P., Wolf, C., & Forster, F. 2006, arXiv e-prints, astro

Pollack, J. B., Hollenbach, D., Beckwith, S., et al. 1994, The Astrophysical Journal, 421, 615

Popescu, C. C. & Tuffs, R. J. 2002, MNRAS, 335, L41

Popescu, C. C., Tuffs, R. J., Dopita, M. A., et al. 2011, Astronomy and Astrophysics, 527, A109

Portinari, L. & Salucci, P. 2010, Astronomy and Astrophysics, 521, A82

Prada, F., Gutierrez, C. M., Peletier, R. F., & McKeith, C. D. 1996, The Astrophysical Journal Letters, 463, L9

Prieto, M., Battaner, E., Sanchez, C., & Beckman, J. 1985, Astronomy and Astrophysics, 146, 297

Prugniel, P. & Simien, F. 1997, Astronomy and Astrophysics, 321, 111

Pskovskii, I. P. 1977, Astronomicheskii Zhurnal, 54, 1188

Read, J. I., Agertz, O., & Collins, M. L. M. 2016a, MNRAS, 459, 2573

Read, J. I., Iorio, G., Agertz, O., & Fraternali, F. 2016b, MNRAS, 462, 3628

Read, J. I., Lake, G., Agertz, O., & Debattista, V. P. 2008, MNRAS, 389, 1041

Regan, M. W., Thornley, M. D., Bendo, G. J., et al. 2004, The Astrophysical Journal Supplement Series, 154, 204

Relatores, N. C., Newman, A. B., Simon, J. D., et al. 2019, The Astrophysical Journal, 887, 94

Renzini, A. & Ciotti, L. 1993, The Astrophysical Journal Letters, 416, L49

Revaz, Y., Pfenniger, D., Combes, F., & Bournaud, F. 2009, Astronomy and Astrophysics, 501, 171

Richards, E. E., van Zee, L., Barnes, K. L., et al. 2018, MNRAS, 476, 5127

Riess, A. G., Filippenko, A. V., Challis, P., et al. 1998, The Astronomical Journal, 116, 1009

Riess, A. G., Press, W. H., & Kirshner, R. P. 1996, The Astrophysical Journal, 473, 88

Rigault, M., Aldering, G., Kowalski, M., et al. 2015, The Astrophysical Journal, 802, 20

Rigault, M., Brinnel, V., Aldering, G., et al. 2020, Astronomy and Astrophysics, 644, A176

Robertson, A., Massey, R., Eke, V., et al. 2018, MNRAS, 476, L20

Robotham, A. S. G., Bellstedt, S., Lagos, C. d. P., et al. 2020, MNRAS, 495, 905

Rogstad, D. H. & Shostak, G. S. 1972, The Astrophysical Journal, 176, 315

Rubin, V. C., Ford, W. K. J., & Thonnard, N. 1978, The Astrophysical Journal Letters, 225, L107

Rubin, V. C., Ford, W. K. J., & Thonnard, N. 1980, The Astrophysical Journal, 238, 471

Ruiz-Granados, B., Battaner, E., Calvo, J., Florido, E., & Rubiño-Martín, J. A. 2012, The Astrophysical Journal Letters, 755, L23

Ruiz-Granados, B., Rubiño-Martín, J. A., Florido, E., & Battaner, E. 2010, The Astrophysical Journal Letters, 723, L44

Ryle, M. & Vonberg, D. D. 1946, Nature, 158, 339

Saburova, A. S., Kasparova, A. V., & Katkov, I. Y. 2016, MNRAS, 463, 2523

Saintonge, A., Catinella, B., Tacconi, L. J., et al. 2017, The Astrophysical Journal Supplement Series, 233, 22

Salim, S., Boquien, M., & Lee, J. C. 2018, The Astrophysical Journal, 859, 11

Salim, S., Rich, R. M., Charlot, S., et al. 2007, The Astrophysical Journal Supplement Series, 173, 267

Salucci, P., Lapi, A., Tonini, C., et al. 2007, MNRAS, 378, 41

Samurović, S., Vudragović, A., & Jovanović, M. 2015, MNRAS, 451, 4073

Sánchez-Salcedo, F. J. & Reyes-Ruiz, M. 2004, The Astrophysical Journal, 607, 247

Sancisi, R. 2004, in Dark Matter in Galaxies, ed. S. Ryder, D. Pisano, M. Walker, & K. Freeman, Vol. 220, 233

Sancisi, R. & Allen, R. J. 1979, Astronomy and Astropysics, 74, 73

Sandage, A. 1968, The Observatory, 88, 91

Sanders, R. H. 2010, The Dark Matter Problem: A Historical Perspective

Sandstrom, K. M., Leroy, A. K., Walter, F., et al. 2013, The Astrophysical Journal, 777, 5

Santiago Rodrigues, L. F. 2018, GalMag: A Python tool for computing realistic galactic magnetic fields, Zenodo

Sarkar, S. & Jog, C. J. 2020, MNRAS, 499, 2523

Schaap, W. E., Sancisi, R., & Swaters, R. A. 2000, Astronomy and Astrophysics, 356, L49

Schlafly, E. F. & Finkbeiner, D. P. 2011, The Astrophysical Journal, 737, 103

Schlafly, E. F., Finkbeiner, D. P., Schlegel, D. J., et al. 2010, The Astrophysical Journal, 725, 1175

Schlegel, D. J., Finkbeiner, D. P., & Davis, M. 1998, The Astrophysical Journal, 500, 525

Schmidt, B. P., Suntzeff, N. B., Phillips, M. M., et al. 1998, The Astrophysical Journal, 507, 46

Schmidt, M. 1959, The Astrophysical Journal, 129, 243

Schoenmakers, R. H. M., Franx, M., & de Zeeuw, P. T. 1997, MNRAS, 292, 349

Schombert, J., McGaugh, S., & Lelli, F. 2019, MNRAS, 483, 1496

Schruba, A., Leroy, A. K., Walter, F., et al. 2011, The Astronomical Journal, 142, 37

Schwarz, G. 1978, Annals of Statistics, 6, 461

Schwarzschild, M. 1954, The Astronomical Journal, 59, 273

Scolnic, D., Brout, D., Carr, A., et al. 2021, arXiv e-prints, arXiv:2112.03863

Scolnic, D. M., Jones, D. O., Rest, A., et al. 2018, The Astrophysical Journal, 859, 101

Seifried, D., Beuther, H., Walch, S., et al. 2022, MNRAS, 512, 4765

Sérsic, J. L. 1968, Atlas de Galaxias Australes

Shariff, H., Jiao, X., Trotta, R., & van Dyk, D. A. 2016, The Astrophysical Journal, 827, 1

Shi, K., Huang, Y. F., & Lu, T. 2012, MNRAS, 426, 2452

Shukurov, A., Rodrigues, L. F. S., Bushby, P. J., Hollins, J., & Rachen, J. P. 2019, Astronomy and Astrophysics, 623, A113

Simon, J. D., Bolatto, A. D., Leroy, A., & Blitz, L. 2003, The Astrophysical Journal, 596, 957

Smith, M. W. L., Vlahakis, C., Baes, M., et al. 2010, Astronomy and Astrophysics, 518, L51

Smith, S. 1936, The Astrophysical Journal, 83, 23

Sofue, Y. & Rubin, V. 2001, Annual Review of Astronomy and Astrophysics, 39, 137

Spekkens, K. & Sellwood, J. A. 2007, The Astrophysical Journal, 664, 204

Spergel, D. N. & Steinhardt, P. J. 2000, Physical Review Letters, 84, 3760

Sternberg, A., Gurman, A., & Bialy, S. 2021, The Astrophysical Journal, 920, 83

Stetson, P. B. 1987, Publications of the Astronomical Society of the Pacific, 99, 191

Stevens, J. A., Amure, M., & Gear, W. K. 2005, MNRAS, 357, 361

Stil, J. M. & Israel, F. P. 2002a, Astronomy and Astrophysics, 389, 29

Stil, J. M. & Israel, F. P. 2002b, Astronomy and Astrophysics, 389, 42

Sullivan, M., Conley, A., Howell, D. A., et al. 2010, MNRAS, 406, 782

Sullivan, M., Guy, J., Conley, A., et al. 2011, The Astrophysical Journal, 737, 102

Sutter, J. & Fadda, D. 2022, The Astrophysical Journal, 926, 82

Suzuki, N., Rubin, D., Lidman, C., et al. 2012, The Astrophysical Journal, 746, 85

Swaters, R. A., Bershady, M. A., Martinsson, T. P. K., et al. 2014, The Astrophysical Journal Letters, 797, L28

Swaters, R. A., Sancisi, R., van Albada, T. S., & van der Hulst, J. M. 2011, The Astrophysical Journal, 729, 118

Swaters, R. A., Sancisi, R., van der Hulst, J. M., & van Albada, T. S. 2012, MNRAS, 425, 2299

Takamiya, T. & Sofue, Y. 2000, The Astrophysical Journal, 534, 670

Tanimura, H., Hinshaw, G., McCarthy, I. G., et al. 2019, MNRAS, 483, 223

Thilker, D. A., Bianchi, L., Meurer, G., et al. 2007a, The Astrophysical Journal Supplement Series, 173, 538

Thilker, D. A., Boissier, S., Bianchi, L., et al. 2007b, The Astrophysical Journal Supplement Series, 173, 572

Thornley, M. D. 1996, The Astrophysical Journal Letters, 469, L45

Tremonti, C. A., Heckman, T. M., Kauffmann, G., et al. 2004, The Astrophysical Journal, 613, 898

Tripp, R. 1997, Astronomy and Astrophysics, 325, 871

Tripp, R. 1998, Astronomy and Astrophysics, 331, 815

Tsikoudi, V. 1979, The Astrophysical Journal, 234, 842

Tully, R. B. & Fisher, J. R. 1977, Astronomy and Astrophysics, 500, 105

Übler, H., Naab, T., Oser, L., et al. 2014, MNRAS, 443, 2092

Valenzuela, O., Hernandez-Toledo, H., Cano, M., et al. 2014, The Astronomical Journal, 147, 27

van Albada, T. S., Bahcall, J. N., Begeman, K., & Sancisi, R. 1985, The Astrophysical Journal, 295, 305

van de Hulst, H. C. 1945, Nederlandsch Tijdschrift voor Natuurkunde, 11, 210

van de Hulst, H. C., Raimond, E., & van Woerden, H. 1957, Bulletin of the Astronomical Institutes of the Netherlands, 14, 1

Van de Vyvere, L. 2018, Master's thesis, ULiège

van der Kruit, P. C. 1981, Astronomy and Astrophysics, 99, 298

van der Kruit, P. C. 1988, Astronomy and Astrophysics, 192, 117

van der Kruit, P. C. & Freeman, K. C. 2011, Annual Review of Astronomy and Astrophysics, 49, 301

van der Kruit, P. C. & Searle, L. 1981, Astronomy and Astrophysics, 95, 105

Verheijen, M. A. W. 1997, PhD thesis, University of Groningen

Verstappen, J., Fritz, J., Baes, M., et al. 2013, Astronomy and Astrophysics, 556, A54

Visser, M. 2004, Classical and Quantum Gravity, 21, 2603

Vitral, E. & Mamon, G. A. 2020, Astronomy and Astrophysics, 635, A20

Vittorio, N. & Silk, J. 1984, The Astrophysical Journal Letters, 285, L39

Vonlanthen, M., Räsänen, S., & Durrer, R. 2010, Journal of Cosmology and Astroparticle Physics, 2010, 023

Wagner, J. & Meyer, S. 2019, MNRAS, 490, 1913

Walcher, J., Groves, B., Budavári, T., & Dale, D. 2011, Astrophysics and Space Science, 331, 1

Walker, M. A., Tuntsov, A. V., Bignall, H., et al. 2017, The Astrophysical Journal, 843, 15

Wall, R. E., Kilic, M., Bergeron, P., et al. 2019, MNRAS, 489, 5046

Walter, F., Brinks, E., de Blok, W. J. G., et al. 2008, The Astronomical Journal, 136, 2563

Wei, J.-J. 2018, The Astrophysical Journal, 868, 29

Wei, J.-J., Wu, X.-F., & Melia, F. 2015a, The Astronomical Journal, 149, 165

Wei, J.-J., Wu, X.-F., Melia, F., & Maier, R. S. 2015b, The Astronomical Journal, 149, 102

Wenger, M., Ochsenbein, F., Egret, D., et al. 2000, Astronomy and Astrophysics Supplement, 143, 9

Werner, M. W., Roellig, T. L., Low, F. J., et al. 2004, The Astrophysical Journal Supplement Series, 154, 1

Wiese, W. L. & Fuhr, J. R. 2009, Journal of Physical and Chemical Reference Data, 38, 565

Williams, B. F., Dalcanton, J. J., Stilp, A., et al. 2010, The Astrophysical Journal, 709, 135

Wolfire, M. G., Hollenbach, D., & McKee, C. F. 2010, The Astrophysical Journal, 716, 1191

Wulandari & Wulandari, H. 2019, in Journal of Physics Conference Series, Vol. 1245, Journal of Physics Conference Series, 012018

Xilouris, E. M., Byun, Y. I., Kylafis, N. D., Paleologou, E. V., & Papamastorakis, J. 1999, Astronomy and Astrophysics, 344, 868

Xu, Y.-Y. & Zhang, X. 2016, European Physical Journal C, 76, 588

Yoachim, P. & Dalcanton, J. J. 2006, The Astronomical Journal, 131, 226

York, D. G., Adelman, J., Anderson, John E., J., et al. 2000, The Astronomical Journal, 120, 1579

Young, J. S. & Scoville, N. 1982, The Astrophysical Journal Letters, 260, L41

Young, L. M., Bureau, M., Davis, T. A., et al. 2011, MNRAS, 414, 940

Ysard, N., Köhler, M., Jones, A., et al. 2015, Astronomy and Astrophysics, 577, A110

Yuan, H. B., Liu, X. W., & Xiang, M. S. 2013, MNRAS, 430, 2188

Zaritsky, D., Kennicutt, Robert C., J., & Huchra, J. P. 1994, The Astrophysical Journal, 420, 87

Zasov, A. V. & Terekhova, N. A. 2013, Astronomy Letters, 39, 291

Zhang, J., Abraham, R., van Dokkum, P., Merritt, A., & Janssens, S. 2018, The Astrophysical Journal, 855, 78

Zibetti, S., Charlot, S., & Rix, H.-W. 2009, MNRAS, 400, 1181

Zschaechner, L. K. & Rand, R. J. 2015, The Astrophysical Journal, 808, 153

Zwaan, M. A., Briggs, F. H., Sprayberry, D., & Sorar, E. 1997, The Astrophysical Journal, 490, 173

Zwicky, F. 1933, Helvetica Physica Acta, 6, 110

Zwicky, F. 1937, The Astrophysical Journal, 86, 217